

TOWARDS SELECTIVE C–H OXIDATION WITH AEROBICALLY GENERATED
HYPERVALENT IODINE REAGENTS

A Dissertation

by

ASHLEY DANIELLE CARDENAL

Submitted to the Office of Graduate and Professional Studies of
Texas A&M University
in partial fulfillment of the requirements for the degree of

DOCTOR OF PHILOSOPHY

Chair of Committee,	David C. Powers
Committee Members,	Karen L. Wooley
	Oleg V. Ozerov
	Michael Nippe
	Thomas D. Meek
Head of Department,	Simon W. North

December 2019

Major Subject: Chemistry

Copyright 2019 Ashley D. Cardenal

ABSTRACT

Enzymatic hydrocarbon oxidation allows for the selective late-stage functionalization of complex molecules by utilizing O₂ as the terminal oxidant. We are interested in the development of abiological systems that enable functionalization of complex organic molecules using O₂ by utilizing metal-organic framework (MOF) catalysts to effect selective C–H oxidation and to combine this with the environmentally-friendly generation of hypervalent iodine reagents, commonly used oxidants in MOF catalysis.

To reach this long-term goal, there are fundamental studies that must be addressed. In order to access the pore space of a porous material for selective catalysis, the rates of substrate diffusion and catalytic reaction must be considered. Thus, it is necessary to understand what is known of the diffusion processes relevant to porous materials and methods for probing the relative rates of catalytic reactions to diffusion. In this vein, we investigate the use of *cis*-decalin as a stereochemical probe for differentiating interstitial from interfacial catalysis for C–H oxidation reactions for porphyrinic metal-organic frameworks. In addition, we examine the effect particle size has on oxidation selectivity and further optimize reaction conditions for the selective oxidation of 1,4-*cis*-dimethylcyclohexane by 2-D layered porphyrinic materials. Lastly, we initiate investigations of coupling the generation of hypervalent iodine chemistry with MOF catalysis by first analyzing the reactivity of hypervalent iodine reagents with soluble analogues of the metaloclusters that serve as secondary building units in MOFs.

ACKNOWLEDGEMENTS

Upon entering the chemistry graduate program at Texas A&M University, Dr. Simon North gave a speech to our incoming class comparing graduate school to a roller coaster. The highs are exhilarating and propel you forward, and the lows can be dark and difficult. Without the support of many people in the department and my life in general, I am certain this coaster would have derailed.

I would like to thank the chemistry department as a whole. As the first student in a new group there was a lot of borrowing in the early days. For example, my first reaction in the Powers lab was completed with almost entirely borrowed glassware. The rate of our success and growth as a lab has certainly been expediated by being a part of such a supportive department and I hope that our group continues in this example of good departmental stewardship.

On the technical side, I'd like to thank Dr. Nattamai Bhuvanesh for teaching me fundamental X-ray crystallography and Dr. Greg Wiley and Dr. Doug Elliot for many great NMR-centered discussions and for frequently going out of their way to help us with experiments.

I have had the support and mentorship of many wonderful teachers in the department. Dr. Joanna Pellois, Dr. Soon Mi Lim, and Dr. Tamara Powers have led by example and demonstrated to me what it means to be an enthusiastic teacher. These three individuals have tremendously impacted my philosophy of teaching and have shown me what can be achieved with student-focused instruction. On a more personal note, Dr.

Powers and Dr. Pellois, in addition to Sandy Horton, have been extremely supportive in times of stress and for that I am extremely grateful.

I'd like to thank my group as a whole for being colleagues and friends over the last four years. Thank you all for being patient with my literal and figurative mess. I have had the pleasure of working with a slew of talented undergraduates, and I'd like to specifically thank Kacey Ortiz, Victoria Akwaowo, and Connor Hoffman for keeping the lab fun. In addition, I'd like to thank Sung-min Hyun for listening to my crazy ideas, working together on a failed project, and being a great friend. Working with you was some of the best times I had in the lab and I know that wherever you end up that you will be an excellent scientist and a great collaborator.

I am deeply grateful to my advisor, Dr. David Powers, for giving me a chance to learn from him and grow as a researcher in his lab. Starting a new lab is hard, grant writing seems like a pain, and I cannot even imagine the stress of dealing with a lab budget (especially in a group who loves running mass-specs), but Dave has always found the time to discuss progress and ideas with us. Though impatient when waiting for research results, I am incredibly impressed with the patience that was afforded to me during struggles with my mental health. I know I have not been the easiest graduate student to work with and I am indescribably thankful to Dave for helping me stay in the program. Without such a supportive advisor, I certainly would not be in my current position.

Lastly, my warmest thanks to my partner, John Cain. You know better than anyone the blood, sweat, and tears that have gone into this degree. Thank you for letting me bounce ideas off you, for providing constructive criticism for multiple pieces of writing

and talks, and for being there in times of emotional need. Thank you for expanding my scientific horizons by discussing your research and scientific interests with me. Thank you for the encouragement I needed to keep moving forward. I know you hate roller coasters; thank you for riding this one with me.

CONTRIBUTORS AND FUNDING SOURCES

Contributors

This work was supervised by a dissertation committee consisting of my advisor Professor David Powers, Professors Karen Wooley, Oleg Ozerov, and Michael Nippe of the Chemistry Department and Professor Thomas Meek of the Department of Biochemistry and Biophysics.

Dr. Wen-Yang Gao contributed equally to the work presented in Chapter I. Dr. Hye-Jeong Park contributed synthetic methods that were used to generate porous catalysts in Chapter II. Cody Chalker acquired and analyzed the SEM images described in Chapter II. Optical microscopy described in Chapter III was conducted in the lab of Dr. James Batteas and with help from Cody Chalker. Asim Maity completed the EPR studies and developed a new synthesis for 2-(*tert*-butylsulfonyl)iodosylbenzene as described in Chapter IV. Sung-Min Hyun completed the $^1\text{O}_2$ trapping studies featured in Chapter IV. Dr. Wen-Yang Gao completed the work associated with exposing zinc containing MOFs to iododisubstituted benzenes in Chapter IV. The structure of the 2-(*tert*-butylsulfonyl)iodosylbenzene adduct with HFIP was solved with the help of Anuvab Das. Lastly, Rahym Ashirov grew the crystal of the zirconium cluster 2-(*tert*-butylsulfonyl)iodosylbenzene adduct and Dr. Wen-Yang Gao solved and refined the structure.

Funding Sources

This work was also made possible in part by financial support from Texas A&M University, The Welch Foundation (A-1907), and the National Science Foundation

(CAREER-1848135). Use of the Advanced Photon Source, an Office of Science User Facility operated for the U.S. Department of Energy (DOE) Office of Science by Argonne National Laboratory, was supported by the U.S. DOE under Contract No. DE-AC02-06CH11357.

NOMENCLATURE

MOF	metal-organic framework
QENS	quasi-elastic neutron scattering
PFG	pulsed-field gradient
btc	1,3,5-benzenetricarboxylate
TOF	turnover frequency
dobdc	2,5-dioxido-1,4-benzenedicarboxylate
TON	turnover number
tbhp	<i>tert</i> -butylhydroperoxide
bpdc	4,4'-biphenyldicarboxylate
bdc	1,4-benzenedicarboxylate
hmtt	5,5',10,10',15,15'-hexamethyltruxene-2,7,12-tricarboxylate
KIE	kinetic isotope effect
H ₂ bdpb	1,4-bis[(3,5-dimethyl)-pyrazol-4-yl]benzene
dabco	1,4-diazabicyclo[2.2.2]octane
tcpp	5,10,15,20-tetrakis(4-carboxyphenyl)porphyrin
btp	1,3-di(1H-1,2,4-tirazol-1-yl)propane
DEA	<i>N,N'</i> -diethylacetamide
DEF	<i>N,N'</i> -diethylformamide
DMF	<i>N,N'</i> -dimethylformamide
bpy	4,4'-bipyridine

bpe	1,2-bis(4-pyridyl)ethane
bpp	1,3-bis(4-pyridyl)propane
TGA	thermogravimetric analysis
PXRD	powder X-ray diffraction
SXRD	single-crystal X-ray diffraction
EtOH	ethanol
HAA	hydrogen-atom abstraction
GC	gas chromatography
DMSO	dimethylsulfoxide
tpp	5,10,15,20-tetraphenylporphyrin
tmpp	5,10,15,20-tetrakis(4-methoxycarbonylphenyl)porphyrin
SEM	scanning electron microscopy
NMR	nuclear magnetic resonance spectrometry
FTIR	Fourier transform infrared spectrometry
UV-vis	ultraviolet-visible
ICP-MS	inductively coupled plasma mass spectrometry
MALDI-TOF	matrix-assisted laser desorption/ionization time-of-flight
VP	variable pressure
UHP	ultra-high purity
FID	flame ionization detector
ANOVA	analysis of variance
3c-4e	3-center, 4-electron bond

^s PhIO	2-(<i>tert</i> -butylsulfonyl)iodosylbenzene
HFIP	hexafluoroisopropanol
NBO	natural bond order
DQCOSY	double-quantum filtered correlated spectroscopy
HSQC	heteronuclear single quantum coherence spectroscopy
HMBC	heteronuclear multiple bond correlation
EPR	electron paramagnetic resonance spectroscopy
PPF	porphyrin-paddlewheel framework
PBN	<i>N-tert</i> -butyl- α -phenylnitron

TABLE OF CONTENTS

	Page
ABSTRACT	ii
ACKNOWLEDGEMENTS	iii
CONTRIBUTORS AND FUNDING SOURCES.....	vi
NOMENCLATURE.....	viii
TABLE OF CONTENTS	xi
LIST OF FIGURES.....	xiii
LIST OF TABLES	xviii
PROLOGUE.....	xix
CHAPTER I INTRODUCTION: <i>IN OPERANDO</i> ANALYSIS OF DIFFUSION IN POROUS METAL-ORGANIC FRAMEWORK CATALYSTS.....	1
I.1 Introduction.....	1
I.2 Diffusion in Porous Solids.....	4
I.3 Measuring Sorbate Diffusion Rates.....	7
I.4 Critical Need for <i>In Operando</i> Tools to Study Diffusion during Catalysis.....	11
I.5 <i>In Operando</i> Probes of Diffusion in MOF Catalysis.....	11
I.6 Conclusions.....	25
CHAPTER II <i>CIS</i> -DECALIN OXIDATION AS A STEREOCHEMICAL PROBE OF INTERSTITIAL VS. INTERFACIAL MOF CATALYSIS.....	28
II.1 Introduction	28
II.2 Results and Discussion.....	29
II.3 Conclusions	56
II.4 Experimental Details	57
CHAPTER III CRYSTAL-SIZE DEPENDENCE ON <i>CIS</i> -DECALIN OXIDATION AND THE SYNTHESIS OF 2-D LAYERED MATERIALS FOR STEREORETENTIVE C–H OXIDATION.....	73
III.1 Introduction.....	73

III.2 Results and Discussion.....	74
III.3 Conclusion.....	87
III.4 Experimental Details.....	88
CHAPTER IV IODOSYLBENZENE COORDINATION CHEMISTRY RELEVANT TO MOF CATALYSIS.....	
IV.1 Introduction.....	96
IV.2 Results and Discussion	105
IV.3 Conclusions.....	127
IV.4 Experimental Details.....	129
CHAPTER V CONCLUDING REMARKS AND FUTURE DIRECTIONS	
REFERENCES.....	194

LIST OF FIGURES

	Page
Figure I-1 Impact of relative rates of diffusion and catalyst turnover..	3
Figure I-2 Diffusion mechanisms in porous materials..	6
Figure I-3 Size selective epoxidation with a core-shell catalyst..	14
Figure I-4 Epoxidation rate as a function of pore size..	16
Figure I-5 Cyclohexane oxidation in an isorecticular family of materials..	18
Figure I-6 Particle size dependent rate of oxidation of cyclohexene..	20
Figure I-7 Particle size dependent rate of oxidation for triphenyl methane..	21
Figure I-8 Stereoselectivity as a tool to differentiate interstitial from interfacial catalysis..	23
Figure I-9 Kinetic isotope effects as a tool for probing the rate of diffusion in relation to rate of C–H amination. .	25
Figure II-1 Solvothermal Synthesis of Fe(btp) and characterization by PXRD.....	31
Figure II-2 UV-vis spectroscopy of Fe(btp) and its constituents.	32
Figure II-3 Digestion of Fe(btp) allows for linker quantification..	33
Figure II-4 IR spectrum of Fe(btp) indicates presence of NO ₃ ⁻	34
Figure II-5 The simulated structures of Fe(btp) with (a) AA and (b) AB stacking.	35
Figure II-6 Single crystal X-ray diffraction images of Fe(btp) ..	36
Figure II-7 The PXRD analysis of Fe(btp) for AA and AB stacking.....	37
Figure II-8 Single crystal X-ray diffraction image of Fe(bpy)	39
Figure II-9 Comparison of the PXRD pattern of Fe(bpy) with the simulated and experimental PXRD patterns for PPF-3 and PPF-5 materials, which feature AB- and AA-stacking motifs, respectively.....	39
Figure II-10 PXRD of Fe(btp) , Fe(bpy) , Fe(bpe) , Fe(bpp) , and Fe(dabco)	40

Figure II-11 Diffuse reflectance spectra of Fe(btp) , Fe(bpy) , Fe(bpe) , and Fe(bpp)	40
Figure II-12 IR spectra of Fe(btp) , Fe(bpy) , Fe(bpe) , and Fe(bpp) prepared by solvothermal (a) synthesis and by (b) linker-exchange chemistry.	41
Figure II-13 PXRD patterns of solids prepared with increasing quantities of bpy.	43
Figure II-14 PXRD patterns of solids prepared with increasing quantities of btp.....	44
Figure II-15 Collapse of Fe(btp) long-range structure. PXRD patterns for Fe(btp)	45
Figure II-16 TGA data for porous materials.	46
Figure II-17 CO ₂ sorption isotherms for Fe(btp)	47
Figure II-18 <i>In situ</i> variable-pressure PXRD data obtained for Fe(btp) during activation and with high-pressure CH ₄ loading..	48
Figure II-19 <i>In situ</i> variable-pressure PXRD data obtained for Fe(btp) during high-pressure CO ₂ loading..	49
Figure II-20 Absorptivity of rhodamine 6G in CH ₃ CN and DMSO.	51
Figure II-21 Epimerization of <i>cis</i> -decalin-derived radicals provides a mechanism to generate both <i>cis</i> - and <i>trans</i> - 2.1 during radical hydroxylation.....	52
Figure II-22 SEM data of as-synthesized and ground Fe(btp)	54
Figure II-23 Histogram of particle distribution in (a) unground and (b) ground Fe(btp)	55
Figure III-1 The influence of synthesis time on Fe(btp) crystal growth..	77
Figure III-2 20 μm crystals of Fe(btp)	78
Figure III-3 3.3 μm crystals of Fe(btp)	79
Figure III-4 PXRD comparison of [Zn ₂ Fe(tcpp)] _n with literature materials..	81
Figure III-5 Potential stacking models for [Zn ₂ Fe(tcpp)] _n , featuring (a) AA and (b) AB stacking modes.	82
Figure III-6 Comparison of [Zn ₂ Fe(tcpp)] _n with models generated from AA and AB stacking modes.....	83
Figure III-7 Oxidation of <i>cis</i> -decalin by [Zn ₂ Fe(tcpp)] _n	84

Figure III-8 PXRDs of $[\text{Zn}_2\text{Fe}(\text{tcpp})]_n$ before and after catalysis.	87
Figure IV-1 Summary of high-valent organoiodine compounds.	98
Figure IV-2 Orbital picture for the 3c-4e bonding in hypervalent iodine compounds. ...	99
Figure IV-3 Typical reaction chemistry of hypervalent iodine compounds..	101
Figure IV-4 The oxidation of styrene by iodosyl- and iodyllarene.	104
Figure IV-5 NBO orbitals of 2-(<i>tert</i> -butylsulfonyl)iodosylbenzene.	106
Figure IV-6 Formation of an adduct between HFIP and 2-(<i>tert</i> -butylsulfonyl)iodosylbenzene.	108
Figure IV-7 2-D NMR data of 2-(<i>tert</i> -butylsulfonyl)iodosylbenzene..	109
Figure IV-8 2-D NMR data of the adduct made between HFIP and 2-(<i>tert</i> -butylsulfonyl)iodosylbenzene.	110
Figure IV-9 Dissolution of $(\text{PhIO})_n$ polymer occurs upon its dissolution in HFIP to form 4.4	111
Figure IV-10 The aerobic oxidation of 2-(<i>tert</i> -butylsulfonyl)iodobenzene..	112
Figure IV-11 Various methods for the synthesis of 2-(<i>tert</i> -butylsulfonyl)iodosylbenzene.	113
Figure IV-12 EPR experiments demonstrate preparation-sensitive behavior of 2-(<i>tert</i> -butylsulfonyl)iodosylbenzene.	115
Figure IV-13 Effect of light on 2-(<i>tert</i> -butylsulfonyl)iodosylbenzene prepared by Method B.C.	116
Figure IV-14 EPR spectrum obtained following PBN addition to KClO_3	116
Figure IV-15 IR spectra of 2-(<i>tert</i> -butylsulfonyl)iodosylbenzene synthesized by Method B and KClO_3	117
Figure IV-16 Kinetics for the disproportionation of 2-(<i>tert</i> -butylsulfonyliodosyl)benzene.	119
Figure IV-17 Summary of observations 1-4.	122
Figure IV-18 Ligand exchange chemistry observed between Zn_2 and Zr_6 metal clusters with iodosylbenzene.	124

Figure IV-19 Reaction of Zr ₆ cluster with 2-(<i>tert</i> -butylsulfonyl)iodosylbenzene..	126
Figure IV-20 Reaction of iodosylbenzene with HFIP.....	139
Figure IV-21 Reaction of 2-(<i>tert</i> -butylsulfonyl)iodosylbenze with acetic acid.....	146
Figure IV-22 EPR spectrum obtained following PBN addition to 2-(<i>tert</i> -butylsulfonyl)iodosylbenzene prepared by Method B.....	147
Figure IV-23 EPR spectrum obtained following PBN additions to 2-(<i>tert</i> -butylsulfonyl)iodosylbenzene prepared by Method D.	149
Figure IV-24 Light sensitivity of 2-(<i>tert</i> -butylsulfonyl)iodosylbenzene upon addition of KClO ₃	151
Figure IV-25 Comparison of first and second order fits for disproportion of 2-(<i>tert</i> -butylsulfonyl)iodosylbenzene.....	153
Figure IV-26 Disproportionation of 2-(<i>tert</i> -butylsulfonyl)iodosylbenzene at 74.0 °C..	154
Figure IV-27 Disproportionation of 2-(<i>tert</i> -butylsulfonyl)iodosylbenzene at 71.3 °C..	155
Figure IV-28 Disproportionation of 2-(<i>tert</i> -butylsulfonyl)iodosylbenzene at 58.2 °C..	156
Figure IV-29 Disproportionation of 2-(<i>tert</i> -butylsulfonyl)iodosylbenzene at 47.8 °C..	157
Figure IV-30 Disproportionation of 2-(<i>tert</i> -butylsulfonyl)iodosylbenzene at 32.2 °C..	158
Figure IV-31 Summary of temperature-dependent disproportionation kinetics. Summary of obtained disproportionation rate data in the form of (a) Arrhenius and (b) Eyring plots, which allow for the calculation of E _a , ΔH [‡] , and ΔS [‡]	159
Figure IV-32 Exposure of 2-(<i>tert</i> butylsulfonyl)(diacetoxyiodo)benzene to acetaldehyde.	162
Figure IV-33 Exposure of 2-(<i>tert</i> butylsulfonyl)(diacetoxyiodo)benzene to CoCl ₂ ..	163
Figure IV-34 Exposure of 2-(<i>tert</i> -butylsulfonyl)(diacetoxyiodo)benzene to Co(OAc) ₃	164
Figure IV-35 Aldehyde promoted aerobic oxidation of 2-(<i>tert</i> -butylsulfonyl)(diacetoxyiodo)benzene (4.5).....	166
Figure IV-36 Oxidation of 2-(<i>tert</i> -butylsulfonyl)iodosylbenene with peracetic acid. ...	168

Figure IV-37 Generation of $^1\text{O}_2$ During Oxidation of 2-(<i>tert</i> -butylsulfonyl)iodobenzene with peracetic acid.	170
Figure IV-38 Reduction of 2-(<i>tert</i> -butylsulfonyl)iodosylbenzene with H_2O_2	172
Figure IV-39 Reduction of 2-(<i>tert</i> -butylsulfonyl)iodylbenzene (4.2) with H_2O_2	174
Figure IV-40 Reaction of iodosylbenzene with $[\text{Zn}_2(\text{benzoate})_4\text{py}_2]$	176
Figure IV-41 Reaction of iodosylbenzene with $\text{Zr}_6\text{O}_4(\text{OH})_4(\text{OMc})_{12}$	178
Figure IV-42 Reaction of 2- <i>tert</i> -butylsulfonyliodosylbenzene with $[\text{Zn}_2(\text{benzoate})_4\text{py}_2]$	180
Figure IV-43 Reaction of 2-(<i>tert</i> -butylsulfonyl)iodosylbenzene with $\text{Zr}_6\text{O}_4(\text{OH})_4(\text{OMc})_{12}$	182
Figure IV-44 Exposure of UiO-67 to 2-(<i>tert</i> -butylsulfonyl)iodosylbenzene	183
Figure IV-45 Exposure of UiO-67 to iodosylbenzene..	184
Figure IV-46 Exposure of MOF-508b to 2-(<i>tert</i> -butylsulfonyl)iodosylbenzene..	185
Figure IV-47 Exposure of MOF-508b to iodosylbenzene.	186
Figure IV-48. Generation of 4.5 from 4.1	189
Figure IV-49 $^{13}\text{C}\{^1\text{H}\}$ NMR of 4.5	189
Figure IV-50 ^1H NMR experiment demonstrating equilibrium of 4.1 with AcOD.	190

LIST OF TABLES

	Page
Table II-1 Zn:Fe and Fe(tcpp):linker ratio calculated from ICP-MS and NMR/UV-vis experiments, respectively, of Fe(btp) , Fe(bpy) , Fe(bpe) , and Fe(bpp)	34
Table II-2 Comparison of the unit cell parameters of Fe(btp) , Fe(bpy) , and Fe(bpe) with PPF-3-Zn/Fe and PPF-5-Zn/Ni.....	42
Table II-3 Summary of results from dye-uptake experiments	50
Table II-4 Oxidation of <i>cis</i> -decalin affords a mixture of <i>cis</i> - and <i>trans</i> -decahydronaphthalen-9-ol (2.1). Catalysis with soft material Fe(btp) affords the highest selectivity.	54
Table III-1 Summary of results for one-way ANOVA	79
Table III-2 Optimization of oxidation of <i>cis</i> -1,4-dimethylcyclohexane	86
Table III-3 Catalyst loading screening for oxidation of <i>cis</i> -1,4-dimethylcyclohexane by [Zn ₂ Mn(tcpp)] _n	95
Table IV-1 Analysis of select bond distances in iodosylarene 4.1 and adducts of 4.1 with transition metal complexes.	126
Table IV-2 Atomic coordinates of the optimized structures of 4.1	140
Table IV-3 Atomic coordinates of the optimized structure of 4.1 ·HFIP.....	141
Table IV-4 Atomic coordinates of the optimized structure of PhIO.....	142
Table IV-5 ¹³ C and ¹ H assignments for 4.1	144
Table IV-6 ¹³ C and ¹ H Assignments for 4.1 ·HFIP.....	145
Table IV-7 Crystal data and structure refinement for 4.1 ·HFIP	187
Table IV-8 Crystal data and structure refinement for 4.8	188

PROLOGUE

Oxidative functionalization of aliphatic C–H bonds provides a means to rapidly increase molecular complexity and converts simple molecules into more complex scaffolds. Applications extend from valorization of simple hydrocarbons,¹⁻² such as the transformation of methane to methanol, to the oxidation of more complex molecules,³⁻⁴ such as the site-selective oxidation of drug molecules to produce drug metabolites for pharmaceutical evaluation. Biology has addressed both of these challenges using enzymes that couple O₂ reduction with C–H oxidation.⁵ For these reasons, the mimicry of biological enzymes as catalysts towards both fine chemical⁴ and commodity chemical synthesis⁶ is a major frontier of research. We are interested in pursuing the development of catalysts that effect C–H oxidation with high stereo- and regioselectivity and coupling this chemistry with new methods of utilizing O₂ as a terminal oxidant.

Substantial research has been devoted to the development of catalysts for C–H oxidation using both homogeneous^{1,3,7-8} and heterogeneous^{2,9} systems. In the field of heterogeneous catalysis, metal-organic frameworks (MOFs), which are porous scaffolds composed of inorganic nodes bound together by organic linking units have been advanced as promising catalysts for C–H oxidation chemistry due to 1) the potential for site isolation of the catalyst, which protects them from unproductive or deleterious side reactions and 2) the opportunity to leverage the pore space as a unique chemical environment, which may garner novel site-selectivity.¹⁰⁻¹⁵ In comparison to zeolite catalysts, which are microporous aluminosilicate materials that are often utilized as porous catalyst materials, MOFs offer a wider range of functionality: a variety of organic linking units and metal

clusters can be combined to access diverse topologies, a range of pore sizes (up to >1 nm in diameter), and varied catalytic properties.¹⁶ A major challenge inherent to utilizing a porous material as a catalyst is the role of diffusion and the relationship between the rates of diffusion and catalyst turnover.¹⁷ In order to leverage the pore space of a MOF, diffusion must be relatively quick in comparison to the rate of catalyst turnover.¹⁷ Chapter I summarizes the processes at play in the diffusion of molecules into porous materials, enumerates factors that effect substrate adsorption, and highlights techniques that allow for differentiation of interstitial from interfacial MOF catalysis. Chapter II represents a research effort towards the goal of probing whether catalysis occurs interstitially or interfacially on porous materials by utilizing *cis*-decalin oxidation as a stereochemical probe.¹⁵ Finally, in Chapter III we build on this preliminary work by examining the effect of particle size on the selectivity of *cis*-decalin oxidation and by exploring stereospecific C–H oxidation of other substrates.

Towards the development of methods to allow for the utilization of O₂ as a selective oxidant, our group has harnessed reactive intermediates produced during the autoxidation of aldehydes for the oxidation of aromatic iodine compounds to generate hypervalent iodine reagents.¹⁸⁻¹⁹ Hypervalent iodine reagents, such as iodosylbenzene and its derivatives, can serve as oxidants in a number of organic transformations, such as the oxidative 1,2-difunctionalization of olefins,²⁰ oxidative dearomatization chemistry,²¹⁻²⁴ and cross-coupling reactions.²⁵ Utilizing aldehyde autoxidation to generate hypervalent iodine has allowed these transformations to be conducted with catalytic amounts of iodoarene species and with O₂ as the terminal oxidant.¹⁸

Hypervalent iodine compounds are also used extensively as group transfer reagents towards organometallic catalysts.²⁶ These reagents are important in the field of C–H functionalization chemistry, where iodosylbenzene is frequently paired with organometallic catalysts to effect oxidation of C–H bonds.^{3,27} As a result of commonly being paired with catalysts capable of C–H functionalization, hypervalent iodine compounds have found utilization with metal-organic frameworks featuring porphyrinic^{15,28} and salen-based²⁹⁻³¹ organic linkers and catalytically active metal-oxo clusters nodes.³²⁻³³ We are interested in the potential of coupling the catalytic, aerobic generation of hypervalent iodine reagents with catalysts capable of mediating C–H oxidation reactions. This effort would ultimately allow for the oxidation of C–H bonds by utilizing O₂ as a terminal oxidant and the ability to generate these oxidants *in situ* with catalytic amounts of aryl iodide would circumvent the often needed (super)stoichiometric amounts of oxidant required for these transformations.

The insolubility of hypervalent iodine reagents, such as iodosylbenzene, presents a challenge in regard to coupling the generation of these compounds with catalysis conducted by porous, heterogeneous materials. Towards this end, 2-(*tert*-butylsulfonyl)iodosylbenzene, a hypervalent iodine reagent with enhanced solubility, has gained popularity in the MOF community.^{31-32,34} Chapter IV highlights that a common method for the preparation of this reagent produces material that contains trace impurities, resulting in unpredictable disproportionation kinetics, submits a new method for its preparation, and examines the interaction of 2-(*tert*-butylsulfonyl)iodosylbenzene and

iodosylbenzene with homogeneous, molecular analogues of clusters commonly utilized as the inorganic nodes in MOFs.

CHAPTER I

INTRODUCTION: *IN OPERANDO* ANALYSIS OF DIFFUSION IN POROUS METAL-ORGANIC FRAMEWORK CATALYSTS*

I.1 Introduction

Metal-organic frameworks (MOFs) are porous materials comprised of polytopic organic ligands and metal-containing secondary building units.^{10,35} In analogy to zeolitic catalysts, which are heterogeneous catalysts based on porous aluminosilicate materials that are commonly employed in industrial-scale applications,³⁶⁻³⁹ the ability to generate single-site catalysts in MOFs has led to the development of MOF catalysts for a variety of commodity-scale chemical transformations.⁴⁰⁻⁴⁶ In analogy to enzymatic catalysis, in which substrate confinement within enzyme active sites can alter the chemo- and stereoselectivity of substrate functionalization, the potential to systematically tune the topology and chemical functionality of molecular-scale pores within MOFs has inspired application of MOF catalysts to chemical transformations of relevance to fine chemicals.^{10,29,47-48} Among the motivations for applying MOF catalysts to fine chemical synthesis is the potential to utilize host-guest interactions to access stereo- or chemoselectivities that are orthogonal to those accessible with solution-phase catalysts.^{15,49-51} The intense study of MOF porosity has largely focused on application of MOFs in gas storage and separation,⁵²⁻⁵⁵ which rely on diffusion of low-density, small gaseous substrates into activated porous materials. In order to rationally apply MOF

* Data, figures, and text in this chapter were adapted with permission from reference Gao, W. -Y.; Cardenal, A. D.; Wang, C. -H.; Powers, D. C. *Chem. Eur. J.* **2019**, *25*, 3465–3476), copyright 2018 the John Wiley and Sons, Inc.

catalysts to fine chemical synthesis, understanding the design parameters that control the diffusion of relatively large, stereochemically complex substrates through solvent-filled porous materials is required.

The intrinsically high porosity of many MOFs implies that the majority of available catalyst sites are housed at interstitial sites, with a relatively small number of solvent-exposed, interfacial sites. For example, if one considers an idealized $0.25 \times 0.25 \times 0.25$ mm cubic crystal of MOF-5 (where the surface area of a single face of the unit cell is 0.0625 \AA^2), only 0.006% of Zn_4O clusters are located on external crystal surfaces. The relative abundance of interstitial sites may lead to the assumption that catalysis with highly porous MOF catalysts proceeds at the far more abundant interstitial sites. However, if substrate diffusion is slower than catalyst turnover and the activity of interfacial and interstitial catalyst sites is similar, then the reaction will proceed at or near the surface of catalyst particles and very few interstitial catalyst sites will contribute to the observed catalysis (**Figure I-1a**).⁵⁶⁻⁵⁷ In contrast, if diffusion is faster than catalyst turnover, most or all the catalytic active sites will participate in the observed catalysis (**Figure I-1b**). The ability to access and utilize interstitial sites for substrate functionalization catalysis depends intimately on the relative rates of substrate functionalization and diffusion.

This Chapter discusses critical issues that impact the diffusion of sorbates in solvated porous materials, which is necessary in utilizing MOF catalysts for fine chemical synthesis. First, the diffusional processes available to substrates within porous materials are summarized. Second, the critical factors that influence substrate diffusion rates in porous materials — the relative size of substrate and pore, the enthalpy of adsorption, the

presence of crystal defects, surface barriers, and crystallite size — are described. Third, we discuss available *in operando* tools for the evaluation of substrate diffusion during catalysis. *In operando* tools that evaluate the relative rates of catalyst turnover and substrate diffusion are critical because absolute diffusion rates are rarely available and intrinsic catalyst turnover frequencies are challenging to obtain for heterogeneous catalysts.⁵⁸ We anticipate that improved understanding of the mobility of stereochemically complex molecules into and within porous materials will provide the rationale to develop new MOF catalysts for fine-chemical applications.

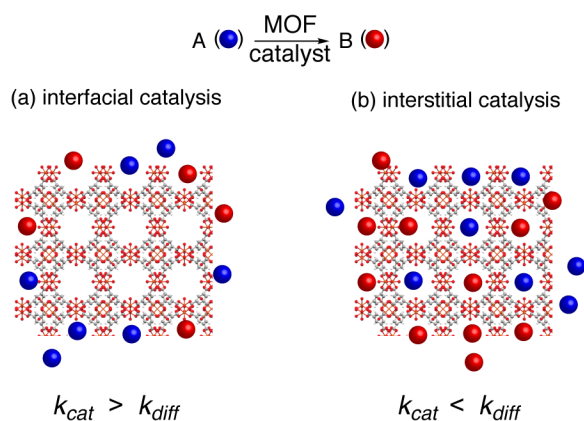


Figure I-1 Impact of relative rates of diffusion and catalyst turnover. The relative rates of substrate diffusion and catalyst turnover dictate the fraction of potential catalyst sites that are utilized in catalysis. (a) If diffusion is slower than catalyst turnover, only interfacial catalyst sites will participate in catalysis. (b) If diffusion is faster than catalyst turnover, interstitial catalyst sites will contribute to catalysis.

I.2 Diffusion in Porous Solids

Fick's law of diffusion relates the flux of a molecule through a given cross-sectional area to the concentration gradient across which the molecule is moving.⁵⁹ Molecular diffusivity (*i.e.* the diffusion coefficient) is a molecule-specific descriptor of a given molecule's propensity to diffuse through a given medium.⁵⁹⁻⁶⁰ Diffusivity depends on the mean-free-path of the diffusing species, which is the average distance a molecule travels between successive intermolecular collisions. In bulk, the mean-free-path of a diffusing molecule is limited by collisions with other molecules. In porous materials, the mean-free-path of a diffusing molecule is limited by collisions with other diffusing molecules as well as by collisions with the pore walls. The introduction of collisions between diffusing molecules and pore walls inherently depresses the diffusivity of molecules in porous materials relative to the bulk phase. The extent to which the diffusivity is inhibited within a porous material is referred to as the degree of confinement.⁶¹⁻⁶² Related concepts, such as the tortuosity factor or the labyrinth factor have been developed to describe the impact of pore confinement on diffusing small molecules in porous substrates.⁶³⁻⁶⁴ Depending on the degree of confinement of a sorbate within a porous material, four diffusional regimes have been described (**Figure I-2**).

1. Molecular diffusion: When the density of the sorbate is high or the pore holes are large, the mean-free-path of sorbate molecules is dominated by sorbate-sorbate collisions; the role of pore wall/surface is relatively insignificant. This diffusion regime is also referred to as ordinary diffusion.⁶⁴

2. Knudsen diffusion: When the density of the sorbate is low or the pores become smaller, the mean-free-path of diffusing sorbate molecules is dominated by collisions between the sorbate and the pore wall.^{60,65}

3. Intracrystalline diffusion: When the pore diameter is similar to the sorbate size, diffusion proceeds via a hopping mechanism in which the sorbate travels along the pore wall. This mechanistic regime is dominated by strong interaction of the sorbate with the pore wall. Intracrystalline diffusion is also referred to as surface, configurational, zeolitic, or micropore diffusion.⁶⁶

4. Molecular sieving: When a potential sorbate is larger than the available pores, diffusion of the sorbate into the pore does not proceed.⁶⁷⁻⁶⁸ Under some conditions, such as low-temperature, even sorbates that are smaller than the pore dimensions can display prohibitively slow diffusion.⁶⁷ Network flexibility or fluxionality can sometimes enable diffusion of guests that are larger than the pore size measured by crystallography.⁶⁹

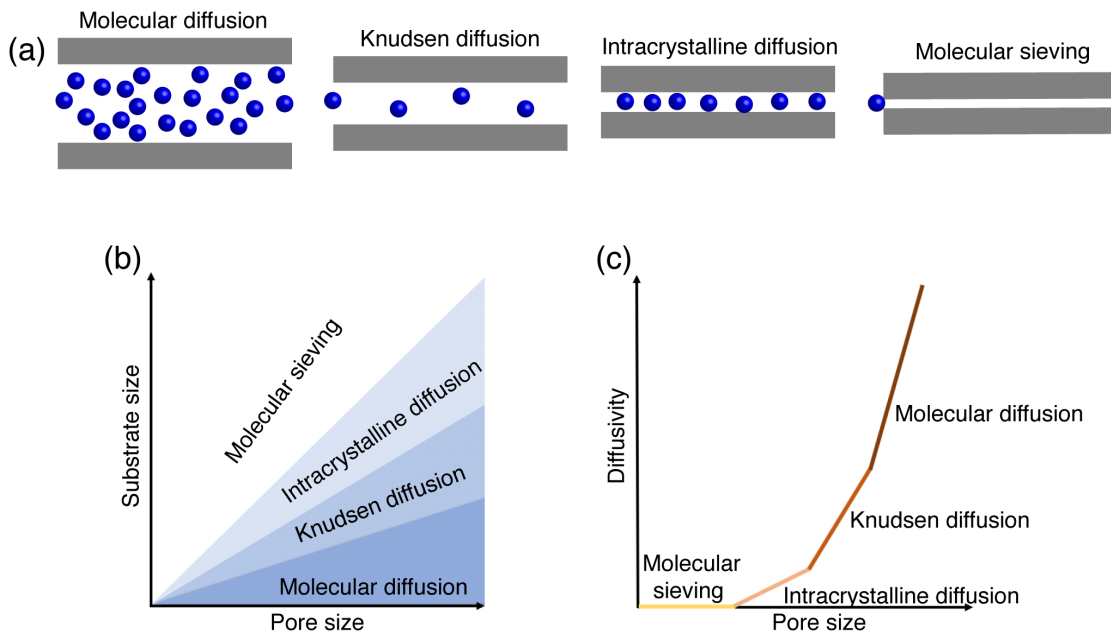


Figure I-2 Diffusion mechanisms in porous materials. (a) The mechanisms of diffusion of sorbates in porous materials depend on the degree of confinement of the sorbate. (b) Illustration of the relationship between substrate and pore size on the mode of sorbate diffusion. (c) Illustration of the relationship of pore size on diffusivity for a given sorbate.

The effective diffusion rate of a sorbate arises from contributions of all diffusion processes that are available to the sorbate within a given porous material and depends on factors such as pore size, substrate size, adsorption enthalpy, material flexibility, and the presence of defects. In addition to the barriers to diffusion within a porous material, surface barriers, which inhibit diffusion of a sorbate from the bulk phase into a porous material, must be considered.^{66,70-71} For example, collapse of the crystallographically determined pore structure at crystallite interfaces or strong multi-layer sorption, which leads to either the narrowing or blockage of the accessible pore windows, both contribute to barriers that sorbates must confront at particle boundaries.⁶⁵ In addition, in multi-

component systems such as those encountered in catalysis, other components present in the reaction mixture can give rise to diffusional barriers by generating a boundary layer around porous particles.

I.3 Measuring Sorbate Diffusion Rates

The diffusivity of small molecules in porous materials has received substantial attention, both from experimental and theoretical investigators.⁶¹ Significant effort has been dedicated to developing experimental tools to quantify diffusion rates in porous materials.⁷²⁻⁷³ Diffusion processes can be classified as either transport diffusion or self-diffusion. Transport diffusion is the net flux of molecules across a concentration gradient, such as the uptake of small-molecule sorbates into activated MOFs. Self-diffusion is the process by which molecules translate in space in the absence of a concentration gradient. An example of self-diffusion is the exchange of position between two sorbate molecules resulting from random Brownian motion.

Broadly, the available experimental techniques to measure diffusivity can be categorized as non-equilibrium measurements, which probe transport diffusion — including spectroscopic methods,⁷⁴⁻⁷⁷ gravimetric methods (gravimetric or quartz-crystal microbalance),⁷⁸⁻⁸¹ zero length column⁸²⁻⁸³ and coherent quasi-elastic neutron scattering (QENS)⁸⁴⁻⁸⁵ — or equilibrium measurements, which evaluate self-diffusion — such as pulsed-field gradient (PFG) NMR,⁸⁶⁻⁸⁷ incoherent QENS⁸⁴ and other labeling experiments.⁸⁸⁻⁸⁹ Depending on the length scale of diffusion that is probed by a given technique, experiments are further classified as either macroscopic techniques (e.g.,

gravimetric methods and zero length column), which evaluate diffusion over hundreds of micrometers,⁹⁰ or microscopic techniques (e.g., PFG NMR, QENS, interference microscopy, and IR micro-imaging), which typically evaluate diffusion over distances of a few micrometers or less.⁶⁵ Macroscopic techniques can probe both surface barriers and diffusional barriers within the pore, whereas microscopic experiments investigate a much smaller domain with focus on diffusion within the pore. Thus, unsurprisingly, discrepancies in diffusivities have been observed when rates derived from macroscopic and microscopic measurements are compared.⁷³

In this section, selected examples of MOF-based experiments that highlight critical factors that impact the diffusivity of small molecules within porous materials are discussed.

1.3.1 Pore Size

The impact of pore size on sorbate diffusivity has been extensively studied in zeolites. In general, substrate diffusion is significantly faster in hierarchical mesoporous zeolites than in analogous microporous materials.⁵⁹ Fewer studies have systematically examined the impact of pore size on substrate diffusivity in MOFs. Li *et al.* reported the kinetic separation of propane and propylene by systematically changing the aperture size of a family of ZIF-8 isostructures.⁹¹ The observed kinetic separation was attributed to the faster diffusion rate of propylene than that of propane, which is controlled by pore size. Network flexibility can substantially influence the diffusion rate of guest molecules. For example, Jobic and Maurin *et al.* demonstrated that CO₂ diffusivity in MIL-53(Cr), a

material that displays substantial network flexibility, varied by two orders of magnitude in response to changing pore dimensions.⁸⁵

1.3.2 Substrate Size

Lin *et al.* examined substrate diffusion rates in solvated MOFs using luminescence quenching experiments. These experiments, which relied on diffusion of variously sized amine-based quenchers (*i.e.* NEt_3 , NPr_3 , NBu_3 , EtNiPr_2 , and 4-MeOPhNPh₂), demonstrated a negative correlation between quencher size and diffusivity.⁹²

1.3.3 Enthalpy of Adsorption

Ramsahye *et al.* utilized a combination of QENS measurements and molecular dynamics simulations to demonstrate that the diffusivity of N_2 (kinetic diameter = 3.6 Å) is higher than that of CO_2 (kinetic diameter = 3.3 Å) through the small channel of MIL-91(Ti).⁹³ The contrasting diffusion rates were attributed to the higher enthalpy of CO_2 adsorption than N_2 . Similarly, the faster diffusion of CH_4 than CO_2 in NPC-4, a Cu_2 paddlewheel-based MOF, was attributed to the higher enthalpy of adsorption of CO_2 compared to CH_4 (kinetic diameter = 3.8 Å).⁹⁴

1.3.4 Surface Barriers

In addition to diffusional barriers through porous materials, surface barriers, which inhibit the entrance of small-molecule sorbates into the crystallites of a porous material, can be present. Using interference microscopy and Monte Carlo simulations, Kärger *et al.* demonstrated the presence of a substantial surface barrier for the diffusion of small hydrocarbons into $\text{Zn}(\text{tbip})$ (tbip = 5-tert-butyl-isophthalate).⁷⁰ The authors proposed that the observed surface barrier was due to blockage of interfacial pore apertures. Heinke *et*

al. reported an investigation of the diffusivity of cyclohexane into a series of thin- films of HKUST-1 that displayed varying thicknesses.⁹⁵ These experiments demonstrated that cyclohexane diffusion through HKUST-1 proceeds via an intracrystalline diffusion mechanism. In addition to examining pristine thin films, the authors also investigated diffusion into films that had been exposed to moisture. Diffusion into these films displayed substantial surface barriers, which was attributed to collapse of the interfacial structure and attendant aperture blockage. This study indicates that surface barriers are not an intrinsic property of HKUST-1 and highlights the importance of considerations, such as environmental moisture, on MOF surfaces and sorbate uptake kinetics.

1.3.5 Crystallite Size

The impact of crystallite size on diffusion is particularly pronounced with small crystallites.⁹⁶ Tanaka and Denayer *et al.* reported that *n*-butanol uptake in small crystallites of ZIF-8 (0.06–2.1 μm) was limited by surface barriers, while the diffusion rate of larger crystallites (88 μm) was governed by intracrystalline diffusion.⁹⁷ In contrast, Ruthven *et al.* observed no change in diffusivities when studying diffusion of several gases into multiple crystallite sizes of 4 Å (7.3–40 μm) and 5 Å (7.3–55 μm) zeolites.⁹⁸⁻⁹⁹ For large crystals of Cu_3btc_2 (btc = 1,3,5-benzenetricarboxylate, HKUST-1) (0.7, 1.0 and 1.3 mm) the diffusivity of CO_2 differed in the range of 0.0014 – 0.0020 mm^2/s with crystal size.⁸⁰

1.3.6 Experimental Conditions

In addition to factors related to the structure of the porous material and the specific sorbate of interest, diffusion kinetics are also influence by experimental conditions such

as temperature,¹⁰⁰⁻¹⁰¹ the concentration/loading of the sorbate,^{94,102} and the orientation of crystallites with respect to the sorbate solution.¹⁰³⁻¹⁰⁴

I.4 Critical Need for *In Operando* Tools to Study Diffusion during Catalysis

Direct measurements of absolute sorbate diffusion rates are rarely directly relevant to the development of new catalysts because diffusion rates are typically measured using pristine samples of porous materials and a single diffusing substrate. Catalytic reactions are inherently multicomponent systems: the spatially dependent concentrations of starting materials, products, and reagents (each of which have unique adsorption enthalpies) can change as a function of reaction progress. In addition, the average crystallite size of porous catalyst materials, the presence of structural defects, and other materials properties can change during catalysis, for example, in response to mechanical stirring. Knowledge of the absolute diffusivities of substrates, products, and reagents would be useful if catalyst turnover frequencies (TOFs), average crystallite size, and active site concentration were also known. However, these parameters can be challenging to determine for many heterogeneous catalysts.⁵⁸ Therefore, in order to probe the relative rates of diffusion and reaction, the development of unique tools to provide *in operando* analysis of diffusion during porous catalysis is highly desired.

I.5 *In Operando* Probes of Diffusion in MOF Catalysis

A variety of experimental approaches have been advanced to assess whether MOF catalysis proceeds at interfacial or interstitial catalyst sites (*i.e.* experiments that evaluate

the relative rates of diffusion and catalyst turnover). This section describes *in operando* approaches that have been developed to experimentally evaluate the role of diffusion on the observed kinetics of catalysis. A series of strategies that examine both surface barriers and barriers within the porous material during catalysis have been developed. Broadly, these strategies can be classified as 1) evaluation of catalysis with core-shell architectures in which catalytically active materials are encased in inactive shells to remove potential interfacial sites, 2) systematic examination of the kinetics of substrate functionalization as a function of pore size using isorecticular catalysts, 3) interrogation of the impact of crystallite size on the outcome of a transformation of interest, and 4) experiments in which the chemo- or stereoselectivity of MOF catalysts is examined in comparison to homogeneous catalyst. In addition to these experimental approaches, this section discusses the use of kinetic isotope effects in C–H oxidation reactions as a strategy to examine the relative rates of diffusion within porous materials and interstitial chemical reactions in the absence of potential surface barriers.

1.5.1 Core-Shell Catalyst Architectures

Core-shell architectures, in which a MOF catalyst core is confined within a shell of a non-catalytically active material, have been utilized to probe the relative contributions of interfacial and interstitial sites in MOF catalysis. Encapsulation of a catalyst particle within a catalytically inactive shell effectively removes potential interfacial catalyst sites. Comparison of catalysis using core-shell motifs with catalysis that is accomplished with the un-modified parent material provides indirect information about the potential role of interfacial sites in catalysis. Here we highlight results obtained from core-shell structures

that were generated by 1) post-synthetic demetallation of interfacial catalyst sites and 2) growing non-catalytically active materials around catalyst particles.

Post-Synthetic Demetallation During studies of olefin epoxidation chemistry catalyzed by Mn(salen)-based MOFs, Hupp and Nguyen *et al.* demonstrated that treatment of the catalyst material with H₂O₂ resulted in the selective oxidative demetallation of surface exposed metalloporphyrin sites, thus generating core-shell catalyst particles.³⁰ The activity of these core-shell structures in the epoxidation of a mixture of olefins **1.1** and **1.2**, which are chemically similar but differently sized substrates, was assayed using 2-(*tert*-butylsulfonyl)iodosylbenzene (**1.5**) as the terminal oxidant (**Figure I-3**). The core-shell catalysts were found to be highly selective for the epoxidation of the smaller substrate: at early reaction times a 1 : 16 mixture of **1.3** and **1.4** was obtained. In comparison, the as-synthesized catalyst material was poorly size selective when challenged with a mixture of **1.1** and **1.2** (produced a 1 : 2 mixture of **1.3** : **1.4**). At longer reaction times, the product selectivity generated by the core-shell materials was found to decrease substantially (1 : 2), which was attributed to crystal fragmentation and the concurrent generation of poorly selective interfacial catalyst sites. Together, these observations suggest that diffusion of (at least) large substrates is slow relative to epoxidation, and that interfacial catalyst sites are kinetically significant in epoxidation chemistry catalyzed by as-synthesized Mn(salen)-based MOFs. Upon surface demetallation, surface reactivity is suppressed allowing for a size-selective process.

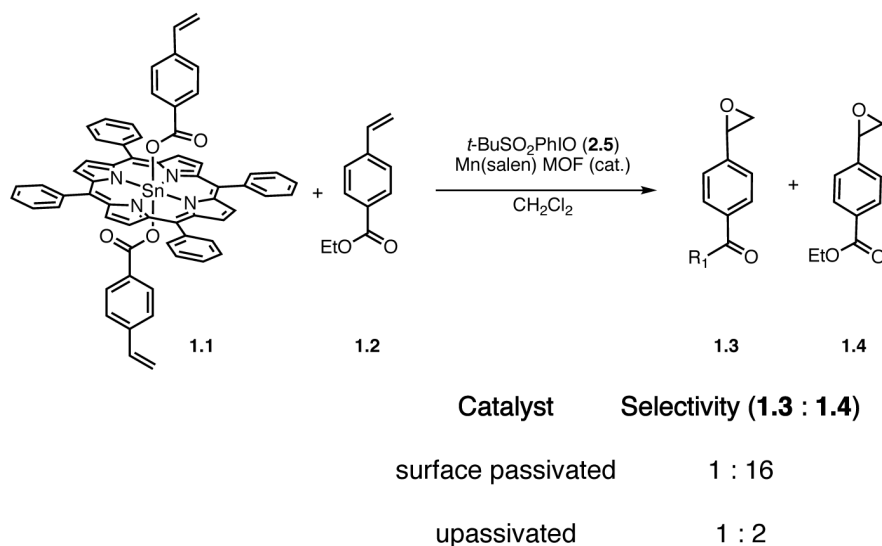


Figure I-3 Size selective epoxidation with a core-shell catalyst. Hupp and Nguyen *et al.* examined the epoxidation of mixtures of olefins **1.1** and **1.2** using a Mn(salen) MOF and core-shell catalysts obtained by selective demetallation of interfacial catalyst sites. The core-shell catalyst accomplished epoxidation with greater size selectivity than the parent Mn(salen) MOF.

Direct Synthesis of Core-Shell Structures The development of synthetic approaches to well-defined core-shell structures would provide expanded opportunities to utilize core-shell architectures to interrogate the relative importance of catalysis at interfacial and interstitial sites. Zhou *et al.* utilized the distinct nucleation kinetics of different MOF materials to generate a series of porous MOF@MOF core-shell composites. For example, a catalytically active MOF (PCN-222(Fe)) core built from Fe porphyrin-based linkers was confined in various catalytically nonactive MOF shells, such as UiO-67.¹⁰⁵ The core-shell structure demonstrated low conversion (<1% for 24 h) with bulky substrate molecules. In comparison, PCN-222(Fe) without any shell produced conversions of 40-60% in 12 h for the same bulky substrates. These experiments suggest

that bulky substrates are excluded from the catalytically active core due to the introduction of significant diffusional barriers. The ready availability of rationally synthesized core-shell architectures provides the tools required to obtain kinetic data to bolster the conclusions about the relative importance of interfacial and interstitial catalyst sites.

While core-shell heterostructures comprised of two MOF phases have not yet been widely explored in catalysis, core-shell structures comprised of a catalytically inactive MOF shell and a catalytically active metal nanoparticle core have been developed. For example, Tsung *et al.* reported the synthesis of Pd nanoparticles encased in a shell of ZIF-8.¹⁰⁶ The resulting core-shell catalyst was competent for the hydrogenation of cyclohexene, but not for the hydrogenation of cyclooctene. In contrast, Pd deposited onto ZIF-8 produced similar activities for the hydrogenation of both cyclooctene and cyclohexene. These data demonstrate the potential to utilize diffusional barriers to control chemical selectivity.

1.5.2 Isorecticular Catalyst Materials

The availability of isorecticular catalysts, which are MOF catalysts that share the same network topology but differ in pore size,¹⁰⁷ provides the opportunity to systematically interrogate the impact of pore dimensions on catalyst performance. Lin *et al.* reported a detailed investigation of the kinetics of the epoxidation of 2,2-dimethyl-2H-chromene (**1.6**) to generate epoxide **1.7** catalyzed by a family of isorecticular Mn(salen)-based MOFs (**Figure I-4**).³¹ These experiments revealed that the reaction rate of olefin epoxidation was positively correlated with the pore size of MOFs. Further, the reaction rate within the large pore approached that of the rate of epoxidation using a soluble

molecular Mn(salen) catalyst. These data suggest that for sufficiently large pore sizes, diffusion is not rate limiting and catalyst activity is limited by the intrinsic activity of the lattice-confined catalyst sites. These data are consistent with participation of interstitial catalyst sites in epoxidation and substantial diffusional barriers for small-pore materials. The lack of appropriate molecular analogues for many catalyst sites in MOFs precludes widespread utilization of this strategy for interrogating the impact of diffusional barriers on catalysis.

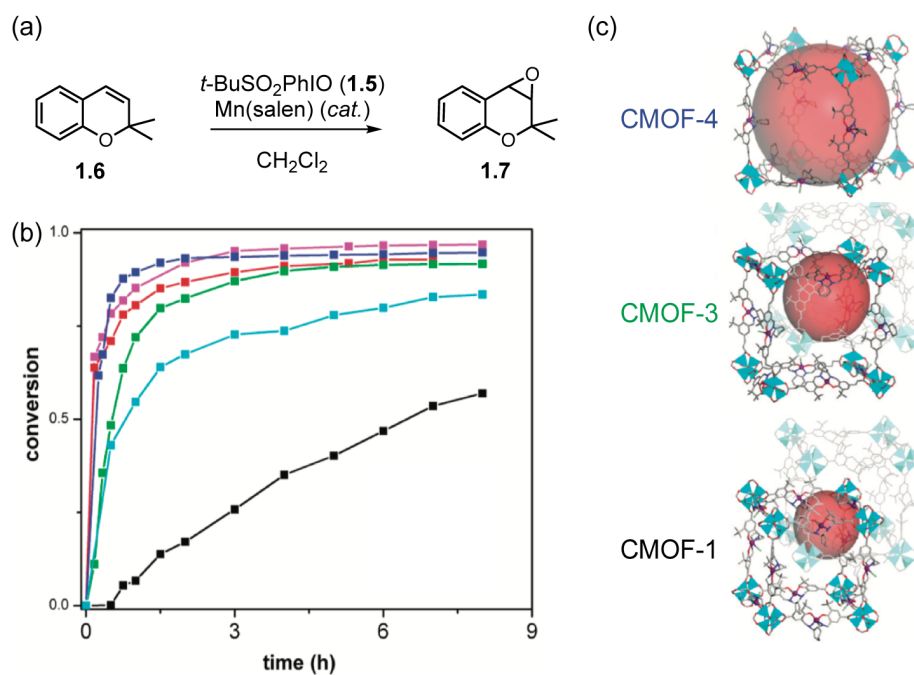


Figure I-4 Epoxidation rate as a function of pore size. (a) The epoxidation of 1.6 to generate 1.7 is catalyzed by Mn(salen)-based MOFs. (b) The rate of epoxidation increases with pore size. (c) Selected Mn(salen)-based isorecticular catalysts that were examined in the epoxidation of 1.6 to afford 1.7.

Long *et al.* investigated isorecticular Fe(II)-based MOFs for the oxidation of simple hydrocarbons (**Figure I-5**).³² Fe-MOF-74 (based on 2,5-dioxido-1,4-benzenedicarboxylate (dobdc) linkers; pore diameter of 8 Å), displayed no activity towards the oxidation of cyclohexane using **1.5** as the terminal oxidant (van der Waals volume of **1.5** is 221 Å³ assuming **1.5** is approximately spherical; diameter = 7.5 Å). For comparison, Fe-MOF-74 did show activity in ethane oxidation to generate ethanol using N₂O as the terminal oxidant.¹⁰⁸ Pore expansion using extended dobdc linkers provided isorecticular catalysts with 19 and 27 Å pores. Upon linker extension, oxidation of cyclohexane (**1.8**) to cyclohexanol (**1.9**) and cyclohexanone (**1.10**) was observed. These data suggest that potential interfacial catalyst sites are inactive (perhaps due to different surface-termination geometries) and interstitial sites are active. The use of a relatively large oxidant (*i.e.* **1.5**) precludes efficient diffusion of the required reagent in small-pore materials, and thus cyclohexane oxidation was not observed with Fe-MOF-74.

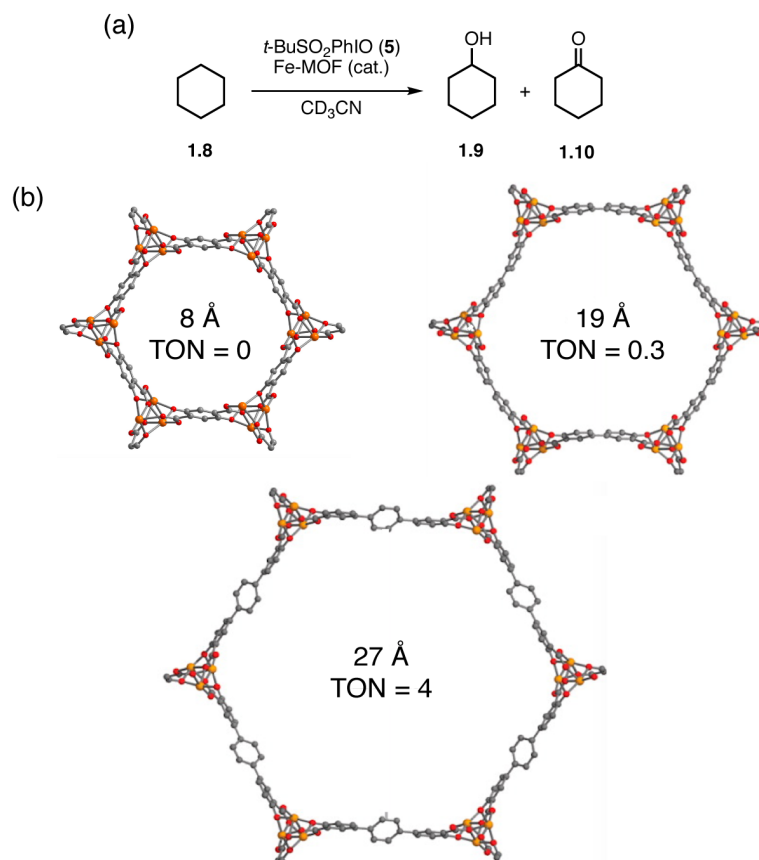


Figure I-5 Cyclohexane oxidation in an isorecticular family of materials. (a) Cyclohexane (**1.8**) oxidation to **1.9** and **1.10** is catalyzed by Fe-MOF-74 analogues. (b) The smallest Fe-MOF-74 analogue produced no oxidation products, while increasing the aperture size led to increasing turnover numbers (TONs).

1.5.3 Differently Sized-MOF Crystallites

The proportion of interfacial sites relative to interstitial sites increases as crystallite size decreases. Therefore, observing the impact that crystallite size has on the selectivity or kinetics of a reaction can provide insight into the relative contributions of interfacial and interstitial sites in catalysis. The relationship of crystallite size and proportion of interfacial catalyst sites has been described in chemical engineering by the concepts of

Thiele modulus and the effectiveness factor, which describe the relationship between diffusion and reaction. Assuming large crystallites and very fast chemical reactions, the Thiele modulus assumes only interfacial sites will be accessed.^{57,109}

Volkmer *et al.* studied the oxidation of cyclohexene (**1.11**) using *tert*-butylhydroperoxide (tbhp) as the terminal oxidant catalyzed by MFU-1 ($[\text{Co}_4\text{O}(\text{bdpb})_3]$; $\text{H}_2\text{bdpb} = 1,4\text{-bis}[(3,5\text{-dimethyl-pyrazol-4-yl})\text{benzene}]$).¹¹⁰ Two preparations of MFU-1 have been reported — one based on solvothermal synthesis and the other based on microwave heating. Crystallites obtained from the microwave-assisted method were smaller and more uniform than those obtained by solvothermal synthesis; the external surface area of the microwave-derived material was approximately 8 times higher than that of the crystals obtained through solvothermal synthesis. The authors proposed that if oxidation proceeded at interfacial sites exclusively, there should be an 8 times difference in the reaction rate between the two catalyst preparations. The smaller crystallites catalyzed oxidation only about 2 times faster than the large crystallites, which was interpreted as evidence that the rate of oxidation is limited by pore diffusion (**Figure I-6**).

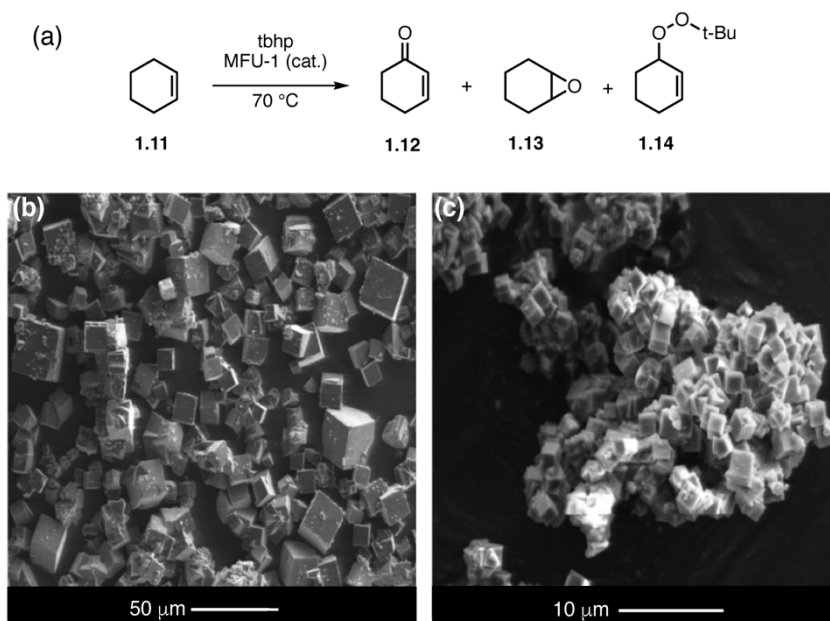


Figure I-6 Particle size dependent rate of oxidation of cyclohexene. (a) Oxidation of cyclohexene (**1.11**) to products **1.12**, **1.13**, and **1.14**. (b) Larger crystals (5-30 μm) of MFU-1 were obtained through solvothermal synthesis. (c) Small crystals (<2.5 μm) were obtained via microwave synthesis. The rate of oxidation was found to be 2 times higher for small crystals of MFU-1.

In order to probe the influence of particle size on catalytic activity, Garcia *et al.* examined three MIL-100 (Fe) samples at different average crystal sizes (60-70 nm, 120-130 nm, and 400 nm) for oxidation of thiophenol with oxygen, diphenylmethane with tbhp, and triphenylmethane with tbhp, respectively.¹¹¹ It was observed that the reaction rate for oxidation of thiophenol and diphenylmethane catalyzed MIL-100(Fe) was independent of the particle size. However, the initial rate of oxidation of triphenylmethane (**1.15**) heavily relied on the average crystal size of the catalyst: the smaller the crystal size, the faster the oxidation reaction (**Figure I-7**). These data suggest that for small substrates,

diffusion is rapid and catalysis proceeds at interstitial sites. For large substrates, diffusion is slow and interfacial sites have significant contributions to the observed rate of catalysis.

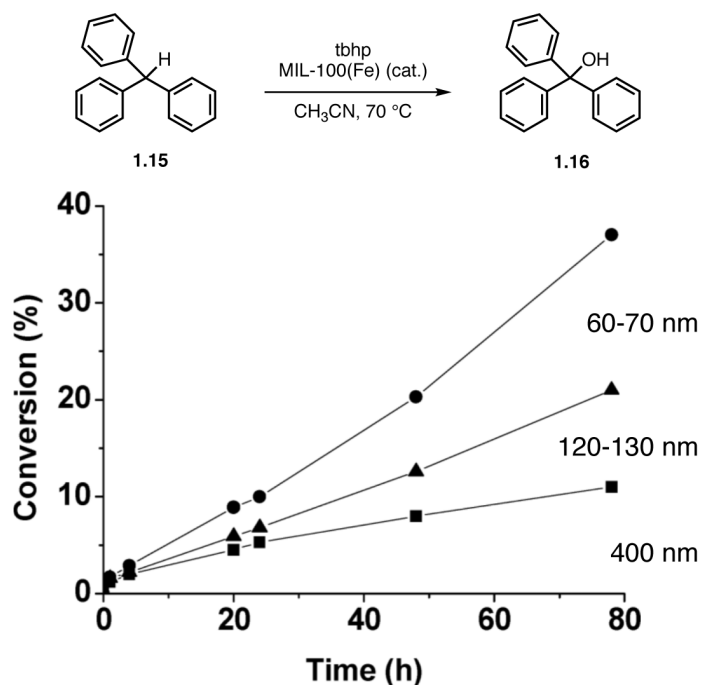


Figure I-7 Particle size dependent rate of oxidation for triphenyl methane. The rate of triphenyl methane (**1.15**) oxidation to **1.16** was found to increase with decreasing particle size, which suggests that oxidation proceeds at interfacial catalyst sites.

1.5.4 Chemo- and Stereoselectivity

In cases where soluble molecular analogues of MOF-confined catalyst sites are available, comparison of the chemo-¹¹² or stereoselectivity¹¹³⁻¹¹⁴ between heterogeneous MOF catalysts and soluble catalyst analogues can help delineate the relative contributions of interfacial and interstitial active sites. The analysis typically assumes that solvent-

exposed interfacial sites will catalyze a given reaction with similar selectivity as is obtained with homogeneous catalysts.

During the Friedel-Crafts reaction of indole with imines (**Figure I-8a**), Lin *et al.* observed the enantioselectivity of a heterogeneous chiral MOF catalyst was opposite from that of a soluble molecular analogue.¹¹⁴ Chiral MOF catalysts were constructed from dicopper secondary building units and enantiopure 1,1'-binaphthyl-2,2'-phosphoric acid-based linkers. The major product of the Friedel-Crafts reaction of indole **1.17** with imine **1.18** was *R*-**1.19**. In contrast, use a soluble molecular analogue afforded the *S*-enantiomer of **1.19**. The opposite sense of enantioinduction was interpreted as evidence of interstitial catalysis.

Similarly, Telfer *et al.* demonstrated that the enantioselectivity of the aldol reaction of acetone and *p*-nitrobenzaldehyde catalyzed by a prolinyl unit embedded in MUF-77, $[\text{Zn}_4\text{O}(\text{bdc})_{1/2}(\text{bpdc})_{1/2}(\text{hmtt})_{4/3}]$ ((bpdc = 4,4'-biphenyldicarboxylate, bdc = 1,4-benzenedicarboxylate, hmtt = 5,5',10,10',15,15'-hexamethyltruxene-2,7,12-tricarboxylate), was sensitive to the structure of the organic linker used, which suggests that interstitial catalysis is operative (**Figure I-8b**).¹¹³

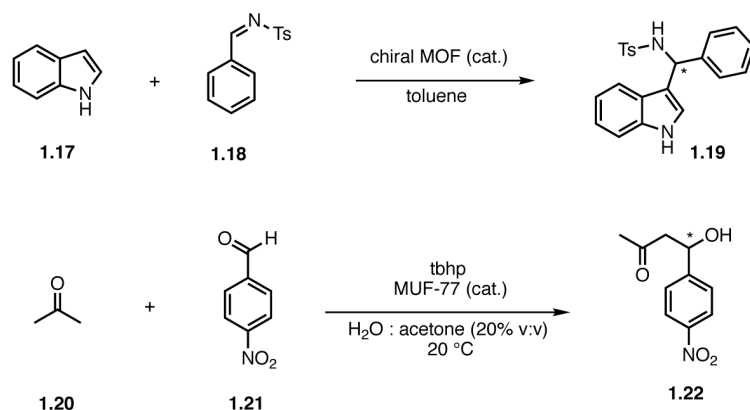


Figure I-8 Stereoselectivity as a tool to differentiate interstitial from interfacial catalysis. (a) Friedel-Crafts reaction of indole (**1.17**) and imine (**1.18**) catalyzed by a chiral phosphoric acid-based MOF afford *R*-**1.19**, while catalysis with a molecular analogue afforded *S*-**1.19**. (b) The aldol reaction of acetone and p-nitrobenzaldehyde catalyzed by MUF-77 proceeded with the opposite sense of asymmetric induction as compared to aldol reactions catalyzed by homogeneous catalysts.

Chapter II will discuss the development of a method based on the stereospecificity of *cis*-decalin oxidation to inform on the relative rates of interstitial and interfacial catalysis.

1.5.5 Isolating Diffusion through Pores from Surface Barriers

Each of the experiments described above examines the impact of diffusion during catalysis and information derived from these experiments reports on diffusion barriers through porous materials as well as surface barriers that may prevent diffusion into crystallites of porous catalysts. Increasingly, it is becoming clear that multi-layer packing of organic compounds within porous networks leads to a greater degree of confinement than would be anticipated based on the relative sizes of substrate and pore alone.¹¹⁵⁻¹¹⁸ In order to better understand the relative size of substrate and pore that gives rise to effective

substrate flux through porous materials, experimental approaches that isolate diffusion within porous materials with other variables, such as surface barriers, are needed.

In 2018, Powers *et al.* described a method to probe the relative rates of diffusion and substrate functionalization based on comparison of the magnitudes of intra- and intermolecular kinetic isotope effects (KIEs).¹¹⁹ KIEs arise from the difference in reaction rate that results from isotopic substitution. Intramolecular KIEs are measured using partially deuterated substrates and thus the kinetic discrimination between C–H and C–D bonds that gives rise to the observed KIEs is done between bonds in the same molecule. Intermolecular KIEs are measured using a mixture of perdeuterated and undeuterated substrate and thus the kinetic discrimination between C–H and C–D bonds that gives rise to the observed KIEs is done between bonds in different molecules.

During an investigation of C–H amination mediated by Ru₂ nitride intermediates confined within porous materials, it was found that the intramolecular KIE value of $k_H/k_D = 7.86(3)$ was obtained for amination of toluene-*d*₁ and the intermolecular KIE value of $k_H/k_D = 1.02(2)$ for an equimolar mixture of toluene and toluene-*d*₈ (**Figure I-9**). The large intramolecular KIE suggests hydrogen-atom abstraction is a primary chemical step and that nitrogen-atom transfer to toluene is slower than the methyl group rotation that underpins kinetic selection between H and D. The small intermolecular KIE indicates that C–H bond cleavage is not involved in the product-determining step in the amination of a mixture of toluene and toluene-*d*₈. The relative lack of discrimination between H and D reflected in the absence of an intermolecular KIE suggests that substrate self-exchange in this MOF is slow relative to C–H amination. The combination of large intramolecular

KIEs and small intermolecular KIEs has been interpreted to indicate that while C–H cleavage is involved in the reaction, diffusion barriers, which are not sensitive to isotopic substitution, are rate-determining. The observation of slow diffusion relative to C–H functionalization is notable given that the kinetic diameter of toluene (5.9 \AA)¹²⁰ is significantly smaller than the apertures (7.3 \AA)¹¹⁹ of the Ru_3btc_2 material used in this study.

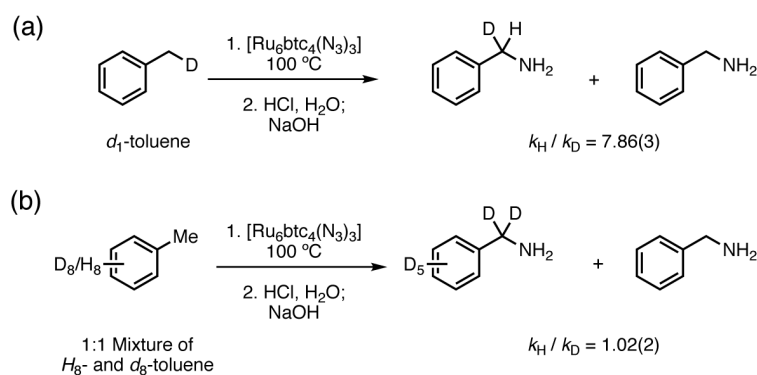


Figure I-9 Kinetic isotope effects as a tool for probing the rate of diffusion in relation to rate of C–H amination. (a) The large intramolecular KIE (7.86) for nitrogen-atom transfer suggests that amination of toluene in Ru_2 -based materials proceeds via initial hydrogen-atom abstraction. (b) The small intermolecular KIE (1.02) suggests that toluene self-diffusion is slow relative to C–H amination.

I.6 Conclusions

While the potential to utilize MOF catalysts as platforms for fine-chemical synthesis is attractive, serious challenges related to transport of relatively large, stereochemically complex substrates and products into and out of porous materials must be overcome. This Chapter examined the diffusional processes that are available in porous materials – molecular, Knudsen, intracrystalline, and molecular sieving – which depend

on the relative size of available pores and the sorbate molecules. Direct measurement of diffusion rates of sorbates in porous materials has led to the identification of a series of parameters which are critical for small molecule diffusion, such as pore size, network flexibility, and enthalpy of adsorption. The complexity inherent in catalytic reactions, in which mixtures of starting materials, products, and reagents, display time-dependent changes in concentration, renders utilization of diffusion coefficients for the rational development of new catalysts, a challenge.

To understand the transport of large organic molecules into and through porous catalyst materials, *in operando* experimental tools that evaluate the relative rates of diffusion and catalyst turnover are needed. A family of *in operando* strategies, such as utilizing core-shell catalyst architectures, investigating isorecticular MOF catalysts, examining the impact of crystallite size on catalysis, comparing the chemo- and stereoselectivity of porous catalysts with soluble molecular analogues, and analyzing the relative magnitudes of intra- and intermolecular kinetic isotope effects, have been developed. These studies have provided evidence that while in some cases interstitial catalyst sites contribute significantly to the rate of catalysis, in many cases interfacial sites are at least as important. Diffusion of stereochemically complex molecules is sufficiently slow in many circumstances that despite the fact that far more interstitial sites are available than interfacial sites, interfacial sites are kinetically significant. Even when substrates are smaller than available aperture sizes, diffusion can be slow relative to interstitial chemistry. An ongoing challenge in the development of MOF catalysts for fine-chemical synthesis will be to define how large a pore needs to be before organic molecules, even

simple ones such as solvent, diffuse at rates relevant to catalysis. We anticipate that improved experimental and computational approaches to the *in operando* evaluation of diffusion will contribute meaningfully to the rational development of new catalyst systems for application in fine chemical synthesis.

CHAPTER II

CIS-DECALIN OXIDATION AS A STEREOCHEMICAL PROBE OF INTERSTITIAL VS. INTERFACIAL MOF CATALYSIS*

II.1 Introduction

Enzymatic C–H oxidation during xenobiotic metabolism and biosynthesis is accomplished with catalyst-controlled selectivity within substrate-adaptive enzyme active sites.^{5,121-122} In contrast, most synthetic C–H hydroxylation methods proceed with substrate-controlled selectivity at either the weakest or the most sterically unencumbered C–H bond.^{7,123} The development of strategies for catalyst-controlled C–H hydroxylation could provide direct entry into complex functional molecules, such as metabolites.¹²⁴⁻¹²⁵ We are interested in utilizing flexible metal-organic frameworks (MOFs) as catalysis platforms to achieve oxidation selectivities that are challenging to access in solution-phase chemistry.

MOFs are a class of materials comprised of metal nodes and organic linking elements that typically display rigid 3-dimensional structure and network porosity.¹²⁶⁻¹²⁸ Porphyrinic MOFs, in which metalloporphyrins are incorporated as linking elements, have garnered intense interest due to the potential use of these materials as biomimetic heterogeneous oxidation catalysts.¹²⁹⁻¹³⁰ Among the challenges to developing efficient oxidation catalysis based on porphyrinic materials are: 1) generating large-pore, non-

* Data, figures, and text in this chapter were adapted with permission from reference Cardenal, A. D.; Park, H. J.; Chalker, C. J.; Ortiz, K. G.; Powers, D. C. *Chem. Commun.* **2017**, *53*, 7377–7380, copyright 2017 the Royal Chemical Society.

interpenetrating materials that support substrate diffusion,^{30,129,131-133} 2) controlling M–L binding to access materials with open metal sites,¹³⁴⁻¹³⁶ and 3) accessing robust frameworks that maintain structure during guest removal or exchange.¹³⁷ Even with these criteria met, it remains a substantial challenge to differentiate catalysis on materials (*i.e.* at surface sites) from catalysis in materials. We are interested in porphyrinic materials that feature flexible organic linkers as platforms for catalyst-controlled oxidation of organic molecules based on the contention that network flexibility¹³⁸⁻¹⁴¹ may provide substrate-specific reaction environments in which to accomplish substrate oxidation. Critical to development of catalysts for these applications is determining if catalysis is accomplished inside the catalyst pores. Here we report the synthesis of a new family of porphyrinic materials, demonstrate hydrocarbon oxidation catalysis, and present a stereochemical test based on *cis*-decalin oxidation to differentiate catalysis in materials from catalysis on materials.

II.2 Results and Discussion

Solvothermal combination of 5,10,15,20-tetrakis(4-carboxyphenyl)porphyrin iron chloride (Fe(tcpp)Cl), 1,3-di(1H-1,2,4-triazol-1-yl)propane (btp), and Zn(NO₃)₂·6H₂O in *N,N'*-diethylacetamide (DEA) and ethanol (EtOH) at 80 °C affords a dark-purple crystalline material with the empirical formula [Zn₂(Fe(tcpp))(btp)(NO₃)₃]_n (**Fe(btp)**, **Figure II-1**). The chemical composition of **Fe(btp)** was evaluated by: 1) elemental analysis; 2) acid digestion followed by UV-vis and ¹H NMR analyses to define the Fe(tcpp) and btp content, respectively (**Figures II-2** and **II-3**); 3) ICP-MS analysis of an

acid-digested sample to establish the Fe:Zn ratio (**Table II-1**); and 4) diffuse reflectance UV-vis spectroscopy (**Figure II-2**). Elemental analysis and IR spectroscopy (**Figure II-4**) indicate that the chloride counterions of the Fe(tcpp)Cl starting material are replaced by nitrate ions during solvothermal synthesis of **Fe(btp)**. The Fe(tcpp):btp ratio determined for acid-digested samples is 0.8, which indicates the presence of some ligand absences from the ideal $[\text{Zn}_2(\text{Fe}(\text{tcpp}))(\text{btp})(\text{NO}_3)]_n$ empirical formula.

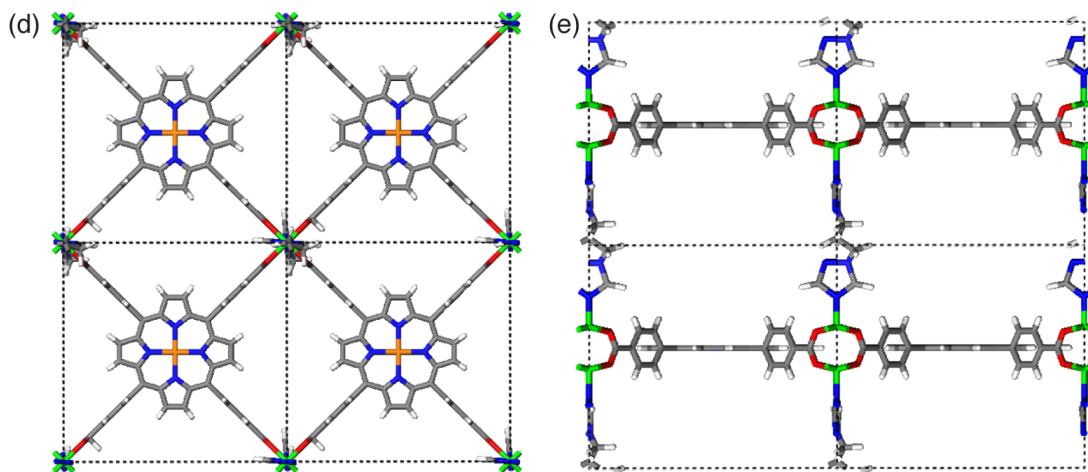
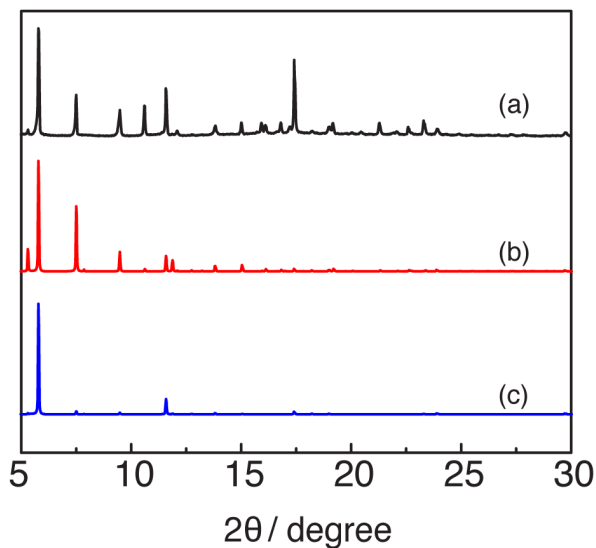
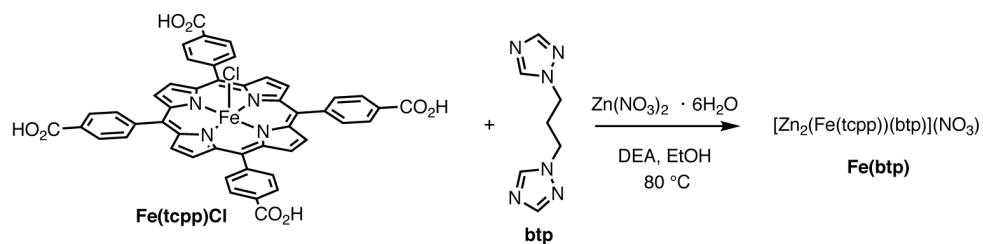


Figure II-1 Solvothermal Synthesis of Fe(btp) and characterization by PXR. (a) PXR pattern of as-synthesized Fe(btp), (b) simulated PXR pattern for Fe(btp), and (c) simulated PXR pattern for Fe(btp) with application of a [00 l] preferred orientation. Structure model of Fe(btp) along the (d) crystallographic c -axis, and (e) crystallographic a -axis, which was generated using both PXR and SCXR data.

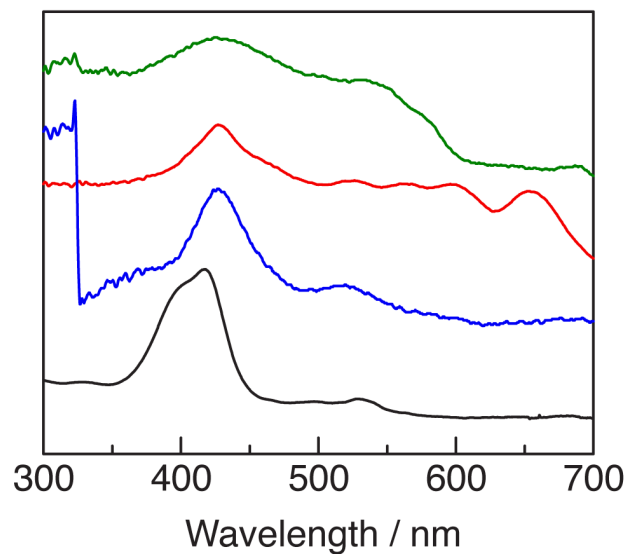


Figure II-2 UV-vis spectroscopy of Fe(btp) and its constituents. Diffuse reflectance spectra of **Fe(btp)** (—), H₂tcpp (—), and Fe(tcpp)Cl (—). For comparison, the electronic absorption spectrum of Fe(tcpp)Cl obtained as a DMSO solution (—).

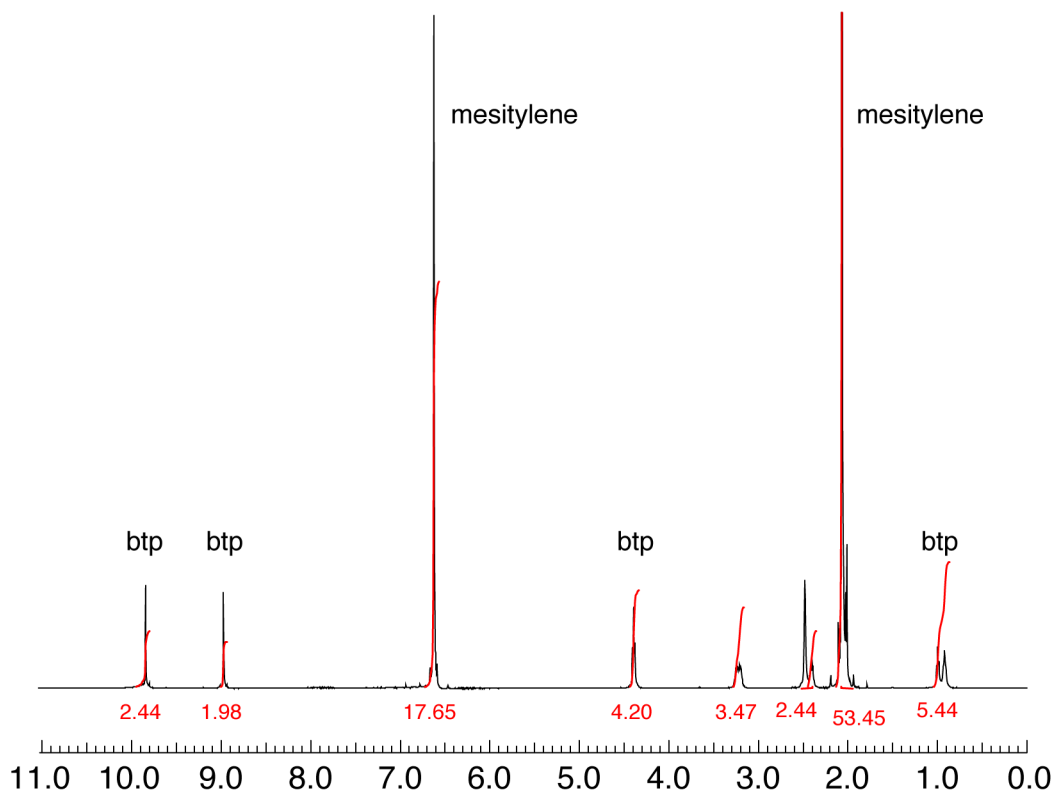


Figure II-3 Digestion of Fe(btp) allows for linker quantification. After drying at 23 °C under vacuum, Fe(btp) solid was dissolved in d_6 -DMSO (0.5 mL) and D_2SO_4 (0.05 mL). Mesitylene was used as an internal standard.

Table II-1 Zn:Fe and Fe(tcpp):linker ratio calculated from ICP-MS and NMR/UV-vis experiments, respectively, of **Fe(btp)**, **Fe(bpy)**, **Fe(bpe)**, and **Fe(bpp)**.

MOF	Zn:Fe	Fe(tcpp):linker
Fe(btp)	2:0.932	1:0.63-0.95
Fe(bpy)	2:0.827	1:0.81
Fe(bpe)	2:0.766	1:0.77
Fe(bpp)	2:1.079	1:0.74
PPF-3-Zn/Fe		1:1.76

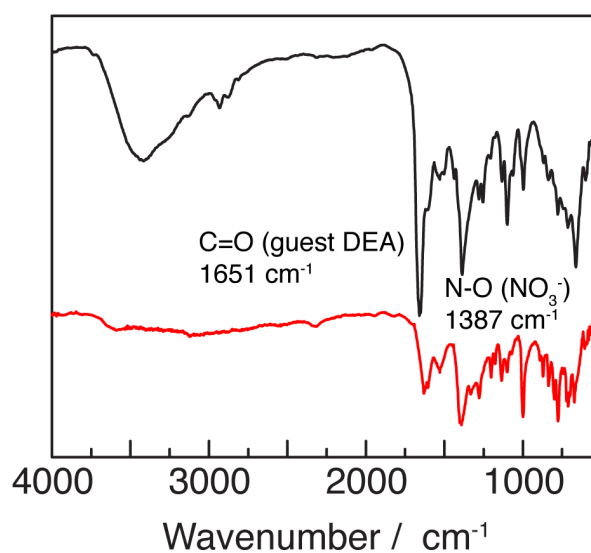


Figure II-4 IR spectrum of **Fe(btp)** indicates presence of NO_3^- . IR spectrum of as-synthesized **Fe(btp)** (—) and **Fe(btp)_{act}** (—). Removal of DEA guest molecules during activation is evidenced by the disappearance of the peak at 1651 cm^{-1} .

A wide variety of network topologies are available for a family of porphyrin-paddlewheel frameworks (PPF).^{134,136} For example, while PPF-5-Zn/Ni (where Zn is the metal composing the paddlewheel motif and Ni is in the porphyrin), which is a layered material comprised of Ni(tcpp), 4,4'-bipyridine (bpy), and dizinc tetracarboxylate nodes, features an AA stacking motif in which dizinc sites are connected by bpy, PPF-3-Zn/Fe, which is a layered material comprised of Fe(tcpp), bpy, and dizinc tetracarboxylate nodes features an AB stacking motif, in which dizinc sites are bound to metalloporphyrin sites (Figure II-5).¹³⁶

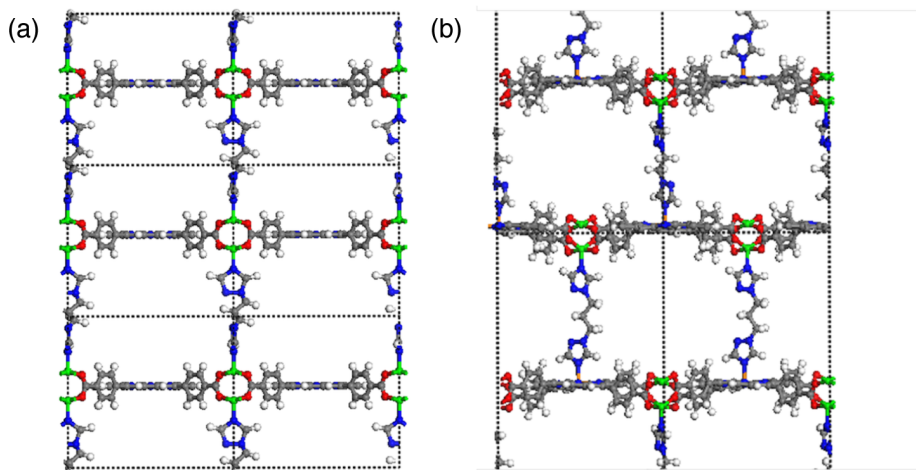


Figure II-5 The simulated structures of Fe(btp) with (a) AA and (b) AB stacking.

We have used a combination of single-crystal X-ray diffraction (SCXRD), powder X-ray diffraction (PXRD), and modeling to confirm that **Fe(btp)** features AA-stacking of porphyrinic layers and is isostructural with PPF-5. SCXRD analysis confirmed the 2-D porphyrinic layers in **Fe(btp)** are connected by dizinc tetracarboxylates and indicated AA

stacking of the 2-D layers with alignment of the dizinc units along the crystallographic *c*-axis. Interlayer connectivity, however, could not be established by SCXRD due to severe disordering in the crystallographic *c*-axis (**Figure II-6**). PXRD was collected for **Fe(btp)** and is displayed in **Figure II-1**. We constructed a model based on the 2-D layers determined by SCXRD with a set layer-to-layer spacing of 15.28 Å, which was calculated from the first main peak at $2\theta = 5.78^\circ$ in the measured PXRD pattern. The measured PXRD data are in good agreement with the structure model presented in **Figure II-1d** and **II-1e**. The PXRD data for **Fe(btp)** display a strong [001] preferred orientation, which is common for layered porphyrinic materials¹³⁶ and consistent with the plate morphology of **Fe(btp)** crystallites. We also simulated the PXRD pattern expected of AB stacking (**Figure II-7**) and the observed PXRD is most well-matched to the presented AA stacking model.

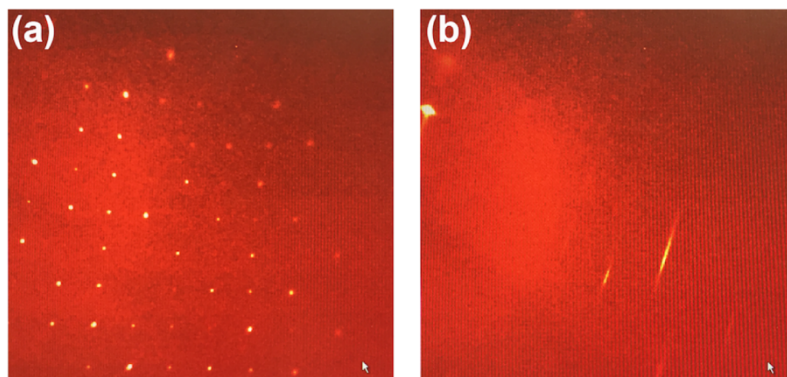


Figure II-6 Single crystal X-ray diffraction images of Fe(btp). (a) **Fe(btp)** crystals diffract strongly in some orientations, but (b) disorder in the crystallographic *c*-axis prevents use of SCXRD to define interlayer connectivity.

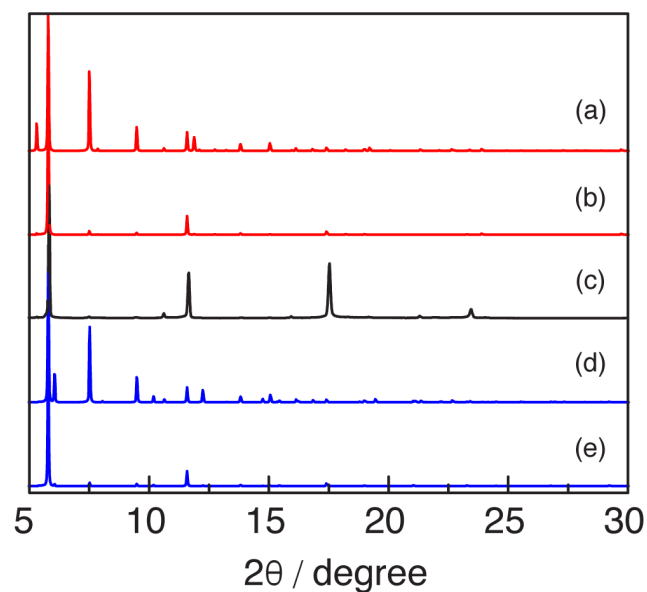


Figure II-7 The PXRD analysis of Fe(btp) for AA and AB stacking. AB stacking requires substantial deformation of the porphyrinic units in the 2-D layers. In addition to the PXRD-based evidence for AA stacking and not AB stacking, the observation that the diffuse reflectance of our materials is unperturbed from free porphyrins suggests that the porphyrin sites in the reported materials are planar. Comparison of PXRD pattern of **Fe(btp)** with the simulated patterns for potential AA and AB stacking motifs: (a) the simulated pattern derived from AA stacking and (b) the simulated pattern derived from AA stacking with application of a [001] preferred orientation; (c) measured pattern for **Fe(btp)**; (d) the simulated pattern derived from AB stacking and (e) the simulated pattern derived from AB stacking with application of a [001] preferred orientation.

The assignment of AA stacking is further bolstered by conversion of **Fe(btp)** to $[\text{Zn}_2(\text{Fe}(\text{tcpp}))(\text{bpy})(\text{NO}_3)]_n$ (**Fe(bpy)**) via post-synthetic linker exchange¹⁴²⁻¹⁴³ chemistry (**Figure II-7**). **Fe(btp)** is unstable in fresh DEA; ¹H NMR analysis of the solvent indicated leaching of btp from the material and PXRD indicated amorphization of the network. In contrast, **Fe(btp)** is indefinitely stable in DEA solutions of btp. Soaking **Fe(btp)** in solutions of bpy resulted in the isolation of an isostructural layered material **Fe(bpy)**. Similar to **Fe(btp)**, interlayer connectivity of **Fe(bpy)** could not be resolved by SCXRD (**Figure II-8**), but the PXRD pattern measured for **Fe(bpy)** indicates that **Fe(bpy)** is an AA-stacked material isostructural with PPF-5 (**Figure II-9**).¹³⁶ Additionally, the unit cell parameters of **Fe(bpy)** ($a = b = 16.70 \text{ \AA}$, $c = 14.05 \text{ \AA}$; P_4/m) are similar to those of PPF-5 ($a = b = 16.65 \text{ \AA}$, $c = 14.05 \text{ \AA}$; P_4/mmm) but dissimilar to those of PPF-3 ($a = b = 16.63 \text{ \AA}$, $c = 25.08 \text{ \AA}$; I_4/mmm). We have extended similar post-synthetic linker exchange chemistry to the preparation of three additional isorecticular frameworks – $[\text{Zn}_2(\text{Fe}(\text{tcpp}))(\text{dabco})(\text{NO}_3)]_n$ (**Fe(dabco)**), $[\text{Zn}_2(\text{Fe}(\text{tcpp}))(\text{bpe})(\text{NO}_3)]_n$ (**Fe(bpe)**) and $[\text{Zn}_2(\text{Fe}(\text{tcpp}))(\text{bpp})(\text{NO}_3)]_n$ (**Fe(bpp)**) – which are based on 1,4-diazabicyclo[2.2.2]octane (dabco), 1,2-bis(4-pyridyl)ethane (bpe) and 1,3-bis(4-pyridyl)propane (bpp) linkers, respectively. The obtained isorecticular family of materials displays linker-dependent layer-to-layer spacing (4.91 Å (**Fe(dabco)**), 14.04 Å (**Fe(bpy)**), 15.28 Å (**Fe(btp)**), 16.39 Å (**Fe(bpe)**), and 16.45 Å (**Fe(bpp)**); **Figure II-10**). Characterization data is collected in **Figures II-11-12** and **Table II-1** and **II-2**.

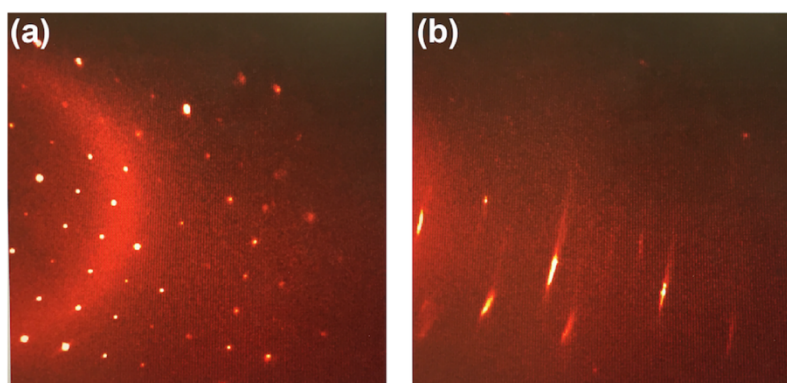


Figure II-8 Single crystal X-ray diffraction image of Fe(bpy). (a) Fe(bpy) crystals diffract strongly in some orientations, but (b) disorder in the crystallographic *c*-axis prevents use of SCXRD to define interlayer connectivity.

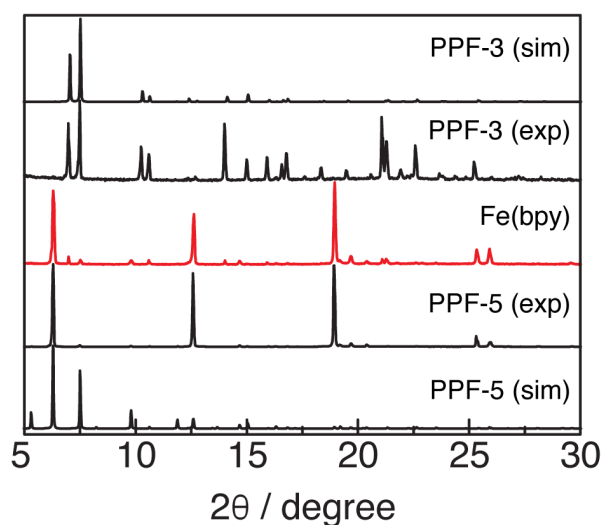


Figure II-9 Comparison of the PXRD pattern of Fe(bpy) with the simulated and experimental PXRD patterns for PPF-3 and PPF-5 materials, which feature AB- and AA-stacking motifs, respectively.

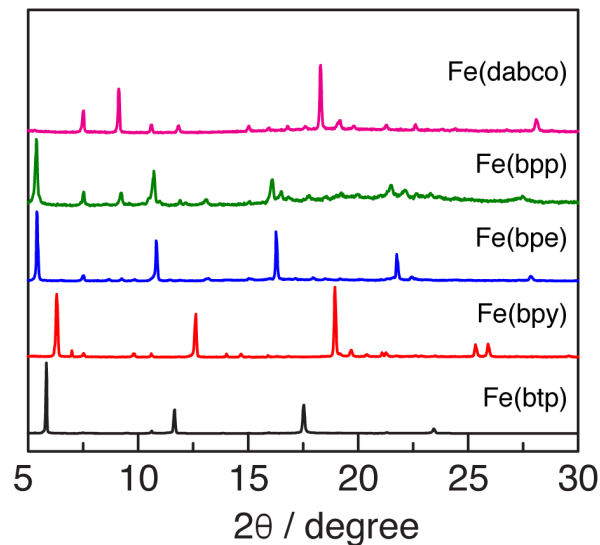


Figure II-10 PXRD of Fe(btp) (—), Fe(bpy) (—), Fe(bpe) (—), Fe(bpp) (—), and Fe(dabco) (—). The patterns reveal an isostructural family of materials that differs in the ligand-defined layer-to-layer separation.

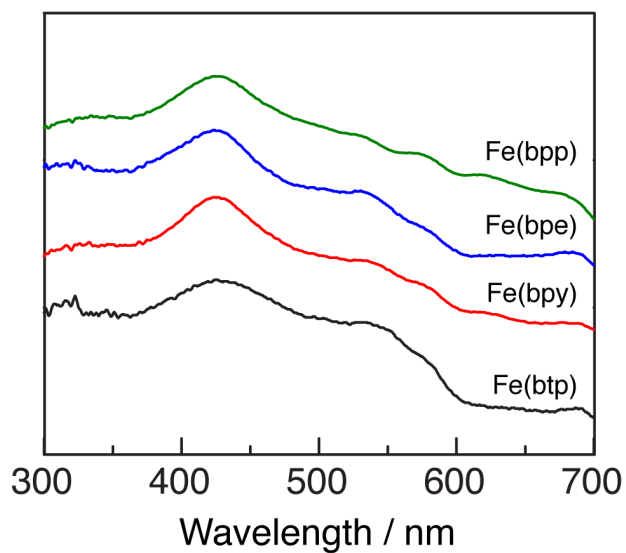


Figure II-11 Diffuse reflectance spectra of Fe(btp) (—), Fe(bpy) (—), Fe(bpe) (—), and Fe(bpp) (—).

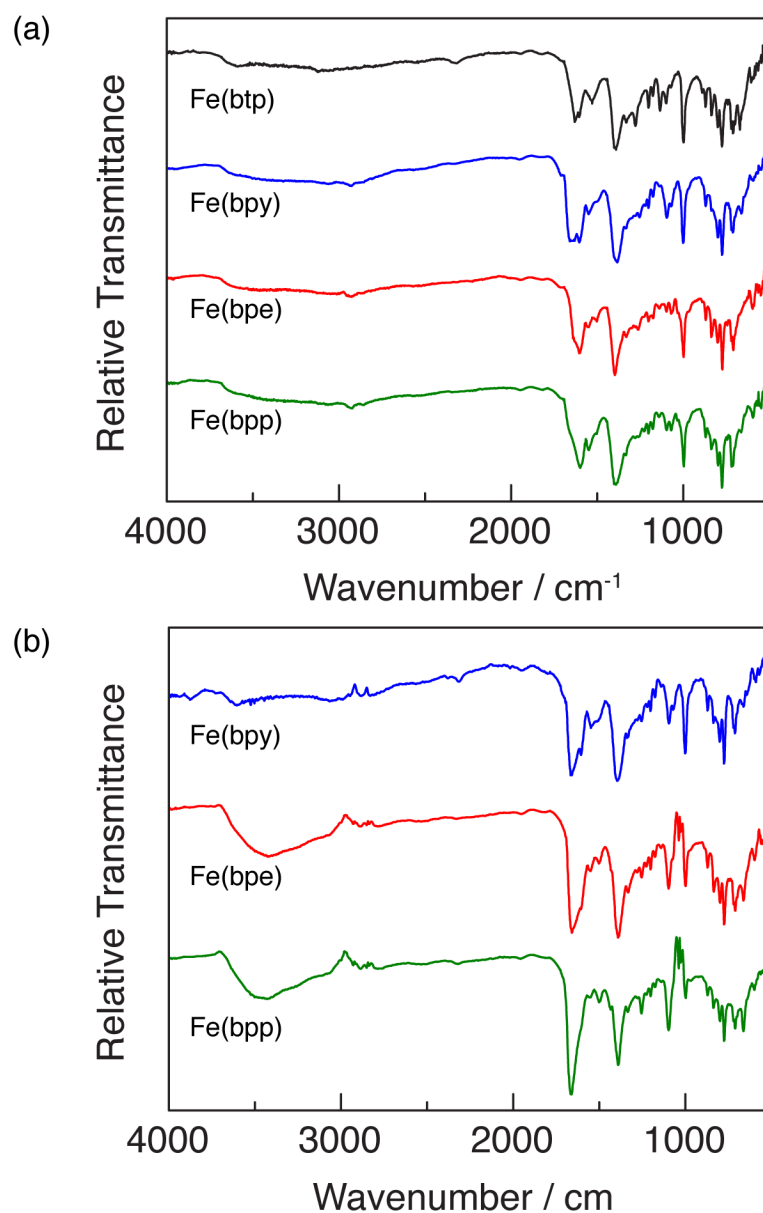


Figure II-12 IR spectra of Fe(btp) (—), Fe(bpy) (—), Fe(bpe) (—), and Fe(bpp) (—) prepared by solvothermal (a) synthesis and by (b) linker-exchange chemistry.

Table II-2 Comparison of the unit cell parameters of **Fe(btp)**, **Fe(bpy)**, and **Fe(bpe)** with PPF-3-Zn/Fe and PPF-5-Zn/Ni.¹³⁶

MOF	Fe(btp)	Fe(bpy)	Fe(bpe)	PPF-3-Zn/Fe	PPF-5-Zn/Ni
Crystal system			<i>Tetragonal</i>		
Space group	<i>P₄/mmm</i>	<i>(P₄/m)</i>	<i>(P₄/m)</i>	<i>I₄/mmm</i>	<i>P₄/mmm</i>
<i>a</i> , Å	16.79(6)	16.69(2)	16.75(4)	16.63(2)	16.65(4)
<i>c</i> , Å	16.11(1)	14.05(3)	16.28(3)	25.07(4)	14.05(7)
<i>d-spacing</i> , Å ^a	15.28	14.04	16.39	12.68	14.04

^a calculated by applying Bragg's law to (00*l*) peaks of measured PXRD patterns.

The original report of PPF-5 explored the solvothermal chemistry of Zn(NO₃)₂, Fe(tcpp), and bpy and showed the evolution of PPF-3, with an AB stacking motif in which the bpy linkers connect Fe(tcpp) and Zn₂ nodes.¹³⁶ We were interested in the observation that linker exchange from **Fe(btp)** provides access to a PPF-5 topology, and specifically were interested in addressing whether templating provided access to network topologies not accessible by direct synthesis. To address this issue, we have carefully examined the impact of bpy loading on the reaction outcome and have found that **Fe(bpy)** is obtained from solvothermal synthesis at low bpy loading, while PPF-3 is obtained at higher loading (**Figure II-13**). Similar stoichiometry-dependent phase isolation was observed when btp loading was varied in **Fe(btp)** syntheses (**Figure II-14**).

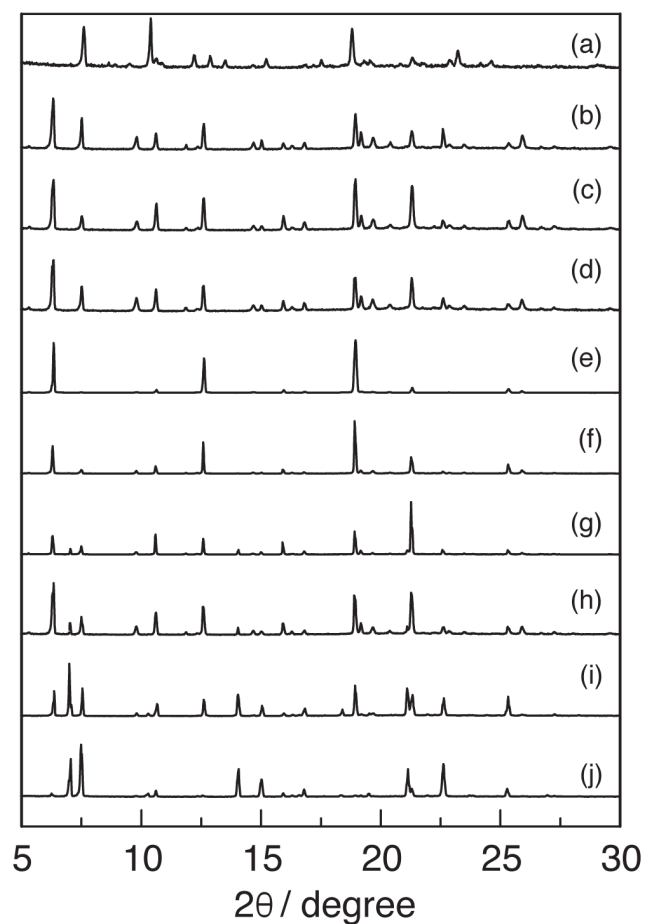


Figure II-13 PXR D patterns of solids prepared with increasing quantities of bpy. PXR D patterns of solids prepared by solvothermal reaction of $\text{Zn}(\text{NO}_3)_2 \cdot 6\text{H}_2\text{O}$, $\text{Fe}(\text{tcp})\text{Cl}$ with (a) 0, (b) 0.5, (c) 0.8, (d) 0.9, (e) 1.0, (f) 1.1, (g) 1.2, (h) 1.5, (i) 2.0, and (j) 4.0 equivalents of bpy. All reactions were carried out in a 3 : 1 mixture of DEF and EtOH at 80 °C.

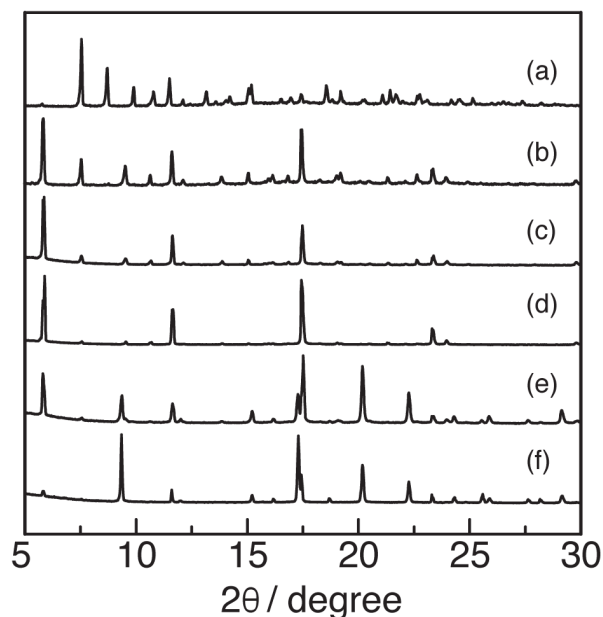


Figure II-14 PXRD patterns of solids prepared with increasing quantities of btp.

PXRD patterns of solids prepared by solvothermal reaction of $\text{Zn}(\text{NO}_3)_2 \cdot 6\text{H}_2\text{O}$, $\text{Fe}(\text{tcpp})\text{Cl}$ with (a) 0, (b) 1, (c) 2, (d) 4, (e) 8, and (f) 16 equivalents of btp. All reactions were carried out in a 4 : 1 mixture of DEA and EtOH at 80 °C.

Fe(btp) undergoes amorphization upon desolvation (**Figure II-15**). Thermogravimetric analysis (TGA) measured under N_2 flow reveals ~50% weight loss between 23–150 °C (**Figure II-16**) and IR spectroscopy shows that this mass loss is associated with removal of DEA from the material (**Figure II-4**). Gas sorption isotherms (up to 1 bar of pressure) were measured for the desolvated solid (**Fe(btp)_{act}**) with N_2 and CO_2 at 77 K and 195 K, respectively, and indicate that **Fe(btp)_{act}** has very low accessible surface area (*i.e.* 89 m^2/g based on CO_2 isotherm, **Figure II-17**). Network structure, as probed by PXRD analysis, did not return after soaking **Fe(btp)_{act}** in DEA and EtOH (**Figure II-18**). Additionally, *in situ* PXRD experiments carried out at the Advanced

Photon Source (APS) while sequentially subjecting **Fe(btp)_{act}** to vacuum and then to high pressure gas (up to 100 bar CH₄ or 30 bar CO₂ pressure) indicate that the vacuum-induced phase transition of **Fe(btp)** to **Fe(btp)_{act}** is irreversible (**Figures II-18-19**).

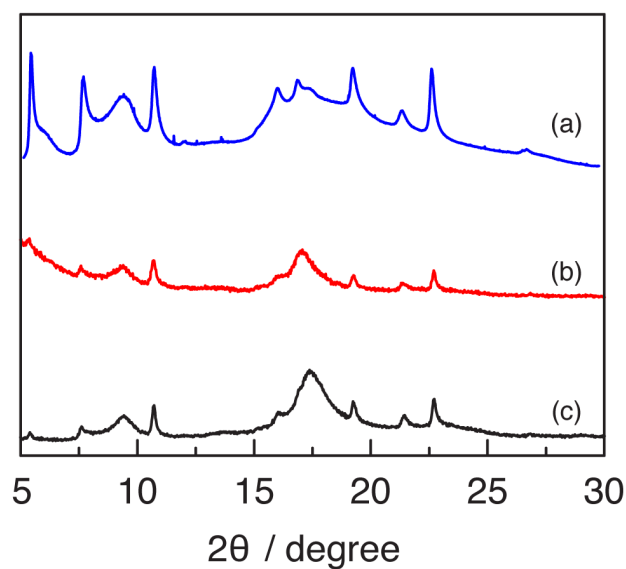


Figure II-15 Collapse of Fe(btp) long-range structure. PXRd patterns for **Fe(btp)**. (a) PXRd from *in situ* activation of **Fe(btp)** in a capillary tube. (b) PXRd of **Fe(btp)_{act}** prepared by drying at 150 °C under vacuum for 12 h. (c) PXRd obtained after soaking **Fe(btp)_{act}** in a mixture of DEA/EtOH for 1 d.

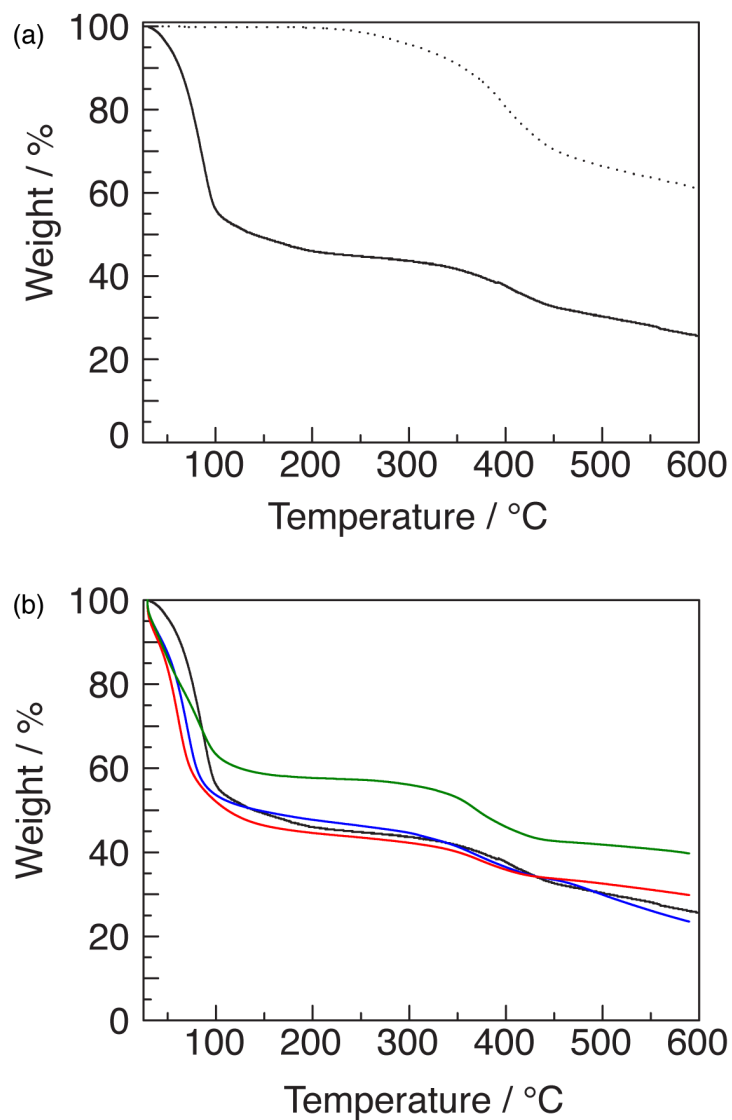


Figure II-16 TGA data for porous materials. (a) TGA traces of as-synthesized (—) and activated (···) Fe(btp). (b) TGA traces of as-synthesized **Fe(btp)** (—), **Fe(bpy)** (—), **Fe(bpe)** (—), and **Fe(bpp)** (—) acquired under a flow of N₂ and a temperature ramp of 5 °C/min.

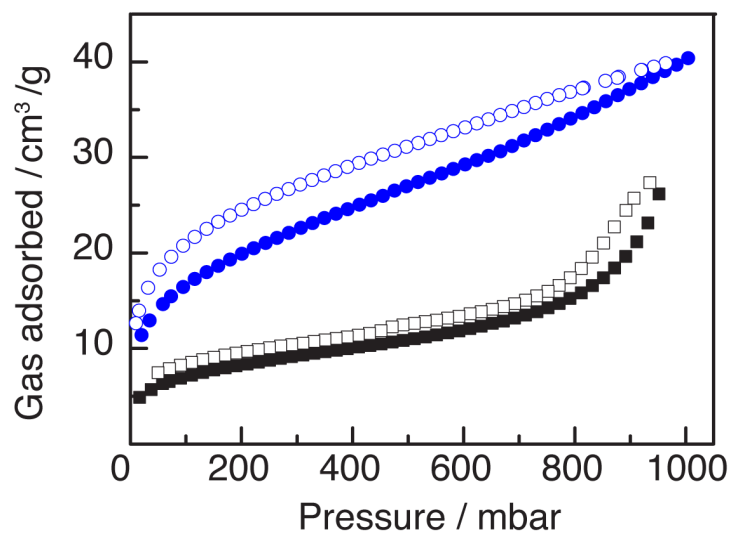


Figure II-17 CO₂ sorption isotherms for Fe(btp). Gas sorption isotherms of activated **Fe(btp)_{act}** for N₂ at 77 K (black) and CO₂ at 195 K (blue). Filled shapes: adsorption; open shapes: desorption. Based on these data, **Fe(btp)_{act}** is a non-porous material.

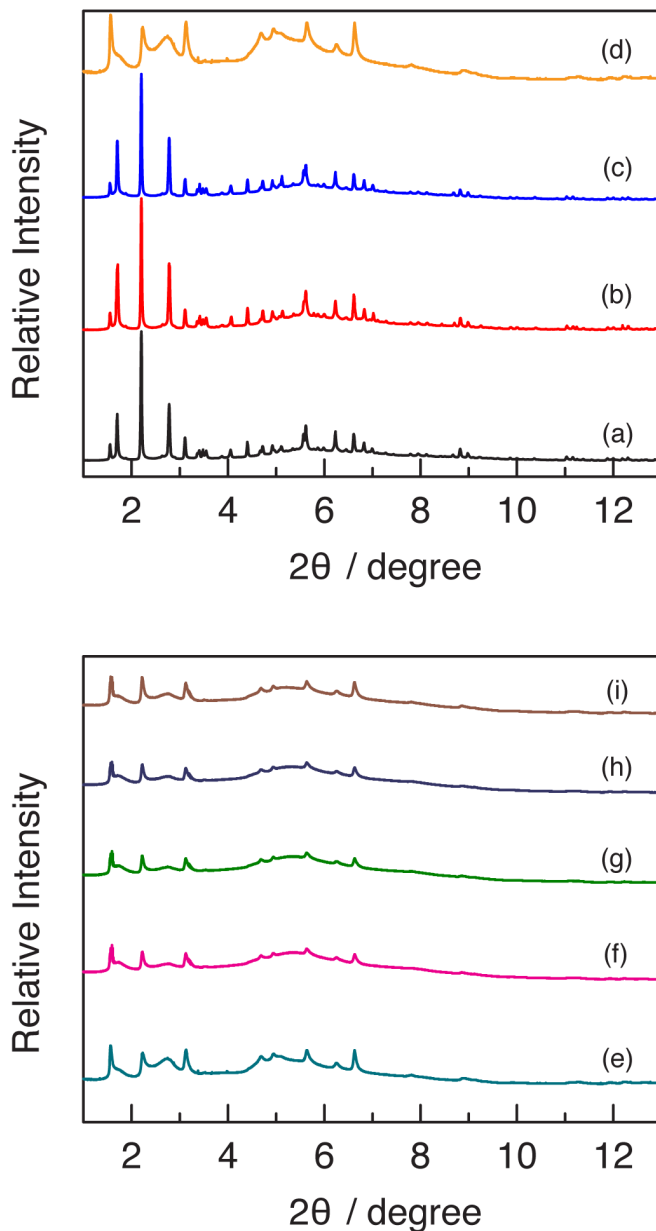


Figure II-18 *In situ* variable-pressure PXRD data obtained for **Fe(btp)** during activation and with high-pressure CH_4 loading. Top: PXRD patterns obtained for **Fe(btp)** (a) as-synthesized, (b) after He gas used to remove excess solvent, (c) during evacuation at 23 °C, and (d) after evacuation at 150 °C. Bottom: PXRD patterns obtained during variable-pressure CH_4 loading. PXRD patterns of (e) **Fe(btp)** after evacuation at 150 °C and with (f) 25 bar, (g) 50 bar, (h) 75 bar, and (i) 100 bar applied CH_4 pressure. No evolution of the PXRD pattern was observed under these conditions.

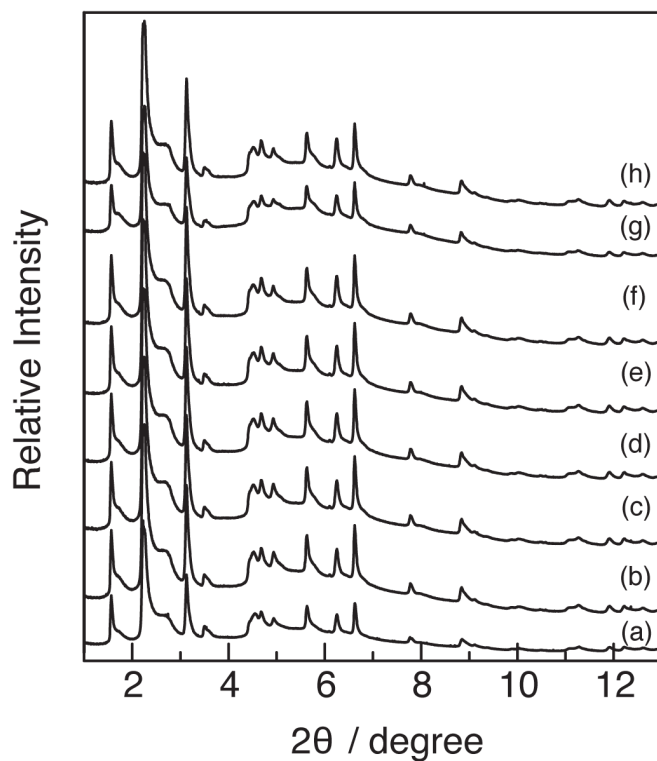


Figure II-19 *In situ* variable-pressure PXRD data obtained for **Fe(btp)** during **high-pressure CO₂ loading**. PXRD patterns obtained during variable-pressure CO₂ loading. PXRD patterns of (a) **Fe(btp)** after evacuation at 150 °C and with (b) 5, (c) 10, (d) 15, (e) 20, (f) 25, and (g) 30 bar applied CO₂ pressure. No evolution of the PXRD pattern was observed under these conditions.

For application to oxidation catalysis, porosity in the absence of guests is not required, only guest exchange is necessary. The layered materials presented here readily participate in guest exchange. Soaking **Fe(btp)** in a CH₃CN solution of fluorescent dye rhodamine 6G¹¹⁶ results in the intercalation of dye into the material (30 wt%), as evidenced by UV-vis analysis of both the soaking liquid and the digested solids (**Table II-3** and **Figure II-20**). The ability for solution-phase guest exchange reactions to proceed demonstrates that the porosity of our materials is maintained in the presence of suitable guests. In contrast, no dye uptake is observed with **Fe(btp)_{act}**.

Table II-3 Summary of results from dye-uptake experiments

Sample	Measured	$\mu\text{mol dye}$ incorporated	mg dye incorporated	mg sample	weight % dye
Fe(btp)	Soaking solution	4.02	1.93	6.3	30
	Digested solid	3.75	1.80	4.0	31
Fe(btp)_{act}	Soaking solution	1.1	0.51	21.4	5.1
	Digested solid	0	0	15.2	0
Fe(btp)_{ground}	Soaking solution	3.6	5.6	5.6	30
	Digested solid	0.73	0.35	0.7	37

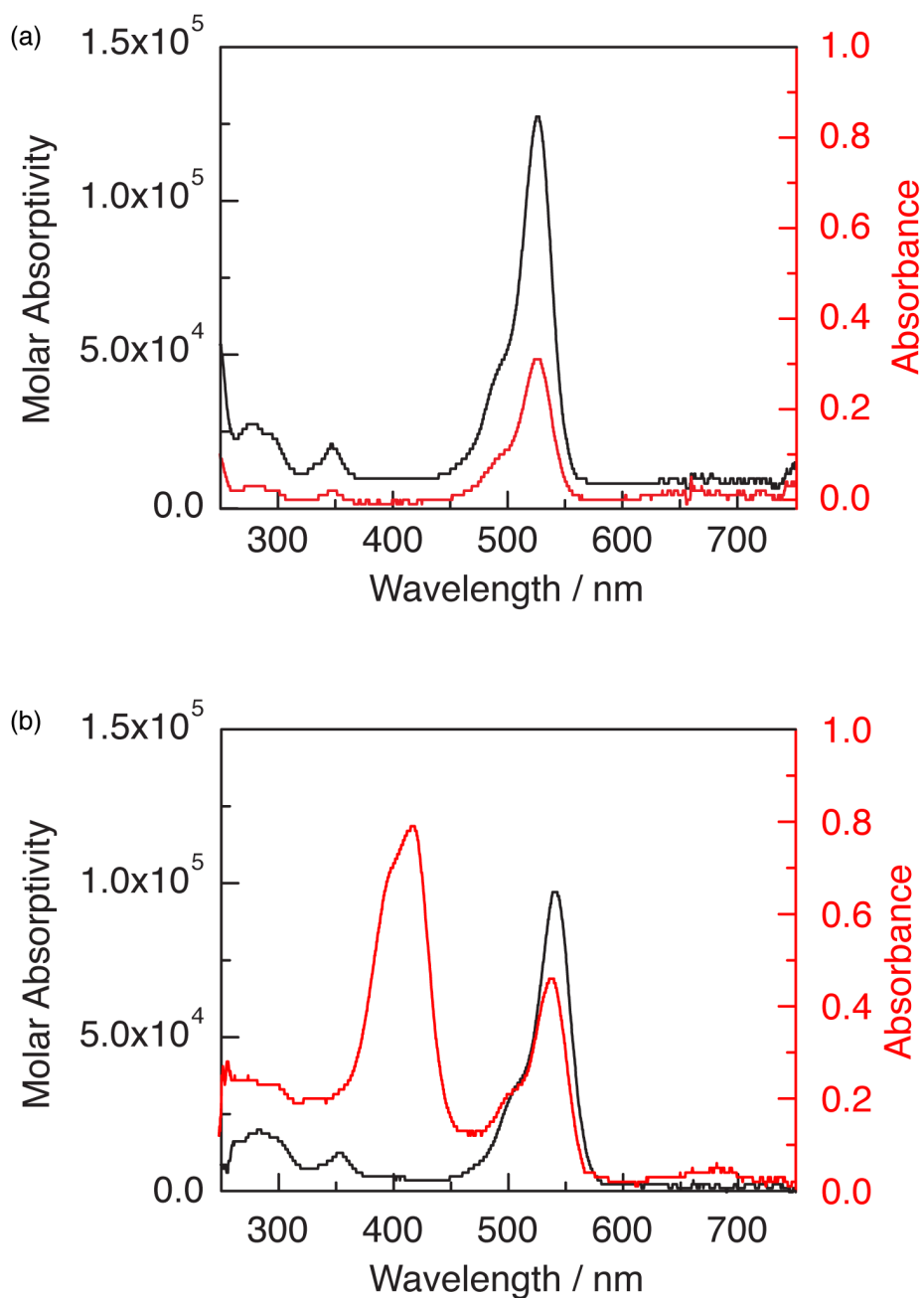


Figure II-20 Absorptivity of rhodamine 6G in CH₃CN and DMSO. (a) Absorptivity of rhodamine 6G in CH₃CN (—) and spectrum used to establish concentration of rhodamine 6G in the supernatant following dye uptake (—). (b) Absorptivity of rhodamine 6G in DMSO (—) and spectrum used to establish concentration of rhodamine 6G in the supernatant following dye uptake in the digested solids (—).

We selected *cis*-decalin as an initial substrate for hydroxylation catalysis using our layered materials for two reasons. First, *cis*-decalin presents multiple chemically and stereochemically distinct C–H bonds. Second, *cis*-decalin provides a stereochemical probe during oxidation: Hydrogen-atom abstraction (HAA) from C9 generates a tertiary radical that can undergo epimerization (**Figure II.21**).¹⁴⁴ The ratio of *cis*- and *trans*-decahydronaphthalen-9-ol (**2.1**) provides information regarding the rate of hydroxylation relative to epimerization. The modest preference for stereoretention during oxidation catalyzed by soluble metalloporphyrins has been rationalized as arising from radical rebound within a solvent cage.¹⁴⁵ This idea of a solvent cage influencing product distributions for reactions involving radical pairs has also been invoked in the photoreaction of 2-iodooctane.¹⁴⁶

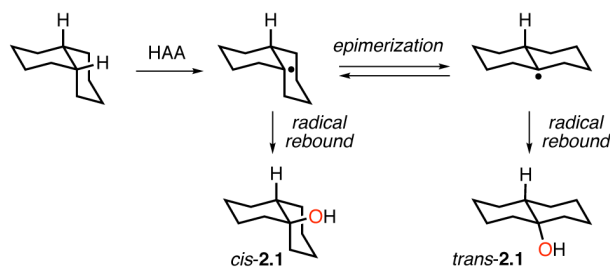


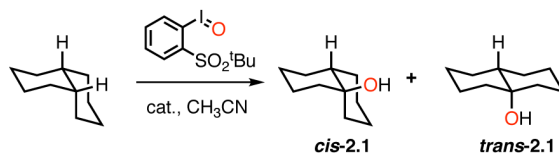
Figure II-21 Epimerization of *cis*-decalin-derived radicals provides a mechanism to generate both *cis*- and *trans*-2.1 during radical hydroxylation.

Treatment of **Fe(btp)** with *cis*-decalin and 2-(*tert*-butylsulfonyl)iodosylbenzene,¹⁴⁷ a common soluble oxygen-atom transfer reagent, afforded a >100:1 mixture of *cis*- and *trans*-**2.1** (**Table II.4**, entry 1). In comparison,

molecular catalysts Fe(tpp)Cl and Fe(tmpp)Cl afforded 3.3:1 and 8.5:1 mixtures of *cis*- and *trans*-**2.1**, respectively (entries 7 and 8; tpp = 5,10,15,20-tetraphenylporphyrin; tmpp = 5,10,15,20-tetrakis(4-methoxycarbonylphenyl)porphyrin). Similarly, catalysis with **Fe(btp)_{act}**, which does not exhibit dye-uptake activity (**Table III.4**), results in a 4:1 mixture of *cis*- and *trans*-**2.1** (Entry 3). Leaching experiments conducted with **Fe(btp)** demonstrated no conversion of *cis*-decalin. Further, **Fe(btp)** was found to be recyclable; reusing **Fe(btp)** gave unchanged conversion and selectivity.

The above data suggest that metalloporphyrin sites housed within **Fe(btp)** accomplish highly stereospecific oxidation while metalloporphyrin sites on the surface accomplish oxidation with low stereospecificity, we evaluated the selectivity that was achieved using ground samples of our porous materials. As synthesized samples of **Fe(btp)** exhibit a broad particle size distribution, with many crystallites exhibiting larger than 100 μm edges. Ground samples of **Fe(btp)** showed narrower particle size distribution centered at $\sim 10 \mu\text{m}$ (SEM images are collected in **Figure II-22-23**). Whereas as-synthesized **Fe(btp)** affords a >100:1 mixture of *cis*- and *trans*-**2.1**, oxidation with a ground sample of **Fe(btp)** provides a 53:1 mixture (Entry 2). Importantly, grinding had no impact on dye uptake capacity (**Table II-4**). A similar trend is observed when **Fe(bpy)** is used as an oxidation catalyst. As synthesized samples afford a 50:1 mixture of *cis*- and *trans*-**2.1** while ground samples afford a 37:1 ratio (Entries 4 and 5).

Table II-4 Oxidation of *cis*-decalin affords a mixture of *cis*- and *trans*-decahydronaphthalen-9-ol (**2.1**). Catalysis with soft material **Fe(btp)** affords the highest selectivity.



	catalyst	conversion (%)	selectivity (c : t)
1	Fe(btp)	6.0	>100
2	Fe(btp)_{ground}	5.2	50
3	Fe(btp)_{act}	2.1	4.3
4	Fe(bpy)	5.1	53
5	Fe(bpy)_{ground}	6.5	37
6	Fe(bpy)_{act}	2.1	3.8
7	Fe(tmp)Cl	0.5	8.5
8	Fe(tp)Cl	0.2	3.3

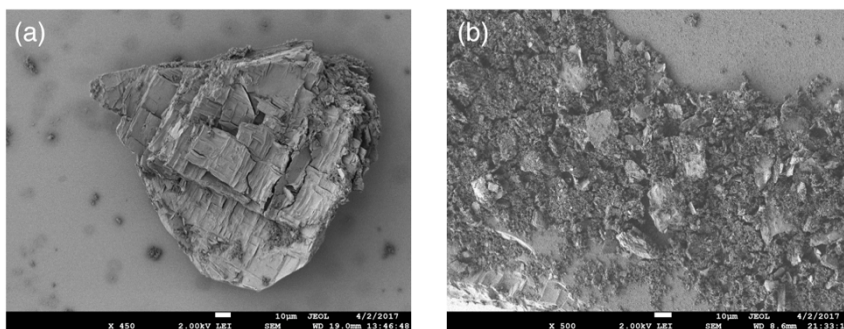


Figure II-22 SEM data of as-synthesized and ground **Fe(btp)**. (a) SEM images of unground **Fe(btp)** at 450x. (b) SEM images of ground **Fe(btp)** at 500x magnification.

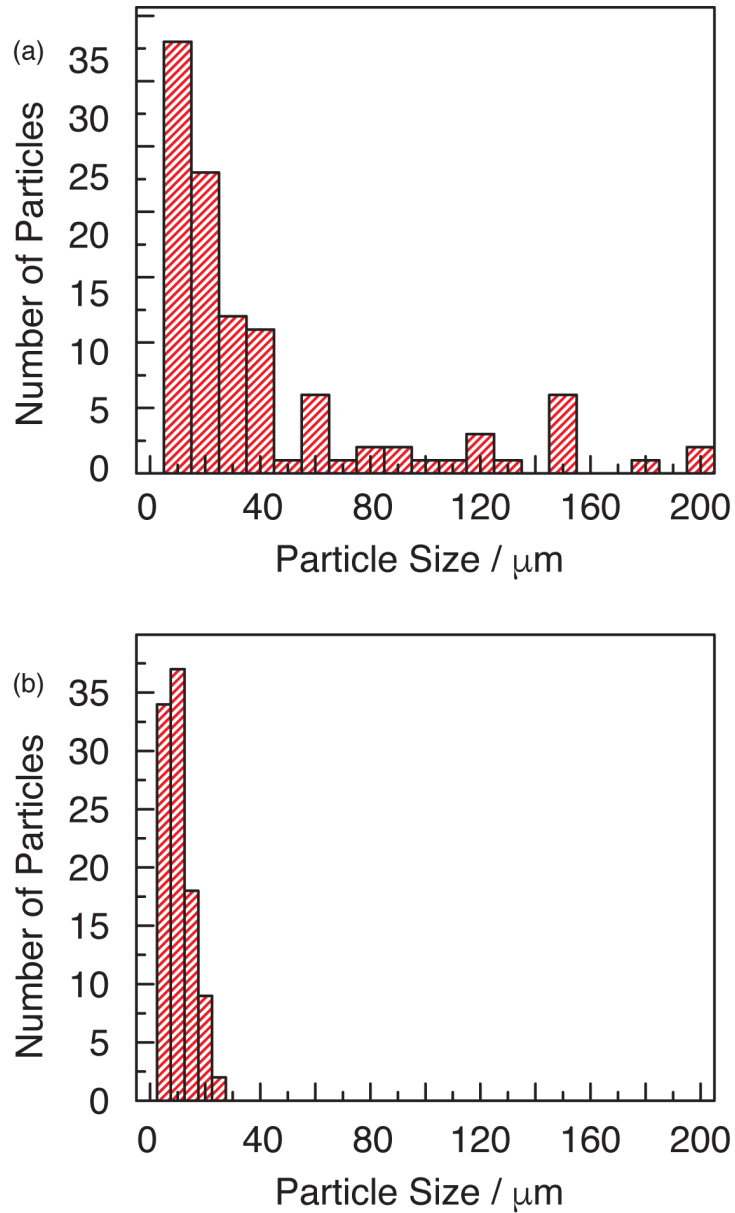


Figure II-23 Histogram of particle distribution in (a) unground and (b) ground Fe(btp). The size distribution (length and width of the particles) was measured using ImageJ. For each image, 100 particles were examined.

The collected data is consistent with rapid hydroxylation of radical intermediates inside our porous materials. Relatively slow hydroxylation of radical intermediates by surface-bound catalysts provides opportunity for loss of stereospecificity during oxidation. These observations suggest that our porous materials effectively function as tight solvent cages and prevent stereochemical scrambling during hydroxylation chemistry. Further, the observed relationship between the outer surface area of catalyst particles and reaction stereospecificity provides a useful tool to differentiate *catalysis in* from *catalysis on* these porous materials.

II.3 Conclusions

In summary, we have prepared a new isorecticular family of layered porphyrinic materials with substrate-accessible unsaturated Fe porphyrin sites. These materials are competent in the hydroxylation of aliphatic C–H bonds. We have shown that these materials affect highly stereospecific oxidation of *cis*-decalin while hydroxylation with homogeneous and non-porous analogs proceeds with low stereospecificity. Stereospecificity can be modulated by grinding the catalyst material to generate particles with greater external surface area, and product selectivity provides a probe for differentiating *catalysis in* versus *catalysis on* these porous materials. Accomplishing *catalysis in* materials is a critical prerequisite to utilizing pore structure to control chemical selectivity. We anticipate that use of *cis*-decalin oxidation specifically, and other stereochemical probes generally, may provide useful tools for evaluating the locus of *catalysis in* with porous materials.

II.4 Experimental Details

II.4.1 General Considerations

Materials Solvents were obtained as ACS reagent grade and used as received, except for DMF, which was stored over 4 Å molecular sieves, and CH₃CN and CH₂Cl₂, which were obtained from a drying column.¹⁴⁸ Sodium hydroxide, and *N,N'*-diethylformamide (DEF) were obtained from EMD Millipore. 1,2,4-triazole and 1,3-bis(4-pyridyl)propane were obtained from TCI America. Pyrrole, chromium(VI) oxide, methyl *p*-formylbenzoate, and absolute ethanol were obtained from Beantown Chemical, Chem Impex, Ark Pharm, and Koptec, respectively. *N,N'*-diethylacetamide (DEA), 1,3-dibromopropane, 4-carboxybenzaldehyde, and FeCl₂·4H₂O were obtained from Alfa Aesar. 1,2-Bis(4-pyridyl)ethane (bpe) was obtained from Acros. Sodium sulfite, benzaldehyde, and D₂SO₄ were obtained from Sigma Aldrich. The aforementioned reagents were used as received. Zn(NO₃)₂·6H₂O was obtained from Strem Chemicals and was dried under vacuum (~50 mbar) at 23 °C prior to use. *Cis*- and *trans*-decalin were purchased through TCI and purified from alcohol impurities by washing with H₂SO₄ and was then dried over Na metal.¹⁴⁹ 4,4'-bipyridine (bpy) was purchased from Sigma Aldrich and purified by sublimation prior to use. Tetrabutylammonium periodate,¹⁵⁰ *cis*- and *trans*-1,4-dimethylcyclohexanol,¹⁵¹ *cis*- and *trans*-decahydronaphthalen-9-ol,¹⁵¹ 1,3-bis(1,2,4-triazole-1-yl)propane (btp),¹⁵ 5,10,15,20-tetraphenylporphyrin (H₂tcpp),¹⁵² 5,10,15,20-tetraphenylporphyrin iron chloride (Fe(tcpp)Cl),¹⁵³ and 2-(*tert*-butylsulfonyl)iodosylbenzene¹⁴⁷ were synthesized according to literature procedures. NMR solvents were purchased from Cambridge Isotope Laboratories and were used as

received. UHP-grade N₂, CO₂, and He, used in gas sorption measurements, were obtained from Airgas.

Characterization Details NMR spectra were recorded on Inova 500 FT NMR operating at 499.53 MHz for ¹H acquisitions and were referenced against solvent signals: CDCl₃ (7.26 ppm, 1H; 77.16 ppm, ¹³C) and DMSO-d₆ (2.48 ppm, 1H).¹⁵⁴ ¹H NMR data are reported as follows: chemical shift (δ, ppm), (multiplicity: s (singlet), d (doublet), t (triplet), m (multiplet), br (broad), integration). UV-vis spectra were recorded at 293 K in quartz cuvettes on an Ocean Optics Flame-S miniature spectrometer with DH-mini UV-vis NIR light source and were blanked against the appropriate solvent. Solid-state UV-vis spectra were recorded as mineral oil dispersions on glass slides using Hitachi U-4100 UV-vis-NIR spectrophotometer and were blanked against the empty glass slide sandwiches. IR spectra were recorded on a Shimadzu FTIR/IRAffinity-1 spectrometer. Spectra were blanked against air and were determined as the average of 128 scans. IR data are reported as follows: wavenumber (cm⁻¹), (peak intensity: s, strong; m, medium; w, weak). Elemental analyses were carried out by Atlantic Microlab, Inc. (Norcross, GA). Inductively coupled plasma mass spectrometry (ICP-MS) were performed by PerkinElmer NexION 300D housed in the Texas A&M Center for Chemical Characterization and Analysis. MALDI-TOF data were obtained with an ABI Voyager DE STR operating in reflector mode with 20 kV voltage. Thermogravimetric analyses were measured up to 600 °C with a scan rate of 5 °C/min using TGA Q500 of TA instruments. Gas chromatography was performed on a Shimadzu GC-2010 with a dimethyl polysiloxane column (15.0 m, 0.25 mm ID). Scanning electron microscopy was performed at the Materials

Characterization Facility on a JEOL JSM-7500F. Samples were prepared via dropcasting onto clean gold coated silicon wafers (Chromium adhesion layer 7 nm; gold layer 200 nm) and solvent was removed by heating to 80 °C for 10 min. A thin 5 nm Pt/Pd layer was sputter coated onto the sample.

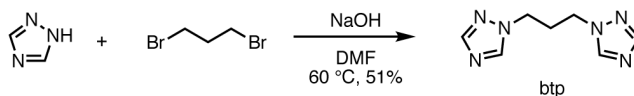
X-ray Diffraction Details Powder X-ray diffraction (PXRD) measurements were carried out on a Bruker D8 Advance Eco X-ray diffractometer (Cu K α , 1.5418 Å; 40 kV, 25 mA) fitted with LynxEye detector. The angular range was measured from 4.00 to 40.00° (2 θ) with steps of 0.020° and a measurement time of 0.3 s per step. Single-crystal X-ray diffraction (SCXRD) data of **Fe(btp)**, **Fe(bpy)**, and **Fe(bpe)** were collected both using radiation from a Cu K α (1.5418 Å) source on a Bruker three-circle D8 goniometer equipped with an Apex II CCD at 293 K and using synchrotron radiation (0.82656 Å; ChemMatCARS located at the Advanced Photon Source housed at Argonne National Laboratory) on a vertically mounted Bruker D8 three-circle platform goniometer equipped with an Apex II CCD and an Cryojet N₂ cold stream operating 95–293 K.

Variable-pressure (VP) *in situ* PXRD data were collected at Beamline 17-BM-B located at the Advanced Photon Source (APS) housed at Argonne National Laboratory (ANL) using synchrotron radiation ($\lambda = 0.45336$ Å). Data were collected in transmission mode with a Perkin Elmer α -Si flat panel detector. Data were collected as ω scans (5 °). Sample temperature was controlled with an Oxford Cryosystems operating between 23–150 °C. SPEC was utilized for beamline control and QXRD for data acquisition. The GSASII5 program was used for data processing and calibration using a LaB6 standard sample. Samples were ground as suspensions in either DMF or DEA and then were loaded

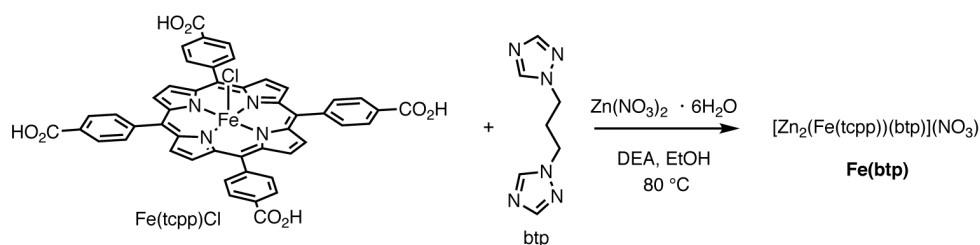
into Kapton capillaries (ID: 0.0395", OD: 0.0435", Wall thickness: 0.0020") as solvent suspensions. Solvent was removed by purging the sample with He at 23 °C (5 mL/min) and evacuating at 23 °C. Samples were activated in the capillaries by heating to 150 °C under vacuum. Following sample activation, samples were cooled to 23 °C for variable pressure data collection. VP diffraction data was acquired from 5–100 bar with 5 bar steps. CH₄ or CO₂ was introduced to the capillary (5 bar) and pressure was subsequently controlled with a piston. The sample was allowed to equilibrate at each pressure for 2 min prior to data collection.

Gas Sorption Details Gas adsorption isotherms for pressures in the range 0–1.0 bar were measured using a volumetric method using a Micromeritics ASAP2020 instrument. Samples were transferred under an N₂ atmosphere to pre-weighed analysis tubes, then capped with a TranSeal. The samples were evacuated at 150 °C until the outgas rate was <10 μbar/min, at which point the tube was weighed to determine the mass of the activated sample. The tube was transferred to the analysis port of the instrument and the outgas rate was again checked to ensure that it was <6 μbar/min. UHP-grade (99.999% purity) N₂, CO₂, and He were used for all adsorption measurements. For all isotherms, both warm and cold free-space measurements were carried out with He; N₂ isotherms were measured at 77 K with liquid nitrogen and CO₂ isotherms at 195 K were measured with dry ice and acetone.

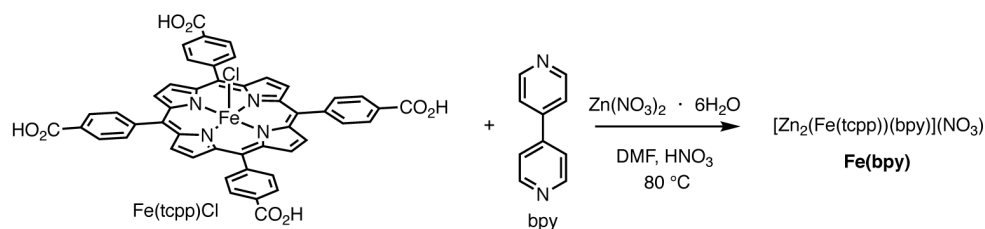
II.4.2 Synthesis



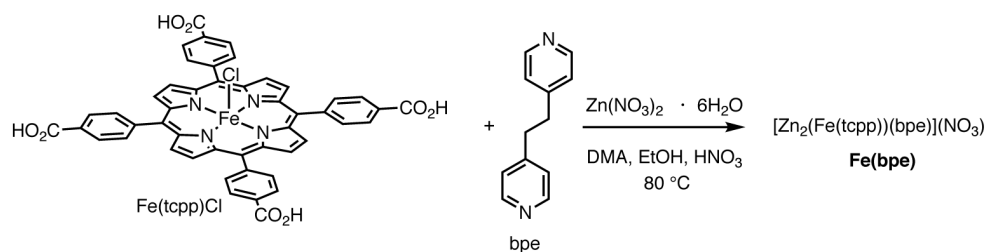
Synthesis of 1,3-bis(1,2,4-triazole-1-yl)propane (btp) 1,3-bis(1,2,4-triazole-1-yl)propane was prepared by the following modification of literature methods.¹⁵⁵ A round-bottom flask was charged with a DMF solution (80 mL) of 1,2,4-triazole (7.04 g, 0.102 mol, 1.31 equiv). Sodium hydroxide (4.15 g, 0.104 mol, 1.34 equiv) was added to the reaction vessel and the reaction mixture was heated at 60 °C for 1 h. 1,3-dibromopropane (6.37 g, 0.0388 mol, 1.00 equiv) was added and the reaction mixture was heated at 60 °C for 2 h and then allowed to cool to 23 °C. Volatiles were removed *in vacuo*. The residue was dissolved in distilled H₂O (100 mL) and then extracted with CHCl₃ (4 × 150 mL). The combined organic layers were dried over MgSO₄ and solvent was removed *in vacuo* to afford a white solid. The obtained solid was purified by recrystallization from CHCl₃/*n*-hexane to afford the title compound as a colorless crystalline solid (3.54 g, 51% yield). ¹H NMR (δ, 23 °C, CDCl₃): 8.13 (s, 2H), 7.98 (s, 2H), 4.21 (m, 4H), 2.46 (m, 2H). The obtained spectral data are well-matched with literature reports.¹⁵⁵



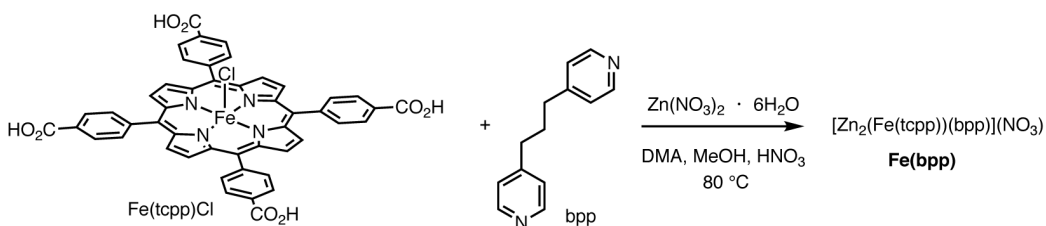
Synthesis of $[\text{Zn}_2(\text{Fe}(\text{tcpp}))(\text{btp})](\text{NO}_3)$ (Fe(btp)) An 8-mL vial was charged with $\text{Zn}(\text{NO}_3)_2 \cdot 6\text{H}_2\text{O}$ (30.0 mg, 0.101 mmol, 2.30 equiv), $\text{Fe}(\text{tcpp})\text{Cl}$ (19.4 mg, 0.0220 mmol, 1.00 equiv), btp (7.6 mg, 0.043 mmol, 2.0 equiv), and a mixture of *N,N*-diethylacetamide (DEA) and EtOH (2.0 mL, v/v 4:1). The reaction mixture was heated at $80\text{ }^\circ\text{C}$ for 24 h, at which time dark red plate-shaped crystals were formed. After cooling to $23\text{ }^\circ\text{C}$, the mother liquor was decanted. DEA (8 mL) was added to as-synthesized crystals and refreshed several times until the solution color became colorless to remove unreacted starting materials. After immersing in DEA for 2 h, the crystals were filtered and washed with DEA. For further characterization, the as-synthesized solid was dried at $150\text{ }^\circ\text{C}$ for 12 h under vacuum. Elemental analysis for $\text{Zn}_2\text{FeC}_{55}\text{H}_{34}\text{N}_{11}\text{O}_{11}$: C 54.53, H 2.83, N 12.72; found: C 54.36, H 3.12, N 12.34, Cl 0.00. IR (cm^{-1}): 1605 (s), 1530 (m), 1393 (s), 1333 (m), 1279 (m), 1204 (m), 1177 (m), 1136 (s), 1101 (m), 999 (m), 871 (m), 835 (m), 800 (m), 775 (s), 710 (m), 671 (m), 605 (m). Relevant physical characterization can be found in **Figure II-1** (PXRD), **Figure II-2** (UV-vis), and **Figure II-4** (IR).



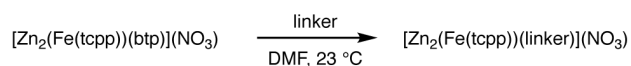
Synthesis of $[Zn_2(Fe(tcpp))(bpy)](NO_3)$ (Fe(bpy)) An 8-mL vial was charged with $Zn(NO_3)_2 \cdot 6H_2O$ (29.3 mg, 0.098 mmol, 2.33 equiv), $Fe(tcpp)Cl$ (18.7 mg, 0.0212 mmol, 1.00 equiv), 4,4'-bipyridine (bpy; 3.7 mg, 0.024 mmol, 1.1 equiv), *N,N*-diethylformamide (DEF, 1.5 mL), and EtOH (0.5 mL). Nitric acid (0.020 mL) was added to the reaction mixture and the resulting reaction mixture was heated at $80\text{ }^\circ C$ for 24 h, at which time dark red plate-shaped crystals were formed. After cooling to $23\text{ }^\circ C$, the mother liquor was decanted. DEF (8 mL) was added to as-synthesized crystals and refreshed several times until the solution color became colorless to remove unreacted starting materials. After immersing in DEF for 2 h, the crystals were filtered and washed with DEF. For further characterization, the as-synthesized solid was dried at $150\text{ }^\circ C$ for 12 h under vacuum. Elemental analysis for $Zn_2FeC_{58}H_{32}N_7O_{11}$: C 58.56, H 2.71, N 8.24; found: C 57.25, H 3.24, N 7.89, Cl 0.00. IR (cm^{-1}): 1659 (m), 1603 (s), 1549 (m), 1383 (s), 1331 (w), 1254 (m), 1221 (w), 1202 (m), 1177 (m), 1096 (s), 1070 (m), 1001 (s), 870 (m), 837 (w), 800 (s), 775 (s), 719 (w), 712 (s), 664 (m), 594 (m). Relevant physical characterization can be found in **Figure II-10** (PXRD), **Figure II-11** (UV-vis), and **Figure II-12** (IR).



Synthesis of $[\text{Zn}_2(\text{Fe}(\text{tcpp}))(\text{bpe})](\text{NO}_3)$ (Fe(bpe)**)** An 8-mL vial was charged with $\text{Zn}(\text{NO}_3)_2 \cdot 6\text{H}_2\text{O}$ (29.6 mg, 0.099 mmol, 2.25 equiv), $\text{Fe}(\text{tcpp})\text{Cl}$ (19.5 mg, 0.0221 mmol, 1.00 equiv), 1,2-bis(4-pyridyl)ethane (bpe; 4.1 mg, 0.022 mmol, 1.0 equiv), and a mixture of DEA and EtOH (2.0 mL, v/v 4:1). Nitric acid (0.020 mL) was added to the reaction mixture and the resulting reaction mixture was heated at 80 °C for 24 h, at which time dark red plate-shaped crystals were formed. After cooling to 23 °C, the mother liquor was decanted. DEA (8 mL) was added to as-synthesized crystals and refreshed several times until the solution color became colorless to remove unreacted starting materials. After immersing in DEA for 2 h, the crystals were filtered and washed with DEA. For further characterization, the as-synthesized solid was dried at 150 °C for 12 h under vacuum. Elemental analysis for $\text{Zn}_2\text{FeC}_{60}\text{H}_{36}\text{N}_7\text{O}_{11}$: C 59.19, H 2.98, N 8.05; found: C 57.72, H 3.20, N 7.82, Cl 0.00. IR (cm^{-1}): 1601 (s), 1549 (m), 1503 (m), 1398 (s), 1333 (m), 1265 (m), 1202 (m), 1175 (m), 1138 (m), 1097 (m), 1070 (m), 999 (s), 870 (m), 837 (m), 800 (m), 773 (s), 710 (s), 598 (m). Relevant physical characterization can be found in **Figure II-10** (PXRD), **Figure II-11** (UV-vis), and **Figure II-12** (IR).



Synthesis of $[Zn_2(Fe(tcpp))(bpp)](NO_3)$ (Fe(bpp)) An 8-mL vial was charged with $Zn(NO_3)_2 \cdot 6H_2O$ (28.0 mg, 0.094 mmol, 2.04 equiv), $Fe(tcpp)Cl$ (19.9 mg, 0.0226 mmol, 1.00 equiv), 1,3-bis(4-pyridyl)propane (bpp; 4.8 mg, 0.024 mmol, 1.0 equiv), and a mixture of *N,N*-dimethylformamide (DMF) and MeOH (2.0 mL, v/v 3:2). Nitric acid (0.020 mL) was added to the reaction mixture and the resulting reaction mixture was heated at $80\text{ }^\circ\text{C}$ for 24 h, at which time dark red plate-shaped crystals were formed. After cooling to $23\text{ }^\circ\text{C}$, the mother liquor was decanted. DMF (8 mL) was added to as-synthesized crystals and refreshed several times until the solution color became colorless to remove unreacted starting materials. After immersing in DMF for 2 h, the crystals were filtered and washed with DMF. For further characterization, the as-synthesized solid was dried at $150\text{ }^\circ\text{C}$ for 12 h under vacuum. Elemental analysis for $Zn_2FeC_{61}H_{38}N_7O_{11}$: C 59.49, H 3.11, N 7.96; found: C 58.41, H 3.53, N 7.84, Cl 0.00. IR (cm^{-1}): 1599 (s), 1549 (m), 1395 (s), 1335 (m), 1280 (m), 1256 (m), 1202 (m), 1179 (m), 1142 (m), 1099 (m), 1070 (m), 997 (s), 870 (m), 837 (m), 799 (s), 775 (s), 719 (s), 664 (m), 596 (m). Relevant physical characterization can be found in **Figure II-10** (PXRD), **Figure II-11** (UV-vis), and **Figure II-12** (IR).



General Procedure for Linker Exchange of Fe(btp) with bpy, bpe, and bpp

As-synthesized crystals of **Fe(btp)** were immersed in DMF. After DMF was repeatedly refreshed until the solution color became colorless, the crystals were soaked in a DMF solution (8.0 mL, ~5.0 mM) of bpy, bpe, or bpp at 23 °C for 2 days to yield linker-exchanged materials of (**Fe(bpy)**), (**Fe(bpe)**), and (**Fe(bpp)**), respectively.

Characterization of Layered Materials Accessed by Linker Exchange: **Fe(bpy)**: IR (cm⁻¹): 1666 (s), 1607 (m), 1549 (m), 1396 (s), 1337 (m), 1256 (m), 1204 (m), 1177 (m), 1096 (s), 1070 (m), 1001 (s), 872 (m), 837 (m), 800 (s), 775 (s), 712 (s), 662 (m), 592 (m), 571 (m), 525 (m). Elemental analysis for Zn₂Fe₁C₅₈H₃₂N₇O₁₁: C 58.56, H 2.71, N 8.24; found: C 58.02, H 3.22, N 7.63. **Fe(bpe)**: IR (cm⁻¹): 1659 (s), 1607 (m), 1551 (m), 1503 (m), 1393 (s), 1333 (m), 1281 (m), 1256 (m), 1227 (m), 1177 (m), 1144 (m), 1097 (s), 1038 (m), 999 (s), 872 (m), 835 (m), 799 (m), 775 (s), 711 (s), 664 (m), 598 (m), 559 (m). Elemental analysis for Zn₂Fe₁C₆₀H₃₆N₇O₁₁: C 59.19, H 2.98, N 8.05; found: C 58.40, H 3.65, N 7.83. **Fe(bpp)**: IR (cm⁻¹): 1661 (s), 1607 (m), 1555 (m), 1501 (m), 1391 (s), 1335 (m), 1254 (m), 1227 (m), 1202 (m), 1177 (m), 1144 (m), 1097 (s), 1038 (m), 997 (s), 872 (m), 837 (m), 799 (m), 775 (s), 710 (s), 662 (s), 600 (m). Elemental analysis for Zn₂Fe₁C₆₁H₃₈N₇O₁₁: C 59.49, H 3.11, N 7.96; found: C 58.73, H 3.59, N 7.83.

II.4.3 Dye Uptake Experiments

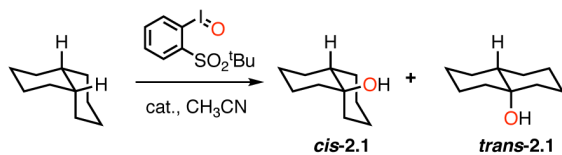
General Procedure for Dye Uptake Experiments To Fe(btp) (20-21 mg) which had previously been washed and dried via vacuum filtration, a rhodamine 6G solution (3.1 mM) in CH₃CN) was added. Solids were allowed to sit in dye solutions for 48 h at 23 °C. The UV-vis spectrum of the resulting soaking solution was measured to determine the concentration of rhodamine 6G remaining in the supernatant. The solids were rinsed with CH₃CN until the filtrate was colorless and dried under vacuum until the mass of the solids stabilized. Materials were digested in DMSO with 25 μL of H₂SO₄ and diluted to 10 mL. The UV-vis spectrum of the digested solids was measured to quantify the amount of rhodamine 6G that had been intercalated into the solid; the contribution of the porphyrin to the absorbance at 541 nm was subtracted using the soret intensity to determine porphyrin concentration. Extinction spectra were measured both in CH₃CN and in acid DMSO to allow easy quantification of the rhodamine 6G by absorption spectroscopy. Results are collected in **Table II-3**.

Determination of Uptake by Analysis of Soaking Solution To determine dye uptake by analysis of the soaking solution, the mass of the **Fe(btp)** material was determined by weighing incompletely dried samples and adjusting the actual mass loading by determining the amount of residual solvent in the loaded sample. For example, for **Fe(btp)**, the incompletely dried sample was found to weigh 21.1 mg. By ¹H NMR, this sample was found to be composed of 70% DEA, thus the mass attributed to the actual MOF is 6.3 mg. This solvent corrected mass was used to calculate weight percent of uptake based on the difference in UV-vis absorption of rhodamine-6G before and after soaking.

Determination of Uptake by Analysis of Solid Digestion In the case of the digestion experiment, the amount of solid digested was directly weighed. Weight % in this case is simply mg dye incorporated (determined by the UV-vis absorption of rhodamine-6G after digestion) divided by the found mass.

Mass Balance of Dye-Uptake Experiments The initial mass of dye used was 2.9 mg for each of **Fe(btp)**, **Fe(btp)_{act}**, and **Fe(btp)_{ground}**. UV-vis of the soaking solution showed that 1.01 mg, 2.58 mg, and 1.15 mg of dye remained in the soaking solutions of **Fe(btp)**, **Fe(btp)_{act}**, and **Fe(btp)_{ground}**, respectively. Materials were isolated from the dye solution, washed with acetonitrile with vacuum filtration to remove surface bound dye, isolated and dried under vacuum to remove any remaining solvent. Solids were then degraded, giving incorporated dye values of 1.80 mg, 0 mg, and 0.35 mg for **Fe(btp)**, **Fe(btp)_{act}**, and **Fe(btp)_{ground}** respectively, giving the following total mass balance following dye uptake: **Fe(btp)** = 2.8 mg; **Fe(btp)_{act}** = 2.6 mg; and **Fe(btp)_{ground}** = 1.5 mg. The relatively low value of the mass balance for **Fe(btp)_{ground}** can be attributed to the small amount of sample that was able to be isolated post-washing (only 0.7 mg in comparison to an initial 5.6 mg).

II.4.4 C–H Hydroxylation



General Procedure for C–H Hydroxylation with MOF Catalysts A vial was charged with MOF as a wet powder (20-25 mg), CH₃CN (2.5 mL), and substrate (0.97 mmol). Oxidant (0.23 mmol) was added to the mixture with stirring (390 rpm) in 5-6 portions over 1 h. The reactions were allowed to stir for 24 h. Upon completion, mesitylene (10 μL, 0.072 mmol) was added and the mixtures were filtered through Celite. The filtrate was analyzed by gas chromatography. The remaining solid was then dissolved in aqueous NaOH (2.5 (M)), extracted with CH₂Cl₂, washed with water, and dried over Na₂SO₄. Mesitylene (10 μL, 0.072 mmol) was added and the solution was analyzed by gas chromatography.

Examination of the Impact of Oxidant Loading on Oxidation Catalysis A vial was charged with **Fe(btp)** as a wet powder (20-25 mg), CH₃CN (2.5 mL), and substrate (0.97 mmol). Oxidant (0.077 mmol) was added to the mixture with stirring (390 rpm) in 5-6 portions over 1 h. The reactions were allowed to stir for 24 h. Upon completion, mesitylene (10 μL, 0.072 mmol) was added and the mixtures were filtered through Celite. The filtrate was analyzed by gas chromatography. Decreasing the oxidant by a third led to increase in conversions (13-17%).

Examination of Potential for Leached Homogeneous Catalysts Giving Rise to Hydroxylation A vial was charged with **Fe(btp)** as a wet powder (20-25 mg), CH₃CN (2.5 mL), and substrate (0.97 mmol) and allowed to stand for 24 h. The catalyst removed and oxidant (0.23 mmol) was added to the mixture with stirring (390 rpm) in 5-6 portions over 1 h. The reactions were allowed to stir at 23 °C for 24 h. Upon completion, mesitylene (10 μL, 0.072 mmol) was added and the mixtures were filtered through Celite and the solution was analyzed by gas chromatography. No *cis*-decalin oxidation products were observed in this experiment.

Evaluation of Recyclability of Fe(btp) Catalyst A vial was charged with **Fe(btp)** as a wet powder (20-25 mg), CH₃CN (2.5 mL), and substrate (0.97 mmol). Oxidant (0.073 mmol) was added to the mixture with stirring (390 rpm) in 5-6 portions over 1 h. The reaction was allowed to stir for 24 h. Upon completion, the supernatant was removed via centrifugation, mesitylene (10 μL, 0.072 mmol) was added and the mixture was filtered through Celite and analyzed by gas chromatography. The remaining solid was washed with CH₃CN (2 × 2.5 mL) and left to soak in CH₃CN (2.5 mL) for 10 h. The mixture was centrifuged and the CH₃CN was replaced with fresh solvent (2.5 mL) and substrate (0.97 mmol) was added. Oxidant (0.074 mmol) was added to the mixture with stirring (390 rpm) in 5-6 portions over 1 h. The reaction was allowed to stir for 12 h. Upon completion, mesitylene (10 μL, 0.072 mmol) was added and the mixture were filtered through Celite and the filtrate was analyzed by gas chromatography. The conversion and selectivity was unchanged following catalyst recycling.

Determination of Reaction Yield and Product Selectivity Calibration curves for both *cis*- and *trans*-**2.1** were measured to determine the FID response factor to these substances. Integrated area, in combination with the experimentally determined response factors, were used to determine molar amounts of products in each sample. To determine conversions in catalytic experiments mesitylene (10 μ L, 0.072 mmol) was added to the crude reaction mixture. Using the integration of the GC signal for mesitylene and the FID response factor for mesitylene, the total volume of the reaction mixture was determined. Concentration of each of *cis*- and *trans*-**1** was then determined using the experimentally defined response factors and integrated GC intensity and product selectivities were determined by $[cis\text{-}2.1]/[trans\text{-}2.1]$. Reaction conversion was calculated by dividing the total molar amount of *cis*- and *trans*-**2.1** by the molar amount of oxidant added.

General Procedure for C–H Hydroxylation with Molecular Catalysts A vial was charged with catalyst (0.046 mmol), CH₃CN (2.5 mL), and *cis*-decalin (0.97 mmol). Oxidant (0.23 mmol) was added to the heterogeneous mixture with stirring (390 rpm) in 5-6 portions over 1 h. The reactions were allowed to stir for 24 h. Upon completion aqueous NaOH (2.5 M) was added and the solution was extracted with CH₂Cl₂, washed with HCl (1 M) and DI water and dried over Na₂SO₄. To remove oxidized porphyrin byproducts prior to GC analysis, NaBH₄ was added to the dark red solution and stirred overnight, resulting in a light orange solution. Mesitylene (10 μ L, 0.072 mmol) was added and the solution was analyzed by gas chromatography.

Control Experiments Probing Potential Hydroxylation with FeCl₂, Zn(NO₃)₂, or H₂tepp A vial was charged with catalyst (0.046 mmol), CH₃CN (2.5 mL), and *cis*-

decalin (0.97 mmol). Oxidant (0.23 mmol) was added to the heterogeneous mixture with stirring (390 rpm) in 5-6 portions over 1 h. The reactions were allowed to stir for 24 h. Upon completion, mesitylene (10 μ L, 0.072 mmol) was added and the mixtures were filtered through Celite. The filtrate was analyzed by gas chromatography. In order to remove Fe byproducts at the conclusion of the control reaction with FeCl₂, the solution was first washed with aqueous HCl (1 M) and extracted with CH₂Cl₂. The CH₂Cl₂ layer was dried with Na₂SO₄, mesitylene was added, and the solution was analyzed by gas chromatography. In all cases, hydroxylation was not observed.

CHAPTER III
CRYSTAL-SIZE DEPENDENCE ON *CIS*-DECALIN OXIDATION AND THE
SYNTHESIS OF 2-D LAYERED MATERIALS FOR STEREORETENTIVE C–H
OXIDATION

III.1 Introduction

Metal-organic framework (MOF) catalysts have been utilized for a variety of oxidative transformations such as epoxidation,^{31,33,50} hydroxylation,³² and amination.³⁴ In addition, MOF catalysts have demonstrated the potential to provide complementary chemical selectivity to solution-phase reactions.¹¹²⁻¹¹⁴ It has been demonstrated by us¹⁵ and others^{30,110-111} that particle size can affect the selectivity and rate of MOF-catalyzed chemical reactions, however, in many studies concerning MOF catalysis, the particle morphology and size is frequently ill-characterized. Particle size and morphology are expected to influence catalyst selectivity if solvent-exposed surface sites behave analogously to a soluble catalysts, while interstitial catalyst sites are influenced by substrate confinement within the pore space. Based on our previous work focused on evaluating the selectivity of *cis*-decalin oxidation in porous materials,¹⁵ we were interested in evaluating the relationship between crystallite size and selectivity for oxidation chemistry.

Beyond investigating the fundamental importance of crystallite size on C–H oxidation stereoselectivity, we also wanted to explore the scope of stereoretentive oxidation chemistry observed for *cis*-decalin oxidation to the oxidation of other substrates.

To this end, we have synthesized layered porphyrinic materials lacking layer-to-layer linking elements. Similar layered porphyrinic MOFs have been synthesized and demonstrate that the layer-to-layer spacing is flexible – varying as a function of temperature.¹⁵⁶ We hypothesized that this observed flexibility could allow for substrate-responsive catalysis upon intercalation of guests. To examine this hypothesis, we proposed to initially study *cis*-decalin oxidation and expand to other substrates.

III.2 Results and Discussion

III.2.1 Controlled Crystal Growth of *Fe(btp)* and Selectivity of *Cis*-decalin Oxidation

The size distribution of $[\text{Zn}_2(\text{Fe}(\text{tcpp}))(\text{btp})(\text{NO}_3)]_n$ (**Fe(btp)**) crystals is dependent on the length of time the samples are heated during solvothermal synthesis. Solvothermal synthesis at 80 °C for 4, 10, and 16 h produced plate-shaped crystals with average side lengths of $2.40 \pm 0.99 \mu\text{m}$, $12.45 \pm 4.12 \mu\text{m}$, and $22.98 \pm 6.02 \mu\text{m}$, respectively (**Figure III-1**). To begin investigating the effect of particle size on the stereoretention of *cis*-decalin oxidation, 20 μm crystals were targeted. Solvothermal reaction at 80 °C for 20 h produced plate-shaped crystals with an average side length of $20.4 \pm 9.0 \mu\text{m}$, as determined by optical spectroscopy (**Figure III-2**). The solid was washed with CH_3CN and immediately subjected to *cis*-decalin oxidation conditions. It was found that the oxidation of *cis*-decalin with crystals in this size regime produced high *c* : *t* selectivity ($> 100 : 1$).

The crystallite size of **Fe(btp)** was also found to be dependent on the concentration of the reaction: Smaller crystals were produced by decreasing the concentration of the

solvothermal reaction conditions from 96 mM to 47 mM, yielding crystals with average side lengths of $3.9 \pm 1.5 \mu\text{m}$ (**Figure III-3**). These observations are similar to previous reports by Zhou *et al.*, which indicated that reaction concentration can influence the crystallite size of metal-organic frameworks.¹⁵⁷ When subjected to *cis*-decalin oxidation conditions, samples with less than 5 μm crystals provided inconsistent results. An initial attempt resulted in *c* : *t* selectivity of 14 : 1, but two additional attempts at replication of this result produced *c* : *t* values of >100 : 1. To determine if the samples were statistically comparable, a one-way analysis of variance (ANOVA) was used. ANOVA is similar to a student's *t*-test, but while the *t*-test is limited to comparing two samples, ANOVA allows for comparison of multiple sample means. ANOVA allows for calculation of F_{calc} , which is the ratio of the variance calculated between sample means to the variance within the samples. This value is then compared to F_{crit} . If F_{calc} exceeds F_{crit} at $\alpha = 0.05$ then the sample means differ with a 5% chance that they are statistically similar. ANOVA of the three data sets generated a F_{calc} of 35.59. In comparison, the F_{crit} for $\alpha = 0.05$ is 3.04. Since $F_{calc} > F_{crit}$ the means of the populations are significantly different (**Table III.1**). This is also confirmed by examining the standard error for the mean values (**Table III.1**). The difference in selectivity could be due to the crystallite sizes not being well-matched between trials. Alternatively, agglomeration of crystallites may be giving rise to the observed variation in selectivity between trials. Crystals of **Fe(btp)** display agglomeration (**Figure III-2**) and it is unknown if this agglomeration causes individual crystallites to behave analogously to a singular, large crystal. Attempted sonication to break-up agglomerates resulted in crystal fragmentation into irregular shapes, making

quantification of side length difficult. The inconsistency of the results of *cis*-decalin oxidation by crystals with 4 μm side-lengths, stands in contrast to the previously completed and reproducible grinding studies.¹⁵ It is of note that crystal agglomeration occurs during the crystal growth process when multiple crystals are able to be in proximity of each other long enough to allow for the formation of an agglomerative bond.¹⁵⁸⁻¹⁵⁹ Crystal agglomeration requires mechanical force to disrupt, such as mechanical grinding,¹⁵⁹ thus it is plausible that grinding **Fe(btp)** actually led to the mechanical breakdown of crystal agglomerates. In addition, it is of note, that average crystallite size could not be determined for ground **Fe(btp)**, but rather a maximum average crystallite size, as sample charging produced poor resolution for small particles. Therefore, the actual size distribution of ground **Fe(btp)** is unknown and the studies presented here cannot be reasonably compared.

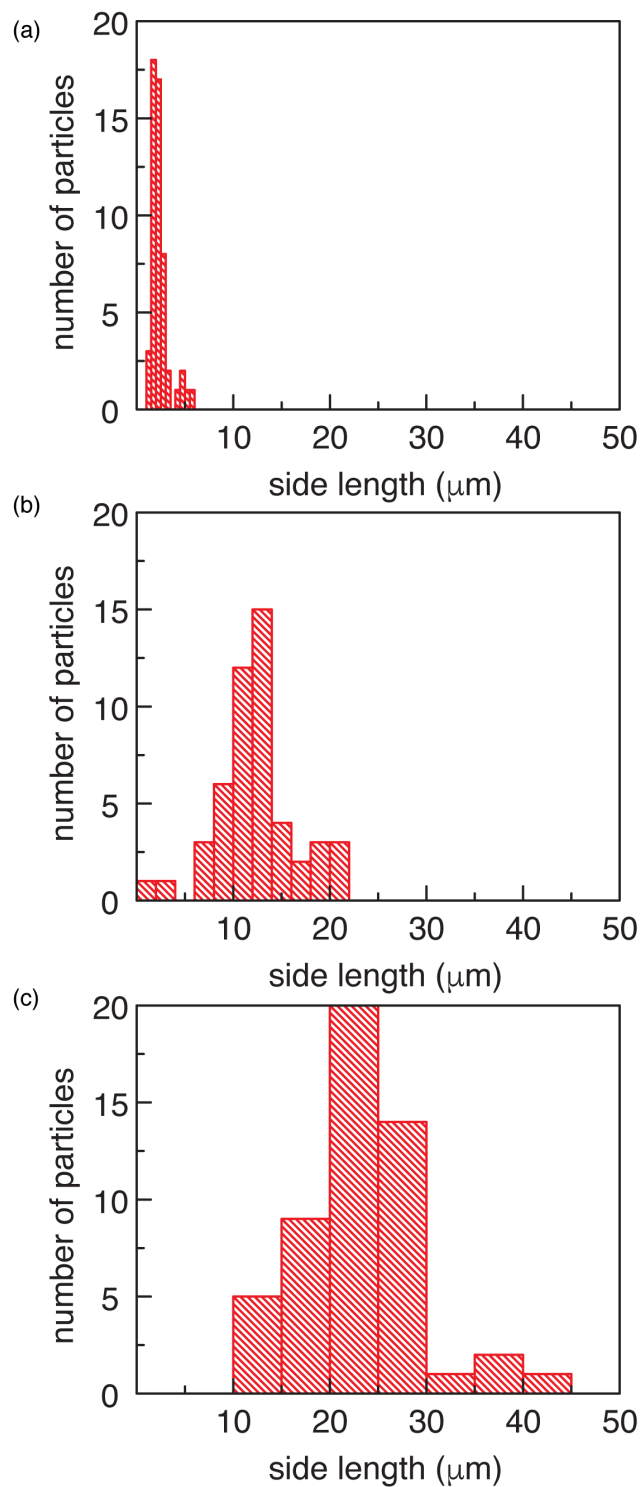


Figure III-1 The influence of synthesis time on Fe(btp) crystal growth. Crystals of Fe(btp) were synthesized solvothermally at 80 °C for (a) 4, (b) 10, and (c) 16 h.

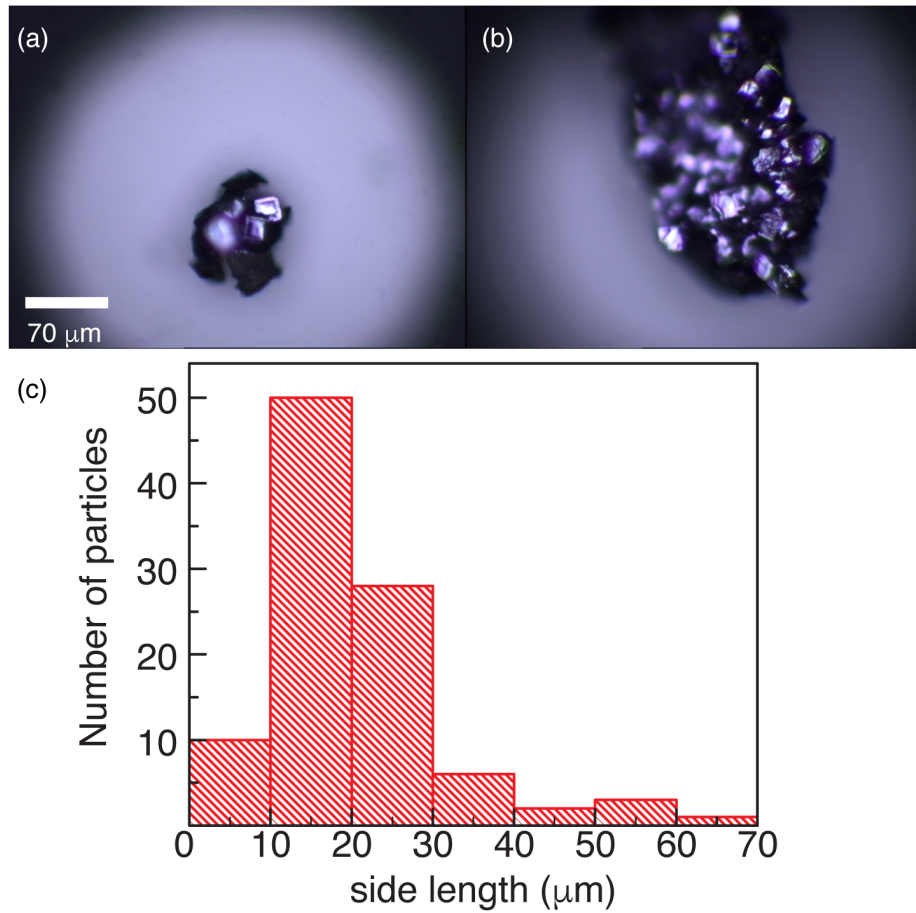


Figure III-2 20 μm crystals of Fe(btp). (a) Microscopic images and (b) of Fe(btp) and (c) histogram demonstrating size distribution for 100 measured crystals.

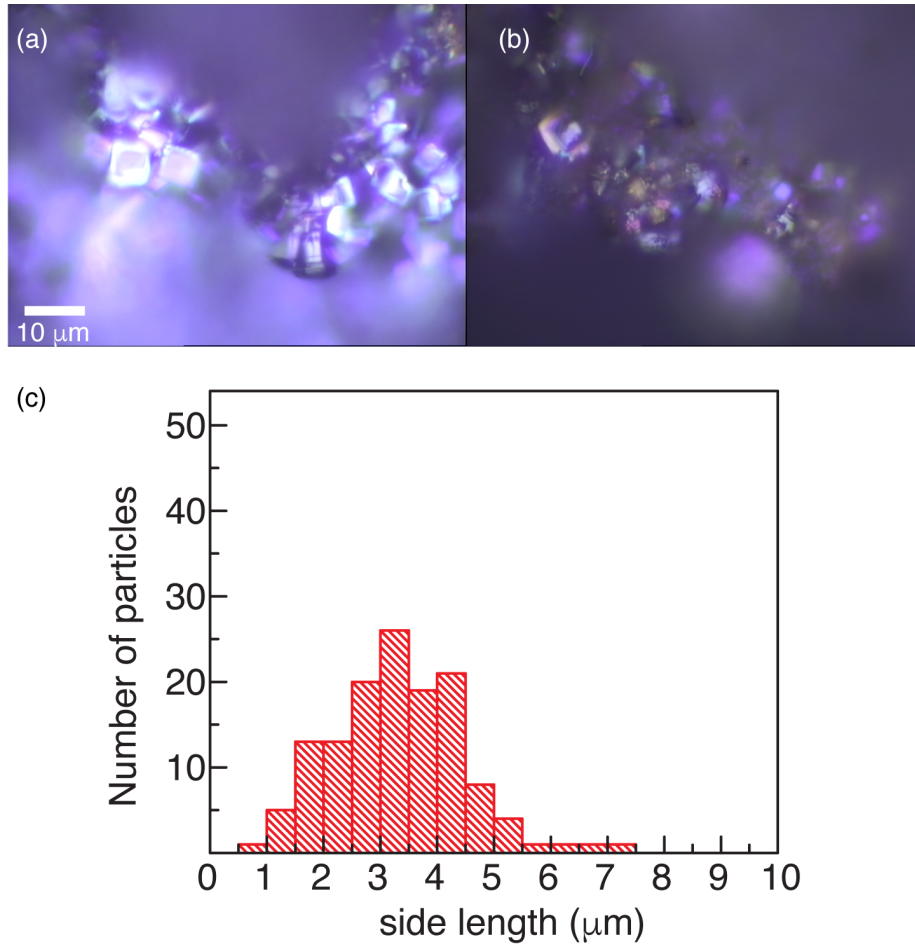


Figure III-3 3.3 μm crystals of Fe(btp). (a) Microscopic images and (b) of Fe(btp) and (c) histogram demonstrating size distribution for 100 measured crystals.

Table III-1 Summary of results for one-way ANOVA

	Sample 1	Sample 2	Sample 3	ANOVA Results
mean (μm)	3.87	3.33	5.14	--
st. dev (μm)	1.47	1.16	2.03	--
st. error (μm)	0.13	0.10	0.23	--
F_{calc}	--	--	--	35.59
$F_{crit} (\alpha = 0.05)$	--	--	--	3.04

III.2.2 Synthesis and Characterization of 2-D Layered Porphyrinic Materials

The layered MOF materials $[\text{Zn}_2\text{M}(\text{tcpp})]_n$ ($\text{M} = \text{Fe}$ or Mn), consisting of 2-D sheets of $\text{Fe}(\text{tcpp})$ connected by Zn_2 -paddlewheels were accessed by solvothermal reaction of $\text{Fe}(\text{tcpp})$, $\text{Zn}(\text{NO}_3)_2 \cdot 6\text{H}_2\text{O}$, and pyrazine in DMF. The resulting microcrystalline solid was analyzed by PXRD (**Figure III-4**). Similar 2-D layered materials have been previously characterized.^{156,160} PPF-1, a 2-D layered material featuring Zn_2 paddlewheels and Zn-metellated porphyrins features an AB stacking pattern,¹⁵⁶ while $[\text{Zn}_2(\text{HCOO}^-)\text{Fe}(\text{tcpp})]_n$ features an AA stacking pattern.¹⁶⁰ In comparison, $[\text{Zn}_2\text{M}(\text{tcpp})]_n$ synthesized in these conditions does not compare well to these previously reported simulated structures and appears to feature a smaller d -spacing, assuming that the peak at $2\theta = 10.7^\circ$ relates to the [001] plane (**Figure III-4**). Models were constructed assuming AA and AB stacking and by utilizing the [001] peak as a guide for setting the c dimension of the unit cell (**Figure III-5**). The generated models show that the resulting solid could be a mixture of both AA and AB stacking motifs (**Figure III-6**), which would be expected in the absence of linking elements. In addition, the experimental PXRD pattern displays peaks that were not observed in the modeled patterns. In addition, the experimental PXRD pattern displays peaks that were not observed in the modeled patterns. These could be due to phase impurities or the actual unit cell being less symmetric than the unit cells utilized as models.

The potential of $[\text{Zn}_2\text{Fe}(\text{tcpp})]_n$ to participate in guest exchange was analyzed by dye uptake studies. It was found that rhodamine 6G intercalated into $[\text{Zn}_2\text{Fe}(\text{tcpp})]_n$ with 67 wt% uptake of dye into the solvated material, as assessed by UV-vis of the digested solid. Similar to the **Fe(btp)**, the activated material $[\text{Zn}_2\text{Fe}(\text{tcpp})]_n$ demonstrated low dye

uptake of 1.4%, suggesting that the activated material does not resolve under these conditions and the inter-layer space is inaccessible to guest molecules.

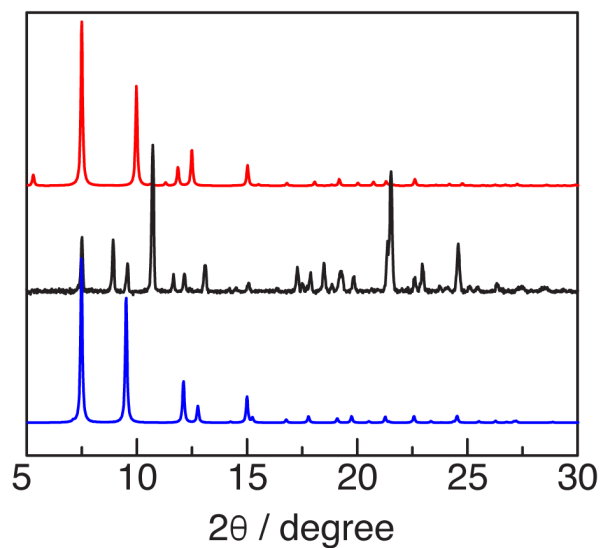


Figure III-4 PXRD comparison of $[\text{Zn}_2\text{Fe}(\text{tcpc})]_n$ with literature materials. The 2-D layered material synthesized here (—) does not compare well to similar previously reported 2-D layered structures (PPF-1 (—), $[\text{Zn}_2(\text{HCOO})\text{Fe}(\text{tcpc})]_n$ (—)).

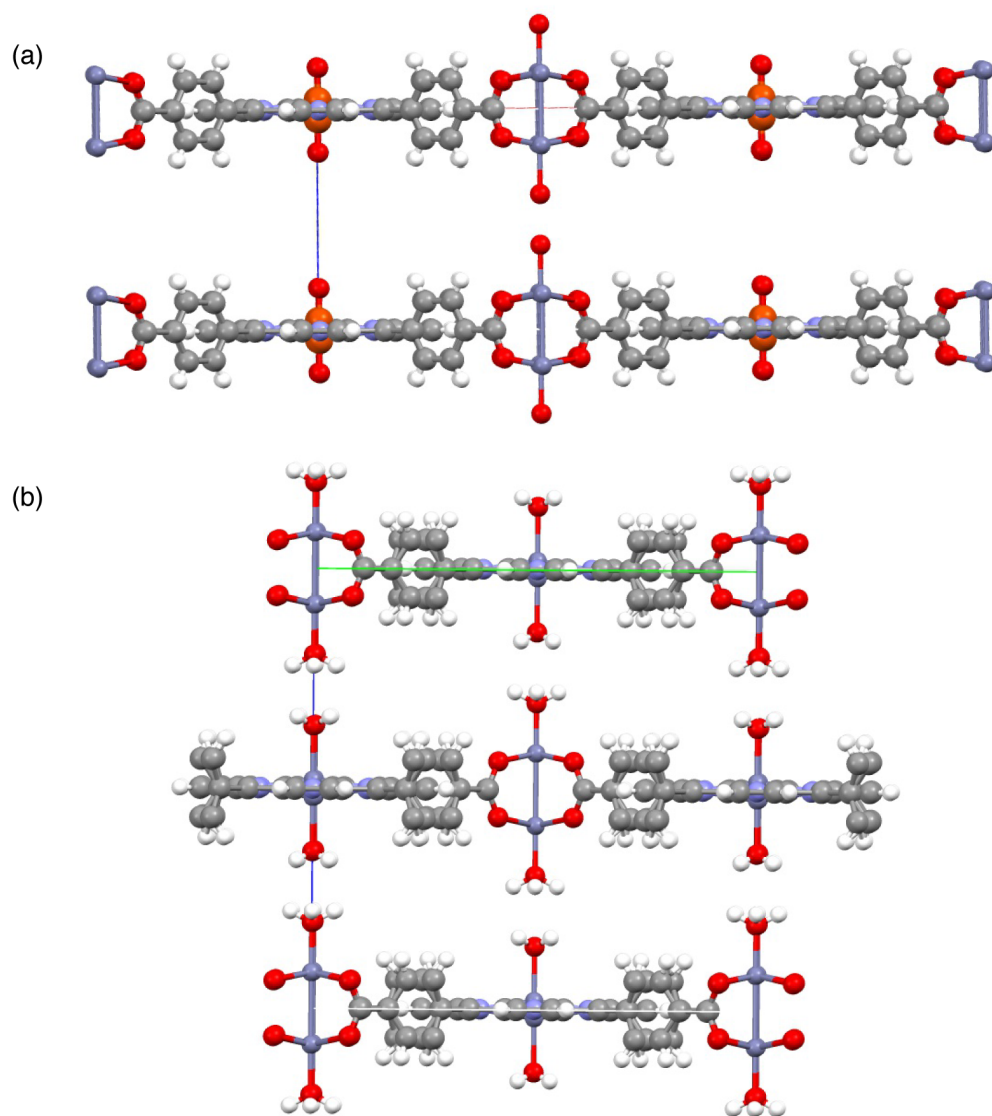


Figure III-5 Potential stacking models for $[Zn_2Fe(tcpp)]_n$, featuring (a) AA and (b) AB stacking modes.

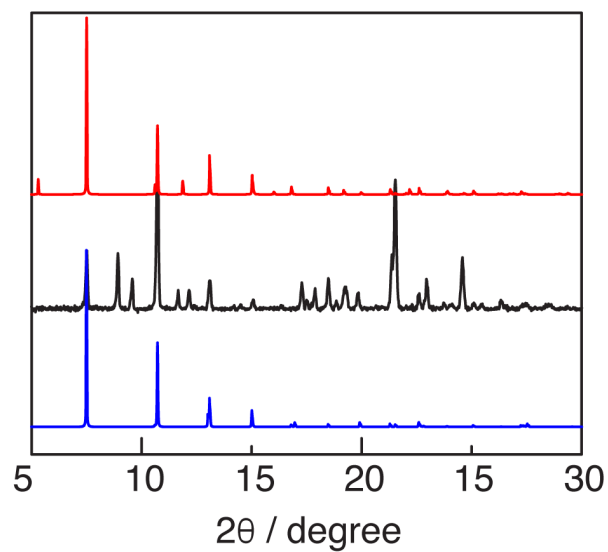


Figure III-6 Comparison of $[\text{Zn}_2\text{Fe}(\text{tcpp})]_n$ with models generated from AA (—) and AB stacking modes (—).

III.2.3 Oxidation of *Cis*-decalin and 1,4-Dimethylcyclohexane by 2-D Layered Porphyrinic Materials

Due to both the increased dye uptake as compared to **Fe(btp)** and the potential for the 2-D layered materials to provide a substrate-responsive reaction environment, we pursued oxidation of *cis*-decalin and *cis*-1,4-dimethylcyclohexane as probes of stereoretentive oxidation chemistry. Oxidation of *cis*-decalin by $[\text{Zn}_2\text{Fe}(\text{tcpp})]_n$ in CH_3CN with 2-(*tert*-butylsulfonyl)iodosylbenzene produced a *cis*-**3.1** to *trans*-**3.1** ratio of 53 : 1 in 6% yield (**Figure III-7**).

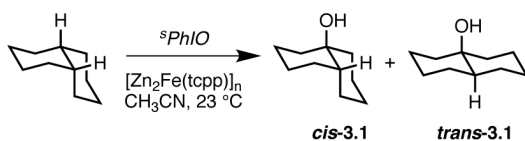


Figure III-7 Oxidation of *cis*-decalin by $[\text{Zn}_2\text{Fe}(\text{tcpp})]_n$.

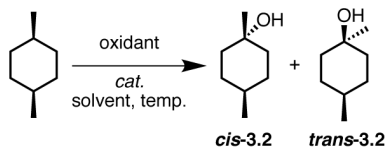
A significant degree of stereoretention was also found to apply in the oxidation of *cis*-1,4-dimethylcyclohexane with $[\text{Zn}_2\text{Fe}(\text{tcpp})]_n$ which proceeded with *cis*-**3.2** : *trans*-**3.2** = 44 : 1 in 2% yield. Attempts to improve the reaction yield were made by altering the oxidant, catalyst, and reaction conditions (**Table III-2**). Replacing 2-(*tert*-butylsulfonyl)iodosylbenzene (${}^s\text{PhIO}$) with (diacetoxyiodo)benzene led to an increase in the yield, while maintaining a high *c* : *t* ratio (81: 1 (5% yield)). In an attempt to further optimize the reaction, $[\text{Zn}_2\text{Mn}(\text{tcpp})]_n$ was synthesized in an analogous manner to the iron containing material. Oxidation of *cis*-1,4-dimethylcyclohexane at $23\text{ }^\circ\text{C}$ in CH_3CN

utilizing a 21% catalyst loading produced a *cis*-**3.2** : *trans*-**3.2** of 97 : 1 but with low conversion (3%) (**Table III-2**). Increasing the temperature to 40 °C resulted in an increase in the yield (5%) but a decrease in selectivity (68 : 1). Decreasing the catalyst loading increased the yield substantially, with a 4% catalyst loading producing > 100 : 1 *c* : *t* with a conversion of 15%. This may be due to worsened crystallite agglomeration inhibiting the diffusion of starting materials into the interstitial spaces of the MOF.

A variety of variables were manipulated to increase the yield of *cis*-1,4,-dimethylcyclohexane oxidation. Changing the solvent to propionitrile, ethyl acetate, DMF, or CHCl₃ produced either a decrease in yield or stereoretention (**Table III-1**). Using nitromethane as solvent gave very similar results to CH₃CN (**Table III-2**). Often, slow addition of oxidant is reported for metalloporphyrin-catalyzed oxidation reactions: In our case, utilization of a syringe pump to deliver the oxidant slowly as a dilute solution did not improve the reaction yield (14%).

To assess the problem of low yield, the recyclability of the catalyst was assessed. Following a reaction producing 20% yield, the material was washed with CH₃CN and re-subjected to oxidation conditions, which resulted in only 2% yield. In addition, the PXRD of the material after one oxidation reaction was analyzed, revealing a phase change (**Figure III-8**). Based on these results, the material [Zn₂Mn(tcpp)]_n is unstable to the reaction conditions. This could be in part due to ligand exchange at (diacetoxyiodo)benzene to generate Zn(OAc)₂ and a hypervalent iodine compound ligated to Mn(tcpp), causing disruption to the framework (see Chapter IV). The crystalline phase present following the reaction has not been identified.

Table III-2 Optimization of oxidation of *cis*-1,4-dimethylcyclohexane



Material	Catalyst Loading	Oxidant	Temperature (°C)	Solvent	<i>c</i> : <i>t</i>	Yield (%)
[Zn ₂ FeTCPP] _n	--	^s PhIO	23	CH ₃ CN	44:1	2
[Zn ₂ FeTCPP] _n	--	(diacetoxyiodo)benzene	23	CH ₃ CN	81:1	5
[Zn ₂ MnTCPP] _n	21%	(diacetoxyiodo)benzene	23	CH ₃ CN	97:1	3
[Zn ₂ MnTCPP] _n	21%	(diacetoxyiodo)benzene	40	CH ₃ CN	68:1	5
[Zn ₂ MnTCPP] _n	4%	(diacetoxyiodo)benzene	23	CH ₃ CN	100:1	15
[Zn ₂ MnTCPP] _n	--	(diacetoxyiodo)benzene	23	propionitrile	34:1	8
[Zn ₂ MnTCPP] _n	--	(diacetoxyiodo)benzene	23	DMF	-	0
[Zn ₂ MnTCPP] _n	--	(diacetoxyiodo)benzene	23	Acetone	-	0
[Zn ₂ MnTCPP] _n	--	(diacetoxyiodo)benzene	23	EtOAc	25:1	5
[Zn ₂ MnTCPP] _n	--	(diacetoxyiodo)benzene	23	CHCl ₃	20:1	6
[Zn ₂ MnTCPP] _n	--	(diacetoxyiodo)benzene	23	nitromethane	100:1	16

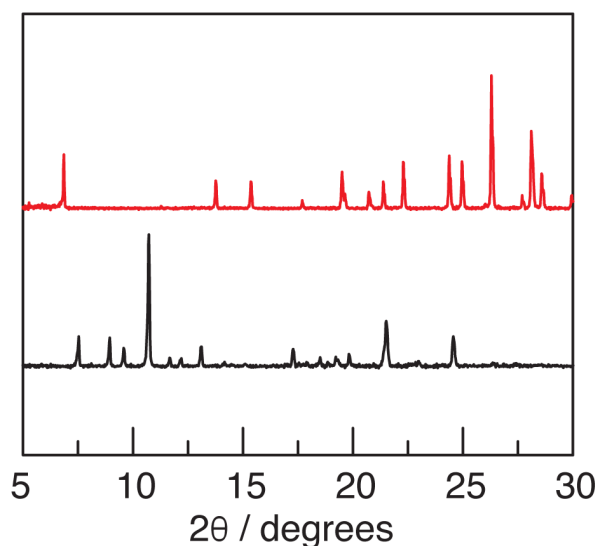


Figure III-8 PXRDs of $[\text{Zn}_2\text{Fe}(\text{tcpp})]_n$ before (—) and after (—) catalysis.

III.3 Conclusion

Adapting the solvothermal conditions previously reported,¹⁵ crystallites of discrete sizes were grown of **Fe(btp)**. However, these investigations were stymied by lack of reproducibility in the synthesis of the particles and in the lack of control of agglomeration.

Application of the stereoretentive chemistry observed with the oxidation of *cis*-decalin to another substrate, *cis*-1,4-dimethylcyclohexane, failed due to the inability to increase the yield to synthetically useful values. In addition, it was found the best catalyst for the reaction, $[\text{Zn}_2\text{Mn}(\text{tcpp})]_n$ was unstable to the reaction conditions, resulting in a phase change as observed by PXR (Figure III-8).

It has been demonstrated here that 2-D layered materials show promise in effecting stereoretentive C–H oxidation chemistry; the material $[\text{Zn}_2\text{Mn}(\text{tcpp})]_n$ was capable of oxidizing *cis*-1,4-dimethylcyclohexane with high selectivity (*cis*-**3.2** : *trans*-**3.2** >100 : 1).

However, the low yield could not be improved through optimization and may be due to the lack of stability of the material. In order to improve upon this system, it is necessary to incorporate inorganic building units with greater stability than Zn₂-paddlewheels. For example, layered materials consisting of Hf and Zr nodes have been constructed¹⁶¹ and these may be better candidates for C–H oxidation catalysis based on the decreased liability of the Zr carboxylate bond.

III.4 Experimental Details

III.4.1 General Considerations

Materials Solvents were obtained as ACS reagent grade and used as received. Sodium hydroxide, and *N,N*-diethylformamide (DEF) were obtained from EMD Millipore. 1,2,4-triazole, *cis*-1,4-dimethylcyclohexane, and 1,3-bis(4-pyridyl)propane were obtained from TCI America. Pyrrole, chromium(VI) oxide, and absolute ethanol were obtained from Beantown Chemical, Chem Impex, and Koptec, respectively, 1,3-dibromopropane, 4-carboxybenzaldehyde, and FeCl₂·4H₂O were obtained from Alfa Aesar. Sodium sulfite, benzaldehyde, pyrazine, and D₂SO₄ were obtained from Sigma Aldrich. The aforementioned reagents were used as received. Mn(OAc)₂·4H₂O and Zn(NO₃)₂·6H₂O were obtained from Strem Chemicals and were dried under vacuum (~50 mbar) at 23 °C prior to use. *N,N*-diethylacetamide (DEA) was obtained from Alfa Aesar and sparged with N₂ for 30 mins prior to use. *N,N*-dimethylformamide (DMF) was obtained from Sigma Aldrich and sparged with N₂ for 30 mins prior to use. *Cis*- and *trans*-decalin were purchased through TCI and purified from alcohol impurities by washing with

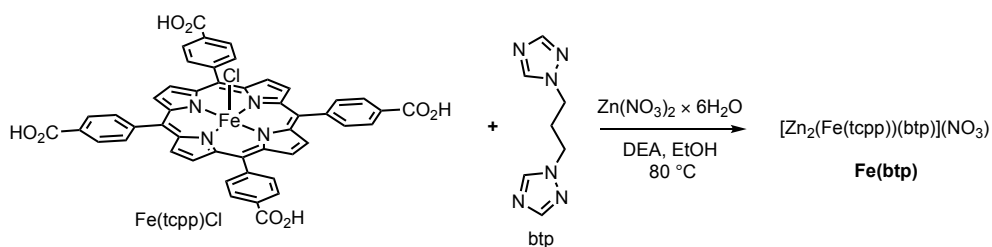
H₂SO₄ and was then dried over Na metal.¹⁴⁹ Tetrabutylammonium periodate,¹⁵⁰ *cis*- and *trans*-1,4-dimethylcyclohexanol,¹⁵¹ *cis*- and *trans*-decahydronaphthalen-9-ol,¹⁵¹ 1,3-bis(1,2,4-triazole-1-yl)propane (btp),¹⁵ 5,10,15,20-tetraphenylporphyrin (H₂tcpp),¹⁵² 5,10,15,20-tetraphenylporphyrin iron chloride (Fe(tcpp)Cl),¹⁵³ 5,10,15,20-tetraphenylporphyrin manganese chloride (Mn(tcpp)Cl),¹⁶² and 2-(*tert*-butylsulfonyl)iodosylbenzene^{31,147} were synthesized according to literature procedures. NMR solvents were purchased from Cambridge Isotope Laboratories and were used as received.

Characterization Details NMR spectra were recorded on Inova 500 FT NMR operating at 499.53 MHz for ¹H acquisitions and were referenced against solvent signals: CDCl₃ (7.26 ppm, 1H; 77.16 ppm, ¹³C) and DMSO-d₆ (2.48 ppm, 1H).¹⁵⁴ ¹H NMR data are reported as follows: chemical shift (δ, ppm), (multiplicity: s (singlet), d (doublet), t (triplet), m (multiplet), br (broad), integration). UV-vis spectra were recorded at 293 K in quartz cuvettes on an Ocean Optics Flame-S miniature spectrometer with DH-mini UV-vis NIR light source and were blanked against the appropriate solvent. IR spectra were recorded on a Shimadzu FTIR/IRAffinity-1 spectrometer. Spectra were blanked against air and were determined as the average of 128 scans. IR data are reported as follows: wavenumber (cm⁻¹), (peak intensity: s, strong; m, medium; w, weak). Thermogravimetric analyses were measured up to 600 °C with a scan rate of 5 °C/min using TGA Q500 of TA instruments. GC analysis was carried out using a Trace 1310 (Thermo Scientific) instrument equipped with a TraceGOLD TG-1M column from Thermo Scientific (length: 30 m, id: 0.53 mm, film thickness: 0.25 μm). The column temperature was maintained at

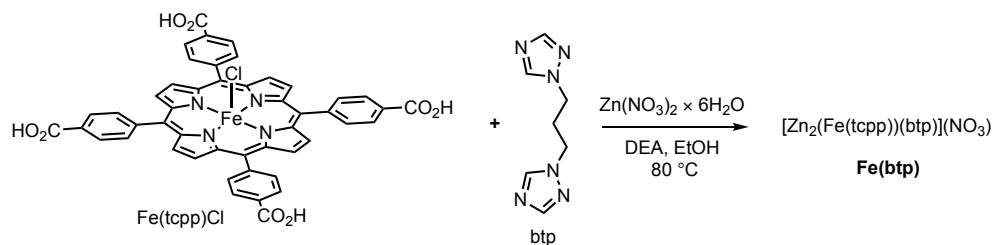
60 °C for 2 min and was raised to 320 °C at 60 °C/min. The final temperature (320 °C) was held for 2 min. Optical microscopy was performed on a WiTec Alpha300.

X-ray Diffraction Details Powder X-ray diffraction (PXRD) measurements were carried out on a Bruker D8 Advance Eco X-ray diffractometer (Cu K α , 1.5418 Å; 40 kV, 25 mA) fitted with LynxEye detector. The angular range was measured from 4.00 to 40.00° (2 θ) with steps of 0.020° and a measurement time of 0.3 s per step.

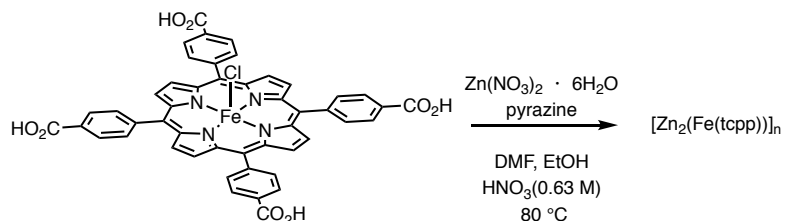
III.4.2 Synthesis



Synthesis of 20 μm Long Plates of Fe(btp) An 8-mL vial was charged with $\text{Zn(NO}_3)_2 \cdot 6\text{H}_2\text{O}$ (30.0 mg, 0.101 mmol, 2.30 equiv), Fe(tcpcp)Cl (19.4 mg, 0.0220 mmol, 1.00 equiv), btp (7.6 mg, 0.043 mmol, 2.0 equiv), and a mixture of *N,N*-diethylacetamide (DEA) and EtOH (2.0 mL, v/v 4:1). The reaction mixture was heated at 80 °C for 20 hr suspended in an oil bath and cooled to 23 °C for 30 mins. The mother liquor was decanted and the solid washed with DEA (3 \times 12 mL) until the solution color became colorless to remove unreacted starting materials. The solid was allowed to dry via vacuum filtration prior to use in catalysis.

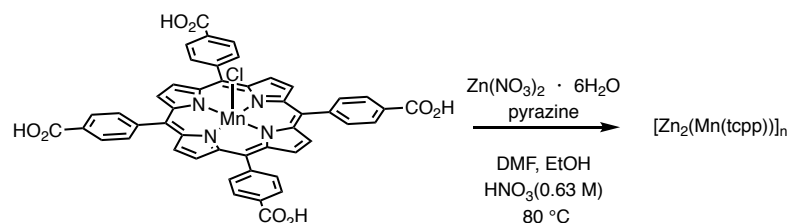


Synthesis of 4 μm Long Plates of Fe(btp) An 8-mL vial was charged with $\text{Zn(NO}_3)_2 \cdot 6\text{H}_2\text{O}$ (15.1 mg, 0.0505 mmol, 2.30 equiv), Fe(tcpp)Cl (9.7 mg, 0.011 mmol, 1.00 equiv), btp (2.0 mg, 0.022 mmol, 2.0 equiv), and a mixture of *N,N*-diethylacetamide (DEA) and EtOH (1.6 mL, v/v 4:1). The reaction mixture was heated at 80 °C for 10 hr suspended in an oil bath and cooled to 23 °C for 30 mins. The solid washed with *N,N*-dimethylformamide (DMF) (3 \times 8 mL) by centrifugation. The solid was washed once with CH_3CN (1.5 mL) and transferred to an 8-mL vial for catalysis. Some solid was deposited on a glass slide as a CH_3CN suspension for characterization by optical microscopy.



Synthesis of $[\text{Zn}_2\text{Fe(tcpp)}]_n$ An 8-mL vial was charged with $\text{Zn(NO}_3)_2 \cdot 6\text{H}_2\text{O}$ (30.0 mg, 0.101 mmol, 2.30 equiv), Fe(tcpp)Cl (18.0 mg, 0.0200 mmol, 1.00 equiv), pyrazine (2.0 mg, 0.025 mmol, 1.2 equiv), and a mixture of DMF and 63 mM HNO_3 in EtOH (2.0 mL, v/v 4:1). Pyrazine serves as a templating reagent and is not observed in the ^1H NMRs of degraded product. The reaction mixture was heated at 80 °C for 24 hr in an oil bath and cooled to 23 °C for 30 mins. The mother liquor was decanted and the solid

washed with DMF (3 × 12 mL) until the solution color became colorless to remove unreacted starting materials. The solid was allowed to dry via vacuum filtration prior to use in catalysis.



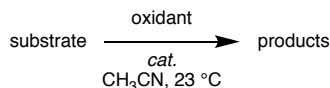
Synthesis of $[\text{Zn}_2\text{Mn}(\text{tcpp})]_n$ An 8-mL vial was charged with $\text{Zn}(\text{NO}_3)_2 \cdot 6\text{H}_2\text{O}$ (30.0 mg, 0.101 mmol, 2.30 equiv), $\text{Mn}(\text{tcpp})\text{Cl}$ (18.0 mg, 0.020 mmol, 1.00 equiv), pyrazine (2.0 mg, 0.025 mmol, 1.2 equiv), and a mixture of DMF and 63 mM HNO_3 in EtOH (2.0 mL, v/v 4:1). The reaction mixture was heated at 80 °C for 24 hr in an oil bath and cooled to 23 °C for 30 mins. The mother liquor was decanted and the solid washed with DMF (3 × 12 mL) until the solution color became colorless to remove unreacted starting materials. The solid was allowed to dry via vacuum filtration prior to use in catalysis.

III.4.3 Dye Uptake Experiments

General Procedure for Dye Uptake Experiments To $[\text{Zn}_2\text{Fe}(\text{tcpp})]_n$ (20-21 mg), which had previously been washed and dried via vacuum filtration, a rhodamine 6G solution (3.1 (mM) in CH_3CN) was added. Solids were allowed to sit in dye solutions for 48 h at 23 °C. The UV-vis spectrum of the resulting soaking solution was measured to determine the concentration of rhodamine 6G remaining in the supernatant. The solids

were rinsed with CH₃CN until the filtrate was colorless and dried under vacuum to constant mass. Materials were digested in DMSO with 25 μ L of H₂SO₄ and diluted to 10 mL with DMSO. The UV-vis spectrum of the digested solids was measured to quantify the amount of rhodamine 6G that had been intercalated into the solid; the contribution of the porphyrin to the absorbance at 541 nm was subtracted using the soret intensity to determine porphyrin concentration. Extinction spectra were measured both in CH₃CN and in acid DMSO to allow for quantification of the rhodamine 6G by absorption spectroscopy.

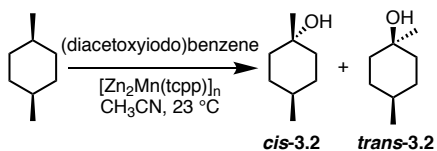
III.4.4 C–H Hydroxylation



General Procedure for C–H Hydroxylation with MOF Catalysts A vial was charged with MOF as a wet powder (20-25 mg), CH₃CN (2.5 mL), and substrate (0.97 mmol, 4.2 equiv). Oxidant (0.23 mmol, 1 equiv) was added to the mixture with stirring (100 rpm) in 5-6 portions over 1 h. The reactions were allowed to stir for 24 h. Upon completion, mesitylene (10 μ L, 0.072 mmol) was added and the mixtures were filtered through Celite. The filtrate was analyzed by gas chromatography.

Procedure for C–H Hydroxylation with on Average 4 μ m Long Fe(btp) Crystals Crystals of Fe(btp) with average side lengths of 4 μ m were too small to be isolated, and thus the following procedure was employed to evaluate the selectivity of catalysis with these materials. Four vials of the preparation described in the synthetic

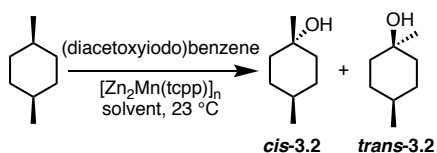
section were combined and washed with DMF by centrifugation. The solid was washed with CH₃CN and transferred to an 8-mL vial. The CH₃CN was removed and fresh CH₃CN (0.5 mL) was added. A drop was deposited on a slide for characterization by optical microscopy. *Cis*-decalin (30 μL, 0.20 mmol, 13 equiv) was added. The vial was placed on a shaker and 2-(*tert*-butylsulfonyl)iodosylbenzene (5.0 mg, 0.015 mmol, 1.0 equiv) was added to the mixture in 5-6 portions over 1 h. Upon completion, mesitylene (2.0 μL, 0.014 mmol) was added and the mixtures were filtered through Celite. The filtrate was analyzed by gas chromatography.



Catalyst Loading Screen of *cis*-1,4-dimethylcyclohexane Oxidation A vial was charged with MOF as a wet powder, CH₃CN (0.5 mL), and *cis*-1,4-dimethylcyclohexane (30 μL, 0.20 mmol, 3.0 equiv). (Diacetoxyiodo)benzene (23.0 mg, 0.0714 mmol, 1.0 equiv) was added to the mixture with stirring (100 rpm) in 5-6 portions over 1 h. The reactions were allowed to stir for 24 h. Upon completion, mesitylene (2.0 μL, 0.014 mmol) was added and the mixtures were filtered through Celite. The filtrate was analyzed by gas chromatography. Results are summarized in **Table III-3**.

Table III-3 Catalyst loading screening for oxidation of *cis*-1,4-dimethylcyclohexane by $[\text{Zn}_2\text{Mn}(\text{tcpp})]_n$.

Catalyst Loading (mg)	Catalyst Loading (%)	<i>c</i> : <i>t</i>	Yield (%)
34.1	21	97 : 1	3
16.8	10	100 : 1	17
7.3	4	100 : 1	15



Solvent Screen of *cis*-1,4-dimethylcyclohexane Oxidation A vial was charged with MOF as a wet powder (7.0-8.0 mg), solvent (0.5 mL), and *cis*-1,4-dimethylcyclohexane (30 μL , 0.20 mmol, 3.0 equiv). (Diacetoxyiodo)benzene (23.0 mg, 0.0714 mmol, 1.0 equiv) was added to the mixture with stirring (100 rpm) in 5-6 portions over 1 h. The reactions were allowed to stir for 24 h. Upon completion, mesitylene (2.0 μL , 0.014 mmol) was added and the mixtures were filtered through Celite. The filtrate was analyzed by gas chromatography.

CHAPTER IV
IODOSYLBENZENE COORDINATION CHEMISTRY RELEVANT TO MOF
CATALYSIS*

IV.1 Introduction

IV.1.1 Background and History

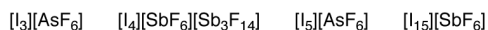
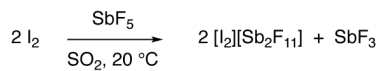
Iodine was discovered in 1811 by Bernard Courtois and was named by Joseph Louis Gay-Lussac in 1813 (the name “iodine” derives from the Greek word *ιώδης*, which means “violet colored”).¹⁶³⁻¹⁶⁵ The chemistry of iodine, which is the largest, least electronegative, and most ionizable of the non-radioactive halogens,¹⁶⁶ is dominated by the (0) and (−1) oxidation states (i.e. I₂ and I[−]). Facile interconversion of I(0) and I(−1) by oxidation-reduction chemistry under-pins the I[−] / I^{3−} redox couple that is critical to the chemistry of dye-sensitized solar cells.¹⁶⁷ The ionizability of iodine is manifest in a rich body of iodine-centered redox chemistry and the availability of families of compounds featuring iodine in oxidation states greater than zero (**Figure IV.1**). For example, exposure of I₂ to SbF₅ results in the formation of the [I²⁺]-containing salt [I₂][Sb₂F₁₁] (**Figure IV.1a**).¹⁶⁸⁻¹⁶⁹ Dimerization of I²⁺ to afford I₄²⁺ has been observed,¹⁷⁰⁻¹⁷¹ and higher-order iodine cations, such as I³⁺, I⁵⁺, I⁷⁺, and I¹⁵⁺ have been characterized.¹⁷⁰ Higher oxidation state iodine species are also commonly encountered in iodine oxyacids of I(I), I(III), I(V),

* Data, figures and text in this chapter were adapted with permission from reference Cardenal, A. D.; Maity, A.; Gao, W.-Y.; Ashirov, R.; Hyun, S.-M., Powers, D. C. *Inorg. Chem.* **2019**, *accepted*, copyright 2019 The American Chemical Society.

and I(VII) (i.e. HIO, HIO₂, HIO₃, and HIO₄), iodine oxides, and iodine fluoride (i.e. IF₇) (**Figure IV.1b**).

Higher oxidation states of iodine are also encountered in organoiodine chemistry (**Figure IV.1c**). In 1886, Willgerodt reported the preparation of PhICl₂, which features an I(III) center, upon passage of Cl₂ through a solution containing PhI.¹⁷² Since this original discovery, an enormous array of I(III) derivatives have been prepared. PhICl₂ is a T-shaped molecule and formally features a d⁶ electronic configuration at iodine. As such, these compounds are termed hypervalent, which Musher defined as: “atomic centers which exceed the number of valences allowed by the traditional theory, and thus utilize more electron-bonding pairs than provide stability in the Lewis Langmuir theory.”¹⁷³ Various nomenclature schemes have been utilized to describe hypervalent I(III) compounds. According to IUPAC convention for compounds with non-standard coordination numbers, organic compounds containing I(III) centers are referred to as λ³-iodanes.¹⁷⁴ Martin-Arduengo N–X–L nomenclature, in which *N* is the number of valence electrons formally assigned to iodine, *X* is the identity of the hypervalent element, and *L* is the number of ligands attached to the hypervalent atom, is also frequently used to describe higher valent organoiodine compounds.¹⁷⁵⁻¹⁷⁶ In addition, a large array of I(V)-containing compounds (i.e. Dess-Martin periodinane and IBX; λ⁵-iodanes), which feature a d⁰ electronic configuration at iodine, have been prepared.^{26,177-180} There are no examples of organic I(VII)-containing compounds.

(a) polyiodine cations



(b) oxyacids and fluorides



(c) higher valent organic iodine species

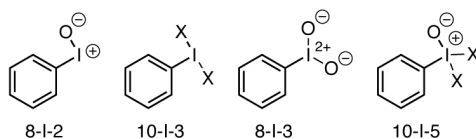


Figure IV-1 Summary of high-valent organoiodine compounds. The low ionization potential of iodine is manifest in families of oxidized iodine compounds. Examples include (a) polyiodine cations, (b) iodine oxyacids and fluorides, and (c) λ^3 - and λ^5 -iodanes.

Historically, bonding models based on either 1) participation of vacant iodine-centered d-orbitals in hybridization, or 2) bonds with greater than 50% ionic character, which would result in localization of electron density on ligand-born orbitals, have been advanced to rationalize the apparent valence expansion at iodine in λ^3 - and λ^5 -iodanes.¹⁸¹ In 1951, Rundle and Pimentel advanced the now-accepted model for hypervalent iodine bonding based on overlap of the 5p orbital at iodine with ligand-centered orbitals to give rise to the electron-rich 3c-4e bonding picture illustrated in **Figure IV-2**.¹⁸²⁻¹⁸³ Population of bond ψ_1 and non-bonding ψ_2 gives rise to the observed linear L–I–L triads. Violation of the octet at iodine is avoided by localization of two electrons in ligand-born ψ_2 . In addition to avoiding violation of the octet rule, this picture rationalizes the observation of highly ionic bonding in hypervalent iodine compounds and the preference for

electronegative substituents to occupy the hypervalent bond. Further experimental support for the ionic bonding in hypervalent iodine molecules is the observation that the iodine center can serve as an acceptor in halogen bonding interactions.¹⁸⁴⁻¹⁸⁵ Due to population of both bonding and non-bonding orbitals, the I–L bond lengths in hypervalent iodine species are typically intermediate between the sum of the covalent and ionic radii of the relevant atoms.¹⁸⁶ The bonding picture of I(V) derivatives mirrors that of I(III) compounds except that there are two (orthogonal) hypervalent 3c-4e bonds.

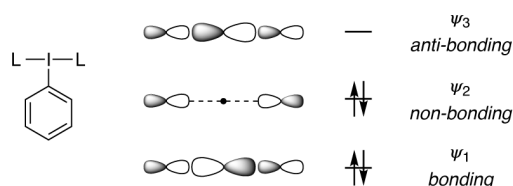


Figure IV-2 Orbital picture for the 3c-4e bonding in hypervalent iodine compounds. Population of ψ_2 , which is ligand centered, allows accommodation of the formal octet violations at iodine without utilizing d-orbital hybridization.

Iodosylbenzene derivatives (*i.e.* 8-I-2 species) also feature I(III) centers. While these species are often drawn with I–L multiple bonds (*i.e.* $\text{PhI}=\text{O}$), the large radius of iodine results in insignificant π -bonding.¹⁸⁷ Poor π overlap results in highly polarized bonding, (*i.e.* PhI^+-O^-). The extensive polarization of the I–O bond often¹⁸⁸⁻¹⁸⁹ results in solid-state $-\text{I}-\text{O}-\text{I}-\text{O}-$ polymerization driven by charge pairing,¹⁹⁰⁻¹⁹¹ which results in poorly soluble materials. Iodosylarenes are metastable with respect to disproportionation to I(I) and I(V) species, although sufficiently large kinetic barriers to disproportionation

often allow for straightforward handling of I(III) species. For example, the disproportionation of $(\text{PhIO})_n$ to generate iodobenzene and iodylbenzene is spontaneous but requires either catalysts (*i.e.* RuCl_3 ¹⁹²) or elevated temperatures¹⁹³ to proceed at appreciable rates. The mechanism of disproportionation has not been extensively investigated but has been suggested to proceed via oxygen-atom transfer chemistry in an oxygen-bridged diiodine intermediate.¹⁹⁴ As a result of the aforementioned disproportionation thermodynamics, iodylarenes are weaker oxidants than iodosylarenes.

The reaction chemistry of hypervalent iodine compounds is frequently described using terminology common to organometallic mechanisms.¹⁹⁵ The oxidation of PhI to PhICl_2 described above represents an oxidative addition reaction at the iodine center (**Figure IV-3**).¹⁷² Ligand exchange chemistry is often facile at iodine; for example, the alkoxide ligand exchange at iodine pictured in **Figure IV-3b** is rapid at room temperature.¹⁹⁶ Both associative and dissociative exchange mechanisms have been proposed.¹⁹⁷ Reductive elimination, in which ligand coupling from the hypervalent iodine center is accomplished with concurrent formation of an aryl iodide are ubiquitous (**Figure IV-3c**). Both inner-sphere ligand coupling and outer-sphere, nucleophilic-aromatic-substitution-based pathways have been suggested for the observed elimination reactions.¹⁹⁸⁻¹⁹⁹ Reductive elimination processes are driven by the hypernucleofugacity of PhI. Finally, group-transfer chemistry of iodosylarenes, for example in the synthesis of metal oxo complexes^{198,200-201} as well as in hydroxylation catalysis are very frequently encountered (**Figure IV-3d**).^{3,27} The importance of hypervalent iodine compounds has

resulted in an extensive review literature of the chemistry and reactivity of these compounds.^{26,178-180}

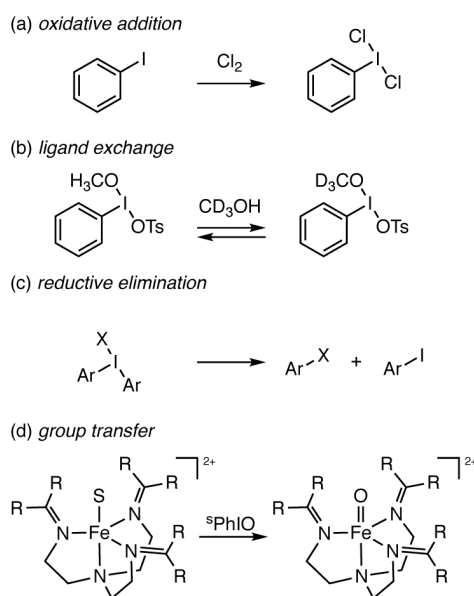


Figure IV-3 Typical reaction chemistry of hypervalent iodine compounds. Hypervalent iodine compounds participate in (a) two-electron iodine-centered oxidation, (b) ligand exchange chemistry, (c) reductive elimination reactions, and (d) group-transfer processes. R = N(CH₃)₃; S = CH₃CN; ^sPhIO = 2-(*tert*-butylsulfonyl)iodosylbenzene (**4.1**).

Interest in hypervalent iodine chemistry has, in large part, been motivated by the utility of these reagents as non-toxic, selective oxidants in synthetic chemistry. Iodosylarene derivatives have been applied to α -oxidation of carbonyls,²⁰² oxidative 1,2-difunctionalization of olefins,²⁰ oxidative dearomatization chemistry,²¹⁻²⁴ cross-coupling reactions,^{25,203} and have found important application as group-transfer reagents in organometallic catalysis.^{26,204} The facility of ligand exchange at hypervalent iodine centers

underpins the breadth of substrate functionalization chemistry that can be achieved with hypervalent iodine compounds: In addition to oxygen transfer, halogen, nitrogen, and hydrocarbyl transfer reactions are all common. I(V) reagents display complementary substrate functionalization chemistry, most notably towards alcohol and amine dehydrogenation reactions.^{26,177-180}

IV.1.2 Towards Hypervalent Iodine Mediated Aerobic Hydrocarbon Oxidation

The proclivity of iodosylarene derivatives to participate in group-transfer chemistry has stimulated substantial interest in using these reagents as terminal oxidants in oxidation catalysis. Motivated by 1) the potential to utilize metal-organic frameworks (MOFs) to prevent bimolecular decomposition chemistry by site-isolating catalyst sites and 2) the potential to leverage network porosity as an opportunity to non-covalently co-localize substrate in proximity of reactive intermediates,¹⁷ iodosylarenes have found widespread application as terminal oxidants in MOF catalysis. The facility with which ligand exchange proceeds at the hypervalent iodine center has enabled both C–H oxygenation³¹⁻³³ and C–H amination³⁴ reactions using MOF catalysts. The solubility of hypervalent iodine reagents is critical to proposals of substrate functionalization in the interstices of porous materials. In this context, 2-(*tert*-butylsulfonyl)iodosylbenzene (**4.1**), in which secondary bonding between the hypervalent iodine center and the proximal Lewis base promotes iodosylbenzene depolymerization and solubilization of monomeric species,²⁰⁵ has emerged as an important terminal oxidant in MOF catalysis.^{31-33,50}

We have been motivated by the potential to develop aerobic hydrocarbon functionalization chemistry by coupling the aerobic generation of hypervalent iodine

reagents with appropriate catalysts. The aerobic synthesis of hypervalent iodine compounds based on intercepting reactive oxidants generated during aldehyde autoxidation with aryl iodides was reported in 2018.¹⁸ In concept, the development of aerobic synthetic approaches to hypervalent iodine species contributes to sustainable synthetic chemistry by avoiding the metal-based oxidants that are often encountered in hypervalent iodine chemistry. To the extent that the developed aerobic oxidation methods can be coupled with iodine catalysis, the methods also contribute to relieving the requirement for (super)stoichiometric loading of hypervalent iodine reagents. Initial efforts to aerobically generate soluble iodosylarene **4.1** failed to provide access to I(III) species, and instead afforded iodylarene **4.2**. The aforementioned disproportionation thermodynamics of I(III) species imply that I(V) reagents are less strongly oxidizing than the related I(III) derivatives. The differing oxidation behaviors of **4.1** and **4.2** are manifest in the Mn(salen) catalyzed epoxidation of styrene (**Figure IV.4**). In the original report of the synthesis of **4.1**, Protasiewicz and co-workers showed that **4.1** is an effective terminal oxidant for this transformation,¹⁴⁷ and this report has been reproduced in our laboratory. In contrast, replacement of I(III) reagent **4.1** with I(V) reagent **4.2** results in the observation of no epoxidation.

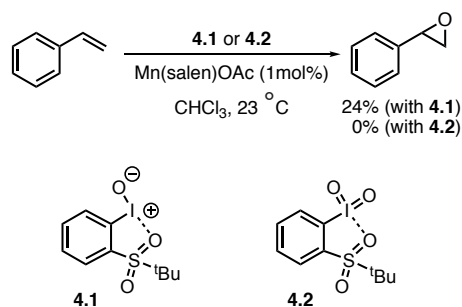


Figure IV-4 The oxidation of styrene by iodosyl- and iodylarene. The oxidation of styrene to styrene oxide proceeds from iodosylarene **4.1** but does not proceed with iodylarene **4.2**.

In order to rationally advance our goals of aerobic oxidation catalysis, we are critically interested in understanding the disproportionation behavior of soluble iodosylarenes in greater detail and potential interactions of those iodosylarene reagents with the transition metal nodes that comprise critical structural units in MOFs. We originally proposed that disproportionation of initially formed I(III) species was promoted by AcOH, which is an obligate by-product of acetaldehyde-promoted aerobic oxidation chemistry. Continued investigations have suggested that AcOH-promoted disproportionation is not a viable pathway for synthesis of **4.2** (*vide infra*). Here we describe preparation-dependent behavior of reagent **4.1** and show that popular methods to prepare this reagent can provide access to material that displays unpredictable disproportionation rates. In addition, we examine the chemistry of reagent **4.1** with both soluble models of the transition metal clusters common to Zr₆- and Zn₂-based MOFs and show that reagent **4.1** forms acid-base adducts with these transition metal clusters. In contrast, iodosylbenzene participates in ligand exchange with the examined clusters.

These observations provide new insight into the structure-dependent behavior of iodosylarenes with structural nodes common to metal-organic framework catalysts.

IV.2 Results and Discussion

IV.2.1 Structure and Bonding of 2-(*tert*-Butylsulfonyl)iodosylbenzene (**4.1**)

Consistent with the analysis of a hypothetical monomeric PhIO by Zhdankin and Boldyrev and co-workers,¹⁸⁷ natural bond order (NBO) analysis indicates the lack of meaningful I–O π -bonding in **4.1**. In addition to the I–O σ bond, the valence at oxygen is completed with three non-bonding electron pairs (**Figure IV-5**). The calculated Wiberg I–O bond order is 1.05 and analysis of the natural charges of iodine (+1.33) and oxygen (–1.06) is consistent with highly ionic I–O bonding. Comparison of the computational results for **4.1** with those for a hypothetical monomeric PhIO unit indicates the natural charge of the iodosyl oxygen atom is slightly more negative in **4.1** than in PhIO (–1.06 vs. –1.01), which is consistent with the presence of a *trans*-influencing sulfonyl ligand at iodine.^{186,206}

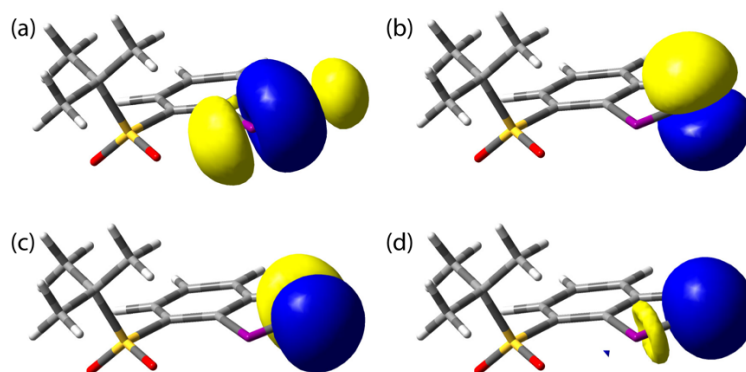


Figure IV-5 NBO orbitals of 2-(*tert*-butylsulfonyl)iodosylbenzene. NBO orbitals for **4.1** that show (a) I–O σ -bonding and (b–d) O-centered lone pairs.

The highly polarized I–O bond in **4.1** manifests in oxygen-centered Lewis basicity which is evidenced by a hydrogen-bonded chloroform molecule in the original crystal structure of this molecule (distance between H-bond donor and acceptor is 3.046 Å).²⁰⁷ Examination of the ¹H NMR spectrum of **4.1** in the presence of hexafluoroisopropanol (HFIP), which is frequently employed as a solvent or additive in iodine-mediated group-transfer catalysis,²⁰⁸⁻²¹¹ revealed [HFIP]-dependent chemical shifts (**Figure IV-6a**). Crystallization of **4.1** in the presence of excess HFIP resulted in the isolation of **4.1**·HFIP in which the HFIP molecule is H-bonded to the iodosylbenzene oxygen (**Figure IV-6b**). The distance between H-bond donor and acceptor in **1**·HFIP is 2.586 Å. The relative shortness of the H-bonding in **1**·HFIP versus between **1** and chloroform is consistent with the relative acidities of HFIP and CHCl₃ (pK_a = 9.3 and 15.5, respectively). Upon binding to HFIP, the I–O bond (I(1)–O(1)) elongates from 1.848(6) to 1.873(4) Å and the I–O distance to the sulfonyl oxygen (I(1)–O(2)) contracts from 2.707(5) to 2.668(3) Å (**Figure IV-6b**).²⁰⁷ NBO analysis of **4.1**·HFIP resulted in natural charges for iodine and oxygen of

+1.38 and -1.06 , respectively, which indicates enhancement of positive charge at iodine upon HFIP binding. A combination of COSY, HSQC, and HMBC NMR experiments enabled unambiguous assignment of the proton resonances of both **4.1** and **4.1**·HFIP (**Figures IV.7-8**). Analysis of the $\Delta\delta$ ^1H resonance of the C–H *para* to iodine vs. [HFIP] enabled the equilibrium constant to be determined ($K_{\text{eq}} = 0.037 \pm 0.004$), which corresponds to $\Delta G = 1.94 \pm 0.06$ kcal/mol (**Figure IV.6**). While HFIP is regularly used as a solvent or additive in hypervalent iodine chemistry, the role of adducts such as **4.1**·HFIP is not clear based on the data we have collected: for example, use of **4.1**·HFIP in the styrene epoxidation illustrated in **Figure IV-4** results in similar styrene oxide yields as when **4.1** is used as the terminal oxidant. In contrast to the adduct formation observed between **1** and HFIP, exposure of iodosylbenzene ((PhIO)_n) to HFIP results in complete dissolution of the solid (PhIO)_n polymer and formation of $\text{PhI}(\text{OC}(\text{H})(\text{CF}_3)_2)_2$ (**Figure IV-9**). Formation of the *bis*-alkoxide adduct is evidenced by the appearance of a methine resonance at 4.20 ppm that integrates for two protons. Similar to the formation of **4.4**, Hill *et al.* reported that (PhIO)_n dissolves in CH₃OH to afford $\text{PhI}(\text{OCH}_3)_2$.²¹² Compound **4.4** is unstable towards isolation, which is consistent with previous reports of fluoroalkoxide adducts of iodosylarenes that have been generated electrochemically.²¹³⁻²¹⁵

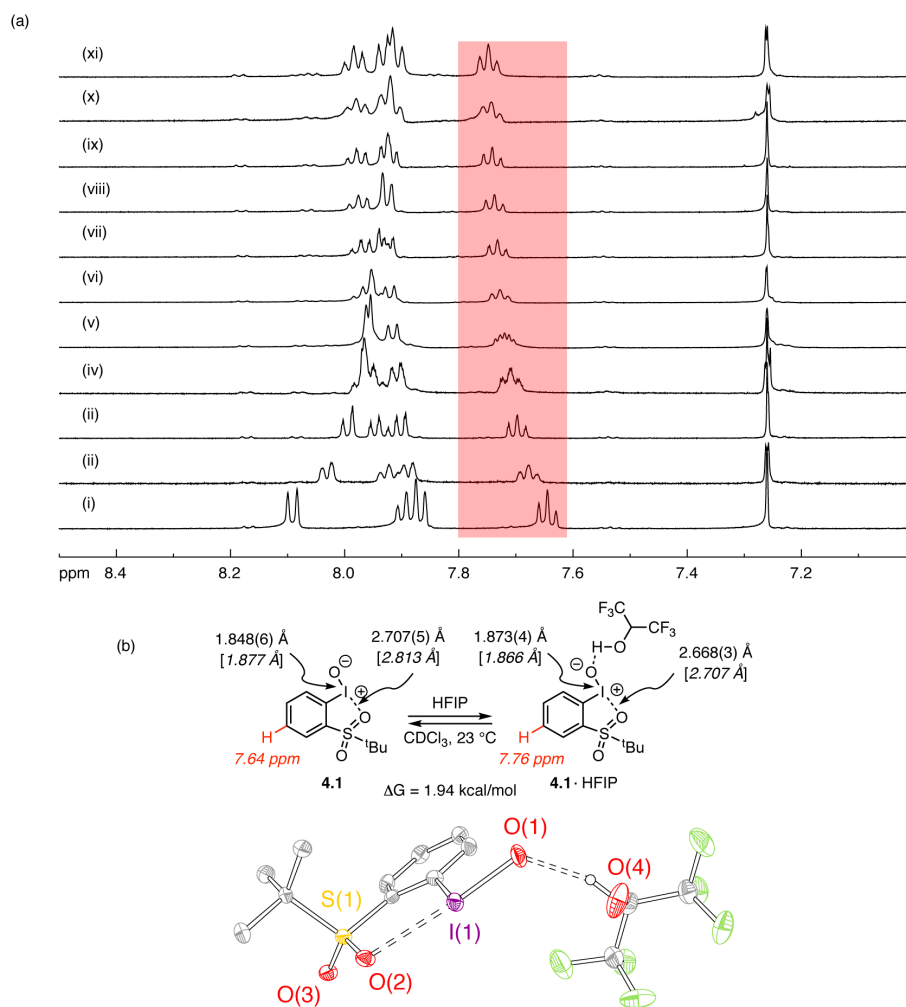


Figure IV-6 Formation of an adduct between HFIP and 2-(*tert*-butylsulfonyl)iodosylbenzene. a) ^1H NMR spectra of **4.1** in the presence of increasing quantities of HFIP ((i) 0 μL , (ii) 1 μL , (iii) 2 μL , (iv) 3 μL , (v) 4 μL , (vi) 5 μL , (vii) 6 μL , (viii) 7 μL , (ix) 8 μL , (x) 9 μL , (xi) 10 μL). Monitoring the chemical shift as a function of $[\text{HFIP}]$ for the highlighted peak enabled determination of K_{eq} and ΔG of HFIP binding as described above. (b) Addition of HFIP to iodosylbenzene **4.1** results in the formation of H-bonded adduct **4.1**·HFIP. The thermodynamics of HFIP binding have been examined by analyzing the perturbation of the chemical shift of proton *para* to iodine as a function of $[\text{HFIP}]$. Bottom: Solid-state structure of **4.1**·HFIP, which shows that the iodanyl I–O bond (I(1)–O(1)) elongates and the contact between hypervalent iodine center and the sulfonyl group (I(1)–O(2)) contracts upon binding with HFIP.

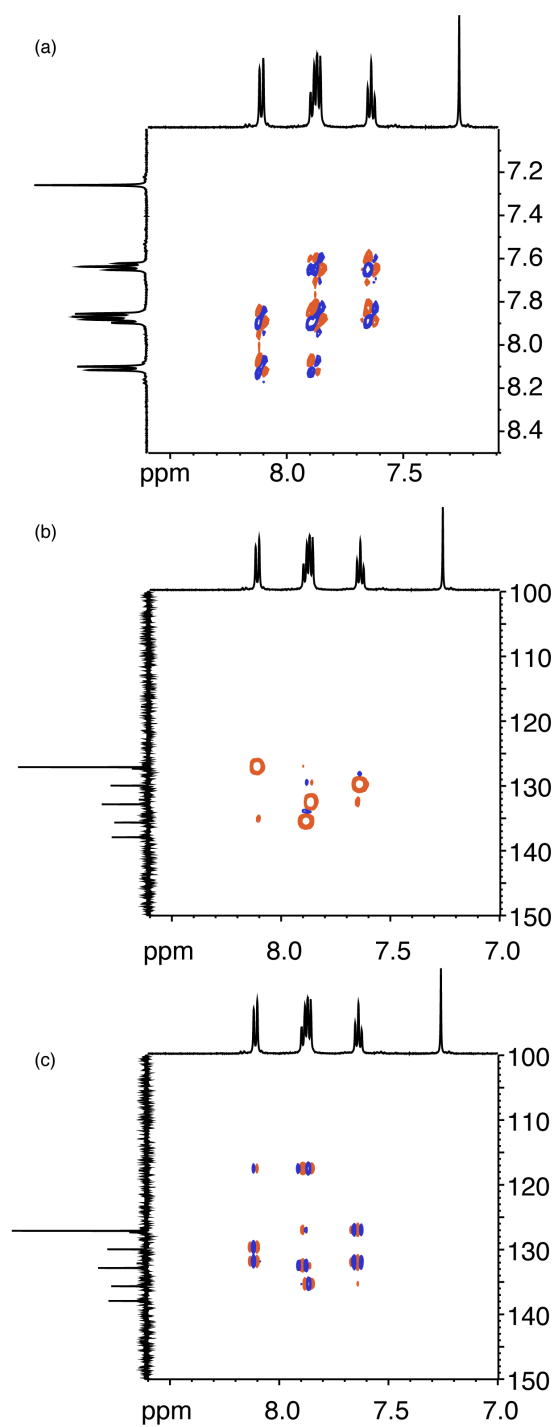


Figure IV-7 2-D NMR data of 2-(*tert*-butylsulfonyl)iodosylbenzene. (a) DQCOSY, (b) HSQC, and (c) HMBC of 4.1 at 23 °C in CDCl_3 .

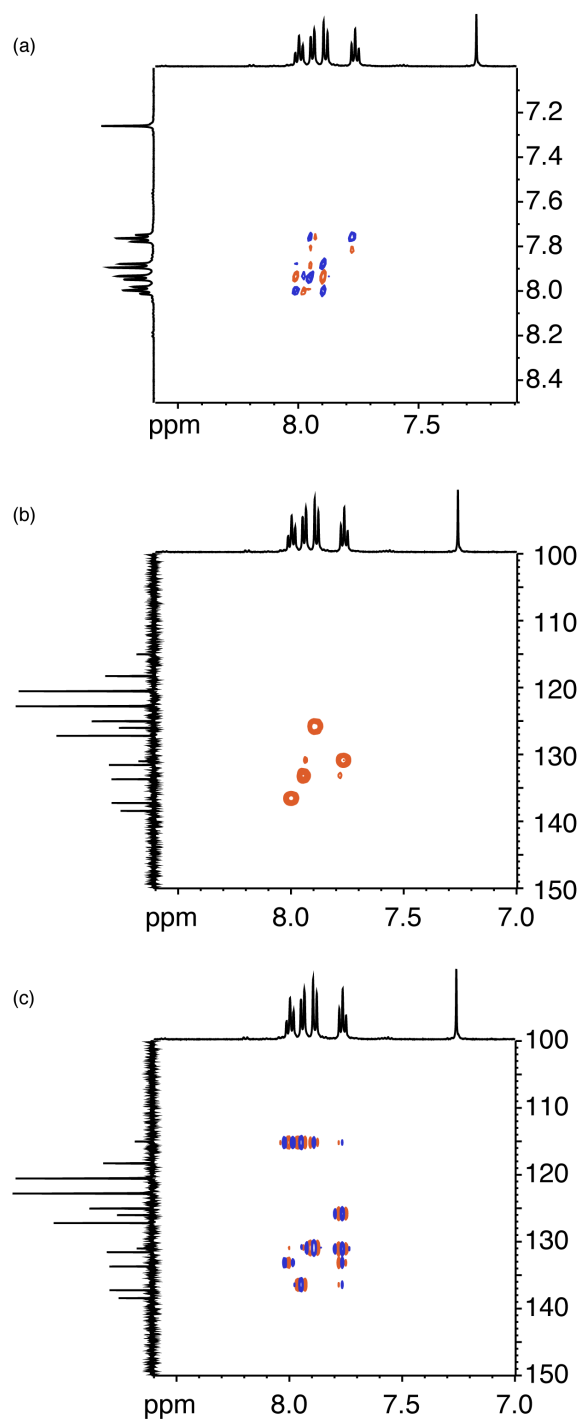


Figure IV-8 2-D NMR data of the adduct made between HFIP and 2-(*tert*-butylsulfonyl)iodosylbenzene.(a) DQCOSY, (b) HSQC, and (c) HMBC of 4.1·HFIP at 23 °C in CDCl₃.

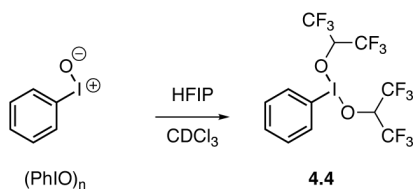


Figure IV-9 Dissolution of $(\text{PhIO})_n$ polymer occurs upon its dissolution in HFIP to form **4.4**.

IV.2.2 On the Aldehyde-Promoted Aerobic Oxidation of 2-(tert-Butylsulfonyl)iodobenzene (4.3)

In our original report of the aerobic oxidation of 2-(*tert*-butylsulfonyl)iodobenzene (**4.3**), we demonstrated that our aldehyde-promoted aerobic oxidation conditions provide direct access to I(V) derivative **4.2** (**Figure IV-10**).²¹⁶ We proposed that the observation of I(V) was due to AcOH-promoted disproportionation of an initially formed iododisylarene intermediate based on the following observations: 1) *in situ* monitoring of the oxidation of iodoarene **4.3** revealed that **4.3** and I(V) compound **4.2** were the only observable iodine-containing species and that I(III) compound **4.1** (or *bis*-acetate adduct **4.5**) was not present in the reaction mixture; and 2) disproportionation of independently synthesized iododisylarene **4.1** to generate equimolar amount of I(I) and I(V) was observed upon addition of AcOH. In addition, the proposed acid-promoted disproportionation was consistent with literature detailing *O*-bridged intermediates in disproportionation reactions in acidic media.^{194,216} *During subsequent investigations of the reaction chemistry of 4.1 with AcOH, we have observed that in contrast to the observed disproportionation, diacetate 4.5 formed in the presence of AcOH and this species appears to be resistant to*

disproportionation in AcOH solution. To clarify the divergent results regarding the disproportionation of **4.1**, we have pursued the following series of experiments.

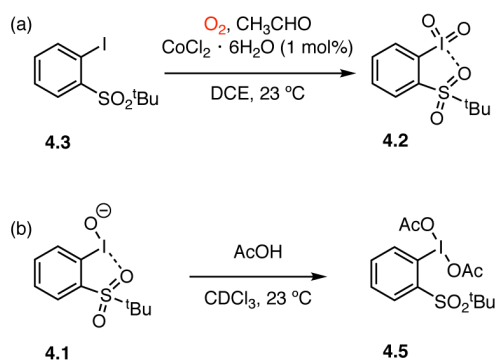


Figure IV-10 The aerobic oxidation of 2-(*tert*-butylsulfonyl)iodobenzene. (a) Aldehyde-promoted aerobic oxidation of 2-(*tert*-butylsulfonyl)iodobenzene (**4.3**) affords iodosylbenzene **4.1**. Iodosylbenzene **4.1** is not observed at intermediate reaction times. (b) Exposure of iodosylbenzene **4.1** to AcOH, which is an obligate byproduct of the autoxidation of acetaldehyde, affords *bis*-acetate **4.5**.

IV.2.3 Synthesis of Iodosylarene **4.1**

A variety of procedures have been reported for the synthesis of **4.1** (Methods A–C, **Figure 4.11**). In the original report from Protasiewicz, aryl iodide **4.1** was treated with H_2O_2 in Ac_2O and then 3 M NaOH to generate **4.1** (Method A).¹⁴⁷ Concerns regarding the safety of this procedure have been raised,²¹⁷ and as a result, methods based on oxidation with either KClO_3 in HCl or NaBO_3 in AcOH followed by hydrolysis with NaOH have been developed.^{31,218} In our hands, Method B, based on treatment of **4.3** with KClO_3 and HCl, provided an analytically pure sample of **4.1** (assayed by combustion analysis). Despite the apparent purity of the samples obtained by this method, we found that samples

of **4.1** prepared by Method B exhibit substantial variation with respect to disproportionation rate: In a series of ^1H NMR experiments using mesitylene as an internal standard, half-lives ranging from less than a minute to six hours have been observed. In addition, the material appeared to be light sensitive, showing accelerated disproportionation when exposed to ambient light.

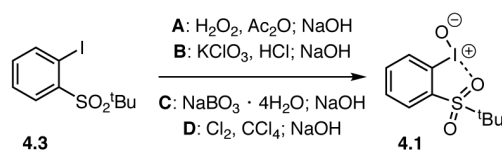


Figure IV-11 Various methods for the synthesis of 2-(*tert*-butylsulfonyl)iodosylbenzene.

We speculated that the unpredictable disproportionation rates displayed by samples of **4.1** prepared by Method B may be due to the presence of a trace impurity in the reagent that is not detected by combustion analysis. To evaluate the potential presence of impurities in the samples of **4.1**, we have pursued EPR and ICP-MS based experiments. Exposure of a sample of **4.1** prepared by Method B to *N-tert*-butyl- α -phenylnitron (PBN), which is a commonly used EPR spin trap,²¹⁹ in CDCl_3 results in the EPR spectrum shown in **Figure IV-12a**, which can be fit as the admixture of the spectrum of oxidized PBN as well as the spectrum of the PBN adduct of hydroxy radical (**Figure IV-12b**). The intensity of the spectral features increases upon exposure of the sample to ambient light (**Figure IV.13**). An identical EPR spectrum can be obtained from KClO_3 in CDCl_3 (**Figure IV-14**). These observations are consistent with the presence of a trace quantity of chlorate that

was not removed despite extensive washing; UV irradiation of chlorate has been reported to promote a variety of radical-generating processes.²²⁰ Dissolution of the sample of **4.1** prepared by Method B in HNO₃ and analysis by ICP-MS indicated the presence of K⁺. We suspect that the source of the observed potassium is the KClO₃ used to prepare **4.1**. Chlorate is not detectable by IR analysis (**Figure IV-15**), however, negative-mode ESI-MS of **4.1** prepared by Method B indicates the presence of ClO₃⁻ ($m/z = 82.953$ (expt); 82.954 (calc)).

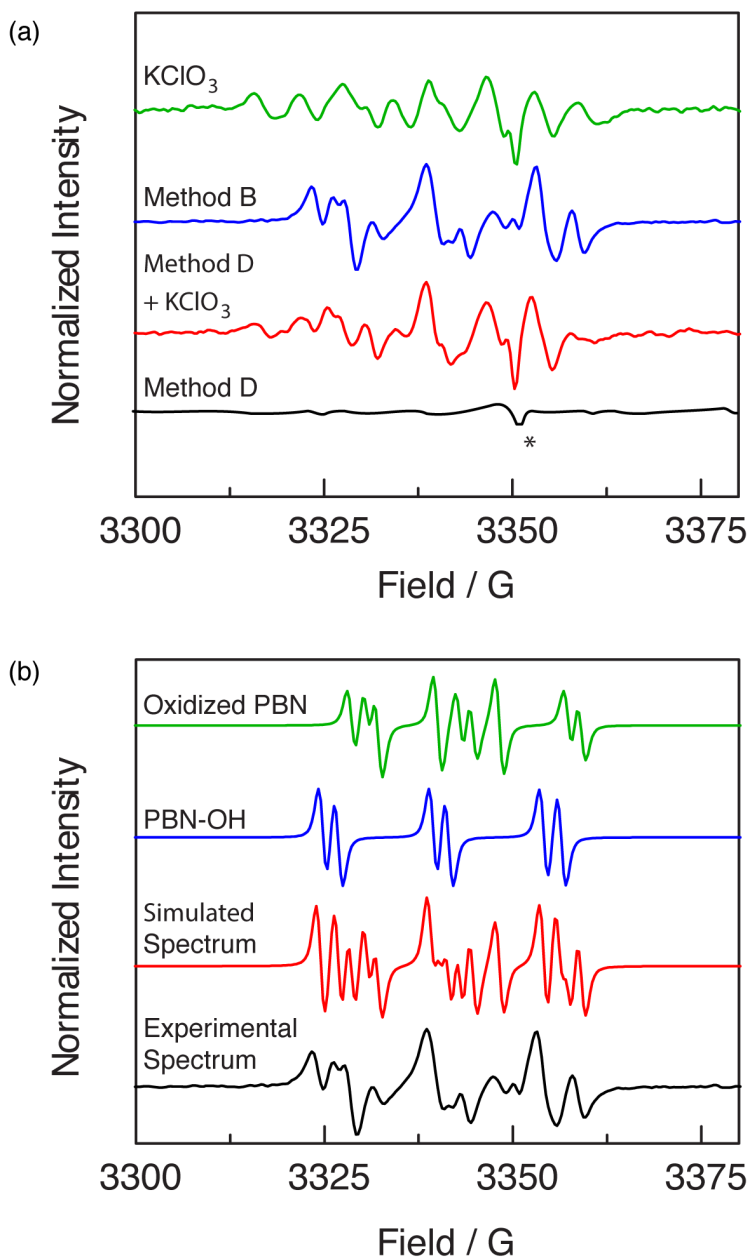


Figure IV-12 EPR experiments demonstrate preparation-sensitive behavior of 2-(*tert*-butylsulfonyl)iodosylbenzene. (a) EPR spectra obtained following PBN addition to **4.1** prepared by Method D (—), **4.1** with added KClO₃ (—), **4.1** prepared by Method B (—), and KClO₃ (—). (b) Simulated EPR components: Experimentally obtained spectrum following PBN addition to **4.1** prepared by Method D with added KClO₃ (—), spectral simulation as admixture of oxidized PBN and hydroxy radical adduct (—), simulated PBN-adduct of hydroxyl radical (—), and simulated spectrum for oxidized PBN (—).

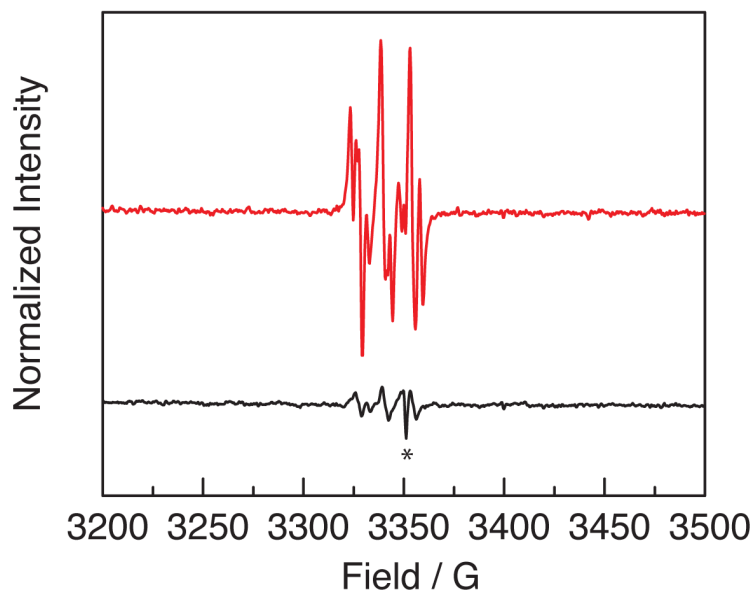


Figure IV-13 Effect of light on 2-(*tert*-butylsulfonyl)iodosylbenzene prepared by **Method B**. Comparison of EPR spectra obtained following PBN addition to **4.1** (prepared by Method B) that have been exposed to ambient light (—) or have been handled with the exclusion of light (—). The peak at 3351 G is due to an impurity in the background of the resonator (*).

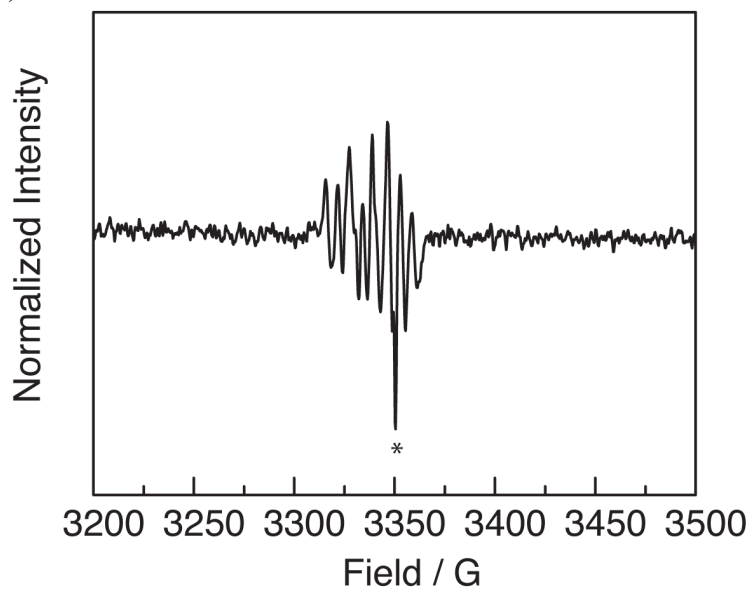


Figure IV-14 EPR spectrum obtained following PBN addition to KClO_3 . The peak at 3351 G is due to an impurity in the background of the resonator (*).

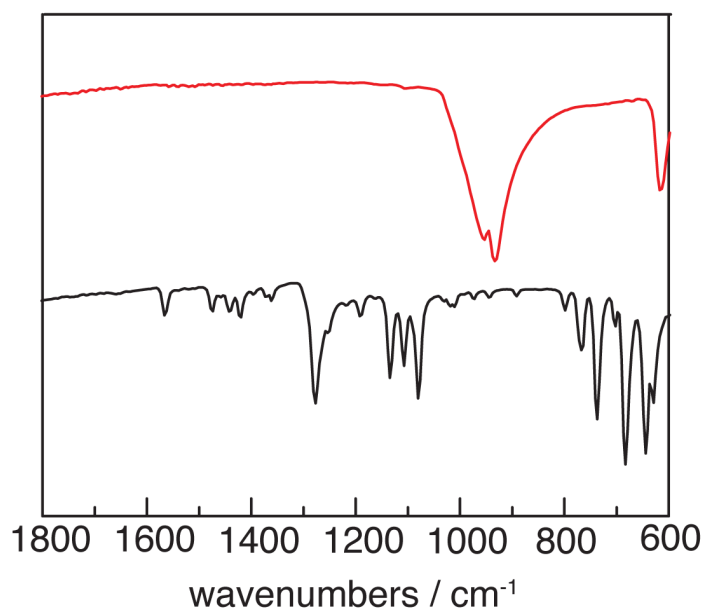


Figure IV-15 IR spectra of 2-(*tert*-butylsulfonyl)iodosylbenzene synthesized by Method B (—) and KClO₃ (—).

Based on the hypothesis that trace impurities associated with KClO_3 were leading to the irreproducible disproportionation behavior of **4.1**, we modified the synthetic protocol as follows: Cl_2 was bubbled through a solution of **4.3** in CCl_4 , the resulting solid was isolated, and was then treated with 5 M NaOH solution (**Figure IV.12**, Method D). The resulting samples of **4.1** display reproducible disproportionation chemistry (*vide infra*). Exposure of material prepared by Method D to PBN did not give rise to an observable EPR signal (**Figure IV.12a**). Addition of KClO_3 to the sample of **4.1** prepared from Method D led to the evolution of an EPR spectrum that overlays the spectrum obtained from Method B (**Figure IV.12a**) and the intensity of the signal increased upon exposure to light. In addition, ICP-MS analysis of **4.1** prepared by Method D did not show the presence of any trace metal ions.

With access to samples of **4.1** obtained from Method D, we have investigated the kinetics of reagent disproportionation. Disproportionation was monitored by ^1H NMR spectroscopy utilizing mesitylene as an internal standard. Monitoring the concentration of **4.1** as a function of time at 48 °C revealed that disproportionation is second-order with respect to **4.1** (**Figure IV.16a**). Examination of the disproportionation as a function of temperature from 35–75 °C allowed construction of the Eyring plot shown in **Figure IV.16b**. From these data, activation parameters for disproportionation — $\Delta H^\ddagger = 15.2 \text{ kcal}\cdot\text{mol}^{-1}$ and $\Delta S^\ddagger = -15.2 \text{ cal}\cdot\text{K}^{-1}\text{mol}^{-1}$ — can be extracted. These parameters are consistent with the room-temperature stability of **4.1** and with the observed slow disproportionation upon standing.

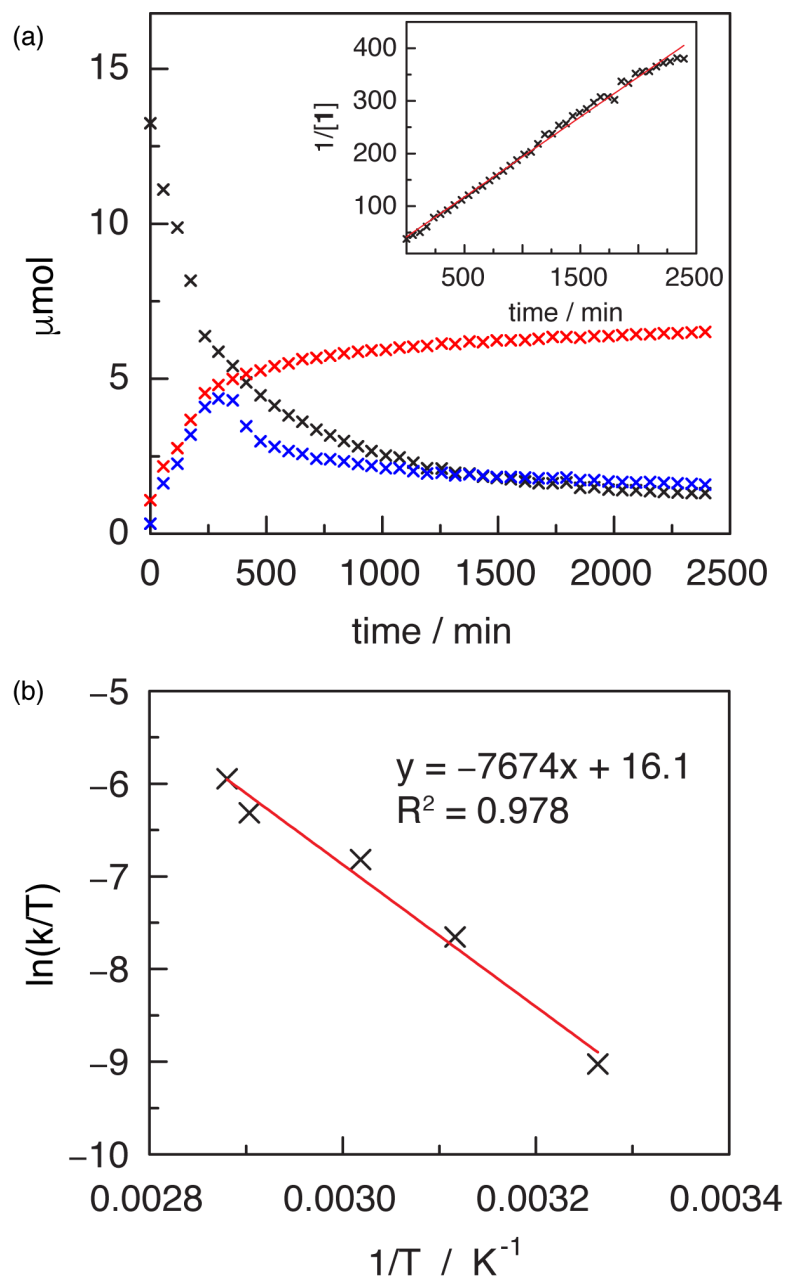


Figure IV-16 Kinetics for the disproportionation of 2-(*tert*-butylsulfonyliodosyl)benzene.(a) Concentration vs. time plot of 2-(*tert*-butylsulfonyl)iodosylbenzene (**4.1**, \times), 2-(*tert*-butylsulfonyl)iodobenzene (**4.3**, \times), and 2-(*tert*-butylsulfonyl)iodyllbenzene (**4.2**, \times) for the disproportionation of **4.1** at 48 °C in CDCl_3 . Inset: Plot of $[\mathbf{4.1}]^{-1}$ vs. time for the disproportionation of **4.1** at 48 °C in CDCl_3 . (b) Eyring plot for the disproportionation of **4.1**. At ~300 minutes, precipitation of **4.2** was observed which accounts for the decreasing concentration at this time.

Regarding the formation of iodylarene **4.2** by aldehyde-promoted aerobic oxidation, the above experimental data suggest that our original proposal of acid-promoted disproportionation of **4.1** was based on the irreproducible disproportionation kinetics of material prepared by Method B. While a detailed understanding of the mechanism of aerobic production of iodylarene **4.2** during aldehyde-promoted aerobic oxidation is beyond the scope of our current work, we note the following relevant observations (summarized in **Figure 4-17**):

(1) While the oxidation of 4-iodotoluene to the corresponding iodylbenzene under the action of O₂, CH₃CHO, and Co(II) proceeds via the initial formation of 4-iodotoluene diacetate (i.e. I(III)) followed by subsequent oxidation of I(III) to I(V)), oxidation of iodobenzene **4.3** affords iodylbenzene **4.2** without the observation of iodosylarene **4.1** or *bis*-acetate **4.5**.¹⁹

(2) Addition of the isolable reaction components of aldehyde-promoted aerobic oxidation, including acetaldehyde, acetic acid, CoCl₂, and Co(OAc)₃, does not induce disproportionation of *bis*-acetate **4.5**.

(3) Exposure of an independently prepared sample of I(III) compound **4.5** to aldehyde-promoted aerobic oxidation (O₂, CH₃CHO, and Co(II) in *d*₄-AcOH) resulted in the observation of both iodylbenzene **4.2** and iodobenzene **4.3** by ¹H NMR. The presence of iodobenzene **4.3** during the aerobic oxidation of **4.5** suggests that a disproportionation mechanism may be operative.

(4) Monitoring the oxidation of iodobenzene **4.3** with commercially available 32 wt% peracetic acid by ¹H NMR revealed 1) two-phase kinetic behavior and 2) initial

buildup and subsequent consumption of *bis*-acetate **4.5**. The two-phase kinetics during the oxidation of iodobenzene **4.3** was observed due to the presence of H₂O₂ in commercially available peracetic acid solutions. During this kinetic phase, H₂O₂ reduces the I(III) (i.e. either **4.1** or **4.5**) formed by peracetic acid to regenerate iodobenzene **4.3** and ¹O₂ (observed as small bubbles).¹⁹ Generation of ¹O₂ was confirmed by the observation of 9,10-dimethyl-9,10-dihydro-9,10-epidioxyanthracene upon addition of 9,10-dimethylanthracene, a common chemical trap for ¹O₂. Independent reaction of either **4.1** or **4.2** with H₂O₂ resulted iodine-centered reduction and evolution of ¹O₂. After the initial kinetic phase, accumulation of **4.5** was observed which is then further oxidized to iodylbenzene **4.2**. Similar generation and trapping of ¹O₂ during reaction of H₂O₂ with Ph(I(O₂CF₃)₂) has previously been observed.²²¹⁻²²²

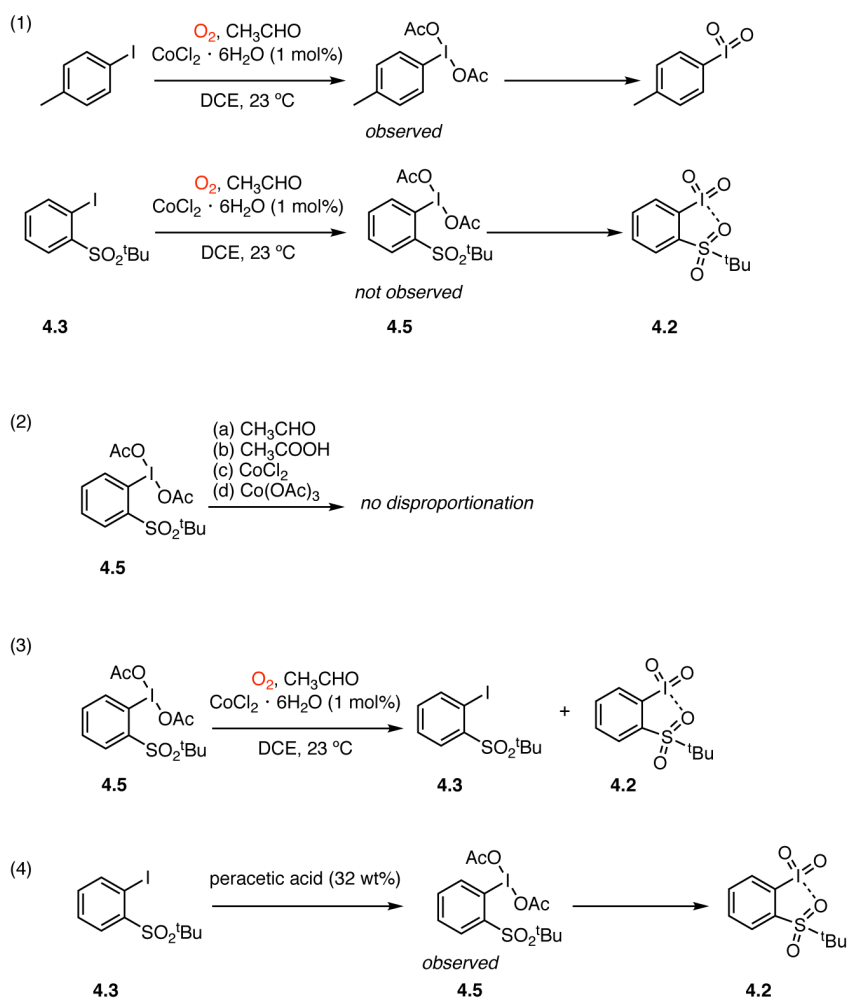


Figure IV-17 Summary of observations 1-4.

IV.2.4 Coordination Chemistry of Iodosylarenes with Soluble Transition Metal Clusters

Following the observation of the disparate coordination chemistry of **4.1** and (PhIO)_n with HFIP, we have undertaken an examination of the potential coordination chemistry of these iodosylarenes with transition metal clusters that are commonly encountered in MOF chemistry. We selected a carboxylate-bridged Zn₂ complex (**4.6**)²²³ and a Zr₆O₄ cluster (**4.7**)²²⁴⁻²²⁵ as exemplary models because 1) these coordination sites are ubiquitous in MOF chemistry,²²⁶ and 2) the ligand exchange rates of Zn and Zr are drastically different,²²⁷ and thus these complexes provide a probe for the impact of M–L bond lability on the interaction of the cluster with iodosylarenes.

Exposure of both Zn₂ and Zr₆ clusters to (PhIO)_n resulted in (PhIO)_n dissolution and the observation of the PhI(OR)₂ species derived from carboxylate exchange; iodobenzene dibenzoate is observed following treatment of Zn₂ complex **4.6** with (PhIO)_n and iodobenzene dimethacrylate is obtained following treatment of Zr₆ cluster **4.7** with (PhIO)_n (**Figure IV.18**). In neither case have we characterized the metal-containing byproducts of these exchange reactions.

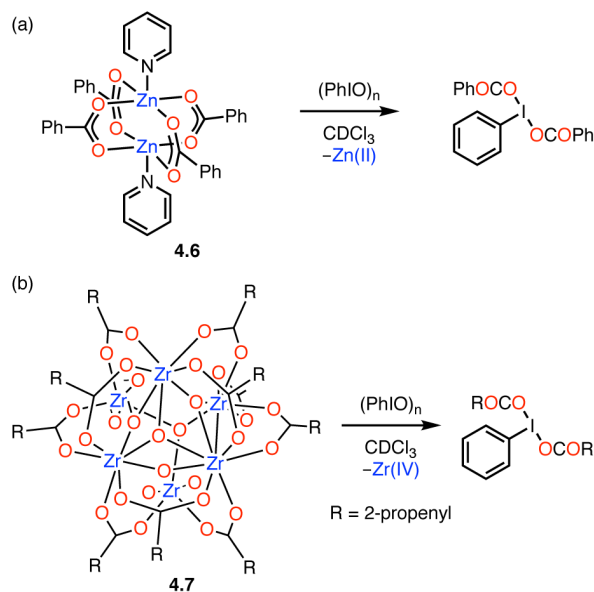


Figure IV-18 Ligand exchange chemistry observed between Zn₂ and Zr₆ metal clusters with iodosylbenzene. Ligand exchange is observed between (PhIO)_n and (a) Zn₂ complex **4.6** and (b) Zr₆ cluster **4.7**.

In contrast to the ligand exchange chemistry observed between (PhIO)_n and complexes **4.6** and **4.7**, iodosylarene **4.1** does not participate in analogous ligand exchange chemistry. Exposure of **4.1** to Zn₂ benzoate complex **4.6** does not result in the observation of benzoate adducts of **4.1**, which would arise by carboxylate exchange similar to that observed for reaction of (PhIO)_n with **4.6**. Treatment of Zr₆ cluster **4.7** with excess iodosylarene **4.1**, such as would be present during catalysis, results in the isolation of a new Zr₆ cluster **4.8** in which four molecules of **4.1** are bound to the Zr₆ core (**Figure IV.19**). Upon binding, the co-ordination mode of the carboxylates change; whereas in the starting Zr₆ cluster nine carboxylate ligands engage in bridging binding modes and three chelate to a single Zr center, in cluster **4.8** eight carboxylates participate in bridging binding modes and four are mono-dentate. These observations indicate that ligation of

iodosylarene to Zr is capable of displacing both bridging and chelating carboxylate ligands. Analysis of the metrical parameters of the iodosylarene fragments bound to Zr indicates that the I–O bond elongates from 1.848(6) to 1.87(1) Å and the secondary bonding interaction between the sulfonyl oxygen and the iodine center contracts from 2.707(5) to 2.62(2) Å. Similarly, I–O bond elongation and contraction of secondary bonding interactions have consistently been observed in the limited number of previously reported transition metal adducts of iodosylarene **4.1** (metrical parameters of transition metal adducts of **4.1** are compared in **Table IV-1**.²²⁸⁻²³² We speculate that the disparate behaviors of (PhIO)_n and **4.1** towards ligand exchange and Lewis adduct formation, respectively, is due to the secondary coordination in **4.1**, which amplifies the basicity of the iodosyl oxygen.

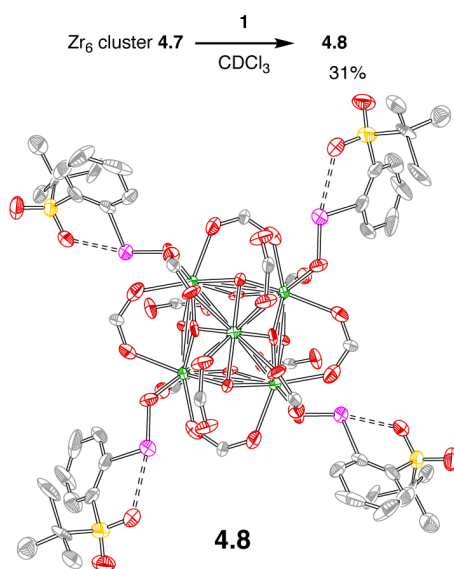


Figure IV-19 Reaction of Zr_6 cluster with 2-(*tert*-butylsulfonyl)iodosylbenzene. Exposure of Zr_6 cluster **4.7** to iodosylarene **4.1** results in isolation of **4.8**; I(1)–O(1) = 1.87(1) Å and I(1)–O(3) = 2.62(2) Å.

Table IV-1 Analysis of select bond distances in iodosylarene **4.1** and adducts of **4.1** with transition metal complexes.

Compound	I–O _{iodosyl} / Å	I–O _{sulfonyl} / Å
Iodosylarene 1	1.848	2.707
1 ·HFIP	1.873	2.668
[LFe ₃ (PhPz) ₃ OMn(^s PhIO)][OTf] ₃ ²²⁹	1.864	2.602
[Rh(Cp*)(2-(2-pyridyl)phenoxide)(^s PhIO)][B(Ar ^F) ₄] ²³³	1.909	2.652
[Co(II)Tp ^{Ad,Me} (^s PhIO)][B(Ar ^F) ₄] ²³⁰	1.878	2.481
[Co(II)Tp ^{tBu} (^s PhIO)][B(Ar ^F) ₄] ²³⁰	1.891	2.520
4.8	1.87	2.62

IV.2.5 Investigation of Potential Coordination Chemistry in MOFs

Based on the observation of ligand exchange processes (with (PhIO)_n) and ligand displacement reactions (with iodosylarene **4.1**) between iodosylarenes and transition metal clusters, we have pursued a preliminary investigation of the potential for similar coordination chemistry to impact the structure of MOFs comprised of these building units. To this end, we have examined the chemistry of UiO-67,²³⁴ which is comprised of Zr₆ nodes, and MOF-508,²³⁵²³⁶ which is based on Zn₂ nodes. These materials were selected because they lack redox-active metal sites, which would complicate analysis by providing pathways for iodosylarene redox chemistry. Incubation of these materials with either **4.1** or (PhIO)_n does not result in the observation of changes to the PXRD patterns or the observation of linker-derived soluble species by ¹H NMR. These observations suggest that the reaction chemistry observed with soluble Zn₂ and Zr₆ clusters is less important in extended materials, which is likely due to effective stabilization of M–L bonds by a macromolecular chelate effect.

IV.3 Conclusions

Hypervalent iodine compounds featuring I(III) and I(V) centers are accessible due to high ionizability of iodine. The bonding in hypervalent iodine compounds, which is based on 3c-4e bonds, results in highly ionic I–L bonding. The facility of oxidation-reduction chemistry at iodine coupled with the ligand exchange chemistry that is characteristic of hypervalent iodine compounds gives rise to reactivity patterns that bear similarity to the reaction chemistry of transition metal complexes. Recently, 2-(*tert*-

butylsulfonyl)iodosylbenzene (**4.1**) has garnered substantial attention from the MOF catalysis community because it exhibits substantially greater solubility in organic solvents than does (PhIO)_n, which is critical to achieving interstitial MOF catalysis. We have been attracted to the challenge of developing aerobic methods to generate soluble iodosylarenes, such as **4.1**, which, in combination with emerging MOF catalysts for C–H functionalization, would facilitate aerobic hydrocarbon oxidation chemistry.

Here, we show that a popular synthetic route to iodosylarene **4.1**, based on KClO₃ and HCl, affords material that displays unpredictable disproportionation rates. The unpredictable behavior arises from trace impurities introduced during synthesis. We develop a new route, based on initial Cl₂ oxidation, that provides routine access to samples of **4.1** that display highly reproducible properties. Given the preparation-dependent disproportionation kinetics of **4.1**, in combination with differences in activity and solubility between iodosylarene **4.1** and iodylarene **4.2**, we believe that the results of catalytic reactions in which **1** is used as the terminal oxidant should be evaluated with care. In addition, we examine the chemistry of iodosylarenes with soluble models of the transition metal clusters common to Zr₆- and Zn₂-based MOFs and show that both ligand-exchange reactions as well as the formation of acid-base adducts are available. These observations may provide insight into potential interactions between iodosylarenes and structural nodes common to metal-organic framework catalysts.

IV.4 Experimental Details

IV.4.1 General Considerations

Materials All chemicals and solvents were obtained as ACS reagent grade and used as received. Anhydrous THF was obtained from a drying column and was stored over activated molecular sieves.¹⁴⁸ Iodobenzene and thiophenol were obtained from Beantown Chemical. Acetaldehyde, potassium chlorate (KClO₃), and zirconium(IV) chloride were obtained from Alfa Aesar. Hexafluoroisopropanol (HFIP) was obtained from Matrix Scientific. Hydrochloric acid was purchased from Macron Fine Chemicals. Ethyl acetate was obtained from EMD Millipore. Mesitylene, *N*-*tert*-butyl- α -phenylnitron (PBN), CoCl₂·6H₂O, 1,2-dichloroethane (DCE), *t*-butanol, diethyl ether, hexanes, peracetic acid (32 wt% solution), acetic acid, *d*₄-AcOH, iodine, sodium peroxide, and 4,4'-bipyridyl were obtained from Sigma Aldrich. Perchloric acid (70 wt%) and *N,N*-dimethylformamide (DMF) were obtained from BDH chemicals. Silica gel (0.060–0.200 mm, 60 Å for column chromatography) was obtained from Acros Organics. Dichloromethane and acetonitrile were obtained from Fisher Scientific. Biphenyl-4,4'-dicarboxylic acid (bpdc) was obtained from Oxchem. Ethanol (EtOH) was obtained from Koptec. Terephthalic acid was obtained from TCI. Iodosylbenzene²³⁷, 2-(*tert*-butylsulfonyl)iodobenzene (**4.1**)²¹⁷ and 2-(*tert*-butylsulfonyl)iodoylbenzene (**4.2**)²⁰⁷ were prepared according to literature methods. The compounds [Zn₂(OBz)₄py₂]²²⁴, Zr₆O₄(OH)₄(OMc)₁₂,^{223,225} UiO-67²³⁸, and MOF-508b²³⁵ were prepared according to literature methods. Deuterated solvents were purchased from Cambridge Isotope Laboratories and were used as received unless otherwise noted. O₂

(99.6%) was obtained from Conroe Welding Supply. All reactions were carried out under ambient atmosphere unless otherwise noted.

Characterization Details NMR spectra were recorded on a Bruker 400 FT NMR, an Inova 500 FT NMR, a Varian VNMRs 500 FT NMR, or a Bruker Ascend™ 400 NMR for ^1H , $^{13}\text{C}\{^1\text{H}\}$, and ^{19}F acquisitions. ^1H and ^{13}C NMR spectra were referenced against solvent resonances: CDCl_3 (7.26 ppm, ^1H ; 77.16 ppm, ^{13}C) and d_4 -AcOH (2.04 ppm, ^1H).^{154,239} ^{19}F spectra were referenced against fluorobenzene (-113.15 ppm).²⁴⁰ ^1H NMR data are reported as follows: chemical shift (δ , ppm), (multiplicity: s (singlet), d (doublet), t (triplet), m (multiplet), br (broad), integration). ^{13}C NMR data are reported as follows: chemical shift (δ , ppm) (multiplicity: s (singlet), d (doublet), t (triplet), m (multiplet)). ^{19}F NMR data are reported as follows: chemical shift (δ , ppm) (multiplicity: s (singlet), d (doublet), t (triplet), m (multiplet)). Mass spectra were recorded on either Orbitrap Fusion™ Tribrid™ mass spectrometer or Q Exactive™ Focus Hybrid Quadrupole-Orbitrap™ mass spectrometer from ThermoFisher Scientific. GC analysis was carried out using a Trace 1310 (Thermo Scientific) instrument equipped with a TraceGOLD TG-1M column from Thermo Scientific (length: 30 m, id: 0.53 mm, film thickness: 0.25 μm). The column temperature was maintained at 60 °C for 2 min and was raised to 300 °C at 60 °C/min. The final temperature (200 °C) was held for 4 min. EPR spectra were recorded at X-band (9.38 GHz) on a Bruker ELEXSYS spectrometer at 23 °C in 2 mm EPR tubes. EPR simulations were performed with Easyspin (version 5.2.17) using the “garlic” function.²⁴¹ IR spectra were recorded on a Shimadzu FTIR/IRAffinity-1 spectrometer. Spectra were blanked against air and were determined as the average of 32 scans.

Elemental analyses were done in Atlantic Microlab, Inc., Norcross, GA. ICP-MS measurements were carried out on a PerkinElmer NexION 300D Quadruple in pulse mode with ASX-520 autoSampler. The collected data were analyzed by NexIon software Version 1.3. Thermal Gravimetric Analysis (TGA) experiments were performed on a TGA Q500 TA instrument. Samples were heated from 23 °C to 800 °C at a heating rate of 20 °C/min under N₂.

X-Ray Crystallography Details Experimental details of crystallization are included in the synthetic procedures for the relevant compounds. Single crystal X-ray diffraction analysis of **4.1**·HFIP was conducted by mounting a suitable crystal on a MiTeGen dual-thickness micromount. The crystal was cooled to 110 K using a cold N₂ stream (Oxford). A Bruker APEX 2 Duo X-ray (three-circle) diffractometer was used for crystal screening, unit cell determination, and data collection. The X-ray radiation employed was generated from a Mo sealed X-ray tube ($K\alpha = 0.70173 \text{ \AA}$ with a potential of 40 kV and a current of 40 mA). Bruker AXS APEX II software was used for data collection and reduction. Absorption corrections were applied using the program SADABS.²⁴² A solution was obtained using XT/XS in APEX2 and refined in Olex2.²⁴³ All non-hydrogen atoms were refined with anisotropic thermal parameters. Hydrogen atoms were placed in idealized positions and refined using a riding model. The structure was refined (weighted least squares refinement on F^2) to convergence.²⁴⁴⁻²⁴⁵ Data are deposited in the Cambridge Crystallographic Data Centre (CCDC 1910636).

Single crystal X-ray diffraction analysis of **4.8** was conducted using synchrotron radiation ($\lambda = 0.33062 \text{ \AA}$) equipped with a Pilatus3 X CdTe 1M detector and an Oxford

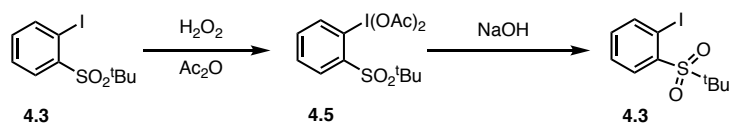
cryostream cooling device operating at 100 K at NSF's ChemMatCARS Sector 15 of Advanced Photon Source (APS) housed at Argonne National Laboratory (ANL). Data were collected as a series of phi scans. Indexing was performed using Bruker APEX3. Data integration and reduction were performed using SaintPlus. Absorption correction was performed by multi-scan method implemented in SADABS.²⁴² The space group was determined using XPREP implemented in APEX3. Structures were solved using SHELXT and refined using SHELXL-2017 (full-matrix least-squares on F^2)²⁴⁴⁻²⁴⁵ with OLEX2 interface program.²⁴³ All non-hydrogen atoms were refined anisotropically. Hydrogen atoms were placed at idealized positions and refined using a riding model. SIMU, DELU, and ISOR commands were used to refine disordered carbon sites in methacrylate ligands. Considering that accessible voids with this structure accommodate heavily disordered guest solvent molecules, the large Q peaks were assigned as water molecules and a solvent mask was employed in OLEX2 to process the refinement. Data are deposited in the Cambridge Crystallographic Data Centre (CCDC 1909655).

PXRD measurements were carried out on a Bruker D8 Advance Eco X-ray diffractometer (Cu $K\alpha$, 1.5418 Å; 40 kV, 25 mA) fitted with a LynxEye detector. The angular range was measured from 3.50 to 40.00° (2θ) with steps of 0.020° and a measurement time of 0.1 or 0.5 second per step.

Computational Details Calculations were performed using the Gaussian 09, Revision D.01 suite of software.²⁴⁶ Geometry optimization was carried out with the PBE0 functional²⁴⁷⁻²⁴⁹ (sdd basis set for I,²⁵⁰ aug-cc-pVTZ for other atoms²⁵¹⁻²⁵²) and the SMD model²⁵³ for dichloromethane. Stationary points were characterized with frequency

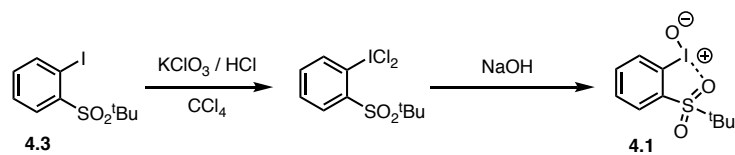
calculations using the same basis set and functionals. This level of theory satisfactorily reproduced metrical parameters of **4.1** and **4.1**·HFIP and was implemented by Boldyrev and Zhdankin in the analysis of the bonding in hypervalent iodine compounds.¹⁸⁷ NBO calculations were carried out with the NBO 6.0 suite.²⁵⁴

IV.4.2 Synthesis and Characterization



Synthesis of 2-tert-butylsulfonyliodosylbenzene (4.1) Method A: Method A for the preparation of compound **4.1** was not attempted at the reported scale due to safety concerns.^{147,217} A 10-mL round-bottomed flask was charged with hydrogen peroxide (30 wt% solution, 0.45 mL) and acetic anhydride (2.0 mL). The resulting solution was stirred for 4 h at 40 °C. 2-(tert-butylsulfonyliodo)benzene (**4.3**, 501 mg, 1.54 mmol, 1.00 equiv) was added, and the resulting solution was stirred at 23 °C for 24 h. Reaction progress was monitored by thin-layer chromatography (SiO₂, eluent of 20% ethyl acetate in hexanes, *R_f* = 0.3). The reaction mixture was concentrated under reduced pressure and the obtained white solid was used for the next step without purification.

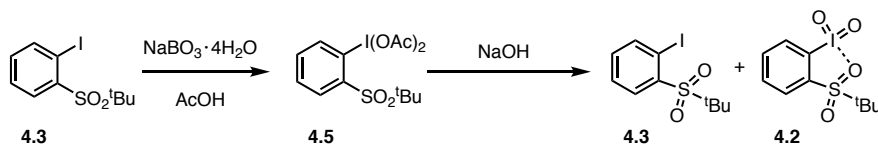
A 10-mL round-bottomed flask was charged with the solid obtained from the previous step. An aqueous NaOH solution (3M, 2.50 mL) was added dropwise with vigorous stirring until pH > 7 was reached and then the reaction mixture was stirred for an additional 30 min. The observed solids were isolated by vacuum filtration and washed with water (25 mL). Analysis via ¹H NMR in *d*₆-DMSO revealed the presence of 2-(tert-butylsulfonyl)iodobenzene (**4.3**).



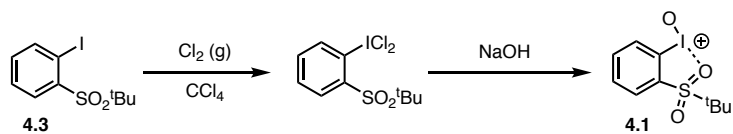
Method B: Method B for the synthesis of compound **4.1** is based on a literature procedure.³¹ A 10-mL round-bottomed flask was charged with 2-(*tert*-butylsulfonyl)iodobenzene (**4.3**, 300 mg, 0.925 mmol, 1.00 equiv), CCl_4 (1.00 mL), and conc. HCl (~0.70 mL), and was cooled to 0 °C with an ice-bath. The reaction mixture was vigorously stirred while KClO_3 (170 mg, 1.39 mmol, 1.5 equiv) was added in portions over 15 minutes. The reaction was stirred for 3 h at 0 °C. The observed solids were isolated by filtration and were washed with ice-cold, aqueous HCl (0.1M, 10 mL) and ice-cold water (25.0 mL) to afford pale yellow powder as product, which was used for the next step without further purification.

A 10-mL round-bottomed flask was charged with the solid obtained from the previous step and cooled to 0 °C with an ice bath. An aqueous NaOH solution (5M, 1.50 mL) was added dropwise. The reaction mixture was stirred for 30 min at 0 °C before 2 mL of water was added. The reaction mixture was then warmed to 23 °C and stirred for 16 h. The obtained solids were isolated by vacuum filtration, washed with ice-cold water (30 mL), and ice-cold diethyl ether (30 mL) to afford **4.1** as bright-yellow solid (128 mg, 40% yield). Elemental analysis: Theoretical C (35.31%), H (3.85%); Found C (35.24%), H (3.81%). $^1\text{H NMR}$ (δ , 23 °C, CDCl_3): 8.10 (d, $J = 8.1$ Hz, 1H), 7.91–7.87 (m, 2H), 7.65

(t, $J = 7.5$ Hz, 1H), 1.42 (s, 9H). The obtained spectrum matches well with the literature reported values.³¹

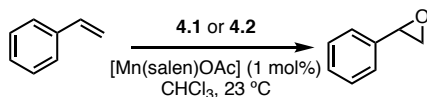


Method C: Method C for the preparation of compound **4.1** was based on a literature procedure.²¹⁸ A 100-mL round-bottomed flask was charged with the 2-(*tert*-butylsulfonyl)iodobenzene (**4.3**, 501 mg, 1.54 mmol, 1.00 equiv), sodium perborate tetrahydrate (3.2 g, 21 mmol, 14 equiv), and glacial acetic (30.0 mL), and the mixture was heated to 45 °C. The reaction mixture was stirred at this temperature for 5 h. Acetic acid was removed *in vacuo*. The reaction mixture was poured into water (20 mL) and then extracted with CH₂Cl₂ (3 × 25 mL). The organic layers were combined, washed with saturated aqueous NaHCO₃ solution until the pH of the solution was >7, and then dried with Na₂SO₄. During evaporation of solvent, the bright yellow solution turned colorless and analysis by crude NMR in *d*₆-DMSO revealed presence of only 2-(*tert*-butylsulfonyl)iodobenzene (**4.3**) and 2-(*tert*-butylsulfonyl)iodylbenzene (**4.2**).

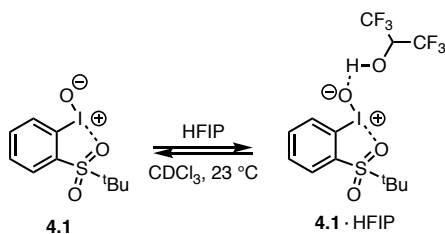


Method D: A 10-mL round-bottomed flask was charged with 2-(*tert*-butylsulfonyl)iodobenzene (**4.3**, 320 mg, 0.987 mmol, 1.00 equiv) and CCl₄ (1.00 mL) and was cooled to 0 °C with an ice-bath. In a separate three-necked round-bottomed flask, conc. HCl (3.00 mL) was added slowly to solid KClO₃ (726 mg, 5.95 mmol, 6.02 equiv). The generated Cl₂ gas was transferred to the the CCl₄ solution containing 2-(*tert*-butylsulfonyl)iodobenzene (**4.3**) using Tygon tubing and glass fittings. This process was repeated two more times producing a bright yellow solid. The obtained solids were isolated by filtration, washed with cold water (25 mL), and used in the next reaction without further purification.

A 10-mL round-bottomed flask was charged with the yellow solid obtained from the previous step and was cooled to 0 °C with an ice bath. An aqueous NaOH solution (5M, 1.50 mL) was added to the reaction vessel dropwise. The reaction mixture was stirred for 30 min at 0 °C before 2 mL of water was added. The reaction mixture was then warmed to 23 °C and stirred for 16 h. The obtained solids were isolated by vacuum filtration and were washed with ice-cold water (25 mL) and ice-cold diethyl ether (25 mL) to afford **4.1** as yellow solid (147 mg, 43% yield). Elemental analysis: Theoretical C (35.31%), H (3.85%); Found C (35.39%), H (3.76%). ¹H NMR (δ, 23 °C, CDCl₃): 8.10 (d, *J* = 8.1 Hz, 1H), 7.91–7.87 (m, 2H), 7.65 (t, *J* = 7.5 Hz, 1H), 1.42 (s, 9H). The obtained spectrum matches well with the literature reported values.³¹



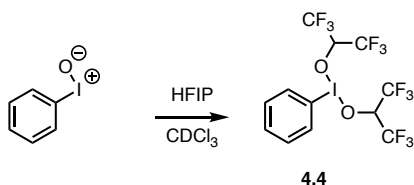
Epoxidation of Styrene Catalyzed by [Mn(salen)OAc] Oxidation of styrene by **4.1** and **4.2** was carried out by the following modification of literature methods.¹⁴⁷ An 8-mL vial was charged with [Mn(salen)OAc] (1.2 mg, 0.0032 mmol, 0.64 mol%), styrene (30 μ L, 0.26 mmol, 5.2 equiv), CHCl₃ (0.75 mL), and oxidant (**4.1** or **4.2**, 0.0500 mmol, 1.0 equiv). The reaction mixture was stirred for 14 h at 23 °C. Mesitylene (2.00 μ L, 0.0141 mmol) was added to each reaction as an internal standard, the reaction mixtures were filtered over Celite, and the resulting solutions were analyzed by GC. Peaks were integrated against mesitylene. Styrene oxide is obtained in 24% and 0% yield when **4.1** and **4.2** are employed as oxidant, respectively. Addition of HFIP (30.0 mL, 0.285 mmol, 5.70 equiv) to the reaction mixture did not produce an appreciable change in the yield of styrene oxide (33%).



Synthesis of 4.1·HFIP An NMR tube was charged with CDCl₃ (0.50 mL), 2-(*tert*-butylsulfonyliodosyl)benzene (**4.1**, 5.0 mg, 0.015 mmol, 1.0 equiv), mesitylene (2.0 μ L, 0.014 mmol), and HFIP (8.0 μ L, 0.076 mmol, 5.0 equiv). The resulting solution was analyzed by NMR spectroscopy. ¹H NMR (δ , 23 °C, CDCl₃): 8.00 (t, *J* = 7.8 Hz, 1H), 7.94 (d, *J* = 7.0 Hz, 1H), 7.89 (d, *J* = 8.2 Hz, 1H), 7.76 (t, *J* = 7.49, 1H), 1.44 (s, 3H). ¹³C NMR

(δ , 23 °C, CDCl₃): 137.3 (s), 133.7 (s), 131.6 (s), 131.0 (s), 125.0 (s), 115.0 (s), 23.1 (s).

Crystals suitable for characterization via SXRD were grown from an NMR sample via slow evaporation at 0 °C.



Synthesis of PhI(OC(CF₃)₂)₂ (4.4) An NMR tube was charged with CDCl₃ (0.50 mL), iodosylbenzene (3.8 mg, 0.017 mmol, 1.0 equiv), and HFIP (100 μ L, 0.952 mmol, 28.0 equiv). The solid completely dissolved and the resulting clear, colorless solution was analyzed by NMR spectroscopy (**Figure IV-20**). ¹H NMR (δ , 23 °C, CDCl₃): 8.07 (d, J = 7.7 Hz, 2H), 7.68 (t, J = 7.5 Hz, 1H), 7.58 (t, J = 7.6 Hz, 2H), 4.19 (m, 2H). ¹³C NMR (δ , 23 °C, CDCl₃): 134.1 (s), 133.6 (s), 132.0 (s), 124.0 (s), 122.3 (m, J = 287.5), 75.3 (m, J = 32.5). ¹⁹F NMR (δ , 23 °C, CDCl₃): -75.13 (d, J = 6.2).

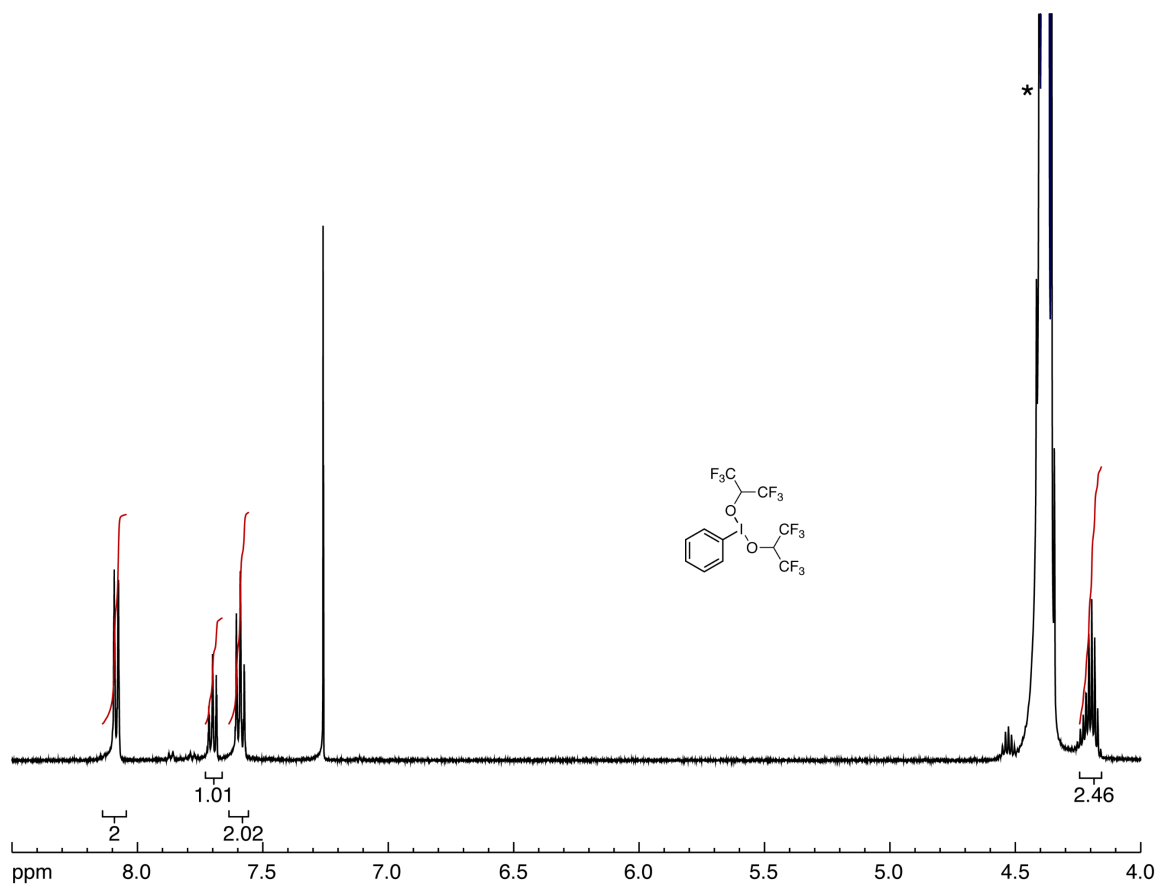


Figure IV-20 Reaction of iodosylbenzene with HFIP. ^1H spectrum of compound **4.4** obtained at 23 °C in CDCl_3 . The methine resonance of **4.4** overlaps with a sideband of the peak at 4.4 ppm is due to excess HFIP (*).

IV.4.3 X, Y, Z Coordinates of Optimized Structures

Atomic coordinates for optimized structures of **4.1**, **4.1**·HFIP, and PhIO are shown in Tables IV-2-4.

Table IV-2 Atomic coordinates of the optimized structures of **4.1**.

Atom	X	Y	Z
C	-0.471075	1.128229	-0.318568
C	0.865235	0.915246	-0.015373
C	1.685124	1.969256	0.328722
C	1.163949	3.253406	0.356369
C	-0.162215	3.481908	0.026649
H	-2.015281	2.586844	-0.583741
H	2.725736	1.765830	0.559806
H	1.807869	4.082019	0.623421
H	-0.560254	4.488082	0.028594
I	1.873728	-0.956052	-0.098434
S	-1.561377	-0.206013	-0.761709
O	-0.687403	-1.340226	-1.094218
O	-2.471738	0.267516	-1.794460
C	-2.544176	-0.671548	0.717669
C	-3.369152	-1.870467	0.265880
H	-3.947753	-2.215727	1.124457
H	-4.064377	-1.605290	-0.530219
H	-2.738012	-2.693302	-0.070235
C	-3.439862	0.490594	1.109212
H	-4.065564	0.817954	0.279365
H	-4.097083	0.147553	1.910591
H	-2.869378	1.337590	1.489541
C	-1.589451	-1.046267	1.836531
H	-0.968841	-1.900361	1.569183
H	-2.185956	-1.319893	2.709074
H	-0.947640	-0.212419	2.123332
O	3.492126	-0.394179	0.662761
C	-0.471075	1.128229	-0.318568
C	0.865235	0.915246	-0.015373

Table IV-3 Atomic coordinates of the optimized structure of **4.1·HFIP**.

Atom	X	Y	Z
S	3.283824	0.359133	0.888317
O	-1.024526	-1.688262	-1.201736
O	2.666486	-0.902650	1.363985
O	3.755051	1.327919	1.881015
C	0.942174	0.419556	-0.608020
C	0.019491	1.029058	-1.443735
H	-0.811583	0.447138	-1.833562
C	0.174316	2.380650	-1.757916
H	-0.551376	2.858154	-2.409953
C	1.233462	3.116136	-1.232020
H	1.335545	4.172625	-1.459526
C	2.168453	2.492242	-0.410374
H	3.001557	3.049649	0.009822
C	2.029596	1.135093	-0.116772
C	4.674924	-0.086265	-0.217841
C	4.157313	-1.065030	-1.267254
H	3.784939	-1.986515	-0.810241
H	4.994304	-1.323406	-1.923740
H	3.370860	-0.623324	-1.889478
C	5.231147	1.186466	-0.851738
H	4.533765	1.620759	-1.574490
H	6.146002	0.917633	-1.388902
H	5.486650	1.935575	-0.096097
C	5.708274	-0.745962	0.701186
H	6.095727	-0.039085	1.439899
H	6.540027	-1.082046	0.074436
H	5.292174	-1.616871	1.216134
F	-1.817349	0.795000	1.278061
F	-3.500681	2.117071	0.969921
F	-3.710713	0.369943	2.229088
F	-5.500980	1.235348	-0.574237
F	-5.729216	-0.579165	0.579613
F	-5.274140	-0.691279	-1.528321
O	-3.113175	-1.317997	0.073545
H	-2.238608	-1.487154	-0.479636
C	-3.516842	-0.017515	-0.122070
H	-3.038185	0.468629	-0.986130
C	-5.019326	-0.008244	-0.401744
C	-3.149046	0.827300	1.101423

Table IV-4 Atomic coordinates of the optimized structure of PhIO.

Atom	X	Y	Z
C	3.475001	0.000005	0.128916
C	2.787003	1.204529	0.074513
C	1.403517	1.212677	-0.038173
C	0.732602	-0.000002	-0.092585
C	1.403520	-1.212678	-0.038139
C	2.787007	-1.204523	0.074545
H	4.555101	0.000007	0.215595
H	3.325439	2.143466	0.118683
H	0.860016	2.148078	-0.080840
H	0.860022	-2.148082	-0.080778
H	3.325445	-2.143458	0.118741
I	-1.375195	-0.000008	-0.251121
O	-1.946571	0.000049	1.545441

IV.4.4 Determination of K_{eq} for HFIP binding to **4.1**

To determine the K_{eq} for the formation of **4.1**·HFIP an NMR tube was charged with $CDCl_3$ (0.50 mL), 2-(*tert*-butylsulfonyl)iodosylbenzene (**4.1**, 5.0 mg, 0.015 mmol, 1.0 equiv) and mesitylene (2.0 μ L, 0.014 mmol). The sample was allowed to equilibrate in the magnet for 5 min before the 1H NMR spectrum was recorded, and the spectrum was remeasured to ensure that equilibrium had been reached. Then HFIP was added incrementally (1.0 μ L, 0.095 mmol portions) via 10 μ L syringe. Data was collected at 22.9 °C. The temperature of the NMR cavity was measured using an ethylene glycol standard. Recorded spectra are collected below.

The equilibrium constant for adduct formation between **4.1** and HFIP was calculated from Eqn 1²⁵⁵

$$K_{eq} = \frac{\Delta\delta_{obs}}{(\Delta\delta_{CA} - \Delta\delta_{obs})\left([HFIP] - \frac{[4.1]\Delta\delta_{obs}}{\Delta\delta_{CA}}\right)} \quad (1)$$

where

$\Delta\delta_{obs}$ = difference between the starting material and the spectrum acquired with HFIP and

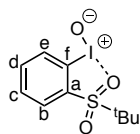
$\Delta\delta_{CA}$ = change in chemical shift between the completely complexed and uncomplexed molecule.

$\Delta\delta_{CA}$ was determined by plugging in values for two measurements into equation 1 and setting them equal to each other. This was repeated for multiple measurements to ensure the consistency of the value. $\Delta\delta_{CA}$ was determined to be 0.116 ppm. K_{eq} was then

calculated individually for 9 different concentrations of HFIP. It was found that $K_{eq} = 0.0375 \pm 0.004$ and that $\Delta G = 1.94 \pm 0.06$ kcal/mol.

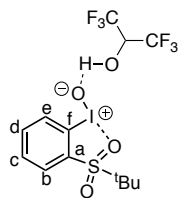
The K_{eq} for HFIP binding to **1** was also determined via the BindFit program provided by supramolecular.org using the Nelder-Mead method ($K_{eq} = 0.032 \pm 0.003$). ^1H and ^{13}C assignments for **4.1** and **4.1**·HFIP are shown in **Tables IV-5-6**.

Table IV-5 ^{13}C and ^1H assignments for **4.1**.



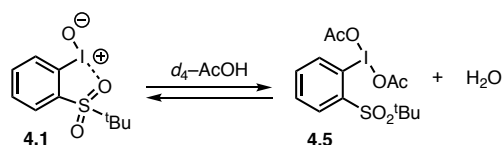
Atom	^{13}C	^1H
a	132.1	--
b	127.3	8.11
c	129.8	7.64
d	135.6	7.90
e	132.8	7.86
f	117.8	--

Table IV-6 ^{13}C and ^1H Assignments for **4.1**·HFIP.



Atom	^{13}C	^1H
a	131.0	--
b	131.6	7.89
c	125.0	7.76
d	137.3	8.00
e	133.7	7.94
f	115.0	--

IV.4.5 Addition of Acetic Acid to 2-(*tert*-Butylsulfonyl)iodosylbenzene (**4.1**)



An NMR-tube was charged with 2-(*tert*-butylsulfonyl)iodosylbenzene (**4.1**, 4.6 mg, 0.014 mmol, 1.00 equiv) and CDCl₃ (0.50 mL), which was passed through a plug of solid NaHCO₃ before being added to the NMR tube. The ¹H NMR spectrum was recorded (**Figure IV-21a**). To this NMR sample, glacial acetic acid (5.00 μL, 0.0874 mmol, 6.24 equiv) was added and the ¹H NMR spectrum was recorded (**Figure IV-21b**).

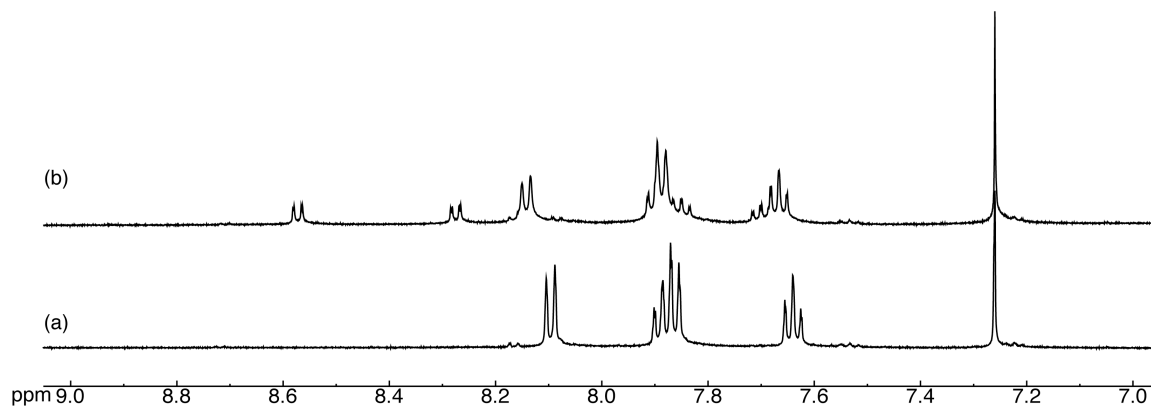


Figure IV-21 Reaction of 2-(*tert*-butylsulfonyl)iodosylbenzene with acetic acid. ¹H NMR spectra of **4.1** collected in CDCl₃ at 23 °C (a) before and (b) after addition of 6.24 equiv of acetic acid.

IV.4.6 Analysis of Impurities in 4.1

EPR Spectrum of 2-(*tert*-butylsulfonyl)iodosylbenzene (4.1) Prepared Using Method B in the Presence of PBN A 20-mL scintillation vial was charged with CDCl_3 (0.50 mL) and 2-(*tert*-butylsulfonyl)iodosylbenzene (**4.1**, 4.7 mg, 0.013 mmol, 1.0 equiv) prepared using Method B. PBN (5.2 mg, 0.029 mmol, 2.5 equiv) was added after 5 min. The reaction mixture was shaken and kept at 23 °C for 3-5 min. The resulting solution was injected into a 2 mm EPR tube and the EPR spectrum in **Figure IV-22** was acquired at 23 °C.

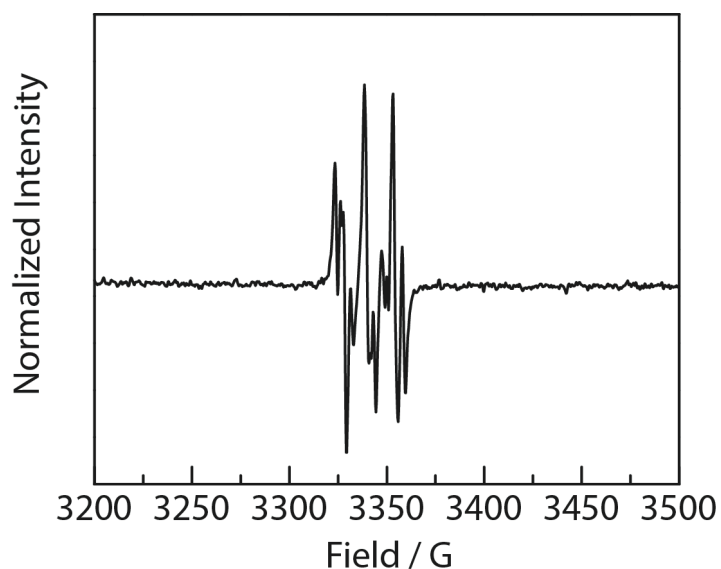


Figure IV-22 EPR spectrum obtained following PBN addition to 2-(*tert*-butylsulfonyl)iodosylbenzene prepared by Method B.

Dependence of EPR Signal Intensity on Light for 2-(*tert*-butylsulfonyliodosyl)benzene (4.1) Prepared Using Method B The following procedure was carried out in a closed room with lights turned-off and all the sample containers were first wrapped with black electrical tape and then with aluminum foil. The EPR tube was covered with aluminum foil until loaded into the probe. An electrical tape- and aluminum foil-wrapped 20-mL scintillation vial was charged with CDCl_3 (0.50 mL), and 2-(*tert*-butylsulfonyliodosyl)benzene (4.1, 4.8 mg, 0.014 mmol, 1.0 equiv) prepared using Method B. To this, PBN (5.3 mg, 0.029 mmol, 2.1 equiv) was added after 5 min, shaken well and let to stand for 3-5 min. The resulting solution was injected into a 2 mm EPR tube and the EPR spectrum was acquired at 23 °C. These data are shown in **Figure IV-13**.

EPR Spectrum of KClO_3 in the Presence of PBN A 20-mL scintillation vial was charged with CDCl_3 (0.50 mL) and KClO_3 (2.1 mg, 0.017 mmol, 1.0 equiv). To this PBN (5.7 mg, 0.032 mmol, 1.9 equiv) was added after 5 min. The reaction mixture was shaken and kept at 23 °C for 3-5 min. The resulting solution was injected into a 2 mm EPR tube, and the following EPR spectrum was acquired after 5 min at 23 °C. This data is shown in **Figure IV-14**.

EPR Spectrum of 2-(*tert*-butylsulfonyliodosyl)benzene (4.1) Prepared Using Method D in the Presence of PBN A 20-mL scintillation vial was charged with CDCl_3 (0.50 mL) and 2-(*tert*-butylsulfonyl)iodosylbenzene (**4.1**, 4.2 mg, 0.012 mmol, 1.0 equiv) prepared using Method D. To this solution, PBN (5.7 mg, 0.032 mmol, 2.7 equiv) was added after 5 min. The reaction mixture was shaken and kept at 23 °C for 3-5 min. The resulting solution was injected into a 2 mm EPR tube and the following EPR spectrum was acquired at 23 °C (**Figure IV-23**).

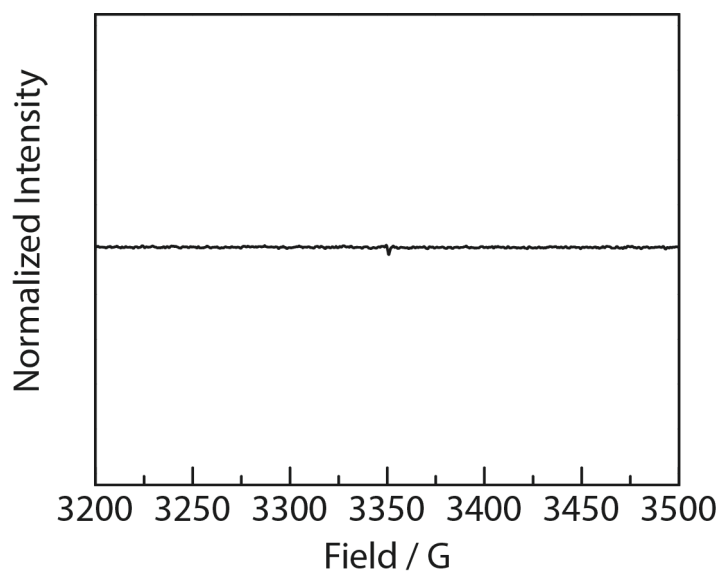


Figure IV-23 EPR spectrum obtained following PBN additions to 2-(*tert*-butylsulfonyl)iodosylbenzene prepared by Method D.

Dependence of Intensity of EPR Signal on Light To further corroborate that the EPR signal observed for **4.1** prepared by Method B is due to the presence of KClO_3 , we have also examined the light sensitivity of the EPR signal obtained following PBN addition to **4.1** (prepared by Method D) with KClO_3 added. Under these conditions, the intensity of EPR signal was also found to be dependent on light.

The following procedure was carried out under ambient light for both preparation and handling of the sample. A 20-mL scintillation vial was charged with CDCl_3 (0.50 mL), PBN (6.0 mg, 0.033 mmol, 2.8 equiv), and 2-(*tert*-butylsulfonyl)iodosylbenzene (**4.1**, 4.9 mg, 0.014 mmol, 1.0 equiv) prepared using Method D. To this, KClO_3 (3.6 mg, 0.029 mmol, 2.1 equiv) was added, the reaction mixture was shaken well, and let to stand for 3-5 min. The resulting solution was injected into a 2 mm EPR tube and the EPR spectrum was acquired at 23 °C (**Figure IV-24**)

The following procedure was carried out in a closed room with lights turned-off and all the sample containers were first wrapped with black electrical tape and then with aluminum foil. The EPR tube was wrapped in aluminum foil before loaded into the probe. An electrical tape and aluminum-foil wrapped 20-mL scintillation vial was charged with CDCl_3 (0.50 mL), PBN (5.7 mg, 0.032 mmol, 2.6 equiv) and 2-(*tert*-butylsulfonyl)iodosylbenzene (**4.1**, 4.6 mg, 0.013 mmol, 1.0 equiv) prepared using Method D. To this, KClO_3 (3.9 mg, .032 mmol, 2.5 equiv) was added after 5 min, shaken well, and let to stand for 3-5 min. The resulting solution was injected into a 2 mm EPR tube and the EPR spectrum was acquired at 23 °C (**Figure IV-24**).

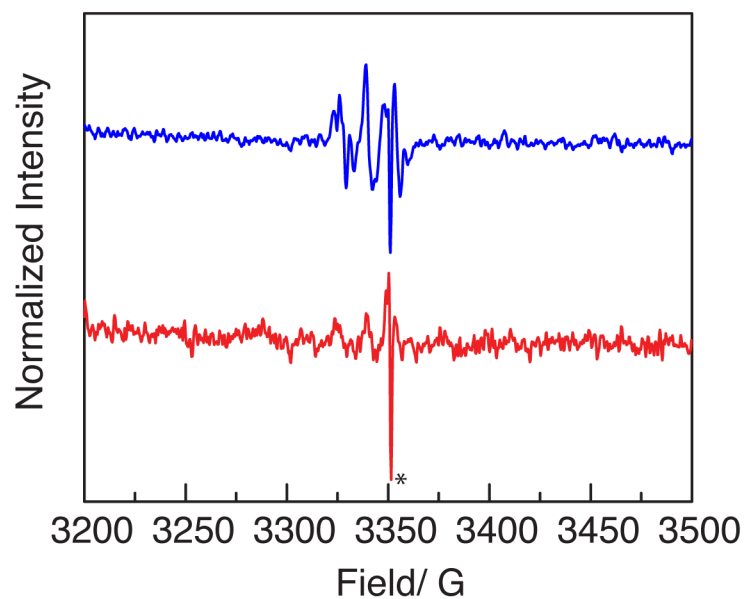
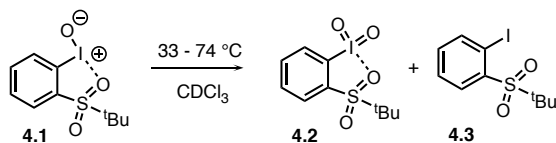


Figure IV-24 Light sensitivity of 2-(*tert*-butylsulfonyl)iodosylbenzene upon addition of KClO_3 . Comparison of EPR spectra obtained following PBN addition to **4.1** prepared by Method D with KClO_3 added under ambient light (—) and with the exclusion of light (—) (sample wrapped in electrical tape and aluminum foil). The peak at 3351 G is due to an impurity in the background of the resonator (*)

IV.4.7 Kinetics of Disproportionation of 4.1



General Procedure for Measuring Disproportionation Kinetics An NMR tube was charged with CDCl₃ (0.50 mL), 2-(*tert*-butylsulfonyl)iodosylbenzene (**4.1**, 5.0 mg, 0.015 mmol, 1.0 equiv), and mesitylene (2.0 μL, 0.014 mmol). The sample was allowed to equilibrate with a pre-heated NMR spectrometer for 90 s before the ¹H NMR spectrum was recorded. The rate of disproportionation was monitored via ¹H NMR at 74.0, 71.3, 58.2, 47.8, and 33.2 °C. Concentration vs. time plots were generated using the integrated intensities of peaks at 8.37 ppm (d, *J* = 7.8 Hz, 1H) for 2-(*tert*-butylsulfonyl)iodosylbenzene (**4.1**), 8.72 ppm (d, *J* = 8.9 Hz, 1H) for 2-(*tert*-butylsulfonyl)iodylbenzene (**4.2**), and 7.53 ppm (t, *J* = 8.3 Hz, 1H) for 2-(*tert*-butylsulfonyl)iodobenzene (**4.3**). The temperature of the NMR instrument was measured using an ethylene glycol standard. Data and plots demonstrating fits for a second order reaction are collected below (**Figure IV-25**).

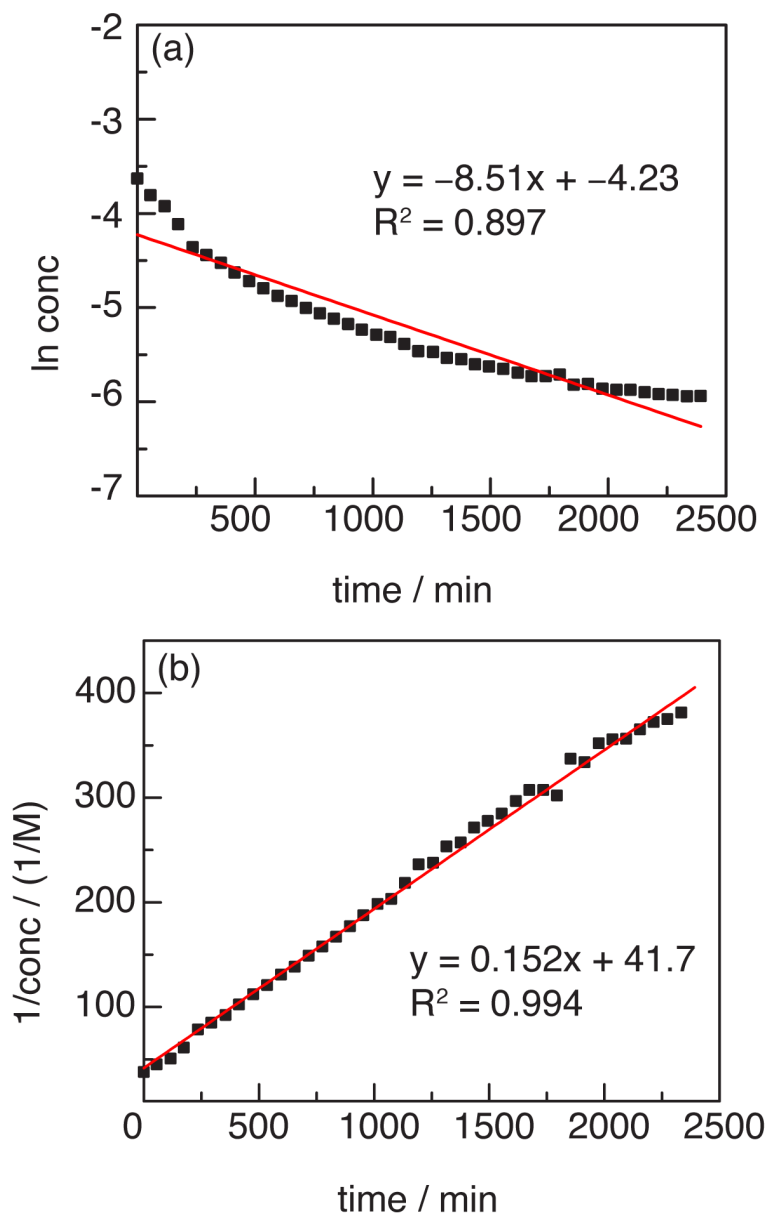


Figure IV-25 Comparison of first and second order fits for disproportionation of 2-(*tert*-butylsulfonyl)iodosylbenzene. Plots of (a) $\ln([4.1]^{-1})$ vs. time and (b) $[4.1]^{-1}$ vs. time for the disproportionation of **4.1**. These plots are consistent with a second-order disproportionation and are inconsistent with a first-order mechanism

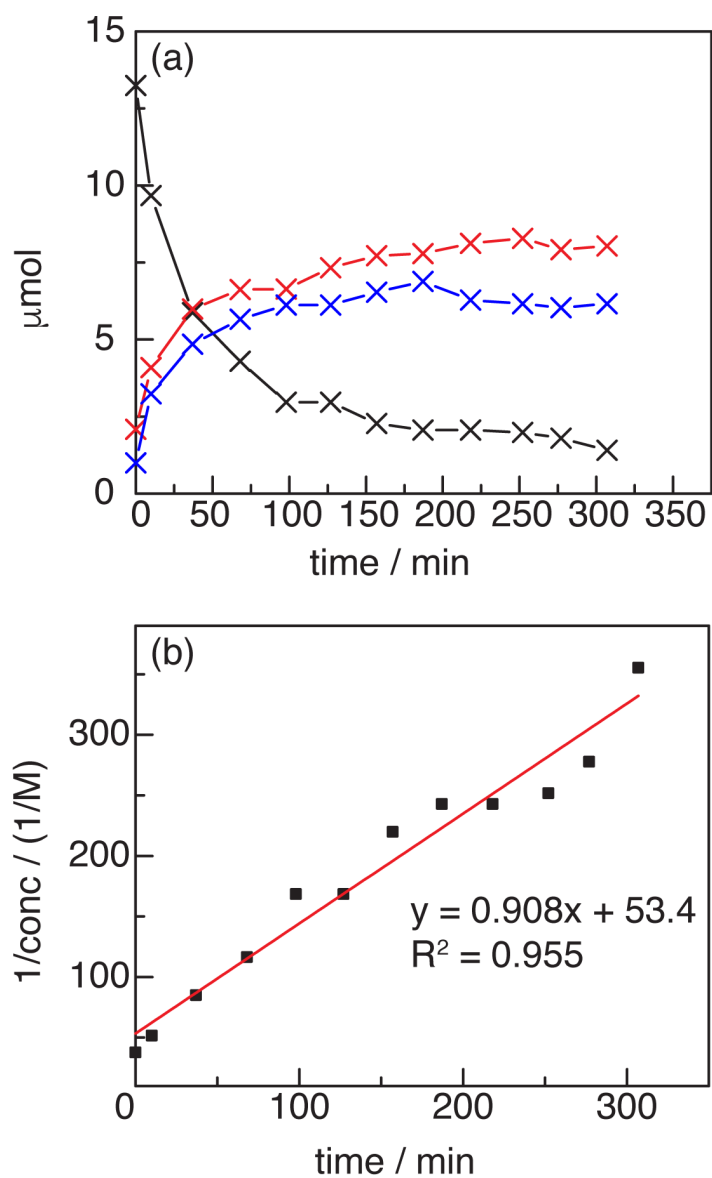


Figure IV-26 Disproportionation of 2-(*tert*-butylsulfonyl)iodosylbenzene at 74.0 °C.(a) Concentration vs. time plot of 2-(*tert*-butylsulfonyl)iodosylbenzene (**4.1**, ×), 2-(*tert*-butylsulfonyl)iodobenzene (**4.3**, ×), and 2-(*tert*-butylsulfonyl)iodyllbenzene (**4.2**, ×) for the disproportionation of **4.1** at 74.0 °C in CDCl_3 . (b) Plot of $[\mathbf{1}]^{-1}$ vs. time for the disproportionation of **4.1**.

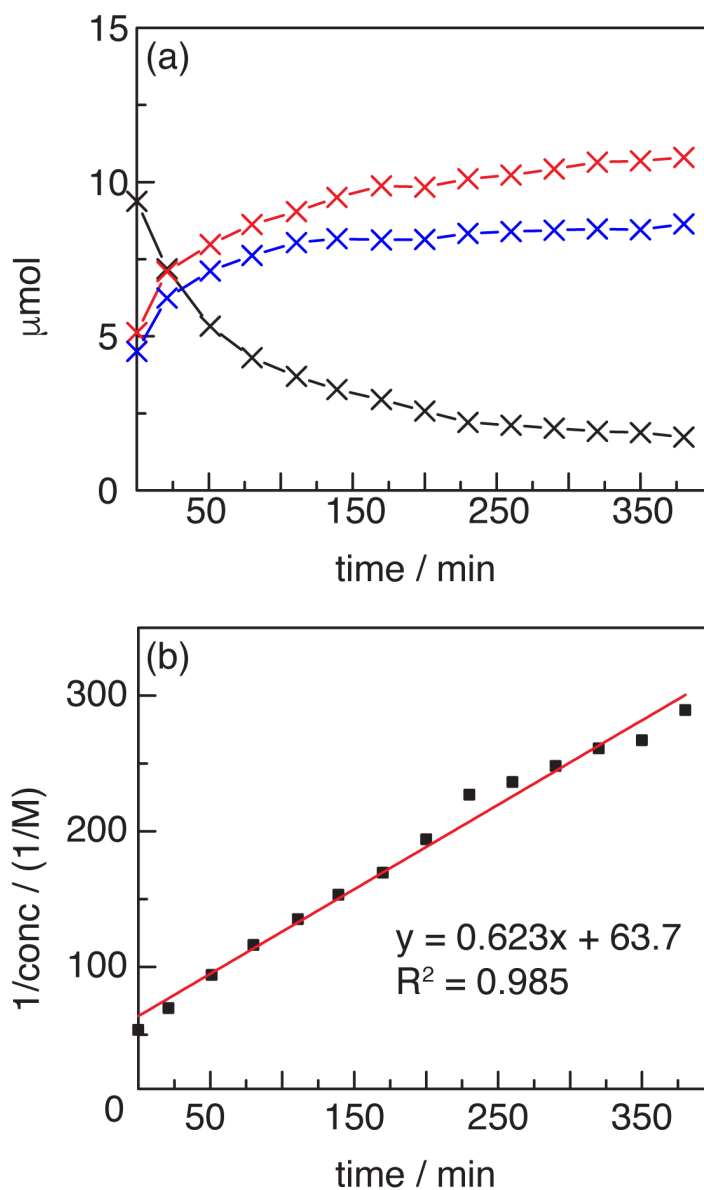


Figure IV-27 Disproportionation of 2-(*tert*-butylsulfonyl)iodosylbenzene at 71.3 °C.(a) Concentration vs. time plot of 2-(*tert*-butylsulfonyl)iodosylbenzene (**4.1**, ×), 2-(*tert*-butylsulfonyl)iodobenzene (**4.3**, ×), and 2-(*tert*-butylsulfonyl)iodyllbenzene (**4.2**, ×) for the disproportionation of **4.1** at 71.3 °C in CDCl_3 . (b) Plot of $[\mathbf{4.1}]^{-1}$ vs. time for the disproportionation of **4.1**.

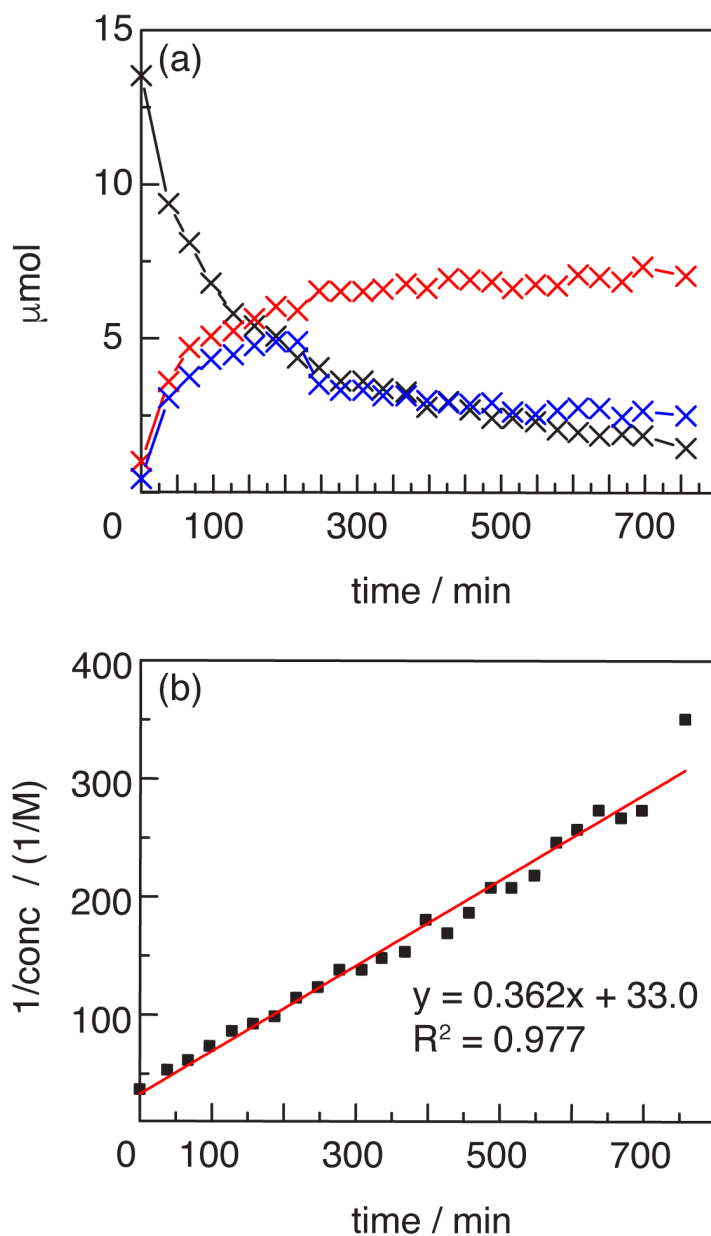


Figure IV-28 Disproportionation of 2-(*tert*-butylsulfonyl)iodosylbenzene at 58.2 °C.(a) Concentration vs. time plot of 2-(*tert*-butylsulfonyl)iodosylbenzene (**4.1**, ×), 2-(*tert*-butylsulfonyl)iodobenzene (**4.3**, ×), and 2-(*tert*-butylsulfonyl)iodyllbenzene (**4.2**, ×) for the disproportionation of **4.1** at 58.2 °C in CDCl_3 . (b) Plot of $[\mathbf{4.1}]^{-1}$ vs. time for the disproportionation of **4.1**.

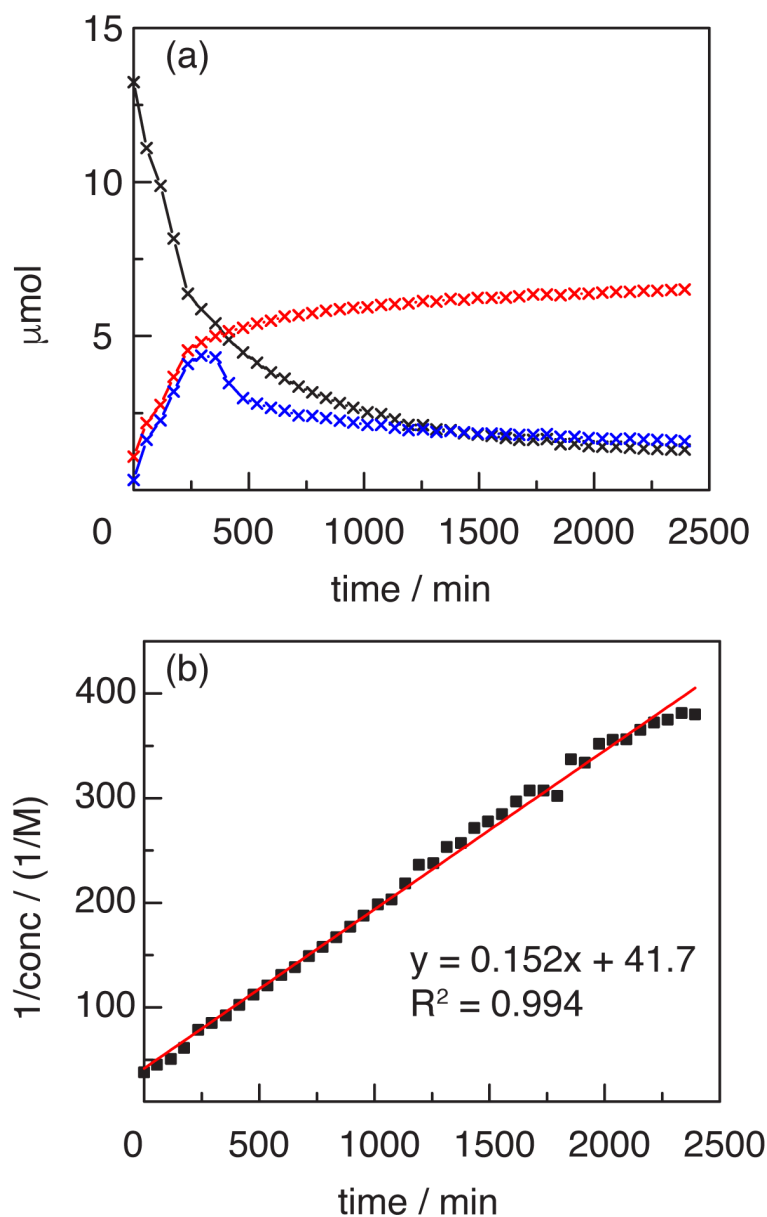


Figure IV-29 Disproportionation of 2-(*tert*-butylsulfonyl)iodosylbenzene at 47.8 °C.(a) Concentration vs. time plot of 2-(*tert*-butylsulfonyl)iodosylbenzene (**4.1**, ×), 2-(*tert*-butylsulfonyl)iodobenzene (**4.3**, ×), and 2-(*tert*-butylsulfonyl)iodyllbenzene (**4.2**, ×) for the disproportionation of **4.1** at 47.8 °C in CDCl_3 . (b) Plot of $[\mathbf{4.1}]^{-1}$ vs. time for the disproportionation of **4.1**.

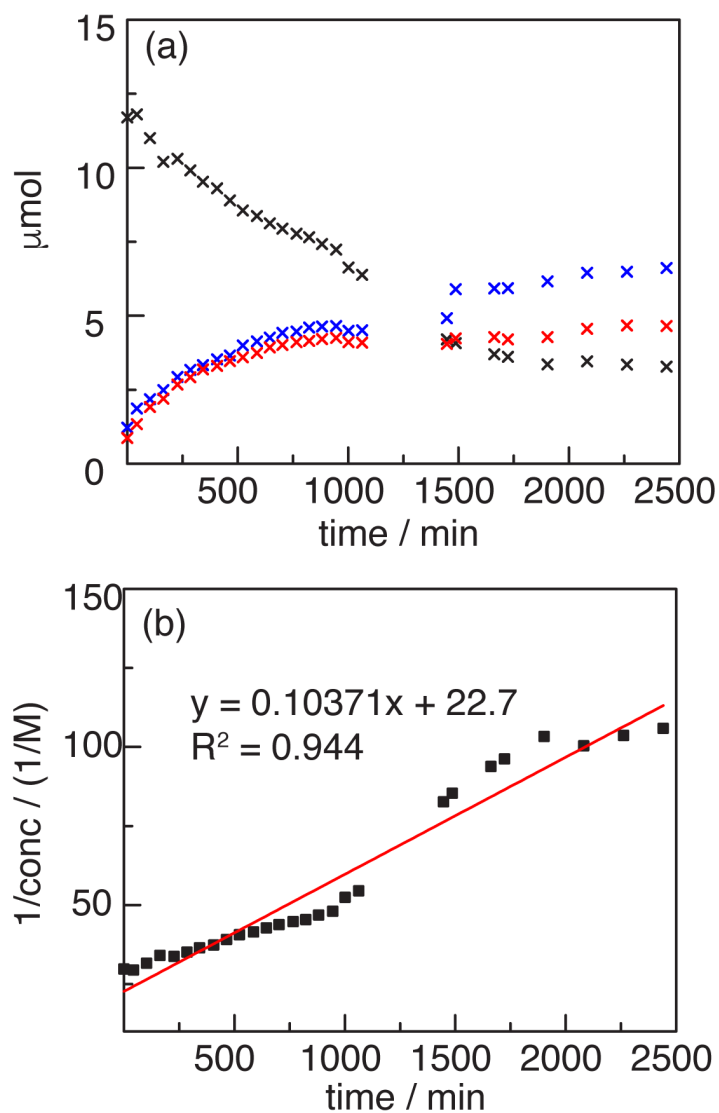


Figure IV-30 Disproportionation of 2-(*tert*-butylsulfonyl)iodosylbenzene at 32.2 °C. (a) Concentration vs. time plot of 2-*tert*-butylsulfonyliodosylbenzene (4.1, x), 2-*tert*-butylsulfonyliodobenzene (4.3, x), and 2-*tert*-butylsulfonyliodolbenzene (4.2, x) for the disproportionation of 4.1 at 32.2 °C in CDCl₃. (b) Plot of $[4.1]^{-1}$ vs. time for the disproportionation

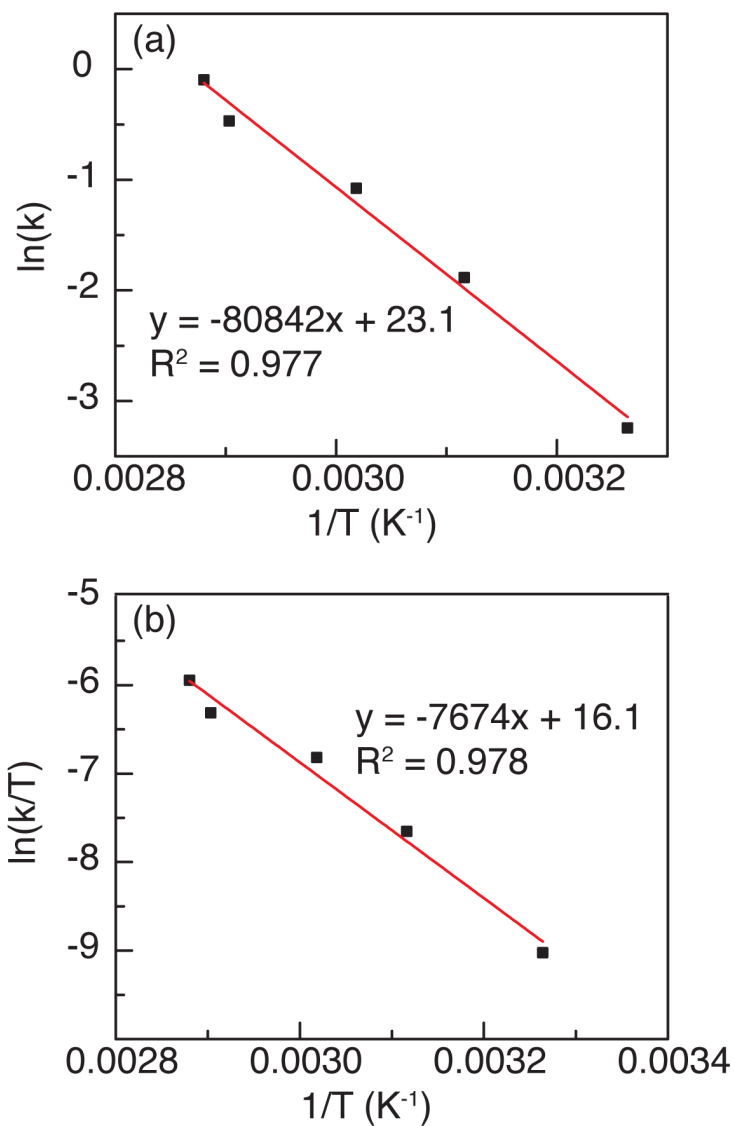


Figure IV-31 Summary of temperature-dependent disproportionation kinetics. Summary of obtained disproportionation rate data in the form of (a) Arrhenius and (b) Eyring plots, which allow for the calculation of E_a , ΔH^\ddagger , and ΔS^\ddagger .

Analysis of Arrhenius and Eyring Plots Plotting kinetics data in the form of an Arrhenius plot where $1/T$ vs. $\ln(k)$ allows for the extraction of the activation energy using Eqn 2:

$$\ln k = \frac{-E_a}{RT} + \ln A \quad (2)$$

where the slope of the line is equivalent to $\frac{-E_a}{RT}$. This gives an E_a value of 15.6 kcal mol⁻¹ for the disproportionation of **4.1**.

Plotting kinetics data in the form of an Eyring plot where $1/T$ vs. $\ln(k/T)$ allows for the extraction of ΔH and ΔS using Eqn 3:

$$\ln \frac{k}{T} = \frac{-\Delta H^\ddagger}{RT} + \ln \frac{k_b}{h} + \frac{\Delta S^\ddagger}{R} \quad (3)$$

where the slope of the line is equivalent to $\frac{-\Delta H^\ddagger}{R}$ and the y-intercept $\ln \frac{k_b}{h} + \frac{\Delta S^\ddagger}{R}$. Utilizing this equation gives a ΔS^\ddagger value of -15.2 cal K⁻¹ mol⁻¹ and a ΔH^\ddagger value 15.2 kcal mol⁻¹ for the disproportionation of **4.1**.

IV.4.8 Aerobic Oxidation of 2-(tert-Butylsulfonyl)iodobenzene (4.3)

Addition of acetaldehyde to 2-(tert-butylsulfonyl(diacetoxyiodo)benzene (4.5)

An NMR tube was charged with 2-*tert*-butylsulfonyliodosylbenzene (1, 10.8 mg, 0.0317 mmol, 1.00 equiv) and *d*₄-AcOH (0.50 mL) and a ¹H NMR spectrum was acquired (Figure IV-30a). To this solution acetaldehyde (10 μL, 0.18 mmol, 5.5 equiv) was added and the ¹H NMR spectrum was obtained (**Figure IV-32**).

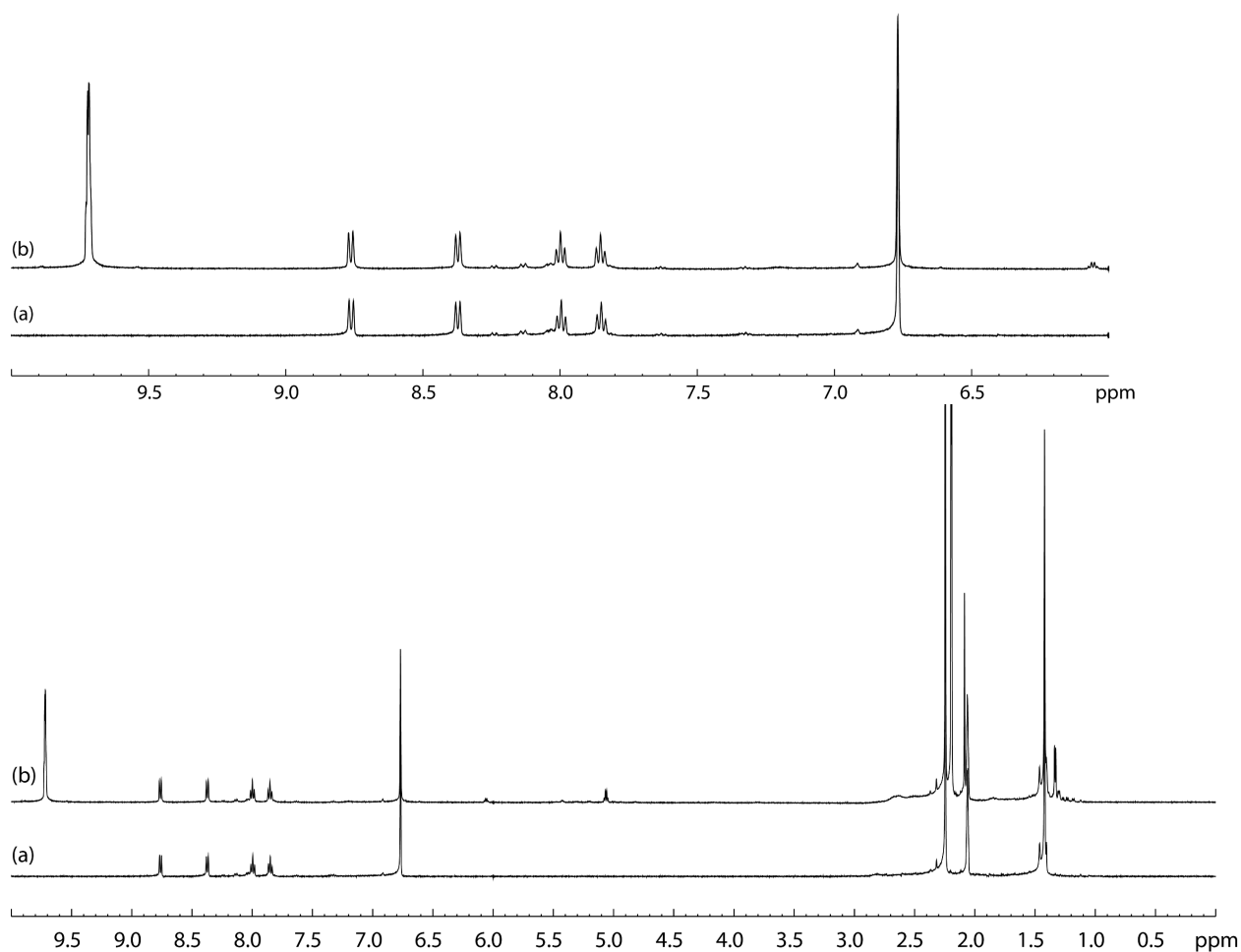


Figure IV-32 Exposure of 2-(tertbutylsulfonyl)(diacetoxyiodo)benzene to acetaldehyde. ¹H NMR spectra of (a) 2-(*tert*-butylsulfonyl)(diacetoxyiodo)benzene (**4.5**), (b) 2-(*tert*-butylsulfonyl)(diacetoxyiodo)benzene (**4.5**) following addition of acetaldehyde collected in *d*₄-AcOH at 23 °C. Top: expansion of the aromatic region; Bottom: full spectral range.

Addition of Co(II) to 2-(*tert*-butylsulfonyl)(diacetoxyiodo)benzene (4.5) An NMR tube was charged with 2-(*tert*-butylsulfonyl)iodosylbenzene (**4.1**, 4.6 mg, 0.012 mmol, 1.0 equiv) and d_4 -AcOH (0.50 mL) and a ^1H NMR spectrum was acquired (**Figure IV-33a**). To this solution CoCl_2 (0.3 mg, 8 mol%) was added and the ^1H NMR spectrum was obtained (**Figure IV-33b**).

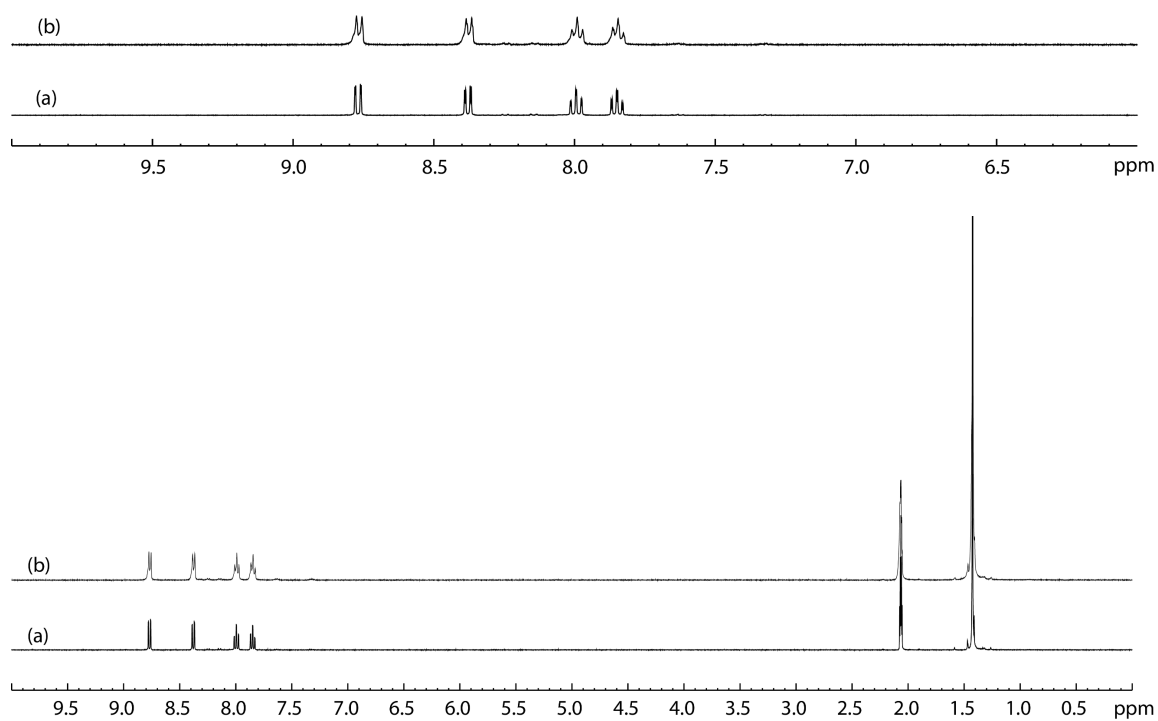


Figure IV-33 Exposure of 2-(*tert*butylsulfonyl)(diacetoxyiodo)benzene to CoCl_2 . ^1H NMR spectra of (a) 2-(*tert*-butylsulfonyl)(diacetoxyiodo)benzene (**4.5**), (b) 2-(*tert*-butylsulfonyl)(diacetoxyiodo)benzene (**4.5**) following addition of Co(II) collected in d_4 -AcOH at 23 °C. Top: expansion of the aromatic region; Bottom: full spectral range.

Addition of $\text{Co}(\text{OAc})_3$ to 2-(*tert*-butylsulfonyl)(diacetoxyiodo)benzene (**4.5**)

An NMR tube was charged with 2-(*tert*-butylsulfonyl)iodosylbenzene (**4.1**, 4.7 mg, 0.012 mmol, 1.0 equiv) and d_4 -AcOH (0.50 mL) and the ^1H NMR spectrum was acquired (Figure IV-32a). In a separate 8-mL scintillation vial, $\text{Co}(\text{OAc})_3$ was generated via addition of peracetic acid (32 wt%, 20 μL , 0.095 mmol, 0.99 equiv) to $\text{Co}(\text{OAc})_2 \cdot 4\text{H}_2\text{O}$ (24 mg, 0.096 mmol, 1.0 equiv) in d_4 -AcOH (0.50 mL). An aliquot of the $\text{Co}(\text{OAc})_3$ solution (50 μL , 0.0090 mmol, 0.79 equiv) was added to the NMR tube and corresponding ^1H NMR spectrum was obtained (Figure IV-34b).

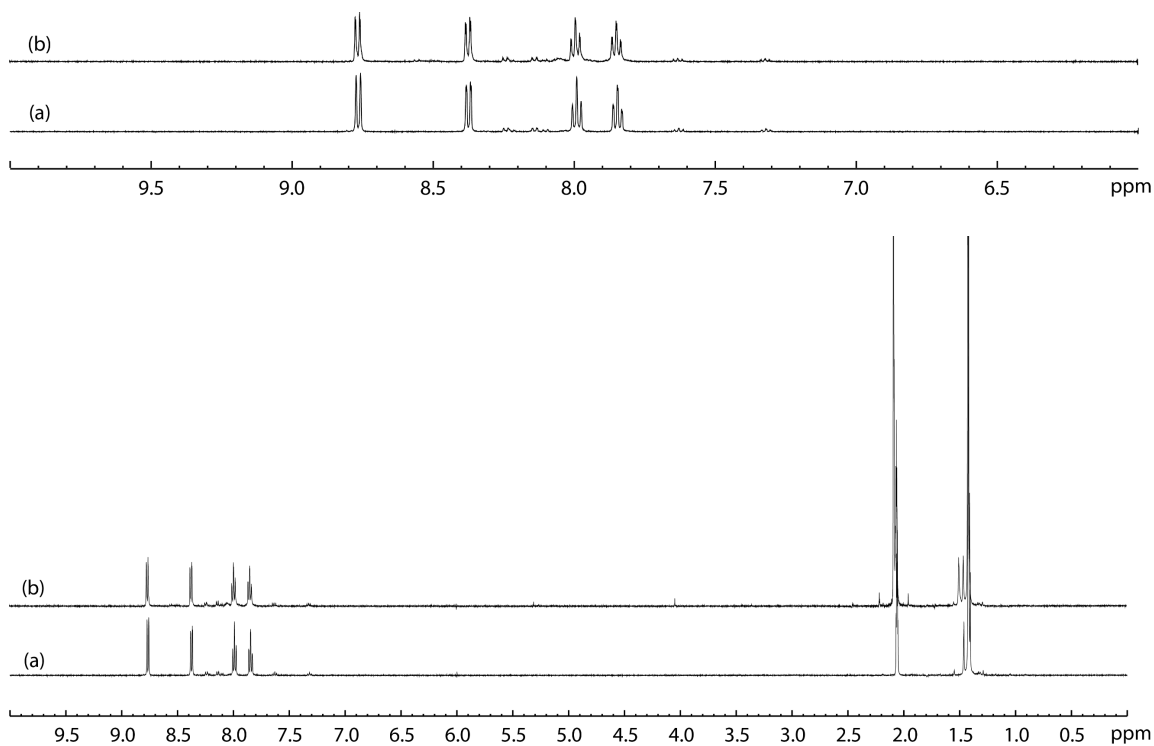
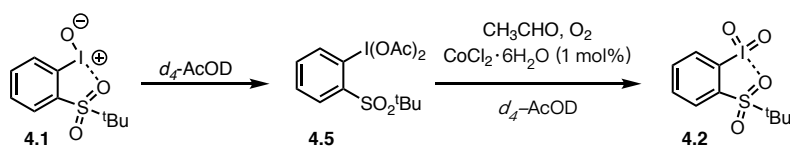


Figure IV-34 Exposure of 2-(*tert*-butylsulfonyl)(diacetoxyiodo)benzene to $\text{Co}(\text{OAc})_3$. ^1H NMR spectra of (a) 2-(*tert*-butylsulfonyl)(diacetoxyiodo)benzene (**4.5**) (b) 2-(*tert*-butylsulfonyl)(diacetoxyiodo)benzene (**4.5**) following addition of $\text{Co}(\text{OAc})_3$ collected in d_4 -AcOH at 23 $^\circ\text{C}$. Top: expansion of the aromatic region; Bottom: full spectral range.



Aldehyde promoted aerobic oxidation of 2-(*tert*-butylsulfonyl)(diacetoxyiodo)benzene (4.5) To synthesize 2-(*tert*-butylsulfonyl)(diacetoxyiodo)benzene (4.5) freshly prepared 2-(*tert*-butylsulfonyl)iodosylbenzene (4.1, 20 mg, 0.059 mmol, 1.0 equiv), prepared via Method D, was treated with d_4 -AcOH (1.0 mL). To this solution was added $\text{CoCl}_2 \cdot 6\text{H}_2\text{O}$ (0.50 mg, 3.5 mol%) and the reaction vessel was purged with O_2 for 5 min. Acetaldehyde (50.0 μL , 0.880 mmol, 14.1 equiv) was added to the reaction vessel and the reaction was stirred under 1 atm O_2 , delivered by inflated balloon, at 23 °C. The progress of the reaction was monitored via ^1H NMR and the corresponding kinetics data is plotted below with 1,2-dichloroethane (25 mg, 0.25 mmol) utilized as an internal standard. The concentrations of the reaction components were determined using the peaks at 8.37 ppm (d, $J = 7.9$ Hz, 1H) for 2-(*tert*-butylsulfonyl)(diacetoxyiodo)benzene (4.5), 8.73 ppm (d, $J = 8.0$ Hz, 2H) for 2-(*tert*-butylsulfonyl)iodylbenzene (4.2), and 7.32 ppm (t, $J = 7.5$ Hz, 1H) for 2-(*tert*-butylsulfonyl)iodobenzene (4.3). The data are summarized in **Figure IV-35**.

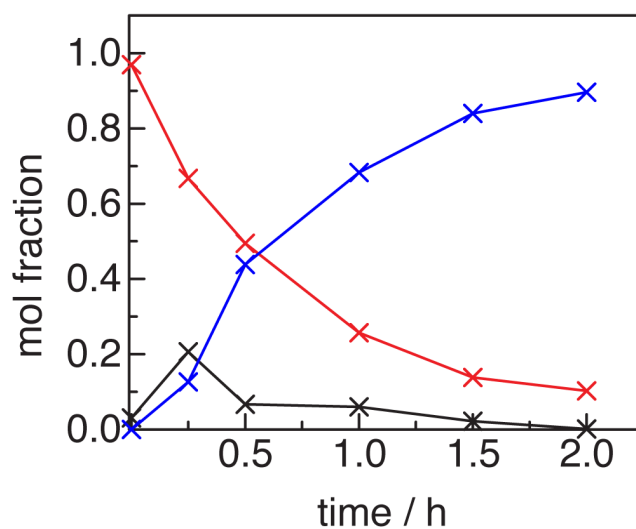
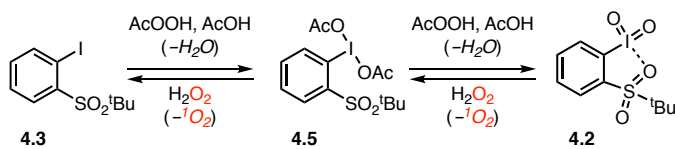


Figure IV-35 Aldehyde promoted aerobic oxidation of 2-(*tert*-butylsulfonyl)(diacetoxyiodo)benzene (4.5). Mol fraction of 2-(*tert*-butylsulfonyl)iodobenzene (4.3, ×), 2-(*tert*-butylsulfonyl)(diacetoxyiodo)benzene (4.5, ×) and 2-(*tert*-butylsulfonyliodol)benzene (4.2, ×) as a function of time for oxidation of 2-(*tert*-butylsulfonyl)(diacetoxyiodo)benzene (4.5) in d_4 -AcOH at 23 °C in presence of acetaldehyde and $\text{CoCl}_2 \cdot 6\text{H}_2\text{O}$.



Oxidation of 4.3 with Peracetic Acid An NMR tube was charged with *d*₄-AcOH (0.70 mL) and 2-(*tert*-butylsulfonyl)iodobenzene (**4.3**, 64 mg, 0.20 mmol, 1.0 equiv). The ¹H NMR spectrum was recorded. To the NMR solution, peracetic acid (32 wt%, 0.050 mL, 0.24 mmol, 1.2 equiv) was added. The reaction mixture was shaken, re-inserted into the NMR probe, and reaction progress was monitored via ¹H NMR. Data and spectra are collected in **Figure IV-36**. To plot the kinetics of the reaction the peak at 8.37 ppm (d, *J* = 7.9 Hz, 1H) for 2-(*tert*-butylsulfonyl)(diacetoxyiodo)benzene (**4.5**), the peak at 8.73 ppm (d, *J* = 8.0 Hz, 2H) for 2-(*tert*-butylsulfonyl)iodylbenzene (**4.2**) and the peak at 7.32 ppm (t, *J* = 7.5 Hz, 1H) for 2-(*tert*-butylsulfonyl)iodobenzene (**4.3**) were integrated. At each time point analyzed, the total mol fraction of all three components is taken to be 1 and the corresponding mol fraction for each individual component is represented as the contribution of that component to the mixture.

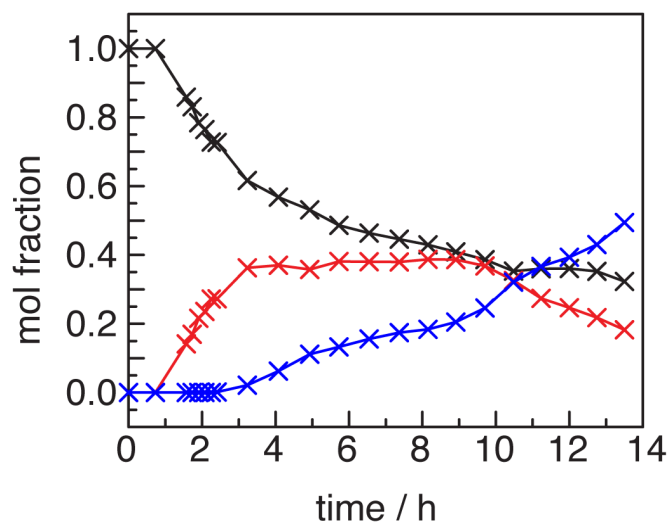
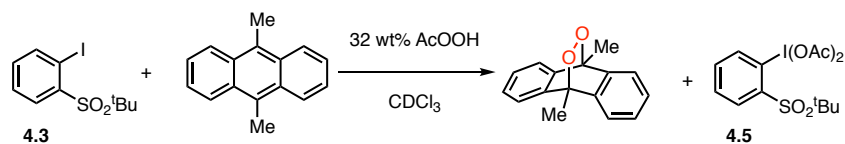


Figure IV-36 Oxidation of 2-(*tert*-butylsulfonyl)iodosylbenene with peracetic acid. Mol fraction of 2-(*tert*-butylsulfonyl)iodobenzene (**4.3**, ×), 2-(*tert*-butylsulfonyl)(diacetoxyiodo)benzene (**4.5**, ×) and 2-(*tert*-butylsulfonyl)iodylbenzene (**4.2**, ×) as a function of time for oxidation of 2-(*tert*-butylsulfonyl)iodobenzene (**4.3**) in *d*₄-AcOH at 23 °C.



Generation of ¹O₂ During Oxidation of 2-(*tert*-butylsulfonyl)iodobenzene (4.3)

with AcOOH Evolution of ¹O₂ during the oxidation of 2-(*tert*-butylsulfonyl)iodobenzene (4.3) with 32 wt% peracetic acid solution was evaluated by addition of 9,10-dimethylanthracene, a known ¹O₂ trap, according to a previously reported procedure.²²¹ A 20-mL scintillation vial was charged with CDCl₃ (2.0 mL), 2-(*tert*-butylsulfonyl)iodobenzene (4.3, 64.0 mg, 0.198 mmol, 1.98 equiv), and 9,10-dimethylanthracene (20.6 mg, 0.100 mmol, 1.00 equiv). Peracetic acid (32 wt%, 0.210 mL, 1.00 mmol, 10.0 equiv) was added to the reaction vessel and the reaction was sealed with a cap and stirred at 23 °C for 2 h. To remove the remaining AcOOH and H₂O₂, the reaction mixture was washed with H₂O (3 mL) and extracted with CH₂Cl₂ (2 × 2 mL). The combined organic layers were dried over anhydrous MgSO₄ and the solvent was removed under reduced pressure. Due to instability of 9,10-dimethyl-9,10-dihydro-9,10-epidioxyanthracene on SiO₂ and the similar solubility of 2-(*tert*-butylsulfonyl)iodobenzene (4.3) and 9,10-dimethyl-9,10-dihydro-9,10-epidioxyanthracene, 9,10-dimethyl-9,10-dihydro-9,10-epidioxyanthracene was not isolated. Characterization and quantification were carried out by comparison of the ¹H NMR spectrum of the crude reaction mixture with an authentic standard (Figure IV-37).

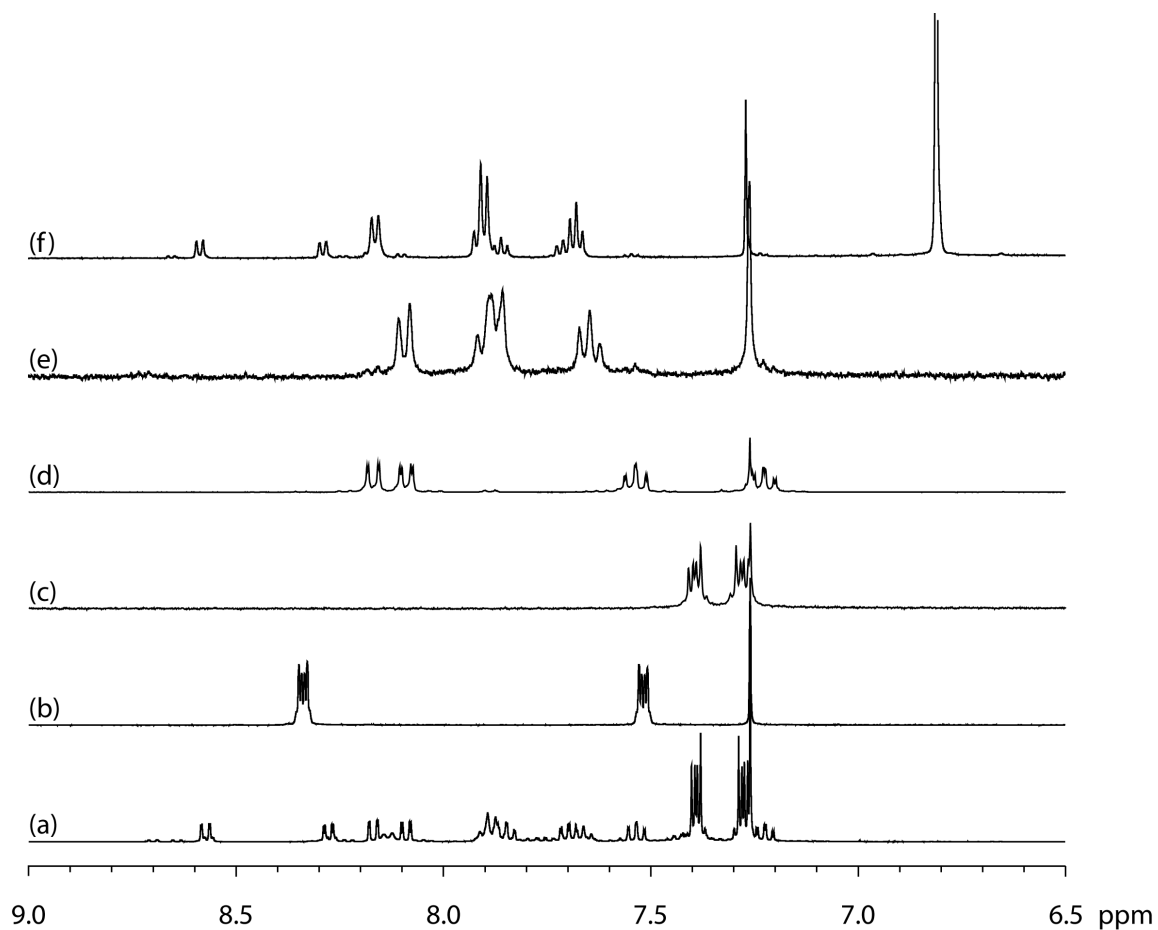
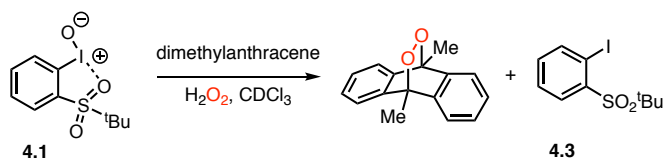


Figure IV-37 Generation of $^1\text{O}_2$ During Oxidation of 2-(*tert*-butylsulfonyl)iodobenzene with peracetic acid. ^1H NMR spectra in CDCl_3 of (a) the reaction mixture of **4.3**, (b) 9,10-dimethylantracene, (c) 9,10-dimethyl-4a,9,9a,10-tetrahydro-9,10-epidioxyanthracene, (d) 2-(*tert*-butylsulfonyl)iodobenzene (**4.3**), (e) 2-(*tert*-butylsulfonyl)iodosylbenzene (**4.1**) and (f) 2-(*tert*-butylsulfonyl)(diacetoxyiodo)benzene (**4.5**). Top: expansion of the aromatic region; Bottom: full spectral range.



Reduction of 2-*tert*-butylsulfonyliodosylbenzene (4.1) with H₂O₂ Evolution of ¹O₂ during the reduction of 2-*tert*-butylsulfonyliodosylbenzene (4.1) by H₂O₂ was evaluated by addition of 9,10-dimethylantracene, a known ¹O₂ trap, according to a previously reported procedure.²²¹ A 20-mL scintillation vial was charged with CDCl₃ (2.0 mL), 2-(*tert*-butylsulfonyl)iodosylbenzene (4.1, 68.0 mg, 0.200 mmol, 2.00 equiv), and 9,10-dimethylantracene (20.6 mg, 0.100 mmol, 1.00 equiv). H₂O₂ (30 wt%, 90 μL, 0.79 mmol, 7.9 equiv) was added to the reaction vessel and the reaction was sealed with a cap and stirred at 23 °C for 5 h. The resulting solution was dried over anhydrous MgSO₄. Due to instability of 9,10-dimethyl-9,10-dihydro-9,10-epidioxyanthracene on SiO₂ and the similar solubility of 2-(*tert*-butylsulfonyl)iodobenzene (4.3) and 9,10-dimethyl-9,10-dihydro-9,10-epidioxyanthracene, 9,10-dimethyl-9,10-dihydro-9,10-epidioxyanthracene was not isolated. Characterization and quantification were carried out by comparison of the ¹H NMR spectrum of the crude reaction mixture with an authentic standard (**Figure IV-38**).

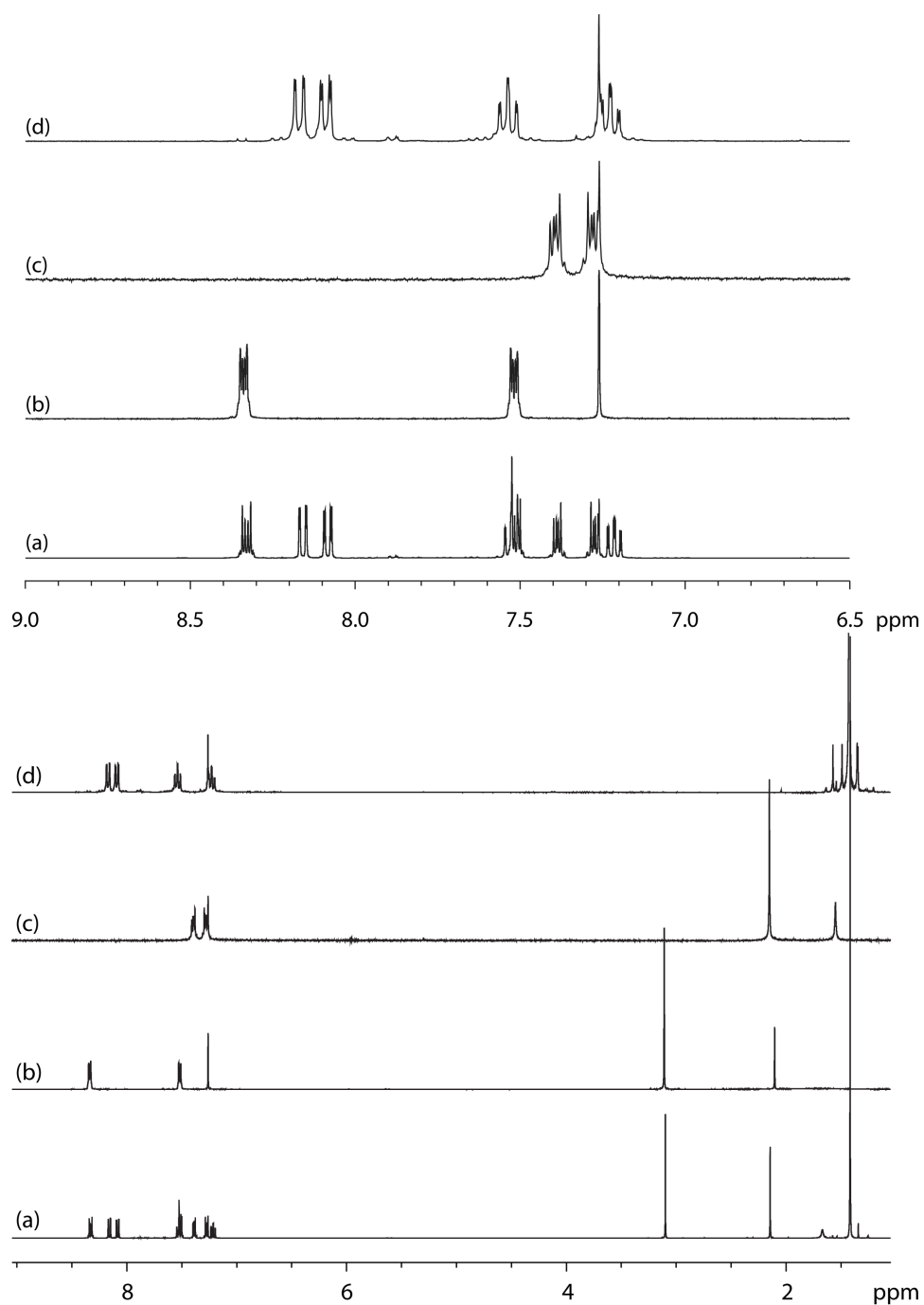
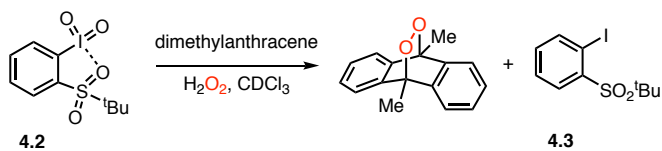


Figure IV-38 Reduction of 2-(*tert*-butylsulfonyl)iodobenzene with H₂O₂. ¹H NMR spectra (CDCl₃) of (a) the reaction mixture of **4.1**, (b) 9,10-dimethylanthracene, (c) 9,10-dimethyl-4a,9,9a,10-tetrahydro-9,10-epidioxyanthracene, and (d) 2-(*tert*-butylsulfonyl)iodobenzene (**4.3**). Top: expansion of the aromatic region; Bottom: full spectral range.



Reduction of 2-*tert*-butylsulfonyliodanylbenzene (2) with H₂O₂ Evolution of ¹O₂

during the reduction of 2-(*tert*-butylsulfonyl)iodylbenzene (**4.2**) by H₂O₂ was evaluated by addition of 9,10-dimethylantracene, a known ¹O₂ trap, according to a previously reported procedure.²²¹ A 20-mL scintillation vial was charged with CDCl₃ (2.0 mL), 2-(*tert*-butylsulfonyliodyl)benzene (**4.2**, 71.2 mg, 0.200 mmol, 2.00 equiv), and 9,10-dimethylantracene (20.6 mg, 0.100 mmol, 1.00 equiv). H₂O₂ (30 wt%, 90 μL, 0.79 mmol, 7.9 equiv) was added to the reaction vessel and the reaction was sealed with cap and stirred at 23 °C for 5 h. Due to instability of 9,10-dimethyl-9,10-dihydro-9,10-epidioxyanthracene on SiO₂ and the similar solubility of 2-(*tert*-butylsulfonyl)iodobenzene (**4.3**) and 9,10-dimethyl-9,10-dihydro-9,10-epidioxyanthracene, 9,10-dimethyl-9,10-dihydro-9,10-epidioxyanthracene was not isolated. Characterization and quantification were carried out by comparison of the ¹H NMR spectrum of the crude reaction mixture with an authentic standard (**Figure IV-39**).

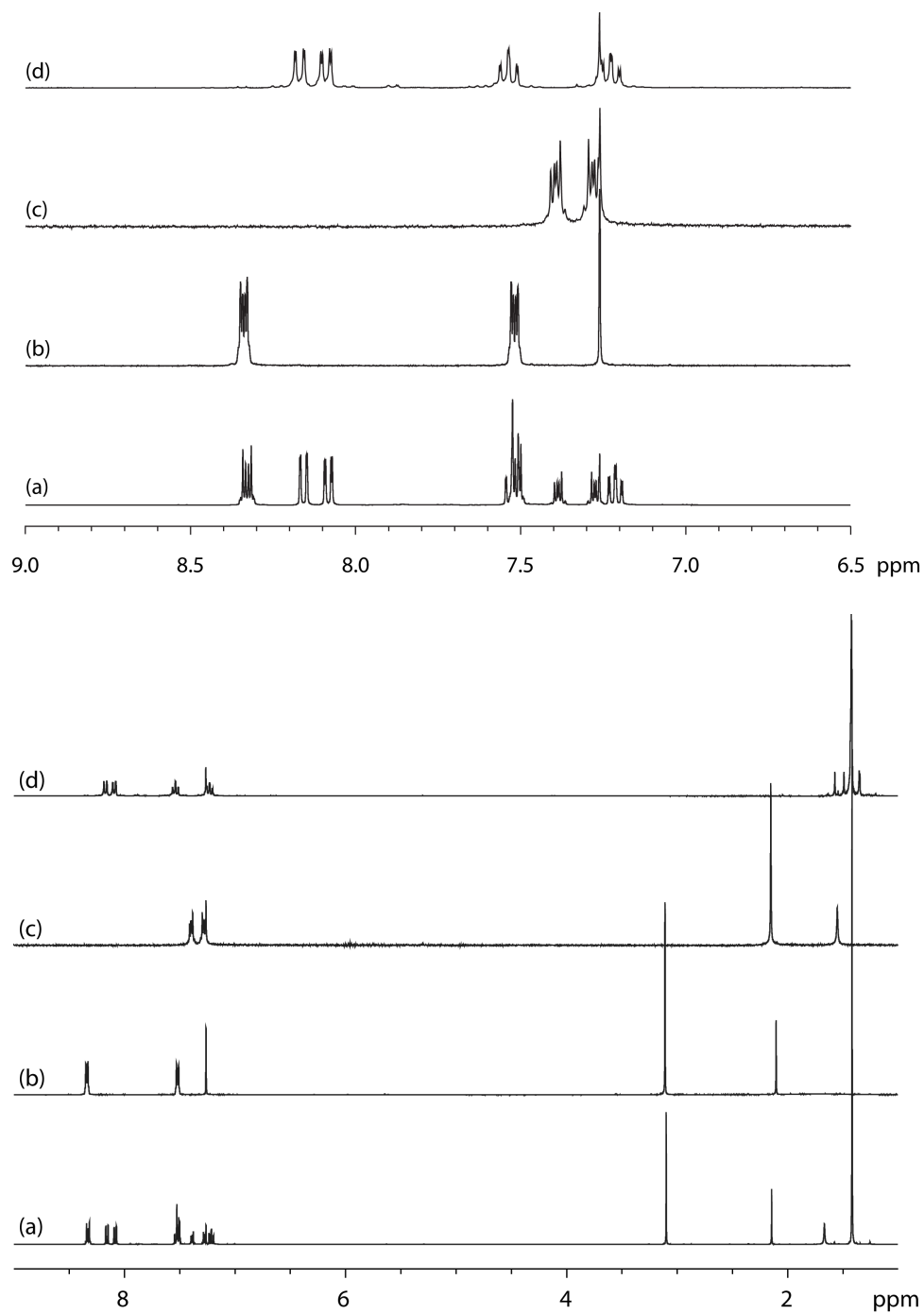
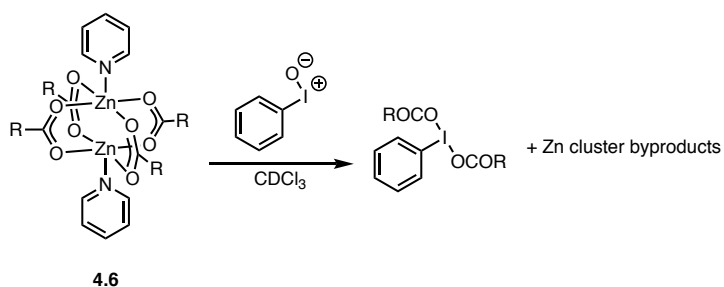


Figure IV-39 Reduction of 2-(*tert*-butylsulfonyl)iodobenzene (2) with H₂O₂. ¹H NMR spectra (CDCl₃) of (a) the reaction mixture of 4.2, (b) 9,10-dimethylanthracene, (c) 9,10-dimethyl-4a,9,9a,10-tetrahydro-9,10-epidioxyanthracene, and (d) 2-(*tert*-butylsulfonyl)iodobenzene (4.3). Top: expansion of the aromatic region; Bottom: full spectral range.

IV.4.9 Examination of Chemistry of Iodosylbenzenes with Soluble Metal Clusters



Reaction of Iodosylbenzene with $[\text{Zn}_2(\text{benzoate})_4\text{py}_2]$ (4.6) An NMR tube was charged with CDCl_3 (0.50 mL), iodosylbenzene (3.9 mg, 0.014 mmol, 1.3 equiv), and $[\text{Zn}_2(\text{OBz})_4\text{py}_2]$ (**4.6**, 14.0 mg, 0.0177 mmol, 1.0 equiv) and the sample was sonicated for 30 s producing a cloudy solution. The ^1H NMR spectrum was collected at 23 °C (**Figure IV-40**).

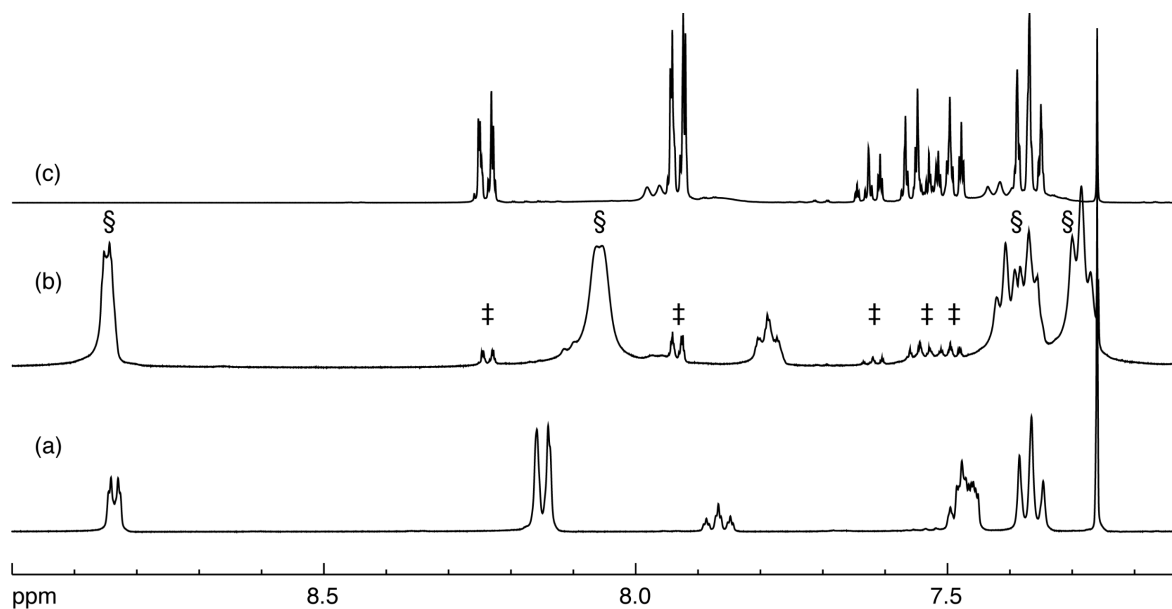
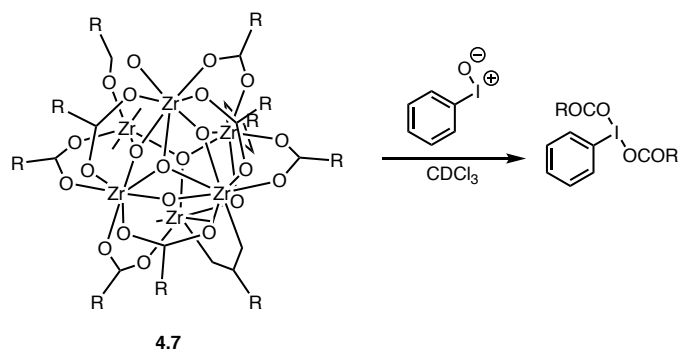


Figure IV-40 Reaction of iodobenzene with $[\text{Zn}_2(\text{benzoate})_4\text{py}_2]$. ^1H NMR spectra collected at 23 °C in CDCl_3 of (a) $[\text{Zn}_2(\text{OBz})_4\text{py}_2]$ (**4.6**), (b) crude reaction mixture of $[\text{Zn}_2(\text{OBz})_4\text{py}_2]$ (**4.6**) with iodobenzene, and (c) crude reaction mixture of iodobenzene with benzoic acid to produce iodobenzene dibenzoate. The crude reaction mixture (b) was found to contain iodobenzene dibenzoate (‡) and unidentified cluster byproducts (§).



Reaction of iodosylbenzene with $\text{Zr}_6\text{O}_4(\text{OH})_4(\text{OMc})_{12}$ An NMR tube was charged with CDCl_3 (0.50 mL), iodosylbenzene (3.0 mg, 0.014 mmol, 3.8 equiv), mesitylene (2.0 μL , 0.014 mmol), and $\text{Zr}_6\text{O}_4(\text{OH})_4(\text{OMc})_{12}$ (**4.7**, 6.3 mg, 0.0037 mmol, 1.0 equiv) and the sample was sonicated for 30 s producing a cloudy solution. The ^1H NMR spectrum was collected at 23 $^\circ\text{C}$ (**Figure IV-41**).

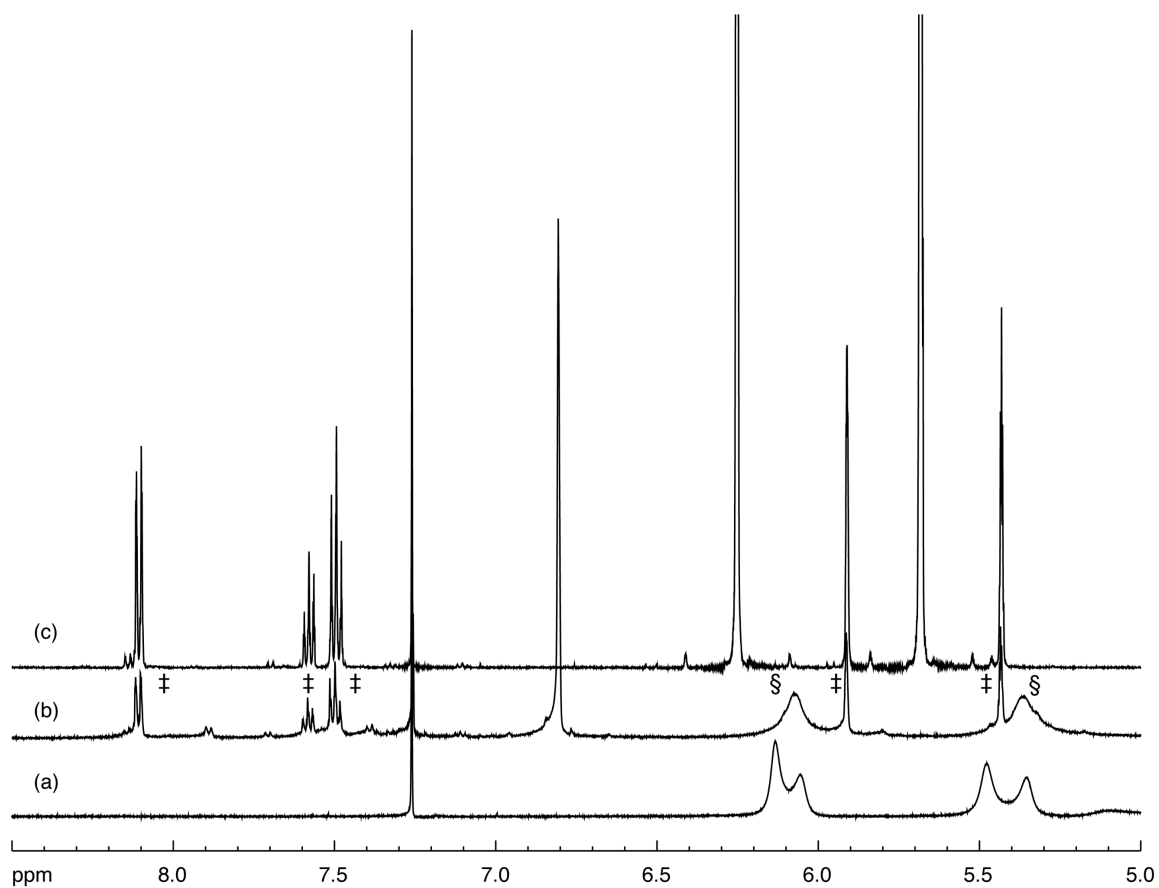
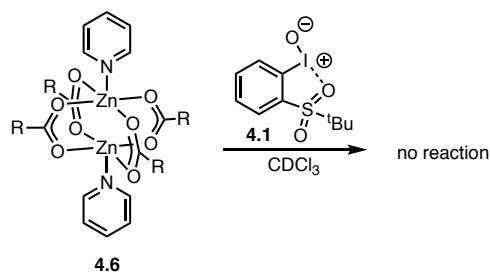


Figure IV-41 Reaction of iodobenzene with $\text{Zr}_6\text{O}_4(\text{OH})_4(\text{OMc})_{12}$. ^1H NMR spectra collected at 23 °C in CDCl_3 of (a) $\text{Zr}_6\text{O}_4(\text{OH})_4(\text{OMc})_{12}$ (**4.7**), (b) crude reaction mixture of $\text{Zr}_6\text{O}_4(\text{OH})_4(\text{OMc})_{12}$ (**4.7**) with iodobenzene, and (c) crude reaction mixture of iodobenzene with excess methacrylic acid. The crude reaction mixture (b) was found to contain iodobenzene dimethacrylate (‡) and unidentified cluster byproducts (§).



Reaction of 2-(*tert*-butylsulfonyl)iodosylbenzene with $[\text{Zn}_2(\text{benzoate})_4\text{py}_2]$ An NMR tube was charged with CDCl_3 (0.50 mL), 2-(*tert*-butylsulfonyl)iodosylbenzene (**4.1**, 5.0 mg, 0.015 mmol, 1.0 equiv), mesitylene (2.0 μL , 0.014 mmol), and $[\text{Zn}_2(\text{OBz})_4\text{py}_2]$ (**4.6**, 11.3 mg, 0.0147 mmol, 1.0 equiv). The ^1H NMR spectrum was collected at 23 $^\circ\text{C}$. Though a small shift in the NMR signals relating to 2-(*tert*-butylsulfonyl)iodosylbenzene (**4.1**) is observed, no peaks for iodobenzene dibenzoate are observed (**Figure IV-42**).

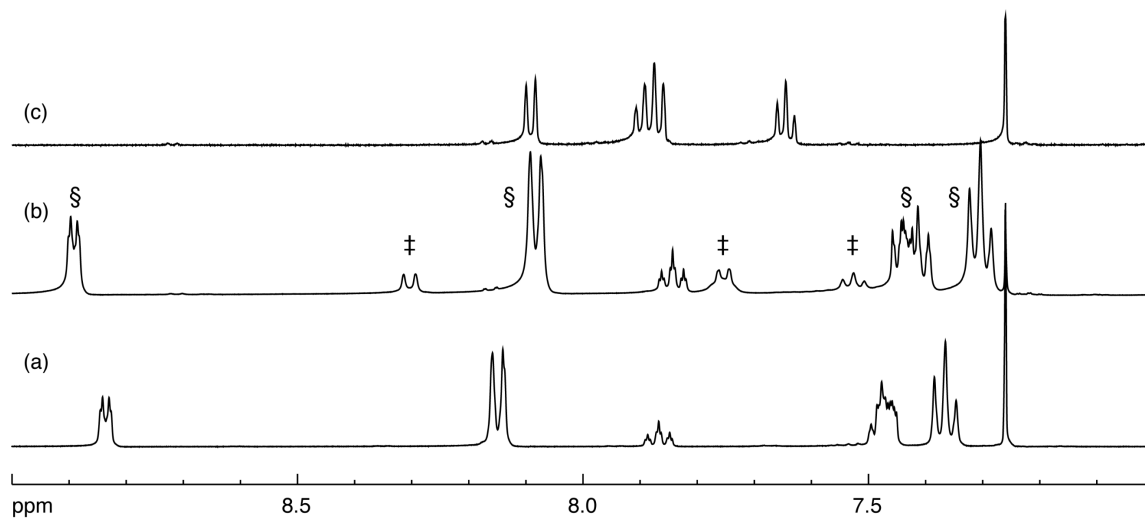
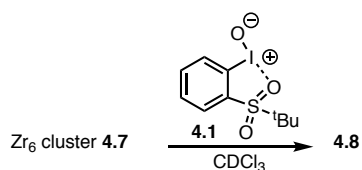


Figure IV-42 Reaction of 2-*tert*-butylsulfonyliodosylbenzene with [Zn₂(benzoate)₄py₂]. ¹H NMRs collected at 23 °C in CDCl₃ of (a) [Zn₂(benzoate)₄py₂] (**4.6**), (b) crude reaction mixture of [Zn₂(OBz)₄py₂] (**4.6**) with 2-(*tert*-butylsulfonyl)iodosylbenzene (**4.1**), and (c) 2-(*tert*-butylsulfonyl)iodosylbenzene (**4.1**). The crude reaction mixture (b) was found to contain **4.1** (‡) and [Zn₂(OBz)₄py₂] (§). The small changes in chemical shifts that is observed upon mixing **4.1** and **4.6** could not be reproduced by exposing **4.1** to each of pyridine, benzoic acid, or Zn(OAc)₂ individually.



Reaction of 2-(*tert*-butylsulfonyl)iodosylbenzene with $\text{Zr}_6\text{O}_4(\text{OH})_4(\text{OMc})_{12}$ An

NMR tube was charged with CDCl_3 (0.50 mL), 2-(*tert*-butylsulfonyl)iodosylbenzene (**4.1**, 5.0 mg, 0.015 mmol, 4.0 equiv), mesitylene (2.0 μL , 0.014 mmol), and $\text{Zr}_6\text{O}_4(\text{OH})_4(\text{OMc})_{12}$ (**7**, 6.3 mg, 0.0037 mmol, 1.0 equiv). The ^1H NMR spectrum was collected at 23 °C. ^1H NMR (δ , 23 °C, CDCl_3): 7.95–7.74 (br, 12H), 7.67–7.56 (br, 9H), 6.20–5.79 (br, 12H), 5.40–5.10 (br, 12H), 1.97–1.67 (br, 54H). Single crystals suitable for X-ray diffraction were obtained following addition of Et_2O (0.25 mL) to the solution utilized for ^1H NMR analysis and allowing the resulting sample to stand at 0 °C (**Figure IV-41**).

In addition to doing this synthesis on NMR scale, we have also isolated **4.8** from the following larger-scale reaction. A 20 mL vial was charged with CHCl_3 (4.0 mL), 2-(*tert*-butylsulfonyl)iodosylbenzene (**4.1**, 40.0 mg, 0.120 mmol, 4.11 equiv) and $\text{Zr}_6\text{O}_4(\text{OH})_4(\text{OMc})_{12}$ (**4.7**, 49.6 mg, 0.0292 mmol, 1.00 equiv) and stirred for 10 min. The solvent was removed in vacuo and the colorless, oily solid was triturated with Et_2O (4.5 mL) for 10 min. The Et_2O was decanted and the resulting solid was dried in vacuo to afford **4.8** as a white solid (28.0 mg, 31% yield) The ^1H NMR spectrum was collected at 23 °C. ^1H NMR (δ , 23 °C, CDCl_3): 8.80 (br, 2H), 7.90 (br, 2H) 7.90–7.55 (br, 16H), 6.20–5.79 (br, 10H), 5.40–5.10 (br, 14H), 1.95–1.60 (br, 67H), 1.47–1.30 (br, 52H).

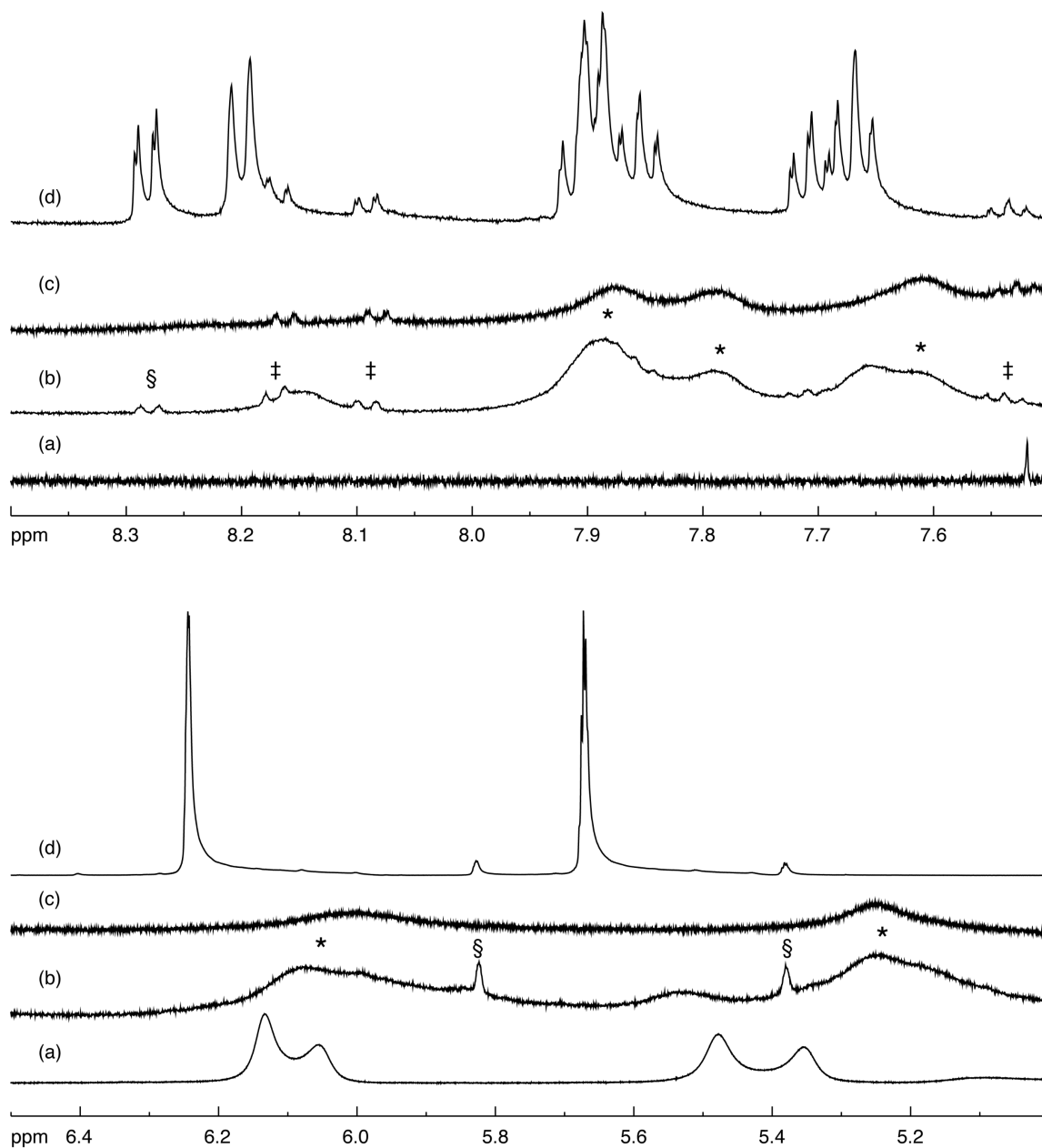


Figure IV-43 Reaction of 2-(*tert*-butylsulfonyl)iodosylbenzene with $\text{Zr}_6\text{O}_4(\text{OH})_4(\text{OMc})_{12}$. ¹H NMR spectra collected at 23 °C in CDCl_3 of (a) $\text{Zr}_6\text{O}_4(\text{OH})_4(\text{OMc})_{12}$, (b) crude reaction mixture of $\text{Zr}_6\text{O}_4(\text{OH})_4(\text{OMc})_{12}$ (**4.7**) with **4.1**, (c) dissolved single crystals of **4.8** adduct, and (d) crude reaction mixture of **1** with methacrylic acid. Top: expansion of the aromatic region; Bottom: expansion of the olefinic region. The crude reaction mixture (b) was found to contain trace 2-(*tert*-butylsulfonyl)(dimethacrylateiodo) benzene (§) (which arises from a methacrylic acid impurity in **4.7**, **4.3** (‡), and **4.8** adduct (*).

IV.4.10 Examination of Chemistry of Iodosylbenzenes with Metal-Organic Frameworks

Exposure of UiO-67 to 1 A 20-mL scintillation was charged with UiO-67 (0.101 g, 0.0476 mmol, 1.00 equiv), **4.1** (16.4 mg, 0.0482 mmol, 1.00 equiv), and CHCl₃ (2.0 mL). After stirring at 23 °C for 24 h, the sample was washed with CHCl₃ (2 × 6 mL) and MeOH (3 × 6 mL). The PXRD pattern was collected of the solid.

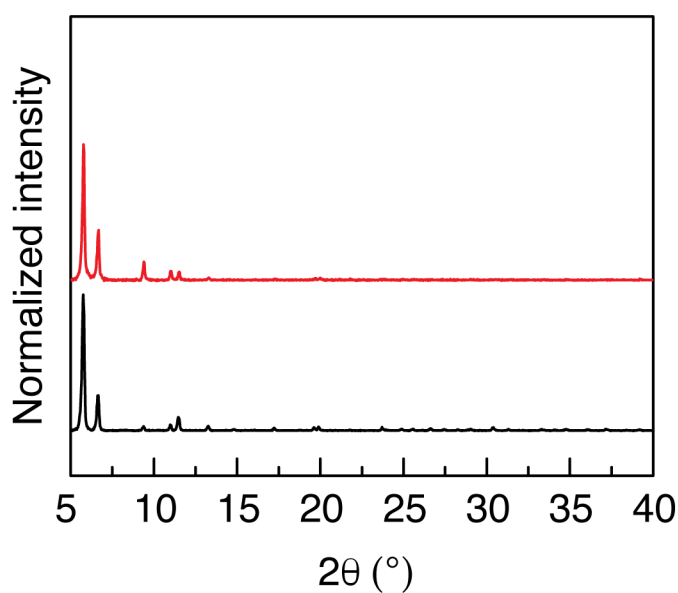


Figure IV-44 Exposure of UiO-67 to 2-(*tert*-butylsulfonyl)iodosylbenzene. PXRD patterns collected of UiO-67 (—) and following exposure of UiO-67 to **4.1** (—).

Exposure of UiO-67 to Iodosylbenzene A 20-mL scintillation was charged with UiO-67 (0.100 g, 0.0472 mmol, 1.00 equiv), iodosylbenzene (10.6 mg, 0.0482 mmol, 1.02 equiv), and CHCl_3 (2.0 mL). After stirring at 23 °C for 16 h, the PXRD pattern was collected of the reaction mixture.

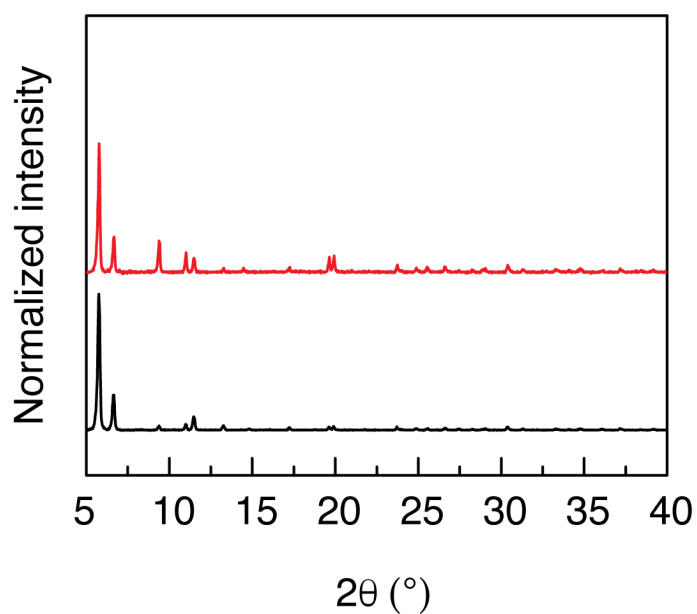


Figure IV-45 Exposure of UiO-67 to iodosylbenzene. PXRD patterns collected of UiO-67 (—) and UiO-67 following exposure to iodosylbenzene (—).

Exposure of MOF-508b to 4.1 A 20-mL scintillation was charged with MOF-508b (0.100 g, 0.150 mmol, 1.00 equiv), **4.1** (51.0 mg, 0.150 mmol, 1.00 equiv), and CHCl_3 (5.0 mL). After stirring at 23 °C for 24 h, the PXRD pattern was collected of the reaction mixture.

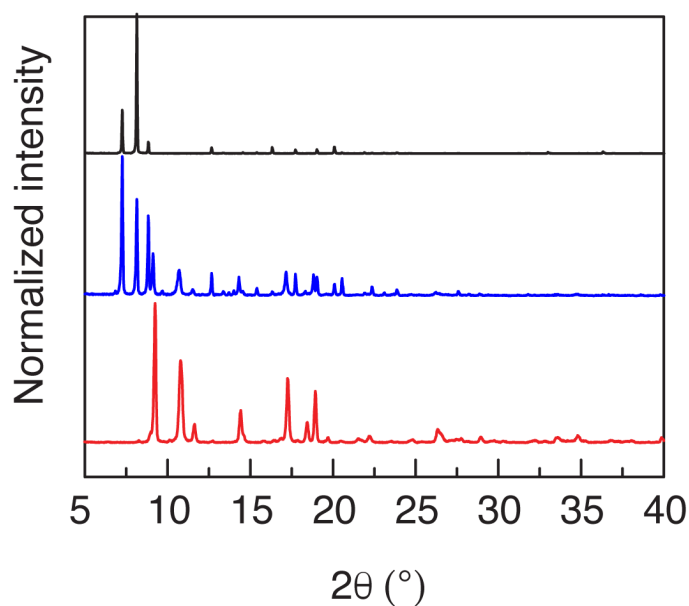


Figure IV-46 Exposure of MOF-508b to 2-(*tert*-butylsulfonyl)iodosylbenzene. PXRD patterns collected of MOF-508b (—), MOF-508b following exposure to iodosylbenzene **4.1** (—), and 2-(*tert*-butylsulfonyl)iodylbenzene (**4.2**, —).

Exposure of MOF-508b to Iodosylbenzene A 20-mL scintillation was charged with MOF-508b (0.100 g, 0.150 mmol, 1.00 equiv), iodosylbenzene (33.0 mg, 0.150 mmol, 1.00 equiv), and CHCl_3 (5.0 mL). After stirring at 23 °C for 24 h, the PXRD pattern was collected of the reaction mixture.

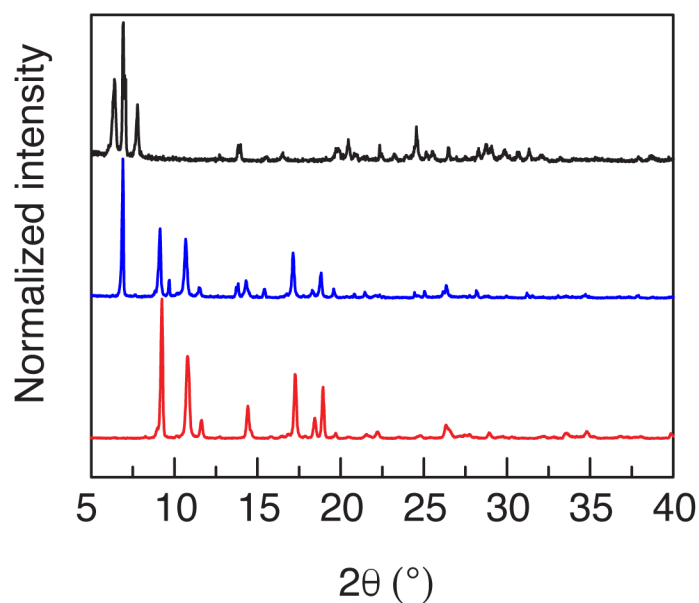


Figure IV-47 Exposure of MOF-508b to iodosylbenzene. PXRD patterns collected of MOF-508b (—), MOF-508b following exposure to iodosylbenzene (—), and iodosylbenzene (—).

IV.4.11 Crystallographic Data

Crystallographic data for **4.1**·HFIP and **4.8** are shown in **Tables IV-7-8**.

Table IV-7 Crystal data and structure refinement for **4.1**·HFIP

<i>Crystal data</i>	
Chemical formula	C ₁₀ H ₁₃ IO ₃ S·C ₃ H ₂ F ₆ O
Fw (g/mol)	508.21
Temperature (K)	110
Crystal system, space group	Monoclinic, <i>P2₁/n</i>
<i>a</i> , <i>b</i> , <i>c</i> (Å)	14.830 (3), 5.5796 (10), 21.816 (4)
α , β , γ (°)	90, 107.885(2), 90
<i>V</i> (Å ³)	1717.9 (5)
<i>Z</i>	4
Radiation type	Mo Ka
μ (mm ⁻¹)	2.06
Crystal size (mm)	0.27 × 0.02 × 0.02
<i>Data collection</i>	
Diffractometer	Bruker <i>APEX-II</i> CCD
Absorption correction	Multi-scan, <i>SADABS</i>
No. of measured, independent and observed [<i>I</i> > 2 σ (<i>I</i>)] reflections	40648, 3527, 2702
<i>R</i> _{int}	0.136
sin(θ/λ) _{max} (Å ⁻¹)	0.628
<i>Refinement</i>	
<i>R</i> [<i>F</i> ² > 2 σ (<i>F</i> ²)], <i>wR</i> (<i>F</i> ²), <i>S</i>	0.038, 0.107, 1.01
No. of reflections	3527
No. of parameters	230
No. of restraints	48
H-atom treatment	H-atom parameters constrained
<i>r</i> _{max} , <i>r</i> _{min} (e Å ⁻³)	1.00, -1.57

Table IV-8 Crystal data and structure refinement for **4.8**

<i>Crystal data</i>	
Chemical formula	C ₈₈ H ₁₁₂ I ₄ O ₄₄ S ₄ Zr ₆ ·16(O)
Fw (g/mol)	3312.93
Temperature (K)	100(2)
Crystal system, space group	Tetragonal, $P\bar{4}2_1c$
<i>a</i> , <i>b</i> , <i>c</i> (Å)	16.574(3), 16.574(3), 26.652(5)
α , β , γ (°)	90, 90, 90
<i>V</i> (Å ³)	7322(3)
<i>Z</i>	2
Radiation type	Synchrotron, $\lambda = 0.33062$ Å
μ (mm ⁻¹)	0.92
Crystal size (mm)	0.07 × 0.07 × 0.05
<i>Data collection</i>	
Diffractometer	Synchrotron, Pilatus3 X CdTe 1M
Absorption correction	Multi-scan, <i>SADABS</i>
No. of measured, independent and observed [<i>I</i> > 2 σ (<i>I</i>)] reflections	178995, 7480, 7057
<i>R</i> _{int}	0.096
sin(θ/λ) _{max} (Å ⁻¹)	0.625
<i>Refinement</i>	
$R[F^2 > 2\sigma(F^2)]$, $wR(F^2)$, <i>S</i>	0.073, 0.195, 1.07
No. of reflections	7480
No. of parameters	373
No. of restraints	48
H-atom treatment	H-atom parameters constrained $w = 1/[\sigma^2(F_o^2) + (0.0781P)^2 + 118.956P]$ where $P = (F_o^2 + 2F_c^2)/3$
<i>r</i> _{max} , <i>r</i> _{min} (e Å ⁻³)	2.07, -1.11

IV.4.12 Additional Data

Figures IV-48 – IV-50 contain additional relevant data.

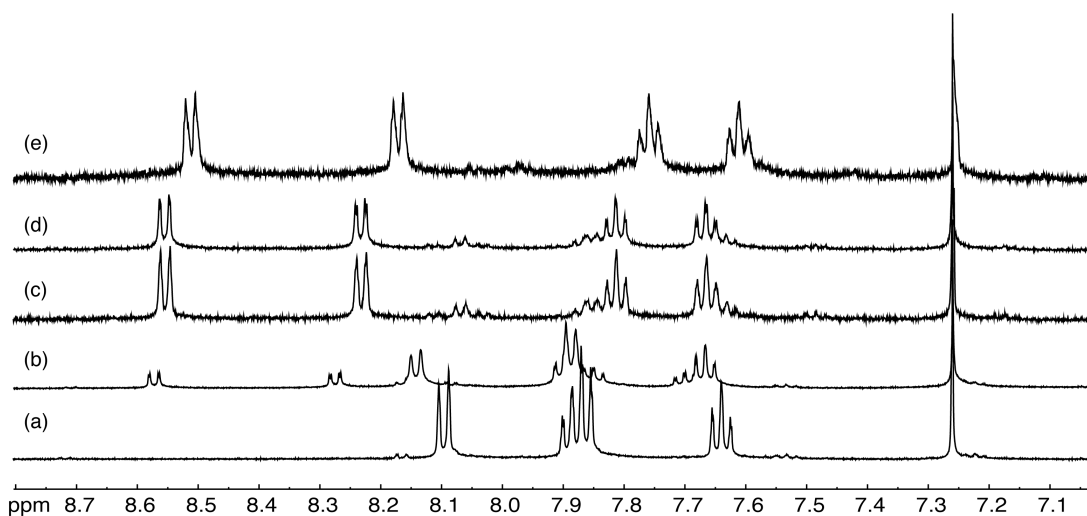


Figure IV-48. Generation of 4.5 from 4.1. ^1H NMR of **4.1** in CDCl_3 at 23 °C with (a) 5 μL , (b) 25 μL , (c) 125 μL , (d) 225 μL , and (e) 325 μL of AcOH. Spectra were referenced to the CHCl_3 signal and the resulting stacked spectra indicate the conversion of **4.1** to **4.5** upon added AcOH.

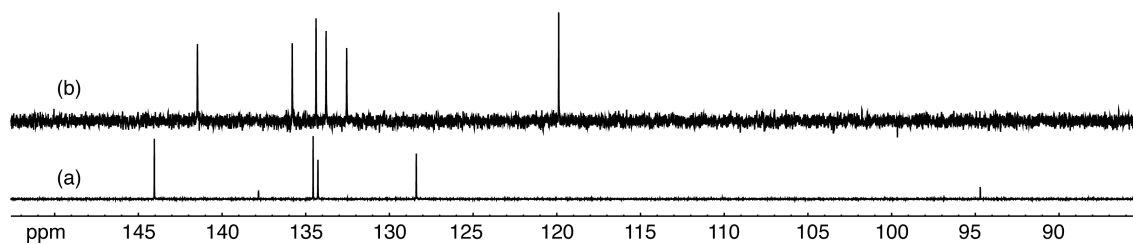


Figure IV-49 $^{13}\text{C}\{^1\text{H}\}$ NMR of 4.5. $^{13}\text{C}\{^1\text{H}\}$ NMR of (a) **3** in CDCl_3 at 23 °C and (b) **4.5** recorded in AcOH-d_6 at 23 °C. Oxidation of **4.3** to **4.5** gives rise to a downfield shift for the peak associated with the carbon connected to the iodine center (94.7 ppm to 120.5 ppm). This is in good agreement with a similar peak shift observed for the oxidation of iodobenzene (94.4 ppm) to (diacetoxyiodo)benzene (122.2 ppm).

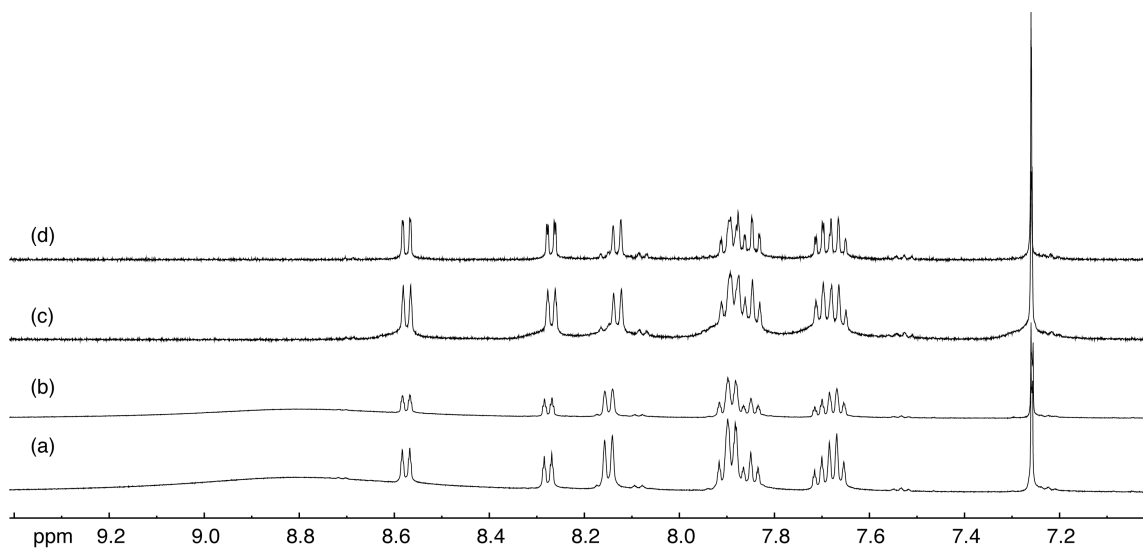


Figure IV-50 ¹H NMR experiment demonstrating equilibrium of 4.1 with AcOD. ¹H NMR in CDCl₃ at 23 °C of 4.1 with AcOD ((a) 5 μL (t = 0 min) (b) 5 μL (t = 20 min), (c) 25 μL (t = 0 min) and (d) 25 μL (t = 20 min)). The initial ¹H NMR shows immediate formation of the 5 and more 5 did not evolve after 20 min, demonstrating that 1 and 5 participate in an equilibrium process with AcOD.

CHAPTER V

CONCLUDING REMARKS AND FUTURE DIRECTIONS

The work presented here describes a suite of efforts towards the goal of developing selective oxidative C–H catalysis with porous materials by utilizing O₂ as a terminal oxidant. Though highly stereoretentive C–H oxidation reactions have been achieved by multiple Zn₂-paddlewheel based materials, efforts towards the use of MOF catalysts have been hindered by low reaction yield and catalyst instability. To move forward, it is necessary to consider MOFs composed of more stable building elements, such as oxozirconium clusters. As we have demonstrated the ability of 2-D layered materials to effect stereoretentive C–H oxidation, analogous materials composed of oxozirconium and oxohafnium clusters should be considered. Though 2-D layered materials featuring these more stable clusters have not yet been reported with porphyrinic linking elements, similar layered materials have been previously synthesized.^{161,256}

Intriguingly, there are no reports of the use of hypervalent iodine reagents as oxidants coupled with oxozirconium based MOFs. In exploratory investigations in our lab that examined the oxidation of hydrocarbons by Fe-PCN-222, a porphyrinic framework composed of oxozirconium clusters, the yield was consistently low (<10%) even though the catalyst appeared unchanged by PXRD. This could be in part due to the possibility of framework interactions with iodosylbenzenes, as described in Chapter IV. For example, coordination of the oxidant to the zirconium cluster would effectively compete with its ability to serve as an oxidant to the porphyrin active site. Though at this time we have been unable to demonstrate interactions of hypervalent iodine reagents with MOFs by PXRD,

there are other techniques that could be considered. For example, Raman spectroscopy may be able to identify the I–O stretch and changes in this stretch could indicate coordination of the hypervalent iodine compound to the framework. In addition, potentiometric titrations have previously been used to identify defect sites in MOFs containing oxozirconium clusters.²⁵⁷ In order to couple the generation of hypervalent iodine compounds by the act of autoxidation of acetaldehyde with MOF catalysis, it is necessary to determine if MOFs of interest are structurally compatible with these reagents.

As the primary goal of the research presented here is the sustainable generation of oxidants coupled with selective C–H oxidation, it is pertinent to consider challenges presented by our current methodology. For example, the utilization of acetaldehyde autoxidation to generate hypervalent iodine intermediates produces acetic acid as a byproduct, which may not be compatible with solid state catalysts. Further, an expansion of the chemistry presented here would include the oxidative installation of other functional groups, for example chlorine or fluorine, onto aliphatic substrates of interest. This could be accomplished by *in situ* ligand exchange at the hypervalent iodine center; however, addition of halogen sources to acetaldehyde-promoted oxidation conditions halt the reaction. This could be due to halogen sources being incompatible with the initiator for the reaction (CoCl_2). Initial investigations into other potential radical initiators have so far been unfruitful, suggesting that the halide salts may not be compatible with acetaldehyde autoxidation for other reasons.

Future growth towards the goal of this project will require both the development of more stable catalytic materials and investigation into the sustainable generation of hypervalent iodine reagents to enhance the compatibility of this process with catalytic reactions.

REFERENCES

1. Gunsalus, N. J.; Koppaka, A.; Park, S. H.; Bischof, S. M.; Hashiguchi, B. G.; Periana, R. A. *Chem. Rev.* **2017**, *117*, 8521–8573.
2. Grant, J. T.; Venegas, J. M.; McDermott, W. P.; Hermans, I. *Chem. Rev.* **2018**, *118*, 2769–2815.
3. White, M. C.; Zhao, J. *J. Am. Chem. Soc.* **2018**, *140*, 13988–14009.
4. Shugrue, C. R.; Miller, S. J. *Chem. Rev.* **2017**, *117*, 11894–11951.
5. Que Jr, L.; Tolman, W. B. *Nature* **2008**, *455*, 333–340.
6. Wang, V. C. C.; Maji, S.; Chen, P. P. Y.; Lee, H. K.; Yu, S. S. F.; Chan, S. I. *Chem. Rev.* **2017**, *117*, 8574–8621.
7. Arndtsen, B. A.; Bergman, R. G.; Mobley, T. A.; Peterson, T. H. *Acc. Chem. Res.* **1995**, *28*, 154–162.
8. Shilov, A. E.; Shul'pin, G. B. *Chem. Rev.* **1997**, *97*, 2879–2932.
9. Copéret, C.; Comas-Vives, A.; Conley, M. P.; Estes, D. P.; Fedorov, A.; Mougél, V.; Nagaé, H.; Núñez-Zarur, F.; Zhizhko, P. A. *Chem. Rev.* **2016**, *116*, 323–421.
10. Liu, J.; Chen, L.; Cui, H.; Zhang, J.; Zhang, L.; Su, C. Y. *Chem. Soc. Rev.* **2014**, *43*, 6011–6061.
11. Ma, L.; Abney, C.; Lin, W. *Chem. Soc. Rev.* **2009**, *38*, 1248–1256.
12. Ma, L.; Falkowski, J. M.; Abney, C.; Lin, W. *Nat. Chem.* **2010**, *2*, 838–846.
13. Huxley, M. T.; Burgun, A.; Ghodrati, H.; Coghlan, C. J.; Lemieux, A.; Champness, N. R.; Huang, D. M.; Doonan, C. J.; Sumbly, C. J. *J. Am. Chem. Soc.* **2018**, *140*, 6416–6425.

14. Liu, J.; Ye, J.; Li, Z.; Otake, K.-i.; Liao, Y.; Peters, A. W.; Noh, H.; Truhlar, D. G.; Gagliardi, L.; Cramer, C. J.; Farha, O. K.; Hupp, J. T. **2018**, *140*, 11174–11178.
15. Cardenal, A. D.; Park, H. J.; Chalker, C. J.; Ortiz, K. G.; Powers, D. C. *Chem. Commun.* **2017**, *53*, 7377–7380.
16. Opanasenko, M. *Catal. Today* **2015**, *243*, 2–9.
17. Gao, W.-Y.; Cardenal, A. D.; Wang, C.-H.; Powers, D. C. *Chem.: Eur. J.* **2019**, *25*, 3465–3476.
18. Maity, A.; Hyun, S.-M.; Powers, D. C. *Nat. Chem.* **2017**, *10*, 200–204.
19. Maity, A.; Hyun, S.-M.; Wortman, A. K.; Powers, D. C. *Angew. Chem.* **2018**, *130*, 7323–7327.
20. Nicolaou, K. C.; Simmons, N. L.; Ying, Y.; Heretsch, P. M.; Chen, J. S. *J. Am. Chem. Soc.* **2011**, *133*, 8134–8137.
21. Turner, C. D. C., M. A. *Arkivoc* **2011**, *i*, 410–428.
22. Ciufolini, M. A. B.; Norbert, A.; Canesi, S.; Ousmer, M.; Chang, J.; Chai, D. *Synthesis* **2007**, *2007*, 3759–3772.
23. Moriarty, R. M. Prakash, O. Oxidation of Phenolic Compounds with Organohypervalent Iodine Reagents. In *Organic Reactions*, Overman, L. E., Ed. John Wiley & Sons, Inc.: 2001; Vol. 57, pp 327-415.
24. Pouységu, L.; Deffieux, D.; Quideau, S. *Tetrahedron* **2010**, *66*, 2235–2261.
25. Samanta, R.; Matcha, K.; Antonchick, A. P. *Eur. J. Org. Chem.* **2013**, 5769–5804.
26. Yoshimura, A.; Zhdankin, V. V. *Chem. Rev.* **2016**, *116*, 3328–3435.

27. Kang, Y.; Li, X.-X.; Cho, K.-B.; Sun, W.; Xia, C.; Nam, W.; Wang, Y. *J. Am. Chem. Soc.* **2017**, *139*, 7444–7447.
28. Farha, O. K.; Shultz, A. M.; Sarjeant, A. A.; Nguyen, S. T.; Hupp, J. T. *J. Am. Chem. Soc.* **2011**, *133*, 5652–5655.
29. Huang, Y. B.; Liang, J.; Wang, X. S.; Cao, R. *Chem. Soc. Rev.* **2017**, *46*, 126–157.
30. Shultz, A. M.; Farha, O. K.; Adhikari, D.; Sarjeant, A. A.; Hupp, J. T.; Nguyen, S. T. *Inorg. Chem.* **2011**, *50*, 3174–3176.
31. Song, F.; Wang, C.; Falkowski, J. M.; Ma, L.; Lin, W. *J. Am. Chem. Soc.* **2010**, *132*, 15390–15398.
32. Xiao, D. J.; Oktawiec, J.; Milner, P. J.; Long, J. R. *J. Am. Chem. Soc.* **2016**, *138*, 14371–14379.
33. Stubbs, A. W.; Braglia, L.; Borfecchia, E.; Meyer, R. J.; Román-Leshkov, Y.; Lamberti, C.; Dincă, M. *ACS Catal.* **2018**, *8*, 596–601.
34. Wang, L.; Agnew, D. W.; Yu, X.; Figueroa, J. S.; Cohen, S. M. *Angew. Chem. Int. Ed.* **2018**, *57*, 511–515.
35. Hendon, C. H.; Rieth, A. J.; Korzyński, M. D.; Dincă, M. *ACS Cent. Sci.* **2017**, *3*, 554–563.
36. Davis, M. E. *Microporous Mesoporous Mater.* **1998**, *21*, 173–182.
37. Vogt, E. T.; Weckhuysen, B. M. *Chem. Soc. Rev.* **2015**, *44*, 7342–7370.
38. Corma, A. *Chem. Rev.* **1997**, *97*, 2373–2420.
39. Smit, B.; Maesen, T. L. *Nature* **2008**, *451*, 671–678.

40. Santos, V. P.; Wezendonk, T. A.; Jaén, J. J. D.; Dugulan, A. I.; Nasalevich, M. A.; Islam, H.-U.; Chojecki, A.; Sartipi, S.; Sun, X.; Hakeem, A. A.; Koeken, A. C. J.; Ruitenbeek, M.; Davidian, T.; Meima, G. R.; Sankar, G.; Kapteijn, F.; Makkee, M.; Gascon, J. *Nat. Commun.* **2015**, *6*, 6451.
41. Phan, A.; Czaja, A. U.; Gándara, F.; Knobler, C. B.; Yaghi, O. M. *Inorg. Chem.* **2011**, *50*, 7388–7390.
42. Ikuno, T.; Zheng, J.; Vjunov, A.; Sanchez-Sanchez, M.; Ortuño, M. A.; Pahls, D. R.; Fulton, J. L.; Camaioni, D. M.; Li, Z.; Ray, D.; Mehdi, B. L.; Browning, N. D.; Farha, O. K.; Hupp, J. T.; Cramer, C. J.; Gagliardi, L.; Lercher, J. A. *J. Am. Chem. Soc.* **2017**, *139*, 10294–10301.
43. Li, Z.; Schweitzer, N. M.; League, A. B.; Bernales, V.; Peters, A. W.; Getsoian, A. B.; Wang, T. C.; Miller, J. T.; Vjunov, A.; Fulton, J. L.; Lercher, J. A.; Cramer, C. J.; Gagliardi, L.; Hupp, J. T.; Farha, O. K. *J. Am. Chem. Soc.* **2016**, *138*, 1977–1982.
44. Park, H. D.; Dincă, M.; Román-Leshkov, Y. *J. Am. Chem. Soc.* **2018**, *140*, 10669–10672.
45. Metzger, E. D.; Brozek, C. K.; Comito, R. J.; Dincă, M. *ACS Cent. Sci.* **2016**, *2*, 148–53.
46. Comito, R. J.; Fritzsching, K. J.; Sundell, B. J.; Schmidt-Rohr, K.; Dincă, M. *J. Am. Chem. Soc.* **2016**, *138*, 10232–10237.
47. Zhu, L.; Liu, X. Q.; Jiang, H. L.; Sun, L. B. *Chem. Rev.* **2017**, *117*, 8129–8176.
48. Cirujano, F. G. *Catal. Sci. Technol.* **2017**, *7*, 5482–5494.
49. Mo, K.; Yang, Y.; Cui, Y. *J. Am. Chem. Soc.* **2014**, *136*, 1746–1749.

50. Xia, Q.; Li, Z.; Tan, C.; Liu, Y.; Gong, W.; Cui, Y. *J. Am. Chem. Soc.* **2017**, *139*, 8259–8266.
51. Cho, S.-H.; Ma, B.; Nguyen, S. T.; Hupp, J. T.; Albrecht-Schmitt, T. E. *Chem. Commun.* **2006**, 2563–2565.
52. Li, B.; Wen, H.-M.; Zhou, W.; Xu, Jeff Q.; Chen, B. *Chem* **2016**, *1*, 557–580.
53. Mason, J. A.; Veenstra, M.; Long, J. R. *Chem. Sci.* **2014**, *5*, 32–51.
54. Li, J.-R.; Sculley, J.; Zhou, H.-C. *Chem. Rev.* **2012**, *112*, 869932.
55. Sumida, K.; Rogow, D. L.; Mason, J. A.; McDonald, T. M.; Bloch, E. D.; Herm, Z. R.; Bae, T.-H.; Long, J. R. *Chem. Rev.* **2012**, *112*, 724781.
56. Hartmann, M.; Machoke, A. G.; Schwieger, W. *Chem. Soc. Rev.* **2016**, *45*, 33133330.
57. Wijngaarden, R. J. K., A. Westerterp, K. R. *Industrial Catalysis: Optimizing Catalysts and Processes*. WILEY-VCH Verlag GmbH: 1998.
58. Boudart, M. *Chem. Rev.* **1995**, *95*, 661-666.
59. Schneider, D.; Mehlhorn, D.; Zeigermann, P.; Karger, J.; Valiullin, R. *Chem. Soc. Rev.* **2016**, *45*, 34393467.
60. Titze, T.; Lauerer, A.; Heinke, L.; Chmelik, C.; Zimmermann, N. E.; Keil, F. J.; Ruthven, D. M.; Karger, J. *Angew. Chem. Int. Ed. Engl.* **2015**, *54*, 14580–14583.
61. Krishna, R. *Chem. Soc. Rev.* **2012**, *41*, 3099–3118.
62. Krishna, R. *J. of Phys. Chem. C* **2009**, *113*, 19756–19781.
63. Petersen, E. E. *AIChE J.* **1958**, *4*, 343–345.
64. Satterfield, C. N. *Mass transfer in heterogeneous catalysis*. M.I.T. Press: 1970.

65. Kärger, J.; Ruthven, D. M.; Theodorou, D. N. *Diffusion in Nanoporous Materials*. Wiley-VCH Verlag & Co. KGaA: 2012; Vol. 1.
66. Hensen, E. J. M.; de Jong, A. M.; van Santen, R. A. *Mol. Sieves* **2008**, *7*, 277–328.
67. Wang, Y.; Zhao, D. *Cryst. Growth Des.* **2017**, *17*, 2291–2308.
68. Chen, K. J.; Madden, D. G.; Pham, T.; Forrest, K. A.; Kumar, A.; Yang, Q. Y.; Xue, W.; Space, B.; Perry, J. J. t.; Zhang, J. P.; Chen, X. M.; Zaworotko, M. J. *Angew. Chem. Int. Ed. Engl.* **2016**, *55*, 10268–10272.
69. Morabito, J. V.; Chou, L.-Y.; Li, Z.; Manna, C. M.; Petroff, C. A.; Kyada, R. J.; Palomba, J. M.; Byers, J. A.; Tsung, C.-K. *J. Am. Chem. Soc.* **2014**, *136*, 12540–12543.
70. Hibbe, F.; Chmelik, C.; Heinke, L.; Pramanik, S.; Li, J.; Ruthven, D. M.; Tzoulaki, D.; Karger, J. *J. Am. Chem. Soc.* **2011**, *133*, 2804–2807.
71. Chmelik, C.; Kärger, J.; Wiebcke, M.; Caro, J.; van Baten, J. M.; Krishna, R. *Microporous Mesoporous Mater.* **2009**, *117*, 22–32.
72. Kärger, J.; Ruthven, D. M. *New J. Chem.* **2016**, *40*, 4027–4048.
73. Kärger, J. *ChemPhysChem* **2015**, *16*, 24–51.
74. Han, S.; Wei, Y.; Valente, C.; Lagzi, I.; Gassensmith, J. J.; Coskun, A.; Stoddart, J. F.; Grzybowski, B. A. *J. Am. Chem. Soc.* **2010**, *132*, 16358–16361.
75. Karge, H. G.; Nießen, W. *Catal. Today* **1991**, *8*, 451–465.
76. Heinke, L.; Chmelik, C.; Kortunov, P.; Ruthven, D. M.; Shah, D. B.; Vasenkov, S.; Kärger, J. *Chem. Eng. Technol.* **2007**, *30*, 995–1002.

77. Heinke, L.; Tzoulaki, D.; Chmelik, C.; Hibbe, F.; van Baten, J. M.; Lim, H.; Li, J.; Krishna, R.; Kärger, J. *Phys. Rev. Lett.* **2009**, *102*, 065901.
78. Zhao, Z.; Li, X.; Huang, S.; Xia, Q.; Li, Z. *Ind. Eng. Chem. Res.* **2011**, *50*, 2254–2261.
79. Zhao, Z.; Li, Z.; Lin, Y. S. *Ind. Eng. Chem. Res.* **2009**, *48*, 10015–10020.
80. Tovar, T. M.; Zhao, J.; Nunn, W. T.; Barton, H. F.; Peterson, G. W.; Parsons, G. N.; LeVan, M. D. *J. Am. Chem. Soc.* **2016**, *138*, 11449–11452.
81. Zybaylo, O.; Shekhah, O.; Wang, H.; Tafipolsky, M.; Schmid, R.; Johannsmann, D.; Woll, C. *PCCP* **2010**, *12*, 8093–8098.
82. Eic, M.; Ruthven, D. M. *Zeolites* **1988**, *8*, 40–45.
83. Liu, J.; Wang, Y.; Benin, A. I.; Jakubczak, P.; Willis, R. R.; LeVan, M. D. *Langmuir* **2010**, *26*, 14301–14307.
84. Jobic, H.; Kärger, J.; Bée, M. *Phys. Rev. Lett.* **1999**, *82*, 4260–4263.
85. Salles, F.; Jobic, H.; Ghoufi, A.; Llewellyn, P. L.; Serre, C.; Bourrelly, S.; Férey, G.; Maurin, G. *Angew. Chem. Int. Ed.* **2009**, *48*, 8335–8339.
86. Stejskal, E. O.; Tanner, J. E. *J. Chem. Phys.* **1965**, *42*, 288–292.
87. Kärger, J.; Pfeifer, H.; Heink, W., Principles and Application of Self-Diffusion Measurements by Nuclear Magnetic Resonance. In *Advances in Magnetic and Optical Resonance*, Waugh, J. S., Ed. Academic Press: 1988; Vol. 12, pp 1–89.
88. Brandani, S.; Hufton, J.; Ruthven, D. *Zeolites* **1995**, *15*, 624–631.

89. Schumacher, R. R.; Anderson, B. G.; Noordhoek, N. J.; de Gauw, F. J. M. M.; de Jong, A. M.; de Voigt, M. J. A.; van Santen, R. A. *Microporous Mesoporous Mater.* **2000**, *35-36*, 315–326.
90. Chmelik, C.; Enke, D.; Galvosas, P.; Gobin, O.; Jentys, A.; Jobic, H.; Karger, J.; Krause, C. B.; Kullmann, J.; Lercher, J.; Naumov, S.; Ruthven, D. M.; Titze, T. *Chemphyschem* **2011**, *12*, 1130–1134.
91. Li, K.; Olson, D. H.; Seidel, J.; Emge, T. J.; Gong, H.; Zeng, H.; Li, J. *J. Am. Chem. Soc.* **2009**, *131*, 10368–10369.
92. Wang, C.; Lin, W. *J. Am. Chem. Soc.* **2011**, *133*, 4232–4235.
93. Pillai, R. S.; Jobic, H.; Koza, M. M.; Nouar, F.; Serre, C.; Maurin, G.; Ramsahye, N. *A. Chemphyschem* **2017**, *18*, 2739–2746.
94. Li, L.; Bell, J. G.; Tang, S.; Lv, X.; Wang, C.; Xing, Y.; Zhao, X.; Thomas, K. M. *Chem. Mater.* **2014**, *26*, 4679–4695.
95. Heinke, L.; Gu, Z.; Woll, C. *Nat. Commun.* **2014**, *5*, 4562.
96. Zhang, L.; Chmelik, C.; van Laak, A. N. C.; Kärger, J.; de Jongh, P. E.; de Jong, K. *P. Chem. Commun.* **2009**, 6424–6426.
97. Tanaka, S.; Fujita, K.; Miyake, Y.; Miyamoto, M.; Hasegawa, Y.; Makino, T.; Van der Perre, S.; Cousin Saint Remi, J.; Van Assche, T.; Baron, G. V.; Denayer, J. F. M. *J. Phys. Chem. C* **2015**, *119*, 28430–28439.
98. Yucel, H.; Ruthven, D. M. *J. Chem. Soc., Faraday Trans. 1* **1980**, *76*, 60–70.
99. Yucel, H.; Ruthven, D. M. *J. Chem. Soc., Faraday Trans. 1* **1980**, *76*, 71–83.
100. Zhang, Z.; Huang, S.; Xian, S.; Xi, H.; Li, Z. *Energy & Fuels* **2011**, *25*, 835–842.

101. Rives, S.; Jobic, H.; Kolokolov, D. I.; Gabrienko, A. A.; Stepanov, A. G.; Ke, Y.; Frick, B.; Devic, T.; Férey, G.; Maurin, G. *J. Phys. Chem. C* **2013**, *117*, 6293–6302.
102. Kortunov, P. V.; Heinke, L.; Arnold, M.; Nedellec, Y.; Jones, D. J.; Caro, J.; Kärger, J. *J. Am. Chem. Soc.* **2007**, *129*, 8041–8047.
103. Lee, C. Y.; Bae, Y. S.; Jeong, N. C.; Farha, O. K.; Sarjeant, A. A.; Stern, C. L.; Nickias, P.; Snurr, R. Q.; Hupp, J. T.; Nguyen, S. T. *J. Am. Chem. Soc.* **2011**, *133*, 5228–5231.
104. Han, S.; Hermans, T. M.; Fuller, P. E.; Wei, Y.; Grzybowski, B. A. *Angew. Chem. Int. Ed. Engl.* **2012**, *51*, 2662–2666.
105. Yang, X.; Yuan, S.; Zou, L.; Drake, H.; Zhang, Y.; Qin, J.; Alsalmé, A.; Zhou, H.-C. *Angew. Chem. Int. Ed.* **2018**, *57*, 3927–3932.
106. Kuo, C.-H.; Tang, Y.; Chou, L.-Y.; Sneed, B. T.; Brodsky, C. N.; Zhao, Z.; Tsung, C.-K. *J. Am. Chem. Soc.* **2012**, *134*, 14345–14348.
107. Eddaoudi, M.; Kim, J.; Rosi, N.; Vodak, D.; Wachter, J.; O’Keeffe, M.; Yaghi, O. M. *Science* **2002**, *295*, 469–472.
108. Xiao, D. J.; Bloch, E. D.; Mason, J. A.; Queen, W. L.; Hudson, M. R.; Planas, N.; Borycz, J.; Dzubak, A. L.; Verma, P.; Lee, K.; Bonino, F.; Crocellà, V.; Yano, J.; Bordiga, S.; Truhlar, D. G.; Gagliardi, L.; Brown, C. M.; Long, J. R. *Nat. Chem.* **2014**, *6*, 590.
109. Folger, H. S. *Elements of Chemical Reaction Engineering*. Fourth edition. ed.; Prentice Hall PTR: Upper Saddle River, NJ, 2006.

110. Tonigold, M.; Lu, Y.; Bredenkötter, B.; Rieger, B.; Bahnmüller, S.; Hitzbleck, J.; Langstein, G.; Volkmer, D. *Angew. Chem. Int. Ed.* **2009**, *48*, 7546–7550.
111. Dhakshinamoorthy, A.; Alvaro, M.; Hwang, Y. K.; Seo, Y.-K.; Corma, A.; Garcia, H. *Dalton Transactions* **2011**, *40*, 10719–10724.
112. Bauer, G.; Ongari, D.; Xu, X.; Tiana, D.; Smit, B.; Ranocchiari, M. *J. Am. Chem. Soc.* **2017**, *139*, 18166–18169.
113. Liu, L.; Zhou, T.-Y.; Telfer, S. G. *J. Am. Chem. Soc.* **2017**, *139*, 13936–13943.
114. Zheng, M.; Liu, Y.; Wang, C.; Liu, S.; Lin, W. *Chem. Sci.* **2012**, *3*, 2623–2627.
115. Mancinelli, R.; Imberti, S.; Soper, A. K.; Liu, K. H.; Mou, C. Y.; Bruni, F.; Ricci, M. *J. Phys. Chem. B* **2009**, *113*, 16169–16177.
116. Falkowska, M.; Bowron, D. T.; Manyar, H.; Youngs, T. G. A.; Hardacre, C. *Angew. Chem. Int. Ed.* **2018**, *57*, 4565–4570.
117. Alba-Simionesco, C.; Dosseh, G.; Dumont, E.; Frick, B.; Geil, B.; Morineau, D.; Teboul, V.; Xia, Y. *Eur. Phys. J. E* **2003**, *12*, 19–28.
118. Abdel Hamid, A. R.; Mhanna, R.; Lefort, R.; Ghoufi, A.; Alba-Simionesco, C.; Frick, B.; Morineau, D. *J. Phys. Chem. C* **2016**, *120*, 9245–9252.
119. Wang, C.-H.; Das, A.; Gao, W.-Y.; Powers, D. C. *Angew. Chem. Int. Ed.* **2018**, *57*, 3676–3681.
120. Baertsch, C. D.; Funke, H. H.; Falconer, J. L.; Noble, R. D. *J. Phys. Chem.* **1996**, *100*, 7676–7679.
121. Clardy, J.; Walsh, C. *Nature* **2004**, *432*, 829–837.
122. Meunier, B.; de Visser, S. P.; Shaik, S. *Chem. Rev.* **2004**, *104*, 3947–3980.

123. Newhouse, T.; Baran, P. S. *Angew. Chem. Int. Ed.* **2011**, *50*, 3362–3374.
124. Zhang, K.; Shafer, B. M.; Demars, M. D.; Stern, H. A.; Fasan, R. *J. Am. Chem. Soc.* **2012**, *134*, 18695–18704.
125. Genovino, J.; Lütz, S.; Sames, D.; Touré, B. B. *J. Am. Chem. Soc.* **2013**, *135*, 12346–12352.
126. Abrahams, B. F.; Hoskins, B. F.; Robson, R. *J. Am. Chem. Soc.* **1991**, *113*, 3606–3607.
127. Yaghi, O. M.; Li, G.; Li, H. *Nature* **1995**, *378*, 703–706.
128. Li, H.; Eddaoudi, M.; O'Keeffe, M.; Yaghi, O. M. *Nature* **1999**, *402*, 276–279.
129. Suslick, K. S.; Bhyrappa, P.; Chou, J. H.; Kosal, M. E.; Nakagaki, S.; Smithenry, D. W.; Wilson, S. R. *Acc. Chem. Res.* **2005**, *38*, 283–291.
130. Gao, W.-Y.; Chrzanowski, M.; Ma, S. *Chem. Soc. Rev.* **2014**, *43*, 5841–5866.
131. Kosal, M. E.; Chou, J.-H.; Wilson, S. R.; Suslick, K. S. *Nat. Mat.* **2002**, *1*, 118–121.
132. Shultz, A. M.; Farha, O. K.; Hupp, J. T.; Nguyen, S. T. *J. Am. Chem. Soc.* **2009**, *131*, 4204–4205.
133. Lv, X.-L.; Wang, K.; Wang, B.; Su, J.; Zou, X.; Xie, Y.; Li, J.-R.; Zhou, H.-C. *J. Am. Chem. Soc.* **2017**, *139*, 211–217.
134. Choi, E.-Y.; Barron, P. M.; Novotny, R. W.; Son, H.-T.; Hu, C.; Choe, W. *Inorg. Chem.* **2009**, *48*, 426–428.
135. Chung, H.; Barron, P. M.; Novotny, R. W.; Son, H.-T.; Hu, C.; Choe, W. *Cryst. Growth Des.* **2009**, *9*, 3327–3332.

136. Barron, P. M.; Wray, C. A.; Hu, C.; Guo, Z.; Choe, W. *Inorg. Chem.* **2010**, *49*, 10217–10219.
137. Abrahams, B. F.; Hoskins, B. F.; Michail, D. M.; Robson, R. *Nature* **1994**, *369*, 727–729.
138. Serre, C.; Millange, F.; Thouvenot, C.; Noguès, M.; Marsolier, G.; Louër, D.; Férey, G. *J. Am. Chem. Soc.* **2002**, *124*, 13519–13526.
139. Kitagawa, S.; Kitaura, R.; Noro, S.-i. *Angew. Chem. Int. Ed.* **2004**, *43*, 2334–2375.
140. Sato, H.; Kosaka, W.; Matsuda, R.; Hori, A.; Hijikata, Y.; Belosludov, R. V.; Sakaki, S.; Takata, M.; Kitagawa, S. *Science* **2014**, *343*, 167–170.
141. Mason, J. A.; Oktawiec, J.; Taylor, M. K.; Hudson, M. R.; Rodriguez, J.; Bachman, J. E.; Gonzalez, M. I.; Cervellino, A.; Guagliardi, A.; Brown, C. M.; Llewellyn, P. L.; Masciocchi, N.; Long, J. R. *Nature* **2015**, *527*, 357–361.
142. Burnett, B. J.; Barron, P. M.; Hu, C.; Choe, W. *J. Am. Chem. Soc.* **2011**, *133*, 9984–9987.
143. Takaishi, S.; DeMarco, E. J.; Pellin, M. J.; Farha, O. K.; Hupp, J. T. *Chemical Science* **2013**, *4*, 1509–1513.
144. Bartlett, P. D.; Pincock, R. E.; Rolston, J. H.; Schindel, W. G.; Singer, L. A. *J. Am. Chem. Soc.* **1965**, *87*, 2590–2596.
145. Groves, J. T.; Nemo, T. E. *J. Am. Chem. Soc.* **1983**, *105*, 6243–6248.
146. Gao, F.; Boyles, D.; Sullivan, R.; Compton, R. N.; Pagni, R. M. *J. Org. Chem.* **2002**, *67*, 9361–9367.

147. Macikenas, D.; Skrzypczak-Jankun, E.; Protasiewicz, J. D. *J. Am. Chem. Soc.* **1999**, *121*, 7164–7165.
148. Pangborn, A. B.; Giardello, M. A.; Grubbs, R. H.; Rosen, R. K.; Timmers, F. J. *Organometallics* **1996**, *15*, 1518–1520.
149. Armarego, W. L.; Li Lin Chai, C. *Purification of Laboratory Chemicals*. 5 ed.; Butterworth Heinemann: 2003.
150. Katsuhiko, I.; Yukiharu, N.; Hiroshi, K. *Bull. Chem. Soc. Jpn.* **1980**, *53*, 565–566.
151. Lee, S.; Fuchs, P. L. *J. Am. Chem. Soc.* **2002**, *124*, 13978–13979.
152. Daly, D.; Al-Sabi, A.; Kinsella, G. K.; Nolan, K.; Dolly, J. O. *Chem. Commun.* **2015**, *51*, 1066–1069.
153. de Carvalho, A. L.; Ferreira, B. F.; Martins, C. H. G.; Nassar, E. J.; Nakagaki, S.; Machado, G. S.; Rives, V.; Trujillano, R.; Vicente, M. A.; Gil, A.; Korili, S. A.; de Faria, E. H.; Ciuffi, K. J. *J. Phys. Chem. C* **2014**, *118*, 24562–24574.
154. Fulmer, G. R.; Miller, A. J. M.; Sherden, N. H.; Gottlieb, H. E.; Nudelman, A.; Stoltz, B. M.; Bercaw, J. E.; Goldberg, K. I. *Organometallics* **2010**, *29*, 2176–2179.
155. Liu, Y. Y.; Li, J.; Ma, J. F.; Ma, J. C.; Yang, J. *CrystEngComm* **2012**, *14*, 169–177.
156. Choi, E.-Y.; Wray, C. A.; Hu, C.; Choe, W. *CrystEngComm* **2009**, *11*, 553–555.
157. Park, J.; Jiang, Q.; Feng, D.; Mao, L.; Zhou, H.-C. *J. Am. Chem. Soc.* **2016**, *138*, 3518–3525.
158. Brunsteiner, M.; Jones, A. G.; Pratola, F.; Price, S. L.; Simons, S. J. R. *Crystal Growth & Design* **2005**, *5*, 3–16.

159. Gielen, B.; Jordens, J.; Thomassen, C. L.; Braeken, L.; Van Gerven, T. *Crystals* **2017**, 7–9.
160. Zou, C.; Zhang, T.; Xie, M.-H.; Yan, L.; Kong, G.-Q.; Yang, X.-L.; Ma, A.; Wu, C.-D. *Inorg. Chem.* **2013**, 52, 3620–3626.
161. Shi, W.; Cao, L.; Zhang, H.; Zhou, X.; An, B.; Lin, Z.; Dai, R.; Li, J.; Wang, C.; Lin, W. *Angew. Chem. Int. Ed.* **2017**, 56, 9704–9709.
162. Farokhi, A.; Hosseini-Monfared, H. *New J. Chem.* **2016**, 40, 5032–5043.
163. Howard, J. A. *Homogeneous Liquid Phase Autoxidations in Free Radicals*. John Wiley & Sons: New York, 1973.
164. Walling, C. *Autoxidation*. Eds. Blackie Academic and Professional: New York, 1995.
165. Greenwood, N. N.; Earnshaw, A. *Chemistry of the Elements*. Elsevier: 2012.
166. Pauling, L. *The Nature of the Chemical Bond*. Cornell university press Ithaca, NY: 1960; Vol. 260.
167. Boschloo, G.; Hagfeldt, A. *Acc. Chem. Res.* **2009**, 42, 1819–1826.
168. Davies, C. G.; Gillespie, R. J.; Ireland, P. R.; Sowa, J. M. *Can. J. Chem.* **1974**, 52, 2048–2052.
169. Kemmitt, R. D. W.; Murray, M.; McRae, V. M.; Peacock, R. D.; Symons, M. C. R.; Odonnell, R. A. *J. Chem. Soc. A* **1968**, 862–866.
170. Faggiani, R.; Gillespie, R. J.; Kapoor, R.; Lock, C. J. L.; Vekris, J. E. *Inorg. Chem.* **1988**, 27, 4350–4355.
171. Gillespie, R. J.; Kapoor, R.; Faggiani, R.; Lock, C. J. L.; Murchie, M.; Passmore, J. *J. Chem. Soc. Chem. Commun.* **1983**, 8–9.

172. Willgerodt, C. *J. Prakt. Chem.* **1886**, 33, 154–160.
173. Musher, J. I. *Angew. Chem. Int. Ed.* **1969**, 8, 54–68.
174. Powell, W. H. *Pure Appl. Chem.* **1984**, 56, 769–778.
175. Martin, J. C. *Science* **1983**, 221, 509–514.
176. Perkins, C. W.; Martin, J. C.; Arduengo, A. J.; Lau, W.; Alegria, A.; Kochi, J. K. *J. Am. Chem. Soc.* **1980**, 102, 7753–7759.
177. Zhdankin, V. V.; Stang, P. J. *Chem. Rev.* **2002**, 102, 2523–2584.
178. Stang, P. J.; Zhdankin, V. V. *Chem. Rev.* **1996**, 96, 1123–1178.
179. Zhdankin, V. V. *Hypervalent Iodine Chemistry: Preparation, Structure and Synthetic Applications of Polyvalent Iodine Compounds*. John Wiley and Sons Ltd.: New York, 2014.
180. Ladziata, U.; Zhdankin, V. V. *Arkivoc* **2006**, 9, 26–58.
181. Reed, A. E.; Schleyer, P. v. R. *J. Am. Chem. Soc.* **1990**, 112, 1434–1445.
182. Hach, R. J.; Rundle, R. E. *J. Am. Chem. Soc.* **1951**, 73, 4321–4324.
183. Pimentel, G. C. *J. Chem. Phys.* **1951**, 19, 446–448.
184. Wang, W. *J. of Phys. Chem. A* **2011**, 115, 9294–9299.
185. Cavallo, G.; Metrangolo, P.; Milani, R.; Pilati, T.; Priimagi, A.; Resnati, G.; Terraneo, G. *Chem. Rev.* **2016**, 116, 2478–2601.
186. Ochiai, M.; Sueda, T.; Miyamoto, K.; Kiprof, P.; Zhdankin, V. V. *Angew. Chem. Int. Ed.* **2006**, 45, 8203–8206.
187. Ivanov, A. S.; Popov, I. A.; Boldyrev, A. I.; Zhdankin, V. V. *Angew. Chem. Int. Ed.* **2014**, 53, 9617–9621.

188. Katritzky, A. R.; Gallos, J. K.; Durst, H. D. *Magn. Reson. Chem.* **1989**, *27*, 815–822.
189. Hiller, A.; Patt, J. T.; Steinbach, J. *Magn. Reson. Chem.* **2006**, *44*, 955–958.
190. Carmalt, C. J.; Crossley, J. G.; Knight, J. G.; Lightfoot, P.; Martín, A.; Muldowney, M. P.; Norman, N. C.; Orpen, A. G. *J. Chem. Soc. Chem. Commun.* **1994**, 2367–2368.
191. Nemykin, V. N.; Koposov, A. Y.; Netzel, B. C.; Yusubov, M. S.; Zhdankin, V. V. *Inorg. Chem.* **2009**, *48*, 4908–4917.
192. Koposov, A. Y.; Karimov, R. R.; Pronin, A. A.; Skrupskaya, T.; Yusubov, M. S.; Zhdankin, V. V. *J. Org. Chem.* **2006**, *71*, 9912–9914.
193. Lucas, H. J. Kennedy, E. R. *Org. Synth.* **1942**, *22*, 72.
194. Vasconcelos, R. S.; Silva, L. F.; Lopes, N. P. *Quim. Nova* **2012**, *35*, 1593–1599.
195. Ochiai, M., Reactivities, properties and structures. In *Hypervalent Iodine Chemistry*, Springer: 2003; pp 5–68.
196. Koser, G. F.; Wettach, R. H. *J. Org. Chem.* **1980**, *45*, 4988–4989.
197. Moriarty, R. M.; Prakash, O. *Acc. Chem. Res.* **1986**, *19*, 244–250.
198. McDonald, A. R.; Que Jr, L. *Coord. Chem. Rev.* **2013**, *257*, 414–428.
199. Yamada, Y.; Kashima, K.; Okawara, M. *Bull. Chem. Soc. Japan* **1974**, *47*, 3179–3180.
200. England, J.; Guo, Y.; Farquhar, E. R.; Young Jr, V. G.; Münck, E.; Que Jr, L. *J. Am. Chem. Soc.* **2010**, *132*, 8635–8644.
201. England, J.; Martinho, M.; Farquhar, E. R.; Frisch, J. R.; Bominaar, E. L.; Münck, E.; Que Jr, L. *Angew. Chem. Int. Ed.* **2009**, *48*, 3622–3626.

202. Moriarty, R. M. P., O., Oxidation of Carbonyl Compounds with Organohypervalent Iodine Reagents. In *Organic Reactions*, Paquette, L. A., Ed. John Wiley & Sons, Inc.: 2004; Vol. 54, pp 273–415.
203. Moreno, I.; Tellitu, I.; Herrero, M. T.; SanMartin, R.; Dominguez, E. *Curr. Org. Chem.* **2002**, *6*, 1433–1452.
204. Charpentier, J.; Fruh, N.; Togni, A. *Chem. Rev.* **2014**, *115*, 650–682.
205. The secondary bonding interactions that are responsible for the availability of monomeric iodosylarene 4.1 could also be described as interactions of the pendent sulfonylgroup with the sigma-hole of the I-O bond. See Polotizer, P.; Murray, J. S.; Clark, T. *Phys. Chem. Chem. Phys.* **2013**, *15*, 11178–11189.
206. Sajith, P. K.; Suresh, C. H. *Inorg. Chem.* **2012**, *51*, 967–977.
207. Macikenas, D.; Skrzypczak-Jankun, E.; Protasiewicz, J. D. *Angew. Chem. Int. Ed.* **2000**, *39*, 2007–2010.
208. Kita, Y.; Morimoto, K.; Ito, M.; Ogawa, C.; Goto, A.; Dohi, T. *J. Am. Chem. Soc.* **2009**, *131*, 1668–1669.
209. Kita, Y.; Tohma, H.; Hatanaka, K.; Takada, T.; Fujita, S.; Mitoh, S.; Sakurai, H.; Oka, S. *J. Am. Chem. Soc.* **1994**, *116*, 3684–3691.
210. Hamamoto, H.; Hata, K.; Nambu, H.; Shiozaki, Y.; Tohma, H.; Kita, Y. *Tetrahedron Lett.* **2004**, *45*, 2293–2295.
211. Dohi, T.; Ito, M.; Yamaoka, N.; Morimoto, K.; Fujioka, H.; Kita, Y. *Angew. Chem. Int. Ed.* **2010**, *49*, 3334–3337.
212. Schardt, B. C.; Hill, C. L. *Inorg. Chem.* **1983**, *22*, 1563–1565.

213. Kajiyama, D.; Saitoh, T.; Nishiyama, S. *Electrochemistry* **2013**, *81*, 319–324.
214. Koleda, O.; Broese, T.; Noetzel, J.; Roemelt, M.; Suna, E.; Francke, R. *J. Org. Chem.* **2017**, *82*, 11669–11681.
215. Broese, T.; Francke, R. *Org. Lett.* **2016**, *18*, 5896–5899.
216. Richter, H. W.; Cherry, B. R.; Zook, T. D.; Koser, G. F. *J. Am. Chem. Soc.* **1997**, *119*, 9614–9623.
217. Macikenas, D.; Skrzypczak-Jankun, E.; Protasiewicz, J. D. *J. Am. Chem. Soc.* **2011**, *133*, 4151–4151.
218. Guo, M.; Dong, H.; Li, J.; Cheng, B.; Huang, Y.-q.; Feng, Y.-q.; Lei, A. *Nat. Commun.* **2012**, *3*, 1190.
219. Sankar, M.; Nowicka, E.; Carter, E.; Murphy, D. M.; Knight, D. W.; Bethell, D.; Hutchings, G. J. *Nat. Commun.* **2014**, *5*, 3332.
220. Domae, M.; Katsumara, Y.; Jiang, P. Y.; Nagaishi, R.; Hasegawa, C.; Ishigure, K.; Yoshida, Y. *J. Phys. Chem.* **1994**, *98*, 190–192.
221. Çatir, M.; Kilic, H.; Nardello-Rataj, V.; Aubry, J.-M.; Kazaz, C. *J. Org. Chem.* **2009**, *74*, 4560–4564.
222. Catir, M. *Turk. J. Chem.* **2017**, *41*, 467–475.
223. Dey, D.; Roy, S.; Dutta Purkayastha, R. N.; Pallepogu, R.; Male, L.; McKee, V. *J. Coord. Chem.* **2011**, *64*, 1165–1176.
224. Kickelbick, G.; Schubert, U. *Chem. Ber.* **1997**, *130*, 473–478.
225. Kogler, F. R.; Jupa, M.; Puchberger, M.; Schubert, U. *J. Mater. Chem.* **2004**, *14*, 3133–3138.

226. Kalmutzki, M. J.; Hanikel, N.; Yaghi, O. M. *Sci. Adv.* **2018**, *4*, eaat9180.
227. Yuan, S.; Qin, J.-S.; Lollar, C. T.; Zhou, H.-C. *ACS Cent. Sci.* **2018**, *4*, 440–450.
228. Protasiewicz, J. D., Organiodine(III) Reagents as Active Participants and Ligands in Transition Metal-Catalyzed Reactions: Iodosylarenes and (Imino)iodoarenes. In *Hypervalent Iodine Chemistry*, Wirth, T., Ed. Springer International Publishing: Cham, 2016; pp 263–288.
229. de Ruiter, G.; Carsch, K. M.; Gul, S.; Chatterjee, R.; Thompson, N. B.; Takase, M. K.; Yano, J.; Agapie, T. *Angew. Chem. Int. Ed.* **2017**, *56*, 4772–4776.
230. Hill, E. A.; Kelty, M. L.; Filatov, A. S.; Anderson, J. S. *Chem. Sci.* **2018**, *9*, 4493–4499.
231. Lennartson, A.; McKenzie, C. J. *Angew. Chem. Int. Ed.* **2012**, *51*, 6767–6770.
232. Wang, C.; Kurahashi, T.; Fujii, H. *Angew. Chem. Int. Ed.* **2012**, *51*, 7809–7811.
233. Turlington, C. R.; Morris, J.; White, P. S.; Brennessel, W. W.; Jones, W. D.; Brookhart, M.; Templeton, J. L. *Organometallics* **2014**, *33*, 4442–4448.
234. Cavka, J. H.; Jakobsen, S.; Olsbye, U.; Guillou, N.; Lamberti, C.; Bordiga, S.; Lillerud, K. P. *J. Am. Chem. Soc.* **2008**, *130*, 13850–13851.
235. Chen, B.; Liang, C.; Yang, J.; Contreras, D. S.; Clancy, Y. L.; Lobkovsky, E. B.; Yaghi, O. M.; Dai, S. *Angew. Chem. Int. Ed.* **2006**, *45*, 1390–1393.
236. MOF-508 features a nominal pore size of $4.0 \times 4.0 \text{ \AA}$ and compound **4.1** has an approximate van der Waals diameter of 7.6 \AA , suggesting that it is too large to enter the pores of MOF-508. However, MOF-508 displays network flexibility and has been demonstrated to uptake guests larger than the nominal pore size (i.e 2,2-

- dimethylbutane, van der Waals di-ameter of 6.3 Å. Goblin, O. C.; Reitmeier, S. J.; Jentys, A.; Lercher, J. A. *J. Phys. Chem. C* **2011**, *115*, 1171–1179).
237. H. Saltzman, J. G. S. *Organic Synthesis* **1963**, *43*.
238. Katz, M. J.; Brown, Z. J.; Colón, Y. J.; Siu, P. W.; Scheidt, K. A.; Snurr, R. Q.; Hupp, J. T.; Farha, O. K. *Chem. Commun.* **2013**, *49*, 9449–9451.
239. Cavani, F.; Teles, J. H. *Chemsuschem* **2009**, *2*, 508–534.
240. Reich, H. J. Fluorine Shifts Overview.
<https://www.chem.wisc.edu/areas/reich/nmr/11-f-data.htm> (accessed 04/18/2019).
241. Stoll, S.; Schweiger, A. *J. Magn. Reson.* **2006**, *178*, 42–55.
242. Sheldrick, G. M. SADABS Program for Absorption Correction for Data of Area Detector Frame. BRUKER AXS Inc., 5465 East Cheryl Parkway, Madison, WI 53711–5373, USA **2000**.
243. Dolomanov, O. V.; Bourhis, L. J.; Gildea, R. J.; Howard, J. A. K.; Puschmann, H. *J. Appl. Cryst.* **2009**, *42*, 339–341.
244. Sheldrick, G. M. *Acta Crystallographica a-Foundation and Advances* **2008**, *64*, 112–122.
245. Sheldrick, G. M. *Acta Crystallographica a-Foundation and Advances* **2015**, *71*, 3–8.
246. Lee, C. T.; Yang, W. T.; Parr, R. G. *Phys. Rev. B* **1988**, *37*, 785–789.
247. Perdew, J. P.; Burke, K.; Ernzerhof, M. *Phys. Rev. Lett.* **1996**, *77*, 3865–3868.
248. Perdew, J. P.; Burke, K.; Ernzerhof, M. *Phys. Rev. Lett.* **1997**, *78*, 1396–1396.
249. Adamo, C.; Barone, V. *J. Chem. Phys.* **1999**, *110*, 6158–6170.
250. Jr., T. H. D.; Hay, P. J. in *Modern Theoretical Chemistry*. 1977; Vol. 3.

251. Kendall, R. A.; Dunning, T. H.; Harrison, R. J. *J. Chem. Phys.* **1992**, *96*, 6796–6806.
252. Woon, D. E.; Dunning, T. H. *J. Chem. Phys.* **1993**, *98*, 1358–1371.
253. Marenich, A. V.; Cramer, C. J.; Truhlar, D. G. *J. Phys. Chem. B* **2009**, *113*, 6378–6396.
254. Glendening, E. D.; Badenhop, J. K.; Reed, A. E.; Carpenter, J. E.; Bohmann, J. A.; Morales, C. M.; Landis, C. R.; Weinhold, F. Theoretical Institute, University of Wisconsin, Madison, WI, 2013. <http://nbo6.chem.wisc.edu>.
255. Drago, R. S. *Physical Methods for Chemists*. 2 ed.; Surfside Scientific Publishers: Gainesville, FL, 1992.
256. Zhao, M.; Huang, Y.; Peng, Y.; Huang, Z.; Ma, Q.; Zhang, H. *Chem. Soc. Rev.* **2018**, *47*, 6267–6295.
257. Klet, R. C.; Liu, Y.; Wang, T. C.; Hupp, J. T.; Farha, O. K. *J. Mat. Chem. A* **2016**, *4*, 1479–1485.